Proceedings of the 23rd Meeting of Japan CF Research Society
JCF23

March 4-5, 2023

Waseda University,

Tokyo Japan

Japan CF-Research Society

Edited by Yasuhiro Iwamura

PREFACE

This publication is the proceedings of the 23rd meeting of the Japan CF-Research Society (JCF23) held on March 4 and 5, 2023, at the School of Science and Engineering, Waseda University, which was organized by Professor Ken Naitoh (Waseda University). While JCF21 and JCF22 were held online due to COVID-19, JCF23 was the first face-to-face meeting in a while. Eleven presentations were given and eleven papers were submitted to the editorial board for publication. These papers were refereed and revised for publication as proceedings.

For all meetings, JCF1 through JCF23, we published the Proceedings.   For the meetings after JCF4, we published electronic versions of the proceedings on our web-site http://jcfrs.org/proc_jcf.html in addition to their printed versions. In view of low efficiency and low effectiveness in distributing information, we decided to discontinue the printed version for the meetings, JCF12. Only the electronic versions have been published thereafter. Any questions and comments are welcomed for the proceedings.

Finally, we would like to thank all the participants and the people who have collaborated in organizing this meeting.

Editor-in-Chief
Yasuhiro Iwamura,
Tohoku University
November 2023

CONTENTS

The Cold Fusion Phenomenon and the ARPA-E Project 2022 of DOE: A Facet of the Sociology of Modern Science

Hideo Kozima

Cold Fusion Research Laboratory
597-16 Yatsu, Aoi, Shizuoka, Japan 421-1202
E-mail : hjrfq930@ybb.ne.jp

Abstract

A sociological perspective for the development of the cold fusion phenomenon (CFP) or the LENR is given in relation to the ARPA-E Project 2022 (referred as "Project" in this paper, hereafter) proposed by DOE, USA on September 13, 2022. Brief summary of characteristics of the experimental data obtained in the CFP closely related to the *Requirement of the Project* is given in relation to the character of the Project. The nature of modern science strongly bound to the social requirement rather than the scientific value itself is discussed using this case as a typical example.

The most important characteristics of the CFP in relation to the Project are the qualitative reproducibility observed and confirmed in the cold fusion materials: The lack of quantitative reproducibility in the CFP, one of the main targets against the CFP raised at first by Huizenga in his book and followed by many critics and opponents, has been an obstacle to understand and to accept the CFP as a part of modern science. We have analyzed and explained the characteristics of the CFP in relation to the qualitative reproducibility using the laws of complexity in nonequilibrium open systems with nonlinear interactions between components. The direct appearance of the laws of complexity in physics is a very rare case and this fact observed in the CFP is the main reason why the science of the CFP is not easily reconciled with the commonsense knowledge of the modern science where the quantitative reproducibility prevails widely due to the linear interaction in the relevant systems.

The requirement of the Project includes "A key goal of the Exploratory Topic (ET)," which demands "The convincing empirical evidence of nuclear reactions in an LENR experiment and publication of the evidence in a top-tier peer-reviewed research journal." The first requirement is a natural one for the novel science including nuclear reactions in solids where is no specific mechanism to accelerate nuclei up to energies possible for usual nuclear reactions considered in nuclear physics hitherto.

It has been shown that the requirement has long been a main obstruction to publish results obtained in this field in the top-tier peer-reviewed research journals for about 30 years. It is, therefore, very difficult to attain the requirement of the Project by the fortunate sudden change of the attitude of the research

journals induced by expected several new experimental data in the Project in a required short period less than 3 years.

It is concluded that the overall object of the Project is too difficult to attain in the asked period of 30 months due to the nature of the CFP even if the Project is able to stimulate recognition of the importance of the qualitative reproducibility ubiquitous in many-body systems. The requirements of the Project may help to shift the tendency of research in this field from application to scientific direction to confirm nuclear reactions in the CF material rather than to pursue materials with higher excess-energy production.

1. Introduction

It is, perhaps, not necessary to recollect again the first announcement of the discovery of the cold fusion phenomenon (the CFP) by Fleischmann et al. in 1989 [Fleischmann 1989] which was honored in a short paper published at the 30th anniversary by the present author [Kozima 2019c].

In a paper presented at JCF17 [Kozima 2017], we investigated the sociological feature of the cold fusion research with strong characteristics toward its application for an energy source demanded by the modern society based on its energy consuming economy. Several negative traditions in the cold fusion research had been pointed out there for the sound development of this science while one of the biased tendencies, the prejudice against protium systems below the deuterium ones, had been largely improved in these several years, fortunately. In this paper, we want to investigate the sociological feature of the cold fusion research again in relation to the ARPA-E Project 2022 proposed by DOE [DOE 2022] as explained briefly below.

On September 13, 2022, ARPA-E of DOE issued "Financial Assistance Funding Opportunity Announcement" [DOE 2022] to ask application to Scientific and Rigorous Approach to New Exploratory Topic Focused on Specific Type of Nuclear Energy (Low-Energy Nuclear Reactions) with a budget of up to $10 Million to be accomplished in 30 months (Let us call this *ARPA-E Project 2022* (the *Project*, in short) and cite it as [DOE 2022] in this paper hereafter).

This Project has had a preparatory national conference, the *ARPA-E Workshop*, held in 2021 [DOE 2021] in the participants of which are included two researchers from Japan.

In this paper, we want to review the Project from our scientific point of view to make it more fruitful as possible if it might be possible by the feeble power of an outsider.

First of all, we want to check the terminology of the scientific branch for the research field where the existence of nuclear reactions has been investigated for more than 30 years since 1989 when Martin Fleischmann et al. declared the discovery of the

Cold Fusion [Fleischmann 1989, DOE1989].

In the ARPA-E Project, the name "low energy nuclear reactions (LENR)" are defined as follows;

"We define LENR as a hypothetical energy-producing process (or class of processes) with system energy outputs characteristic of nuclear physics (>>1 keV/amu/reaction) and energy inputs characteristic of chemistry (~ eV/atom)." [DOE 2022, p. 59].

This definition is practical and enough to use in the Project and we do not hesitate to use it in the discussion. In this paper, however, we would like to use the name "the cold fusion phenomenon (the CFP)" for the LENR used in the Project by the reason explained in the following Note*

Note on the terminology.

The definition of the LENR given above may be replaced by another analogous name RTNR (Room Temperature Nuclear Reaction) defined similarly as follows:

"We define RTNR as a hypothetical energy-producing process (or class of processes) with system energy outputs characteristic of nuclear physics (>>1 keV/amu/reaction) and energy inputs characteristic of chemistry (~ eV/atom)."

This name may be more comfortable to nuclear scientists who have used the low and high energies to express energy ranges divided by 10 MeV (e.g. [bockris 1954, Chapter II]).

On the other hand, however, the materials including the transition metal deuterides (which were used mainly in the first stages) and hydrides, where the observed phenomena were inexplicable without participation of nuclear reactions, were specified by the inclusion of hydrogen isotopes (protium and/or deuterium). Furthermore, the experimental conditions for the realization of these phenomena have been specified by the open (with external particle and energy supplies) and the non-equilibrium state. To be more precise to specify the phenomena we are going to investigate, we would like to use the words Cold Fusion Phenomenon (CFP) used for long by us as defined as follows:

"t*he CFP stands for Nuclear reactions and accompanying events occurring in open (with external particle and energy supply), non-equilibrium system composed of solids with high densities of hydrogen isotopes (H and/or D) in ambient radiation*" belonging to *Solid State-Nuclear Physics (SSNP)*.

(Definition of the cold fusion phenomenon (CFP) in the *CFRL News* e.g. the *CFRL News* #**107**, posted at the CFRL website; http://www.kozima-cfrl.com/News/news.html/

Finally, we give a short comment on the nature of the ARPA-E Project from a scientific viewpoint. We feel the Project is fairly nationalistic when we look into the references in the explanation of the Project where are only books by Americans (Footnote 22 (p. 59) in [DOE 2022]) even if there were invited two Japanese researchers in the ARPA-E Workshop 2021 [DOE 2021] adding an international scent of research in this field.

In Section 2, we check the characteristics of the Project in relation to the facts enumerated in the next Section. In Section 3, important facts in the CFP relevant to the Project are summarized to discuss the objects and methods raised in the Project [DOE 2022].

In Appendix, we cite excerpts from the Project: In Appendix A1, the "Introduction" ([DOE 2022], p. 59); in Appendix A2, the "Topic Description" ([DOE 2022, p. 61]; and in Appendix A3, the "Submissions Specifically Not of Interest" ([DOE 2022, p. 67] to use in the discussion in Section 3. In Appendix 4, we included the decision of DOE made on February 17, 2023 [DOE 2023] where is a list of the eight themes which will receive funding as part of the Advanced Research Projects Agency-Energy (ARPA-E) LENR Exploratory Topic, just for a record without any comment.

It is useful to remember the fundamental spirit of scientific research expressed by great scientists in the modern history of science. Following are the words by Henri Poincaré on "the science and the facts on which the former built up of" [Poincare 1902]: "The man of science must work with method. Science is built up of facts, as a house is built of stones; but an accumulation of facts is no more a science than a heap of stones is a house. Most important of all, the man of science must exhibit foresight."

2. The Point of View of the DOE expressed in the ARPA-E Project 2022 [DOE 2022]

The ARPA-E Project 2022 is a national program by a national organ DOE based on the USA budget to develop the energy technology for U.S. technological leadership on the science of international nature in itself (c.f. Appendix A1 *Topic Description* cited below in the Appendices of this paper). The scientific results obtained in this Project are the common heritage of the world even if the merit of the works belongs naturally to DOE. We are interested in the scientific and technological results of the works in this Project and want to participate positively giving our knowledge if any to help researchers going to work there.

The historical relation of DOE with the CFP is marked by two reports published in 1989 [DOE 1989] and 2004 [DOE 2004] which are briefly reviewed at the ARPA-E

Workshop [DOE 2021]. These Reports have little with the Project directly due to their scopes had been restricted to the evaluation of the works done prior to the Reports.

We want to give short comments on the objects of the Project [DOE 2022] in relation to the experimental facts summarized in Section 3 to assist the works involved in the Project.

2.1 Biased references given by DOE [DOE 2022]

In the Reference 22 of the Project [DOE 2022, p. 59], there are cited only books published in USA even if the workshop held in 2021 [DOE 2021] invited two Japanese researchers as foreigners. This choice of books in the references shows the restricted viewpoint of the ARPA-E in the international world of science at present. This biased view revealed in the choice of references contradicting to the history and the heritage of the CFP research may give negative influence on the works in this Project which have to try to meet the DOE request "Submissions specifically not of interest" cited in Appendix A3 (especially the item A3.3. It is possible to say that the ARPA-E Project is too national to be a project for the scientific problem of international nature in essence.

2.2 Narrow-minded view on the theoretical work for the CFP with characteristic behaviors due to complexity (especially the qualitative reproducibility).

The item "A3.6 Purely theoretical or computational studies" in Appendix A3 [DOE 2022] p. 67) is excluded as "Submissions Specifically Not of Interest." This exclusion shows their inappropriate understanding of the characteristics of the CFP where events have been sporadic with qualitative reproducibility and therefore should be investigated theoretically with a statistical viewpoint for as many data as possible [Kozima 2019a].

2.3 Difficulty to meet the requirement 2A-4 asked by [DOE 2022]

The biased information about the CFP data given in the Reference 22 in Introduction cited in Appendix A1 [DOE 2022].

Characteristics (especially the qualitative reproducibility and the three empirical laws) of the CFP deduced by the phenomenological analysis [Kozima 1998, 2006, 2013, 2019a, 2019b] have not accepted by mainstream journals hitherto. This fact we have experienced in more than 30 years show clearly that the DOE requirement 2A-4 (in Appendix A2) to publish results in a top-tier research journal are difficult to be satisfied in the present situation of physics and chemistry at present.

2.4 Necessity of a right perspective for the target problem

Appropriate preliminary knowledge helps a right research schedule for the difficult theme such as the CFP remaining almost untouched by many scientists for more than 30 years despite of sincere and enormous efforts by a few researchers who have touched the essence of the phenomenon for themselves. Once we personally had a new experience outside of our common knowledge, we are embarrassed with it and consider how to treat it. The personal experience pushes us to plunge into a new idea to explain the experimental facts contradicting to the common knowledge. In the Section 3, we will survey the new ideas thus employed to give a self-consistent explanation of the experimental facts seemingly in contradiction to the commonsense knowledge of the solid state physics and the nuclear physics.

3. Facts of the Cold Fusion Phenomenon (the Low Energy Nuclear Reaction) related closely to the ARPA-E Project 2022

In the long history of the research on the CFP, we have presented several books and many papers giving fundamental knowledge of the science of nuclear reactions in the cold fusion materials including the transition metal hydrides and deuterides, the hydrogen carbons and the biological systems. We will give a brief summary of important evidence of nuclear reactions and their theoretical explanation related closely to the ARPA-E Project 2022 in this Section 3.

3.1 Survey of the Experimental Data in the Cold Fusion Phenomenon (CFP)

At first, we cite three books [Kozima 1998, 2006, Storms 2007] on the CFP useful to investigate the fundamental experimental facts and the mechanisms of nuclear reactions in the materials mentioned above.

The book by H. Kozima published in 1998 [Kozima 1998] has explained many experimental data sets issued by that time using a phenomenological model (TNCF model) with an adjustable parameter n_n (assumed to be the density of the "trapped neutrons") and deduced mutual relations between the observed number N_x and N_y of an event x and another event y (excess heat generation, neutron emission, tritium emission, $^4_2$He generation) observed simultaneously in a protium or a deuterium system.

Tables 3.1 and 3.2 cited below [Kozima 1998, Tables 11.2 and 11.3] summarize relations between experimental data and the results of the model calculation. It should be noticed that there are given a successful explanation of the observed relations between experimental values of observables x's measured simultaneously by the TNCF theory.

The second book by H. Kozima published in 2006 [Kozima 2006] has given a quantum mechanical explanation of the bases of the TNCF model using the idea of the neutron energy bands and also given a proof of complexity in the strength-frequency relation of the excess heat generation. The super-nuclear interaction between neutrons in different lattice nuclei mediated by the interstitial protons/deuterons explained in a paper [Kozima 2002] and in this book is a new idea applicable to other phenomena observed in the transition metal hydrides [Kozima 2023].

The book by E. Storms published in 2007 [Storms 2007] compiled many publications in the cold fusion phenomenon (CFP) more than 1300.

3.2 Characteristics of the Experimental Results obtained in the CFP

The experimental results obtained in the CF materials (mainly in the transition metal hydrides and deuterides) compiled in our books [Kozima 1998, 2006] have shown characteristics of the CFP very different from those obtained in other materials. The most remarkable ones of them are the relations between amounts of such observables as the amount of excess heat (Q), number of tritium (N_t), number of neutron (N_n), and number of ^4_2He (N_{He}). Difficulty of the simultaneous measurement of several observables in an experiment has made the trial scarce recently, and the data compiled in our books is valuable in relation to the Requirement 3-4 of the ARPA-E Project [DOE 2022, p. 67](cf. Appendix A3).

We cite the experimental results by 2006 from our book [Kozima 2006] below.

3.2.1 Summary of Experimental Results [Kozima 2006, pp. 58 – 60]

Facts are related to the true mechanism occurring there in fortunate cases. Simple facts are easily placed in an appropriate position of the frame of reference and accepted as facts. However, complex or ambiguous facts occurring in frontiers of sciences and at interdisciplinary areas are not easily put into the common frame of references. They have to wait long to gain a citizenship in the established world of science.

The cold fusion phenomenon has shown difficulty to be accepted in the established world of modern science due largely to its expected large applicability and partly to its revolutionary novelty . The latter characteristic has a famous example in Wegener's hypothesis of the continent drift proposed in 1912. His hypothesis has proved its validity after almost 50 years when plate tectonics was established in 1950's.

Fleischmann's hypothesis had played a pivotal importance in the first stage of CFP research even if it was criticized in DOE Report 1989 [DOE 1989] to throw CFP decisively out of established world of science at that time. The merit of the possible

realization of the d – d fusion reactions in the CF materials attract, eve in recent research works, attracts several trials to prove its possibility ignoring critical papers by specialists in related proper areas as listed in Subsection 3.3.5 making the gap deeper between CF society and established science community. We have to look at facts with unbiased scientific eyes and also esteem established principles of science and have to have close communication with as wide research fields related to CFP as possible.

We cite two tables from the book published in 1998 below as Tables 3.1 and 3.2 (Tables 11.2 and 11.3 of [Kozima 1998]) where are many experimental data and theoretical results calculated with the TNCF model proposed in 1993 [Kozima 1994].

Table 3.1 Pd/D(H)/Li System. Neutron density n_n and Relations between the Number N_x of Event x obtained by Theoretical Analysis of Experimental Data on the TNCF model ($N_Q \equiv Q$(MeV)/5 (MeV)). Typical value of the surface vs. volume ratio S/V (cm^{-1}) of the sample is tabulated, also. The references cited in this table, e.g. Fleischmann et al.[1], are found in the following pages of the CFRL website,

http://www.kozima-cfrl.com/Books/bookse/bookse01/refer1.htm.

Authors	System	S/V cm^{-1}	Measured Quantities	n_n cm^{-3}	Other Results (Remarks)
Fleischmann et al.[1]	Pd/D/Li	6 ~40	Q, t, n $N_t/N_n \sim 4 \times 10^7$ $N_Q/N_t \sim 0.25$	$\sim 10^9$	(Q=10W/cm^3) $N_t/N_n \sim 10^6$ $N_Q/N_t = 1.0$
Morrey et al.[1-4]	Pd/D/Li	20	$Q,$ ^{4}He ^{4}He in $\ell \leq 25\mu m$	4.8×10^8	$N_Q/N_{He} \sim 5.4$ (If 3% ^{4}He in Pd)
Roulette[1''']	Pd/D/Li	63	Q	$\sim 10^{12}$	
Storms[4]	Pd/D/Li	9	$t(1.8 \times 10^2$Bq/m$\ell)$	2.2×10^7	(τ=250h)
Storms[4']	Pd/D/Li	22	Q (Q_{max}=7W)	5.5×10^{10}	(τ=120h)
Takahashi et al.[5']	Pd/D/Li	2.7	t, n $N_t/N_n \sim 6.7 \times 10^4$	3×10^5	$N_t/N_n \sim$ 5.3×10^5
Miles et al.[18']	Pd/D/Li	5	$Q,$ ^{4}He (N_Q/N_{He}=1~10)	$\sim 10^{10}$	$N_Q/N_{He} \sim 5$
Okamoto et al.[12']	Pd/D/Li	23	Q, NT_D $\ell_0 \sim 1 \mu m$	$\sim 10^{10}$	$N_Q/N_{NT} \sim 1.4$ (^{27}Al$\rightarrow^{28}$Si)
Oya[12-5]	Pd/D/Li	41	Q, γ spectrum	3.0×10^9	(with^{252}Cf)
Arata et al.[14]	Pd/D/Li	7.5 $\times 10^4$	$Q,$ ^{4}He ($10^{20} \sim 10^{21}$ cm^{-3}) $N_Q/N_{He} \sim 6$	$\sim 10^{12}$	(Assume t channeling in Pd wall)
McKubre[3]	Pd/D/Li	125	Q (& Formula)	$\sim 10^{10}$	Qualit.explan.
Passell[3'']	Pd/D/Li	400	NT_D	1.1×10^9	N_{NT}/N_Q=2
Cravens[24'']	Pd/H/Li	4000	Q (Q_{out}/Q_{in}=3.8)	8.5×10^9	(If PdD exists)
Bockris[43]	Pd/D/Li	5.3	$t,$^{4}He;$N_t/N_{He} \sim 240$	3.2×10^6	$N_t/N_{He} \sim 8$
Lipson[15-4]	Pd/D/Na	200	γ (E_γ=6.25MeV)	4×10^5	If effic. =1%
Will[45]	Pd/D$_2$SO$_4$	21	$t(1.8 \times 10^5$/cm^{2}s)	3.5×10^7	(If $\ell_0 \sim 10\mu m$)
Cellucci et al.[51'']	Pd/D/Li	40	$Q,$ ^{4}He N_Q/N_{He}=1~5	2.2×10^9	(IfQ=5W) N_Q/N_{He}=1
Celani[32'']	Pd/D/Li	400	Q (Q_{max}=7 W)	1.0×10^{12}	(If200%output)
Ota[53]	Pd/D/Li	10	Q (113%)	3.5×10^{10}	(τ=220 h)
Gozzi[51']	Pd/D/Li	14	$Q, t,$ ^{4}He	$\sim 10^{11}$	($\tau \sim 10^3$h)
Bush[27']	Ag/PdD/Li	2000	Q (Q_{max}=6W)	1.1×10^9	(τ=54d,Film)
Mizuno[26-4]	Pd/D/Li (If Cr in Pd)	3.4	Q, NT_D $\ell \leq 2 \mu m$)	2.6×10^8	τ=30d,Pd 1cm$\phi \times$10cm
Iwamura[17]	PdD$_x$	20	n (400/s),t	3.9×10^8	$4.4 \times 10^6 t$/s
Itoh[17']	PdD$_x$	13.3	n (22/m),t	8.7×10^7	$7.3 \times 10^{10} t$/s
Itoh[17'']	PdD$_x$	13.3	n (2.1 $\times 10^3$/s)	3.9×10^8	
Iwamura[17''']	PdD$_x$	20	Q (4 W) NT_F(Ti, Cr etc.)	3.3×10^{10}	(NT$_F$? unexplained)
Miley[65]	Pd/H/Li	150	NT_F(Ni,Zn,······)	4.5×10^{12}	
Dash[59]	Pd/D,H$_2$SO$_4$	57	Q, NT_D	$\sim 10^{12}$	Pt$\rightarrow$Au
Kozima[203]	Pd/D,H/Li	200	n (2.5$\times 10^{-4}$/s)	2.5×10^2	Effic. =0.44%

Table 3.2 Ni/H/K System and Others. Neutron density n_n and Relations between the Number N_x of Event x obtained by Theoretical Analysis of Experimental Data on the TNCF model ($N_Q \equiv$ Q(MeV)/5 (MeV)). Typical value of the surface vs. volume ratio S/V (cm^{-1}) of the sample is tabulated, also. The references cited in this table, e.g. Jones[2], are found in the following pages of the CFRL website,

http://www.kozima-cfrl.com/Books/bookse/bookse01/refer1.htm

Authors	System	S/V cm^{-1}	Measured Quantities	n_n cm^{-3}	Other Results (Remarks)
Jones[2]	Ti/D/Li	8.1	n (2.45 MeV)	3.1×10^{11}	
Mills[25]	Ni/H/K	160	Q (0.13 W)	3.4×10^{10}	
Bush[27']	Ni/H/K	~160	NT_D(Ca)	5.3×10^{10}	$N_Q/N_{NT} \sim 3.5$
	Ni/H/Na	~160	NT_D(Mg)	5.3×10^{11}	($^{40}K_T = 0$)
Bush[27'']	Ni/H/Rb	~10^4	NT_D(Sr)	1.6×10^7	$N_Q/N_{NT} \sim 3$
Savva-timova[34'']	Pd/D$_2$	100	NT_D(Ag)	9×10^{10}	
Alekseev[44']	Mo/D$_2$	4.1	t (~10^7/s)	1.8×10^7	(If MoD)
Romoda-nov[44''']	TiC/D	4.1	t (~10^5/s)	~10^6	(D/Ti~0.5assumed)
Reifensch-weiler[38']	TiT$_{0.0035}$	7×10^5	β decay reduction	1.1×10^9	($T = 0 \sim 450°C$)
Dufour[7]	Pd,SS/D$_2$ Pd,SS/H$_2$	48	Q, t, n	9.2×10^{11} 4.0×10^9	(D(H)/Pd~1 is assumed)
Claytor[9]	Pd/D$_2$	400	t (12.5 nCi/h)	1.6×10^{13}	(If D/Pd~0.5)
Srinivasan[16]	Ti/D$_2$	1500	t ($t/d \sim 10^{-5}$)	1.9×10^8	(Aged plate)
De Ninno[6']	Ti/D$_2$	440	n, t	1.2×10^6	(D/Ti=1,1w)
Focardi[23]	Ni/H$_2$	8.2	Q	3.0×10^{12}	(If$N_p = 10^{21}$)
Oriani[52]	SrCeO$_3$/D$_2$	22	$Q \sim 0.7W$	4.0×10^{10}	$V = 0.31 cm^3$
Notoya[35'']	Ni/D,H/K	3.4 $\times 10^4$	Q (0.9 W), t	2.4×10^{13}	(If 1/2 t is in liquid)
Notoya[35-4]	Ni/D,H/K	same	NT_D(Ca)	1.4×10^9	(Sintered Ni)
Yamada[54]	Pd/D$_2$	185	n, NT_D(C)	2.0×10^{12}	
Cuevas[55]	TiD$_{1.5}$	134	n (102 n /s)	5.4×10^{11}	
Niedra[56]	Ni/H/K	80	Q (11.4 W)	1.4×10^9	5km×0.5mmϕ
Ohmori[22'']	Au/H/K	200	Q, NT_F(Fe)	~10^{11}	(Au plate)
Li[57]	Pd/D$_2$	185	Q	1.6×10^{12}	(Pd wire)
Qiao[57']	Pd/H$_2$	185	NT_F(Zn)	3.8×10^{10}	(40%NTin 1y)
Bressani[58']	Ti/D$_2$	$\leq 10^3$?	n (ϵ)	$10^5 - 10^6$	(Ti shaving)
Miley[65']	Ni/H/Li	50	NT_D(Fe,Cr,···)	1.7×10^{12}	

3.2.2 General Characteristics of Experimental Data in the CFP

From experimental data sets introduced in this Chapter, we deduce general characteristics of CFP as follows [Kozima 2006 (Section 2.15.1)].

(0) The cold fusion phenomenon (CFP) does not occur without background thermal neutrons.

(1) CFP occurs in CF materials, in which main research was performed in *transition-metal hydrides and deuterides* with the *fcc* structure and *proton conductors* including high-density hydrogen isotopes.

(2) Events of CFP shows *sporadic and stochastic occurrence* and therefore has only *qualitative reproducibility* but not quantitative.

(3) *Nuclear transmutation (NT) occurs generating almost all nuclides with atomic numbers up to 82 (Pb)* in addition to tritium and helium-4 (by our terminology). Production rates of NT products obey *the stability effect,* i.e. the more stable a nuclide, the more the nuclide is generated.

In addition to NT, there appear other events as tritium, helium-4 and excess heat production in CF materials. The number of reactions N_x generating observable x is determined by experimental data sets and has important meaning giving relations between N_x and $N_{x'}$ of two observables x and x' to compare with their theoretical prediction. Experimental data sets show the following relations;

$N_Q \simeq N_{NT} \simeq N_t \simeq 10^7 N_n$, $N_{He} \simeq (1/m)N_Q$ $(m = 2 - 4)$,

$N_\gamma \simeq 0$, $N_{He3} \simeq 0$. where $N_Q \equiv$ Q (MeV)/5 MeV.

(4) Generated neutrons have shown a *wide-spread distribution* of *energy* up to $E_n \leq 10$ MeV, the upper limit of intended observation. In addition to this interesting high value of neutron energy, another fact shows the number of neutrons with energies higher than 3 MeV is more than half of the measured neutrons.

(5) There is much evidence showing *localization of nuclear reactions* participating to CFP in definite regions of surface and boundary layers with width of about several micrometers (μm). They are the localization of NT products in samples and the detection of helium-4 in surface layer and outside of samples.

(6) Helium-4 is observed only in P*d/D/Li systems* showing an important role of lithium Li in production of this element.

(7) Tritium is observed mainly in *deuterium systems* showing decisive role of deuteron $d = {}^2_1H$ in generation of triton $t = {}^3_1H$.

(8) The most extensively investigated excess heat measurement has shown *the inverse-power law* for the time rate of the N_Q vs. *Q* curve similar to the $1/f$ fluctuation observed widely for phenomena occurring in complex systems.

3.2.3 Three Empirical Laws between Observables in the CFP

There have been observed three experimental laws or regularities between observables [Kozima 2012]. The most impressive law in the three laws, the $1/f$ dependence of the frequency N_P of excess power generation on the power *P,* will be

taken up in Section 3.4.2 below for its importance to show the effect of complexity in the CFP. We give a brief explanation of these laws in this section.

The three empirical laws in the CFP are explained briefly as follows.

(1) The First Law; there is a stability effect for nuclear transmutation products, i.e. the more stable the product nucleus, the more amount appears in the nuclear reaction of the CFP,

(2) the Second Law; the inverse power dependence of the frequency N_P of the event with the intensity of the excess power P, i.e. $N_p = C/P^n$ with C: constant and $n = 1.0 – 2.0$.

and

(3) the Third Law: bifurcation of the intensity of events (neutron emission and excess heat production) in time.

There are two corollaries of the first law: Corollary 1-1: Production of a nuclide $^{A'}_{Z+1}X'$ from a nuclide $^A_Z X$ in the system. Corollary 1-2: Decay time shortening of unstable nuclei in the system.

The second law will be explained in more detail in Section 3.4.2 for its importance in the science of the CFP.

These laws and the necessary conditions for the CFP tell us that the cold fusion phenomenon is a phenomenon belonging to complexity induced by nonlinear interactions between agents in the open and nonequilibrium CF systems as far as we assume a common cause for various events in the CFP, i.e. excess heat production, neutron emission, and nuclear transmutation.

The characteristics of the CF materials for the CFP are investigated using our knowledge of the microscopic structure of the CF materials consulting to the complexity in relation to the three laws explained above. A computer simulation is proposed to reproduce an essential feature of the CFP using a simplified model system (a super-lattice) composed of two interlaced sublattices; one sublattice of host nuclei with extended neutron wavefunctions and another of proton/deuterons with non-localized wavefunctions.

3.3 Riddles of the Cold Fusion phenomenon [Kozima 1998]

Here, we cite the riddles of the cold fusion phenomenon pointed out and listed up in 1998 from our book [Kozima 1998, pp. 127 – 128]. In the days of upheaval about 10 years after the announcement of the discovery, we had very many elaborate experimental results in many various materials valuable to remember after 25 years. The terminology used there has changed a little as the partial irreproducibility instead of the

qualitative reproducibility now used appropriately.

List of the Riddles of Observed Facts in the CFP [Kozima 1998, pp. 127 – 128]

Riddle 1. Irreproducibility

The cold fusion phenomenon has very poor reproducibility or irreproducibility, or rather say has qualitative reproducibility. This is t*he first riddle* of the cold fusion phenomenon.

Riddle 2. Vast excess heat unexplainable by chemical reactions

The excess heat observed in the cold fusion phenomenon is too large to be explained by any chemical reactions considerable in the experimental system. This vast excess heat is *the second riddle* of the cold fusion phenomenon.

Riddle 3. **Excess heat - neutron anomaly**

Number of events generating the excess heat is too large compared to the number of neutrons even if the excess heat is reduced to nuclear reactions between deuterons. This is *the third riddle* called "the excess heat - neutron anomaly" in the cold fusion phenomenon.

Riddle 4. Tritium anomaly

Number of tritons observed in the cold fusion phenomenon is larger than the number of neutrons observed simultaneously in the same system by few orders of magnitude, up to 10^8 times. This is *the fourth riddle* called "the tritium anomaly" in the cold fusion phenomenon.

Riddle 5. **Lack of gamma ray**

It has been noticed that gamma ray could not be measured in experiments where observed the excess heat and other nuclear products except few cases. This is *the fifth riddle* of the cold fusion phenomenon.

Riddle 6. **Lack of simultaneity of several events** anticipated from assumed reactions.

The quantities observed in an experiment show sometimes inconsistency with expectation where these expected to occur simultaneously do not do so. This may be called a *partial irreproducibility.*

Riddle 7. **Decay time shortening of unstable isotopes** in the surface layer of materials containing the trapped thermal neutrons.

Riddle 8. **Nuclear fission induced by thermal neutrons**

Trapped neutron induced nuclear fission in the surface layer of materials or cathodes containing the trapped thermal neutrons.

3.4 Qualitative Reproducibility

We would like to show the peculiarity of the CFP using the qualitative reproducibility which is a special event related to the complexity of nonlinear dynamics; the individual nuclear reactions in the nuclear physics are usually observed as a statistical average in space and time except special cases of the particle emulsion detector used to find tracks of fission products in the detector plate. In the case of the CFP, however, the nuclear products are counted individually due to the space and time of the reaction are possible to determine in the sample. Two typical cases are explained in this section.

3.4.1 Qualitative Reproducibility revealed in the Excess Heat Generation [McKubre 1993]

We pick up here the qualitative reproducibility, one of riddles observed in the CFP. The typical data of this characteristic is seen in the excellent data of excess heat generation obtained by McKubre et al. [McKubre 1993] cited below from our book [Kozima 1998].

Qualitative reproducibility revealed by experimental data, e.g. the data by McKubre et al. shown below as Fig. 3.1 [5 (Fig. 6.2)] is an evidence of dispersion of the excess power P_{xs} for the loading ratio x (= D/Pd). For the same value of x (= D/Pd ratio) in the abscissa determined macroscopically, the excess power output P_{xs} plotted in the ordinate disperses largely as seen in this figure. This is one of the best evidence of the qualitative reproducibility of events in the CFP different from the quantitative reproducibility observed in simple systems governed by linear dynamics.
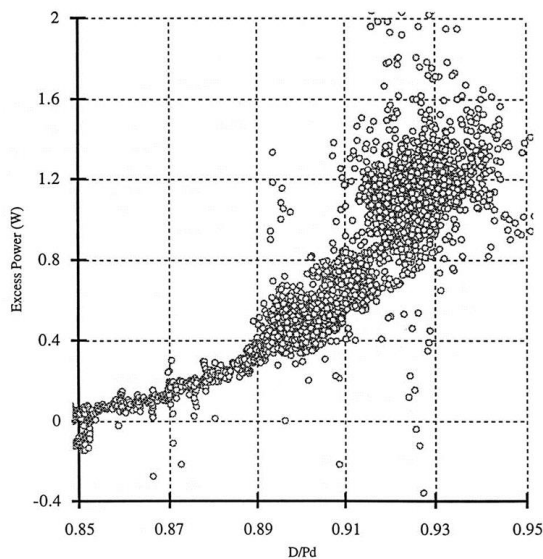

Fig. 3.1. Variation of the excess power P_{xs} with the average loading ratio x (= D/Pd) ([McKubre 1993, Fig. 7]).

3.4.2 The 1/f dependence of the frequency N_P of excess power generation on the power P

In the three laws (or regularities) in the CFP found in the experimental data sets, the most spectacular one is the 1/f dependence of the frequency N_p of excess power generation on the power P [Kozima 2012]. This law clearly shows the complex nature of the CFP. The three laws as a whole will be explained briefly in Section 3.6.
The evidence of the 1/f law in the CFP had been shown for the experiments by McKubre et al. [McKubre 1993] and Kozima et al. [Kozima 2008] and also for the data obtained in both protium and deuterium systems [Lietz 2008] as shown below in Figs. 3.2 – 3.4.

The first example is shown in Fig. 3.2 for the data by McKubre et al.
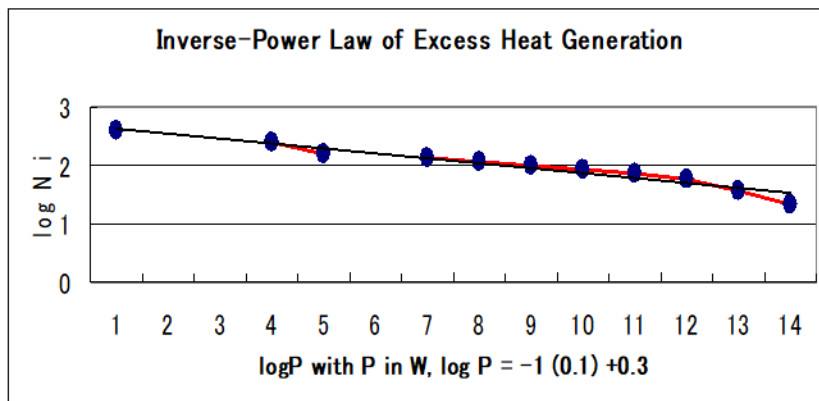
Fig. 3.2. Dependence of the approximate number of measurements N_i of the excess power P on the Power P in the data by McKubre et al. [McKubre 1993] crudely counted from their Fig. 6. The exponent of the dependence is 1.0 in this case.

The second example is obtained for the data by Kozima et al. [Kozima 2008] as depicted in Fig. 3.3. In this case, the exponent of the dependence is 2.
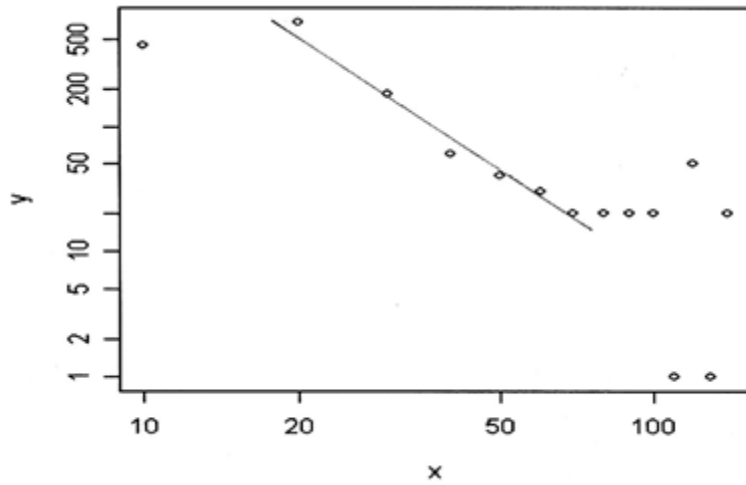
Fig. 3.3. Distribution of the frequency N_p (= y) producing excess power P_{ex} (= x). To depict log-log curve, values of N_p and P_{ex} were arbitrarily multiplied by 10^n (x = 100 in this figure corresponds to P_{ex} = 1 W) [Kozima 2008].

On the other hand, H. Lietz [Lietz 2008] tried to check the inverse power law using the data accumulated by E. Storms in his book [Storms 2007]. The resulting plot by H. Lietz is given in Fig. 3.4 which shows the exponent of 1.0.
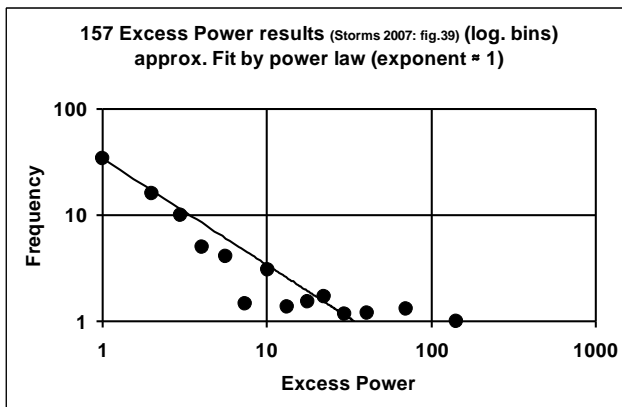

Fig. 3.4. Distribution of 157 excess energy results by Lietz [Lietz 2008] using the data collected by Storms [2007]. Values have been stored in bins of size 10. The line shows a power-law fit to the binned data with an exponent of 1.0 (r^2 = 90%) ([Lietz 2008, Fig. 3])

This data shown in Fig. 3.4 shows that the experimental data obtained in many samples with different components of host metals and hydrogen isotopes show the $1/f$ dependence similarly to the data shown in Figs. 3.2 and 3.3 for PdD samples. This fact is an evidence of the same mechanism is the cause of nuclear reactions in the CFP for

samples with different compositions. This is also shows the effective application of the meta-analysis used in the field of medicine to the CFP [Kozima 2019a].

3.4.3 Ubiquity of the super-nuclear interaction

We would like to give a comment on the ubiquity of the super-nuclear interaction causing the CFP in the CF materials. As we have shown in our papers [Kozima 2019b, 2023], there are many phenomena where we have to assume the super-nuclear interaction to explain the riddles in experimental results observed in materials composed of transition metals and hydrogen isotopes. The riddles will be solved taking into the super-nuclear interaction which has not taken into consideration its existence until now.

3.5 Localization of the Active Regions in the CF Material

One of the characteristics of the CFP interesting from the mechanism of nuclear reactions in the CF material is the localization of the active region at around the surface region with a width of about several micrometers as summarized and explained by the mechanism governed by the complexity in our papers [Kozima 2011, 2013].

In this section, we cite only two figures and one table below to show the peculiar localization of nuclear reactions shown by the observed transmuted nuclei.

The first example is the data obtained by Okamoto et al. [Okamoto 1994] in the early stages of the CF research.
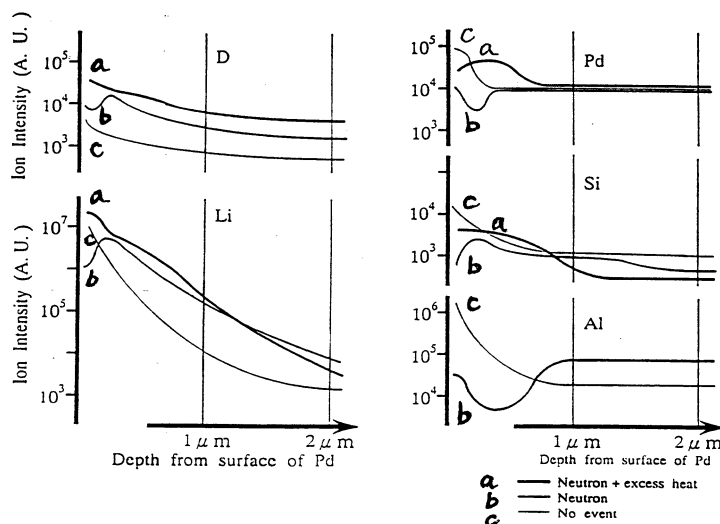

Fig. 3.5. Depth profile of D, Li, Pd, Si and Al observed by Okamoto et al. [Okamoto 1994]

The second example is the data obtained by Iwamura et al. [Iwamura 2006] using the specific sample formed to investigate the nuclear transmutation of Pr.
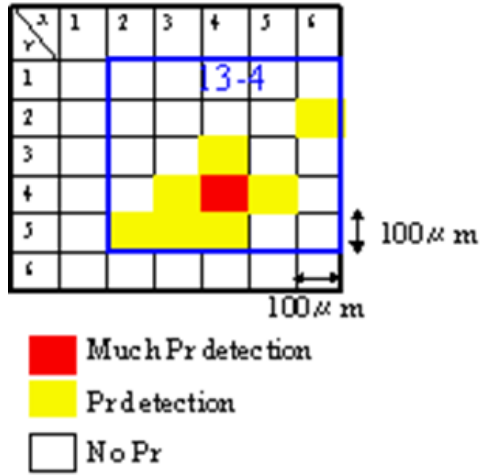

Fig. 3.6. Surface distribution of Pr for FG2 using 500-micron and 100-micron x-ray beams, mapping of Pr by 100-micron beam [Iwamura 2006]

Bockris and Minevsky [Bockris 1995] carried out experiments in which hydrogen was electrolyzed from water in contact with a palladium electrode. They observed two different sets of impurities in Pd cathode after 3 weeks, one set within 50Å of the surface (shown in their Table 1 not shown here) and another set different chemical spaces, about 1μ inside the metal (shown in their Table 2 shown below as Table 3.1).

ELEMENT	ELEMENTS AT 1μm DEPTH (ATOMIC %)		
	VIRGIN Pd		ELECTROLYZED Pd 3 weeks/EDS
	JOHNSON MATTHEY/ICP	PRESENT WORK/ED	
Mg	$<1.0 * 10^{-4}$	- *	6.7 ± 1.0
Ag	$<1.0 * 10^{-4}$	- *	1.9 ± 1.0
Si	$8.0 * 10^{-4}$	- *	10.2 ± 1.0
Cl	-	- *	3.0 ± 1.0
K	$9.0 * 10^{-4}$	- *	1.1 ± 1.0
Ca	$3.5 * 10^{-3}$	- *	19.9 ± 1.0
Ti	$<3.0 * 10^{-4}$	- *	1.6 ± 1.0
Fe	$<4.0 * 10^{-4}$	- *	10.5 ± 1.0
Cu	$4.5 * 10^{-3}$	- *	1.9 ± 1.0
Zn	$<4.0 * 10^{-4}$	- *	4.2 ± 1.0
Pt	$1.0 * 10^{-2}$	- *	7.1 ± 1.0
Pd	99.80	98.10 ± 1.0	31.9 ± 1.0

* Lower than measuring limit of EDS

Table 3.1. Concentrations of impurities (Atomic weight percent) found in virgin Pd after three weeks of electrolysis (EDS) [Bockris 1995 (Table 2)].

From these XPS determinations it can be concluded that the impurities measured, which spread no further than a few tens of Å inside the Pd, originated in the solution by means of electrochemical deposition or adsorption on the electrode surface and subsequent diffusion into the electrode. On the other hand, the elements observed about 1μ inside the metal (shown in Table 3.1) had no relationship to the impurities in the solution and they concluded that these elements were the result of the nuclear reactions in the PdH formed by the electrolysis.

3.5.1 Size effect of the CFP

The localization of the nuclear reactions in the CF material is indirectly shown by the recent experiments with the CF materials based on the hydrides and deuterides of zirconia (e.g. [Kitamura 2013], [Hioki 2017] [Kitamura 2018], [Takahashi 2020]). The overall tendency of the experimental results obtained by these authors will be explained as follows using the mechanism proposed in our phenomenological model (e.g. [Kozima 2013]).

For a material M with a constant volume V (or a constant mass m), the surface area S of M is proportional to L^2 where L is a measure of the linear dimension of M while V is proportional to L^3. Therefore, the surface area per unit mass (or volume) S/V decreases inverse proportionally to L; SL/V = constant.

According to the characteristic localization of the nuclear reactions of the CFP at surface area as determined by experiments [Kozima 2011], the following *size effect* of the CFP. If the volume of the active region is determined by the self-organization of PdD (or NiH) lattice as we considered in our model, the volume V_a of the active region for the nuclear reaction resulting in the CFP is proportional to the surface area S of the sample ; V_a/S = constant.

According to the self-organization mechanism [Kozima 2013, 2020] to form the active region (with volume V_a) of the nuclear reactions for the CFP, V_a/V is proportional to S/V; *then V_aL/V = constant.*

Therefore, the volume V_a per unit volume (or per unit mass) V_a/V (proportional to S/V) is inversely proportional to L; V_aL/V = constant. While the excess heat per unit mass (Q_0) is proportional to the volume ratio V_a/V (and therefore to S/V) and then, Q_0 is inversely proportional to the size L of the sample; $Q_0 L$ = constant.

According to the self-organization mechanism to form the active region (with volume V_a) for the nuclear reactions in the CFP, V_a/V is proportional to S/V; V_a/S = constant. Therefore, the excess heat Q_0 per unit mass (Q_0/V_a= constant) decreases with the linear dimension of the sample; $Q_0 L$ = constant.

This dependence may be observed experimentally if we can control the size of the nano-scale Ni-Pd alloy particles in the mixed matrix of $NiZr_2$ and ZrO_2 [Hioki 2017].

3.6 Recent experimental development with new CF materials all over the world

There is eager research to pursue new materials effective to get high cost-performance ratio for the excess energy generation.

Recent works by Japanese scientists in this field [Takahashi 2020, Ito 2021, Kishimoto 2021, Hasegawa 2022, Iwamura 2022, Narita 2022] show the strong world-wide tendency, a concentration to the excess energy measurement, staying away from difficulty in the essential simultaneous measurement of byproducts of nuclear reactions in addition to the excess energy. This tendency may be the cause of the DOE requirement A3-4 in the "Submissions Specifically Not of Interest" ([DOE 2022, p. 67] cited in Appendix A3).

4. Conclusion

There has appeared a faint light in front of us to recognize the specific nature of the CFP in science journalism. One of the recent examples of this tendency is the positive article by J. Messinger appeared in the *Breakthrough* [Messinger 2023] accepting the reality of the CFP and pointing out its weakness in application correctly as follows; "It may be the case that while real, cold fusion will never be a viable energy technology because LENR effects may occur only in isolated regions of metal hydride surface layers. But if proven and extended to a larger volume of the metal, the applications could be tantalizing." Recognition of the characteristics of the CFP is important in the research of the mechanism of the nuclear reactions in the CF materials and also in application of the CFP scheduled in the Project of DOE.

The supportive trend of the public opinion for the CFP in these days may be one of positive forces to push the DOE to check the reality of the nuclear reactions in the transition metal hydrides after almost 30 years from its announcement in 1989 [Fleischmann 1989]. However, the requirement of the ARPA-E Project 2022 of DOE explained in Section 2 and the experimental results explained briefly in Section 3 show the difficulty to reconcile with each other. The efforts paid by researchers in this field to explain the nature of the transition-metal hydrides resulting in the CFP with the qualitative reproducibility in more than 30 years could not overcome the barrier of misunderstanding adhered firmly by the scientists in the established fields. They did not care much about the qualitative reproducibility which has not appeared directly in the experiments smeared out by statistical averaging in many experiments where observables have not observed individually. The CFP is a rare case where the result of the individual nuclear reactions in the cold fusion material is observed directly showing the randomness of the process and necessarily the qualitative reproducibility.

The history of the cold fusion research shows clearly that it is difficult to satisfy the condition 2A-4 of the ARPA-E Project (cf. the "To constitute convincing empirical evidence" in Appendix A2). One of the characteristics of the CFP is the self-organization of the optimum superlattice structure of the type PdD (and NiH) is a rare example in the science of solid state physics and nuclear physics pointed out in Section 3 and has been the bottleneck to publish papers in this field in a top-tier research journal for more than 30 years. It will need more several years to make the science world recognize the peculiarity of the CFP as pointed out in our papers [Kozima 2021a, 2021b, 2021c, 2023] and accept the papers in this field as ones in a new genre of the material science governed by the complexity.

Even if the difficulty pointed out above is large, it is possible to hope the Project gives a

lucky blow to the science community to recognize the reality of the nuclear reactions in the cold fusion materials with specific compositions where are formed optimum arrangements of hydrogen isotopes and host atoms of transition metals at around room temperature by the self-organization mechanism. Then, there is formed a superlattice of lattice nuclei and occluded hydrogen isotopes to realize the neutron bands by the super-nuclear interaction between neutrons in lattice nuclei and finally the CFP as speculated in our paper [Kozima 2013]. We hope the lucky and happy end will be realized in 30 months of the ARPA-E Project.

Appendices (From [DOE 2022])

A1 Introduction ([DOE 2022], p. 59)
A2 Topic Description ([DOE 2022], p. 61)
A3 Submissions Specifically Not of Interest ([DOE 2022], p. 67)
A4 **LENR：**Project Descriptions

Appendix A1. Introduction ([DOE 2022] p. 59)

This announcement describes an Exploratory Topic (ET) on Low-Energy Nuclear Reactions (LENR).[20] ARPA-E invites Full Applications for financial assistance in pursuit of hypotheses-driven approaches toward producing publishable evidence of LENR that is convincing to the wider scientific community. A goal of this Exploratory Topic is to establish clear practices to rigorously answer the question, "should this field move forward given that LENR could be a potentially transformative carbon-free energy source, or does it conclusively not show promise?". Program objectives, technical categories, and performance metrics are described further in **Section 2**.

[20] We define LENR as a hypothetical energy-producing process (or class of processes) with system energy outputs characteristic of nuclear physics ($>>1$ keV/amu/reaction) and energy inputs characteristic of chemistry ($\sim$ eV/atom). See further materials from the ARPA-E LENR workshop:

  https://arpa-e.energy.gov/events/low-energy-nuclear-reactions-workshop.

ARPA-E acknowledges the complex, controversial history of LENR beginning with the announcement by Martin Fleischmann and Stanley Pons (FP) in 1989 that they had achieved deuterium-deuterium (D-D) "cold fusion" in an electrochemical cell.[21] Multiple books[22] recount the history of "cold fusion" (now known as LENR). DOE reviews in 1989 and 2004 both concluded that the evidence did not support the claim of D-D fusion, but that research proposals on deuterated heavy metals should be evaluated

under the standard peer-review process.[23] However, few such proposals were submitted, and none were funded by DOE.

Despite LENR being largely dismissed by the scientific research community by 1990, many groups from around the world (including the U.S., Japan, Russia, China, and the EU) continued to conduct varied LENR experiments and report evidence of excess heat and nuclear reactions (including neutrons, tritium, ^{3}He, ^{4}He, transmutation products, and isotopic shifts) in hundreds of reports/papers.[24] However, repeatability of the key evidence over multiple trials of seemingly the same experiment remains elusive to this day. This may be due to limitations in experimental or diagnostic techniques, a lack of awareness and/or control of the key triggers and independent variables of LENR experiments, and/or other reasons. Furthermore, results were typically not reported with the level of scientific rigor required by top-tier research journals. As a result, LENR as a field remains in a stalemate with uncertain prospects for scientific advances and impact.

Based on its claimed characteristics to date, LENR may support a form of nuclear energy with potentially low capital cost, high specific power and energy, and little-to-no radioactive byproducts. If LENR can be irrefutably demonstrated and scaled, it could potentially become a disruptive technology with myriad energy, defense, transportation, and space applications, all with strong implications for U.S. technological leadership. For energy applications, LENR could potentially contribute to decarbonizing sectors such as industrial heat and transportation (~50% of U.S. and global CO_2-equivalent emissions).

Within the past decade, there has been renewed interest in supporting LENR research activities in the U.S., with prominent sponsorship (e.g., Google, DARPA, NASA), that has advanced LENR-relevant state-of-the-art capabilities and methodologies.[25] Some of the teams are reporting preliminary evidence[26] of LENR that are possibly consistent with past observations but that do not yet meet the program metrics presented below in **Section 2**, the fulfillment of which could help break the stalemate surrounding LENR.

[21] M. Fleischmann and S. Pons, "Electrochemically induced nuclear fusion of deuterium," *J. Electroanal. Chem. Int. Electrochem.* **261**, 201 (1989); https://doi.org/10.1016/0022-0728(89)80006-3.

[22] See, e.g., J. R. Huizenga, *Cold Fusion*: *The Scientific Fiasco of the Century* (University of Rochester Press, Rochester, NY, 1993); E. Storms, *The Science of Low Energy Nuclear Reaction* (World Scientific, Singapore, 2007); S. B. Krivit, *Hacking the Atom* (Pacific Oaks Press, San Rafael, CA, 2016); and S. B. Krivit, *Fusion Fiasco* (Pacific Oaks Press, San Rafael, CA, 2016).

[23] For the 1989 and 2004 DOE review reports, see

https://www.lenr-canr.org/acrobat/ERABreportofth.pdf

and

https://www.lenr-canr.org/acrobat/DOEreportofth.pdf,

respectively. For a summary presentation of the reviews, see

https://arpa-e.energy.gov/sites/default/files/2021LENR_workshop_Greco.pdf.

[24] See, e.g., https://lenr-canr.org and the bibliographies of the Storms and Krivit books in footnote 4.

[25] See, e.g., C. P. Berlinguette et al., "Revisiting the cold case of cold fusion," *Nature* **570**, 45 (2019); https://doi.org/10.1038/s41586-019-1256-6.

[26] See talks from the ARPA-E LENR workshop:

https://arpa-e.energy.gov/events/low-energy-nuclear-reactions-workshop.

This ARPA-E Exploratory Topic aims to build on the recent progress with strong emphases on testing/confirming specific hypotheses (rather than focusing only on replication), identifying and verifying control of experimental variables and triggers, supporting more comprehensive diagnostics and analysis, improving access to broader expertise and capabilities on research teams, and insisting on peer review and publication in top-tier scientific journals.

Appendix A2. Topic Description ([DOE 2022, p. 61])

This Exploratory Topic (ET) invites Full Applications to advance LENR research by identifying and testing well-articulated hypotheses on how to activate/control LENR and their accompanying empirical signatures. A key goal of the ET is to obtain convincing empirical evidence of nuclear reactions[28] in an LENR experiment and publication of the evidence in a top-tier peer-reviewed research journal (see **Section 2A** for specific suggested criteria for what constitutes "convincing empirical evidence"). ARPA-E is seeking Full Applications that successfully address the highest-priority elements described in the sub-sections immediately below and in greater detail in the Technical Volume (TV) template, which is available for download at the ARPA-E: Funding Opportunity Exchange website (https://arpa-e-foa.energy.gov/).

[28] ARPA-E is agnostic at this time regarding the existence of LENR as a physical phenomenon (as defined in footnote 20), the underlying mechanism(s) of LENR, and the specific nuclear process(es) involved, if any (e.g., fusion, neutron capture, alpha or beta decay, neutronization, etc.).

Additional overarching goals of this Exploratory Topic are to bring together new perspectives and participants, modern state-of-the-art scientific and technical capabilities, and the experiences of long-time LENR practitioners.

2A. Technical Category A: LENR experiments ([DOE 2022, p. 63])

- - - - - - - - -

Please refer to the Technical Volume template (available for download at the ARPA-E: Funding Opportunity Exchange website (https://arpa-e-foa.energy.gov/)), which provides further guidance for preparing your Full Application.

To constitute convincing empirical evidence for LENR, each Applicant must describe how they will meet the following:

2A-1 • Conduct experiments that demonstrably satisfy the definition of LENR given in footnote 20

2A-2 • Achieve statistically significant diagnostic evidence of nuclear reactions above background and relative to control experiments, at a level greater than 99.7% (3s) statistical confidence level

2A-3 • Carefully identify and eliminate "prosaic" explanations, e.g., rogue chemical reactions resulting in excess heat, material and/or environmental contaminants, natural radiation background, etc.

2A-4 • Publish results in a top-tier research journal.

(The items pointed out in this notification are numbered as 2A-x ($x = 1 - 4$) for convenience of citation in the discussion given in the main part.

Appendix A3. Submissions Specifically Not of Interest ([DOE 2022, p. 67])

Submissions that propose the following may be deemed non-responsive and may not be merit-reviewed:

A3-1• Experiments with input energies >500 eV per directly energized particle, or >500 V of applied voltage anywhere in the experiment

A 3-2• No clear hypotheses to be tested

A 3-3• No articulated connection to prior published evidence for LENR and of how this work builds on the earlier work

A 3-4• Calorimetry as the only or primary diagnostic

A 3-5• Lack of a plan for obtaining direct empirical evidence of nuclear reactions

A 3-6• Purely theoretical or computational studies

A 3-7• Research plans requiring substantial diagnostic or code development beyond their adaptation to specific experiments.

<The items pointed out in this notification are numbered as A3-x (x = 1 – 7) at citation for convenience of citations in our discussion given in this paper (H.K.)>

Appendix A4. LENR — Low Energy Nuclear Reactions : Project Descriptions

U.S. Department of Energy Announces $10 Million in Funding to Projects Studying Low-Energy Nuclear Reactions

ARPA-E Selects 8 Projects to Apply Scientific and Rigorous Approach Focused on Specific Type of Nuclear Energy

02/17/2023

Press and General Inquiries:
202-287-5440
ARPA-E-Comms@hq.doe.gov

The following teams have been selected to receive funding as part of the Advanced Research Projects Agency-Energy (ARPA-E) LENR Exploratory Topic:

- **Amphionic (Dexter, MI)** will focus on exploring if LENR are produced in potential wells existing between two nanoscale surfaces by controlling metal nanoparticle (NP) geometry, separation, composition, and deuterium loading. *(Award amount: $295,924)*

- **Energetics Technology Center (Indian Head, MD)** will use electrochemical co-deposition of a deuterated palladium metal compound on a metal substrate conformed onto a plastic scintillator to establish and sustain LENR. *(Award amount: $1,500,000)*

- **Lawrence Berkeley National Laboratory (Berkeley, CA)** will draw from knowledge based on previous work using higher energy ion beams as an external excitation source for LENR on metal hydrides electrochemically loaded with deuterium. The team proposes to systematically vary materials and conditions, while monitoring nuclear event rates with a suite of diagnostics. *(Award amount: $1,500,000)*

- **Massachusetts Institute of Technology (Cambridge, MA)** will develop an experimental platform that thoroughly and reproducibly tests claim of nuclear anomalies in gas-loaded metal-hydrogen systems. *(Award amount: $2,000,000)*
- **Stanford University (Redwood City, CA)** will explore a technical solution based on LENR-active nanoparticles and gaseous deuterium. *(Award amount: $1,500,000)*
- **Texas Tech University (Lubbock, TX)** will focus on advanced materials fabrication, characterization, and analysis, along with advanced detection of nuclear products as a resource for teams within the LENR Exploratory Topic. *(Award amount: $1,150,000)*
- **University of Michigan (Ann Arbor, MI)** will use a gas cycling experiment that passes deuterium gas through a chamber filled with palladium nanocrystalline samples. Variables will include temperature, nanocrystalline size, and laser wavelength. *(Award amount: $1,108,412)*
- **University of Michigan (Ann Arbor, MI)** will provide capability to measure hypothetical neutron, gamma, and ion emissions from LENR experiments. Modern instrumentation will be coupled with best practices in data acquisition, analysis, and understanding of backgrounds to interpret collected data and evaluate the proposed signal. *(Award amount: $902,213)*

Some details:

University of Michigan — Ann Arbor, MI *Ionizing Radiation Detection for Exploratory Experiments in Low-Energy Nuclear Reactions - $902,213*

University of Michigan will provide capability to measure hypothetical neutron, gamma, and ion emissions from LENR experiments. Modern instrumentation will be coupled with best practices in data acquisition, analysis, and understanding of backgrounds to interpret collected data and evaluate the proposed signal.

University of Michigan — Ann Arbor, MI *Systematic Evaluation of Claims of Excess Heat Generation from Deuteration of Palladium-Nickel Nanocomposites - $1,108,412*

The University of Michigan proposes to systematically evaluate claims of excess heat generation during deuteration and correlate it to nuclear and chemical reaction products. The team plans to combine scintillation-based neutron and gamma ray detectors, mass spectrometers, a calorimeter capable of performing microwatt-resolution measurements of heat generation, and ab-initio computational approaches. The proposed research will experimentally and theoretically explore the origin and mechanisms of excess heat generation and LENR.

Texas Tech University — Lubbock, TX *Advanced Materials Characterization and*

Nuclear Product Detection for LENR - $1,150,000

Texas Tech University will develop accurate materials fabrication, characterization, and analysis to attempt to resolve the physical understanding of Low-Energy Nuclear Reactions (LENR). Texas Tech will also provide advanced detection of nuclear reaction products as a resource for ARPA-E LENR Exploratory Topic teams.

Lawrence Berkeley National Laboratory — Berkeley, CA *Quantifying Nuclear Reactions in Metal Hydrides at Low Energies - $1,500,000*

LBNL team proposes to probe for LENR at external excitation energies below 500 eV, systematically varying materials and conditions while monitoring nuclear event rates with a suite of diagnostics. The team will draw from knowledge based on previous work using higher energy ion beams as an external excitation source for LENR on metal hydrides electrochemically loaded with deuterium.

Massachusetts Institute of Technology — Cambridge, MA *Neutron Emission from Laser-Stimulated Metal Hydrides - $2,000,000*

Massachusetts Institute of Technology (MIT) proposes a hypothesis-driven experimental campaign to examine prominent claims of low energy nuclear reactions (LENR) with nuclear and material diagnostics, focusing on unambiguous indicators of nuclear reactions such as emitted neutrons and nuclear ash with unnatural isotopic ratios. The team will develop an experimental platform that thoroughly and reproducibly test claims of nuclear anomalies in gas-loaded metal-hydrogen systems.

Stanford University — Redwood City, CA *Nuclear Product Detection from Deuterated Nanoparticles Under Phonon Stimulation - $1,500,000*

Stanford University will explore a technical solution based on LENR-active nanoparticles and gaseous deuterium. The team seeks to alleviate critical impediments to test the hypothesis that LENR-active sites in metal nanoparticles can be created through exposure to deuterium gas.

Energetics Technology Center — Indian Head, MD

CATHODE (CATHode scintillatOr Detector for Electrochemistry) - $1,500,000

Energetics Technology Center will build upon past successes with co-deposition experiments using palladium, lithium, and heavy water together to create an environment in which LENR can occur. These electrolysis experiments decrease the distance from the cathode (location of LENR) to an electronic detector capable of detecting nuclear reaction products to give these experiments the best chance at reliably detecting nuclear reactions, if they are present.

Amphionic LLC — Dexter, MI *Nanostructured Pd-Anf Composites for Controlled LENR Exploitation - $295,924*

Cathode structure and surface morphology are thought to be essential for LENR reaction rate. Amphionic proposes to optimize cathode design to form Pd-polymeric composites within which the Pd nanoparticle size and shape are varied, and the interfacial separation and geometry are controlled. Experiments will focus on exploring if LENR are produced in potential wells existing between two nanoscale surfaces by controlling metal nanoparticle (NP) geometry, separation, composition, and deuterium loading.

References

[Blatt 1954] J.M. Blatt and V.F. Weisskopf, *Theoretical Nuclear Physics*, John-Wiley & Sons, New York, 1954, ISBN-10: 0-471-08019-5.

[Bockris 1995] J.O'M. Bockris and Z. Minevski, "Two Zones of 'Impurities' Observed after Prolonged Electrolysis of Deuterium on Palladium," *Infinite Energy,* **5 & 6**, 67 – 70 (1995 – 96), ISSN 1081-6372.

[DOE 1989] https://www.lenr-canr.org/acrobat/ERABreportofth.pdf

[DOE 2004] "*Report of the Review of Low Energy Nuclear Reactions*."
http://www.science.doe.gov/Sub/Newsroom/News_Releases/DOE-SC/2004/low_energy/CF_Final_120104.pdf.

A brief version of this report is posted at the following page of the DOE website.
  https://www.lenr-canr.org/acrobat/DOEreportofth.pdf,

[DOE 2021] ARPA-E LENR workshop:
  https://arpa-e.energy.gov/events/low-energy-nuclear-reactions-workshop.

[DOE 2022] ARPA-E Funding Opportunity Announcements (Advanced Research Projects Agency–Energy (ARPA-E), U.S. Department of Energy, Exploratory Topics, Announcement Type: Initial Announcement, Funding Opportunity No. DE-FOA-0002784, CFDA Number 81.135)
https://arpa-e-foa.energy.gov/Default.aspx#FoaId521a7aa4-b255-4c3b-a211-b128d2a4a0e4

[DOE 2023] ARPA-E Exploratory Topics, U.S. Department of Energy Announces $10 Million in Funding to Projects Studying Low-Energy Nuclear Reactions, 02/17/2023
https://arpa-e.energy.gov/news-and-media/press-releases/us-department-energy-announces-10-million-funding-projects-studying

[Fleischmann 1989] M, Fleischmann, S. Pons and M. Hawkins, "Electrochemically induced Nuclear Fusion of Deuterium," *J. Electroanal. Chem.*, **261**, 301 – 308 (1989), ISSN: 1572-6657.

[Hasegawa 2022] M. Hasegawa, A. Takahashi, Y. Mori, J. Hachisuka, Y. Furuyama,

"Characteristics of Excess Power Generation in MHE Experiments by D-System," *Proc. JCF22*, pp. 13 – 26 (2022), ISSN . 2187-2260.

[Hioki 2017] T. Hioki, K. Nakazawa, A. Ichiki, T. Motohiro, A. Kitamura et al., "In-situ XRD and XAFS Analyses for Metal Nanocomposites Used in Anomalous Heat Generation Experiments," *Proc. JCF18*, pp. 46 – 55 (2017), ISSN 2187-2260.

[Huizenga 1992] J.R. Huizenga, *Cold Fusion: The Scientific Fiasco of the Century,* University of Rochester Press, 1992, ISBN 1-878822-07-1.

[Ito 2021] T. Itoh, Y. Shibasaki, J. Kasagi, S Murakami, M. Saito and Y. Iwamura, "Optical Observation on Anomalous Heat Generation from Nano-sized Metal Composite," *Proc. JCF21*, pp. 15 – 25 (2021), ISSN 2187-2260.

[Iwamura 2006] Y. Iwamura, T. Itoh, M. Sakano, N. Yamazaki, S. Kuribayashi, Y. Terada and T. Ishikawa, "Observation of Surface Distribution of Products by X-ray Fluorescence Spectrometry during D_2 Gas Permeation through Pd Complexes" *Proc. ICCF12* pp. 178 – 187 (2006).

[Iwamura 2022] Y. Iwamura, T. Itoh, T. Takahashi, S. Yamauchi, M. Saito, S. Murakami, J. Kasagi, "Energy Generation using Nano-sized Multilayer Metal Composites with Hydrogen Gas; Intentional Induction of Heat Burst Phenomenon," *Proc. JCF22*, pp. 27 – 39 (2022), ISSN 2187-2260.

[Kishimoto 2021] N. Kishimoto, M. Endo, A. Kikuchi, K. Matsuhashi, K. Negishi, S. Narita, "Simulation Study of Heat Conduction in Deuterium Desorption Experiment," *Proc. JCF21*, pp. 26 – 39 (2021), ISSN 2187-2260.

[Kitamura 2013] A. Kitamura, A. Takahashi, R. Seto, Y. Fujita, A. Taniike and Y. Furuyama, "Study on Anomalous Heat Evolution from H-Ni Nanoparticle System at Elevated Temperature with Mass-Flow Calorimetry," *Proceedings of JCF14,* pp. 1 - 13 (2013), ISSN 2187-2260.

[Kitamura 2018] A. Kitamura, A. Takahashi, K. Takahashi. R. Seto et al.," Excess heat evolution from nanocomposite samples under exposure to hydrogen isotope gases." *Int. J. Hydrogen Energy* **43,** pp. 16187 – 16200 (2018), ISSN 0360-3199.

[Kozima 1994] H. Kozima, "Trapped Neutron Catalyzed Fusion of Deuterons and protons in Inhomogeneous Solids," *Trans. Fusion Technol.*, **26**, 508 – 515 (1994).ISSN 0748-1896.

[Kozima 1998] H. Kozima, *Discovery of the Cold Fusion Phenomenon,* Ohtake Shuppan Inc., Tokyo, Japan, 1998. ISBN: 4-87186-044-2.

[Kozima 2002] H. Kozima, "Excited States of Nucleons in   a Nucleus and Cold Fusion Phenomenon in Transition Metal Hydrides and Deuterides," Proc. ICCF9, pp. 186 – 191 (2002). ISSN 7-302-06489-X.

[Kozima 2006] H. Kozima, *The Science of the Cold Fusion Phenomenon*, Elsevier Science, 2006, ISBN-10: 0-08-045110-1.

[Kozima 2008] H. Kozima, W.W. Zhang and J. Dash, "Precision Measurement of Excess Energy in Electrolytic System Pd/D/H_2SO_4 and Inverse-Power Distribution of Energy Pulses vs. Excess Energy," *Proc. ICCF13*, pp. 348 – 358 (2008). ISBN 978-5-93271-428-7.

[Kozima 2011] H. Kozima, "Localization of Nuclear Reactions in the Cold Fusion Phenomenon," *Proc. JCF11,* pp. 59 – 69 (2011), ISSN 2187-2260.

[Kozima 2012] H. Kozima, "Three Laws in the Cold Fusion Phenomenon and Their Physical Meaning," *Proc. JCF12* (Kobe, Japan, December 17 – 18, 2011), pp. 101 – 114 (2012)

[Kozima 2013] H. Kozima, "Cold Fusion Phenomenon in Open, Nonequilibrium, Multi-component Systems – Self-organization of Optimum Structure," *Proc. JCF13,* **13-19,** pp. 134 - 157 (2013), ISSN 2187-2260.

[Kozima 2017] H. Kozima, "The Sociology of the Cold Fusion Phenomenon – An Essay **– ,**" *Proc. JCF17,* **17-13,** pp. 148-219 (2017), ISSN 2187-2260.

[Kozima 2019a] H. Kozima, "Inductive Logic and Meta-analysis in the Cold Fusion Research," *Proc. JCF19,* **19-14**, pp. 85 – 111 (2019), ISSN 2187-2260.

[Kozima 2019b] H. Kozima, "Development of the Solid State-Nuclear Physics," *Proc. JCF19,* **19-15**, pp. 112 – 147 (2019), ISSN 2187-2260.

[Kozima 2019c] H. Kozima, "On the 30th Anniversary of the Discovery of the Cold Fusion Phenomenon," *Infinite Energy*, **145**, pp. 28 - 34 (2019), ISSN 1081-6372.

[Kozima 2020] H. Kozima, "The 'anomalous heat effect' is a normal event in the cold fusion phenomenon – On the paper "excess heat evolution from nanocomposite samples under exposure to hydrogen isotope gases" by Kitamura et al. Published in the *Int. J. Hydrogen Energy* 43, pp. 16,187–16,200 (2018)," *Int. J. Hydrogen Energy* **45**, pp. 19577-19582 (2020), ISSN 0360-3199.

[Kozima 2021a] H. Kozima, "Cold Fusion Phenomenon in the Composite CF Materials – Mixed Hydrogen Isotopes, Alloys, Ceramics, and Polymers –," *Proceedings of JCF21*, 21-2 (2021), ISSN 2187-2260.

[Kozima 2021b] H. Kozima, "Cold Fusion Phenomenon in the Compound CF Materials – Effects of Interfaces –," *Proceedings of JCF21*, **21-3** (2021), ISSN 2187-2260.

[Kozima 2021c] H. Kozima, "The Cold Fusion Phenomenon – Nuclear Transmutations in the CF Materials at Around Room Temperature –," *International Journal of High Energy Physics* 8 (1), pp. 1 – 12 (2021), ISSN 2376-7448.

http://www.sciencepublishinggroup.com/journal/paperinfo?journalid=124&doi=10.1164

8/j.ijhep.20200703.11

[Kozima 2023] H. Kozima, "Peculiarities of Physics and Chemistry in the Transition Metal Hydrides," *J. Condensed Matter Nuclear Science,* **37**, pp. 1 – 13 (2023), ISSN2227-3123 (to be published).

[Lietz 2008] H. Lietz, "Status of the Field of Condensed Material Nuclear Science", Working Paper, Mittweida University, August 2008.

[McKubre 1993] M.C.H. McKubre, S. Crouch-Baker, A.M. Riley, S.I. Smedley and F.L. Tanzella, "Excess Power Observed in Electrochemical Studies of the D/Pd System," *Proc. ICCF3*, pp. 5 - 19, Universal Academy Press, Inc., Tokyo, 1993, ISBN: 4-946443-12-6.

[Messinger 2023] J. Messinger, "Fusion Runs Hot and Cold – How the academy has gotten cold fusion wrong for over three decades –," *The Breakthrough*, May 18, 2023. https://thebreakthrough.org/issues/energy/fusion-runs-hot-and-cold

[Narita 2022] S. Narita, M. Endo, H. Matsuhashi, N. Yanagidate, A. Shoji, "Recent Progress of Deuterium/Hydrogen Desorption Experiments Using Pd-Ni Samples," *Proc. JCF22*, pp. 50 – 57 (2022), ISSN 2187-2260.

[Okamoto 1994] M. Okamoto, H. Ogawa, Y. Yoshinaga, T. Kusunoki and O. Odawara, "Behavior of Key Elements in Pd for the Solid State Nuclear Phenomena Occurred in Heavy Water Electrolysis," *Proc. ICCF4* (Hawaii, USA, Dec. 6 — 9, 1993), Vol.**3**, p.14 (1994), EPRI, Palo Alto, California, USA.

[Poincare 1902] Henri Poincaré, *Science and Hypothesis*, p. 141 (1902). Translated by W.J.G., Dover Publications Inc. 1952. Library of Congress Catalog Card Number 53-13673.

[Storms 2007] E. Storms, *The Science of Low Energy Nuclear Reactions*, World Scientific Publishing, 2007. ISBN-10 981-270-620-8.

[Takahashi 2020] A. Takahashi, T. Yokose, Y. Mori, A. Taniike, et al., "Enhancement of Excess Thermal Power in Interaction of Nano-Metal and H(D)-Gas," *Proc. JCF20*, pp. 15 – 33 (2020), ISSN 2187-2260.

Theory of Nuclear Fusion Chain Reactions in Metal Crystals

Kazuo Ooyama

Ooyama Power Inc.

k1@ ooyama-power.com

Abstract We presented "Nuclear Fusion Mechanism in Metal Crystals [1]" at JCF18 and showed that there are two types of responses to cold fusion. Among these reactions, "Complete combustion (Nuclear fusion chain reaction) [1]" is an important reaction that can become an energy source for human beings in the future. We hypothesized that "Heat after Death [2]" is "Nuclear fusion chain reaction" involving ^{6}Li contained in the electrolyte. If this hypothesis is correct, ^{6}Li should be generated in the Pd electrode. We found evidence of ^{6}Li production by "Heat after Death" from a previous paper [3]. "Start-up of Metal Crystal confinement Fusion Reactor [4]" publishes the creation and start-up of a nuclear reactor using the "Nuclear fusion chain reaction". However, the fusion cross-section is insufficient for a chain reaction to occur, the reaction must be explosive because it completes instantaneously, and the reaction that produces 4He in DD fusion is extremely occur only with a low probability. For these three reasons, the "Nuclear Fusion Chain Reactions" hypothesis is not accepted.

In this paper, we overturn the above three reasons based on the channeling phenomenon in crystals, the cancellation of the Coulomb repulsive force due to fluctuations in the position of interstitial atoms and free electrons due to the uncertainty principle, and a new form of the nuclear force potential that replaces the meson theory.

In addition, the discovery of hydrogen residuals in the Pd samples used in the "Start-up of Metal Crystal confinement Fusion Reactor [4]" and the new form of the nuclear force potential have led to revisions in the interpretation of the experimental results. Therefore, it is presented in this paper.

Keyword: Fusion chain reaction, Metal crystal, Meson theory, Neutron reaction cross section, Nuclear force potential, Binary nucleus, Fusion reactor, Nuclear force barrier

1. Introduction

CF (Cold Fusion) research began in 1989, when Pons et al. reported "Excess enthalpy generation is markedly dependent on the applied current density and is proportional to the volume of the electrodes [5]". This description misled subsequent research into the direction of dissolving a large amount of deuterium in Pd. In the absence of a theory, researchers consider the temperature rise they do not understand to be CF. As time passes, experiments that are easy to enter and that can reliably confirm heat generation and do not emit radiation will become mainstream. In this way, the current state of CF is

that research has entered a dead end.

However, the root cause of this state of affairs is that scientists who should lead the field of nuclear physics have shifted their focus to research on the properties of muons and the discovery of new elementary particles, which are more likely to produce results. They seem to think that the nuclear reaction between hydrogen isotope has been theoretically elucidated. However, in the field of nuclear physics, there are many phenomena whose reasons have not been clarified. For example, neutron reaction cross sections for low-mass nuclei, DD and DT fusion cross sections, discrepancies with theoretical shielding energies in metals, and generation of three-body fusion particles in metals. Investigating the shape of the nuclear power potential, it is necessary to go back to the formula of the nuclear power potential, which was exemplified in the 1935 papers of the Yukawa meson theory [6]. However, in the formula, neutron reaction cross sections for low-mass nuclei and DD and DT fusion cross sections cannot be explained. It is abandoned as a mystery in a state of contradiction from the experiment. Although a thermal fusion reactor is created, experimental data is being implemented without the theoretical analysis of why the DT nuclear cross -sectional area is like this.

In this paper, we will explain the feasibility of the hypothesis of "Nuclear Fusion Chain Reactions" together with the elucidation of these unexplained phenomena.

2. Heat after Death

"Heat after Death [2]" is the title of a 1994 paper by S. Pons and M. Fleischmann. Five years after the announcement in 1989, it's an important paper that they wrote in a sober review of what happened. Figure 1 shows the temperature change of the electrolysis cell, and shows that the Pd cathode maintained a high temperature state for about 3 hours after the electrolyte evaporated and the current stopped flowing in the electrolysis experiment. As a similar phenomenon, Dr. Mizuno's book also describes that the electrolysis cell generated heat for 12 days after the end of electrolysis [7]. The "Heat after Death" is an important phenomenon that can serve as an energy source for humankind in the future.
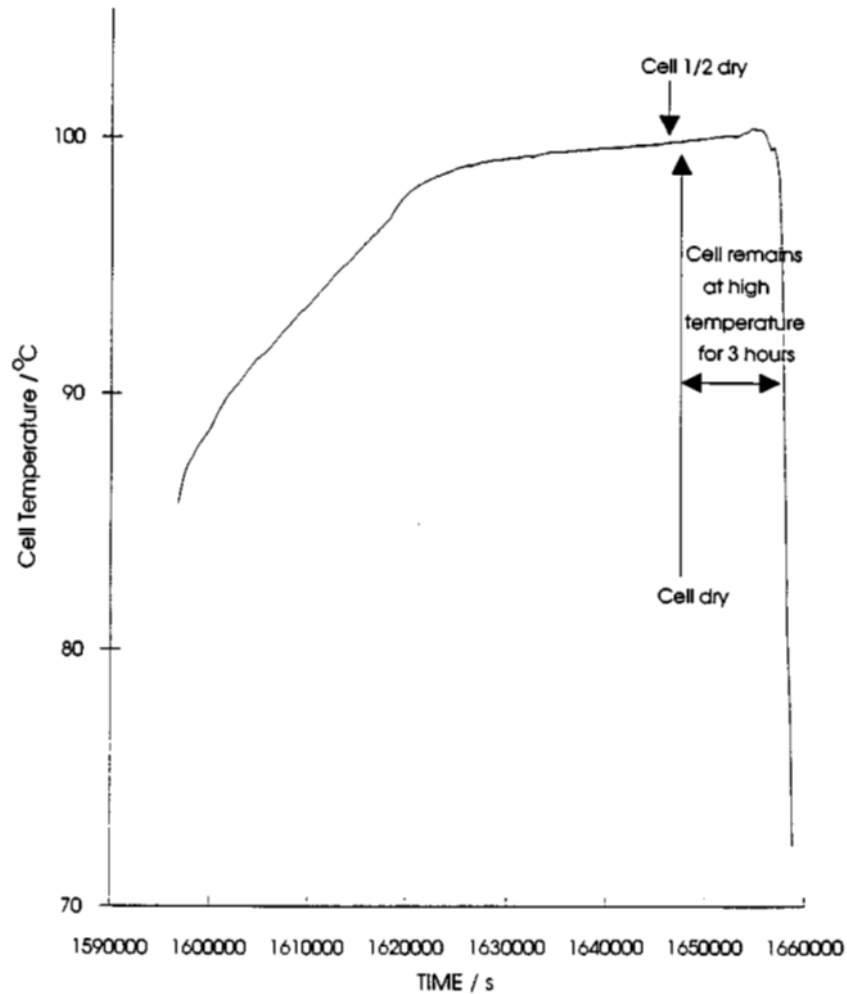
Fig. 1 The temperature-time curve for a cell being driven to boiling showing also the initial part of the cooling curve - 2 mm length Pd cathode polarized in 0.1M LiOD in D_2O; final cell current: 500 mA [2].

3. Hypothesis of Heat Generation Mechanism of Pd Cathode

Since "Heat after Death" is generated after electrolysis of heavy water in which a special lithium hydroxide is dissolved with a palladium electrode, we believe that lithium is involved. We hypothesized the following "Nuclear Fusion Chain Reactions [1] ".

A) $X + {}^2H \rightarrow X + d$

A natural high-energy particle X collides with a D nucleus in Pd, producing a d ion.

B) $d + {}^2H \rightarrow {}^4He$

A d ion collides with a D nucleus, producing a ${}^4He$ nucleus.

C) $d + {}^4He \rightarrow {}^6Li$

   A d ion collides with ^{4}He nucleus to produce ^{6}Li nucleus.

D) $d + {}^6Li \rightarrow 2\alpha$ (22.4MeV)

   A d ion collides with a ^{6}Li nucleus, producing two high-energy α-ions. The α
   ions become X in Formula A, and the nuclear fusion chain reaction occurs.

If the hypothesis is correct, ^{6}Li should have accumulated in the Pd cathode.

4. Evidence for ^{6}Li formation
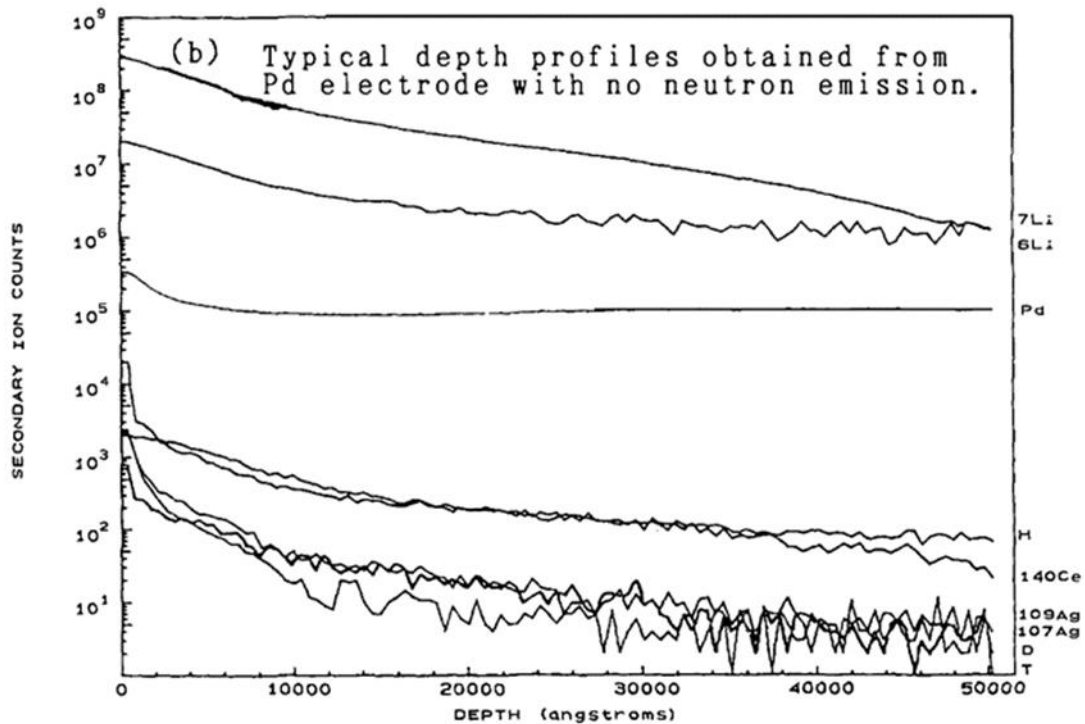
Fig. 2 The typical examples of depth profiles observed by SIMS analysis [3].

Figure 2 shows the typical examples of depth profiles observed by SIMS analysis of the Pd-5 electrode, one of the five electrodes, published in Prof. Okamoto et al.'s paper [3].

The secondary ion number lines of ^{6}Li and ^{7}Li in Figure 2 intersect at a depth of 50000Å. Originally, the two lines should be parallel because the isotope ratio in nature is constant at ^{6}Li/^{7}Li = 7.5/92.5. Although Prof. Okamoto et al. did not describe this point, it is clear evidence that ^{6}Li was generated inside the electrode because the difference in diffusion coefficient due to the difference in isotope mass is not so large. It is stated that this electrode did not generate heat or generate neutrons during electrolysis. Compared to other samples, amount of deuterium and hydrogen are abnormally low,

and amount of Li is large and diffusion of Li is progressing, so it is considered that there is a history of exposure to high temperatures. From these things, we conclude that PD-5 electrodes experience "Heat after Death".

We confirmed the reliability of this data with Prof. Odawara, co-author of the paper [3] and in charge of SIMS, and asked him about the measurement equipment and measurement conditions. We prepared a standard sample of Pd doped with a fixed amount of ^{6}Li, and measured secondary ions by SIMS under the same conditions as possible. We estimated the concentration of ^{6}Li at a depth of 50000Å (5µm) in Pd-5, where ^{6}Li is actively produced, to be 0.059mol% [4].

There are three reasons why nuclear physicists have rejected our claim that "Heat after Death" is the result of a fusion chain reaction, even with clear evidence of such ^{6}Li production. The 1st reason is the problem of fusion cross section. This is because it is believed that nuclear reactions do not occur with such high probability that chain reactions occur in Pd metal, where even alpha rays with MeV-order energies can move only about 10 μm. The 2nd reason is that nuclear reactions are completed instantly, so any chain reaction will be explosive. The 3rd reason is that reactions that produce ^{4}He occur only with extremely low probability, and D(d,n)^{3}He and D(d,p)T occur approximately 50% each in DD fusion. In the following, we show that these three reasons break down in metal crystals, and the results of experimental reactors are shown as evidence.

5. 1st nuclear reaction cross section problem

Since the atoms that make up matter are accompanied by electrons, the electrical repulsive force (Coulombic repulsive force) is reduced compared to the ions of the atomic nucleus alone, making nuclear fusion easier to occur. This is called a shielding effect, and metals exhibit a larger shielding effect than is theoretically expected, but humankind has not yet clarified the reason for this.

Figure 3 shows the measured screening energy versus D concentration [8]. Since the horizontal axis is the reciprocal of the D concentration, the lower the concentration, the higher the shielding energy. Since the state of each metal is not described, it is highly likely that it was not annealed after molding. The d ions are implanted at 2.5 to 10 keV, which is much higher than the binding energy of the crystal lattice, and the D density far exceeds the amount of each metal that can be solid-solved. These points are the same in experiments [14] [15] in which titanium (Ti) metal is irradiated with d ions, which will be described later. In other words, in these experiments, a large number of high-energy d ions are irradiated to destroy the crystal structure, and the d ions irradiation experiments

are performed on a glass-like amorphous material in which metal and deuterium are mixed. The shielding effect of Pd is 310 eV in [8], but 800 eV in [9]. The fact that there is a large variation among operators indicates that the shielding effect varies greatly depending on the condition of the metal. If the metal maintains its original crystal structure, a channeling effect can be expected in which ions are converged into the gaps between the atoms that make up the crystal lattice, which may further increase the probability of nuclear fusion.
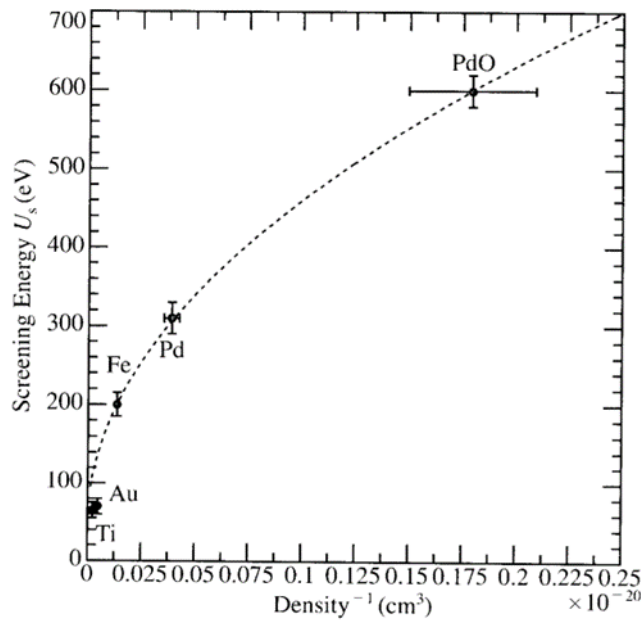
Fig. 3 Deduced screening energy as a function of inverse of the deuteron density [8].

PdO (palladium oxide) is a conductive substance and a member of the metal family. It has a density of 8.3 and a tetragonal crystal structure in which the atoms of O of mass number 16 and Pd of mass number 106 are arranged alternately, but not necessarily in a regular arrangement. Normally, the crystals are in the form of black powder and finely divided, so channeling is difficult to occur, but the low D concentration provides a shielding effect of 600 eV.

Converting the concentration of ^{6}Li of 0.059 mol % described above to the unit of Density on the horizontal axis in Figure 2 gives 2.82×10^{-20}. The shielding effect of a Pd metal crystal with a density of 12, which maintains a crystal structure composed of uniform atoms and is located on the left side of the horizontal axis by 11 times, should show a considerably high value. There are two reasons why metal exhibits such a high shielding effect.

One is the increase in nuclear fusion probability due to the channeling phenomenon.

The channeling phenomenon means that irradiated ions are converged at the center of the crystal gap and penetrate deeper than usual. Due to this phenomenon, it is possible to collide with the D nuclei of the interstitial atoms of the Pd crystal with high probability.
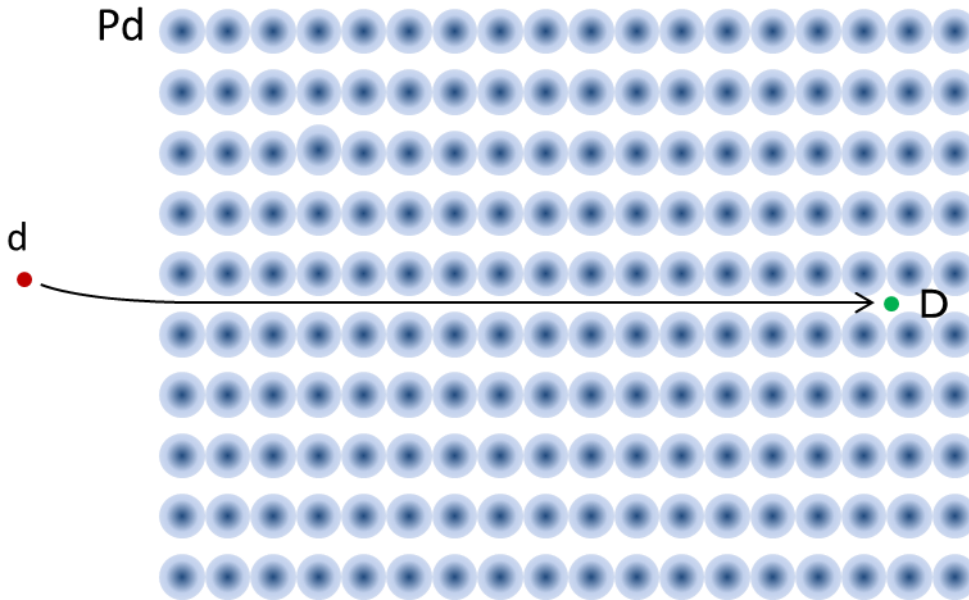
Fig. 4 Image of increase in nuclear fusion probability due to channeling phenomenon

The other is the spread of the standard deviation of the position of the D nucleus due to the uncertainty principle, and the Coulomb repulsion is canceled by the existence of metal free electrons, which increases the fusion probability. By the uncertainty principle, the product of the standard deviation of the momentum and the standard deviation of the position of the D nucleus is larger than $\hbar/2$. Atomic nuclei of atoms between Pd metal crystal lattices have the same temperature as Pd metal due to heat conduction with surrounding metal atoms. If the standard deviation of the temperature of the D nucleus is 80±1°C, the uncertainty principle gives the standard deviation of the position of the D nucleus to be 53.2 Å, which is 14 times wider than the lattice constant of Pd, 3.89 Å. Since the spread extends to 19 interstitial positions ahead, the Coulomb barrier of the D nucleus between crystal lattices becomes extremely low, overlapping with the existence of the surrounding metallic free electrons. And the ions can proceed without disturbance of the channeling trajectory because the presence of D nuclei is distributed like a cloud. Since the ions penetrate the part where the D nucleus is highly probable, the probability of nuclear fusion increases.

From the above, the 1st reason collapses considerably. They suggest that metals suitable for simultaneous fusion chain reactions would be dense, large crystals, low

strain, and low in impurities with crystal structures that match the location of channeling paths and interstitial atoms. Moreover, since it thinks that it is still insufficient to raise a nuclear fusion chain reaction, the nuclear fusion cross section is examined from the form of nuclear force potential.

6. The shape of the nuclear force potential

In order to cause DD fusion, the d ion must overcome the repulsion due to the Coulomb force with the D nucleus and approach until the attraction due to the nuclear force works. Coulomb force Fc is represented by the following equation.

$Fc = - e^2 / (4\pi\varepsilon_0 L^2)$

where L is the distance between D and D. From this, the Coulomb potential Ec is expressed as follows.

$Ec = e^2 / (4\pi\varepsilon_0 L)$

To discuss the nuclear force potential, we must go back to the 1935 Yukawa meson theory paper [10]. At this time, the nuclear force was exemplified as follows.

$En = f \cdot e(-\eta L) / L$

Here, f is the coupling coefficient between D-D. In this paper, f = 7.953E-27 was calculated from the D-D fusion energy of 23.8 MeV at 1.4fm (1.4E-15m).

And η is back-calculated from the meson mass m by the following formula.

$m = h\eta/(2\pi c)$

Here, h is Planck constant and c is the speed of light.
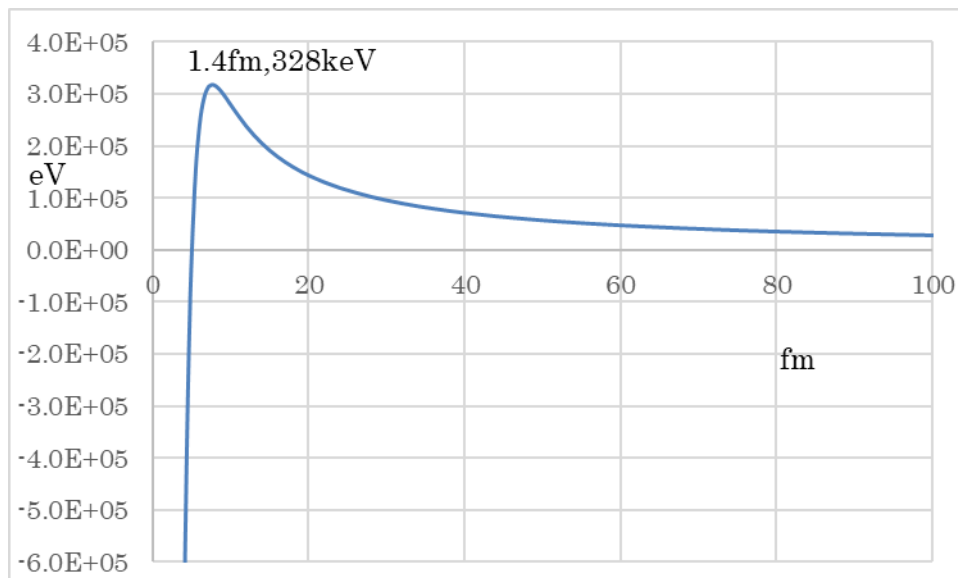
Fig. 5 Sum of DD nuclear potential and Coulomb potential.

Figure 5 shows the total potential Ep of the nuclear force potential En and the Coulomb potential Ec.

Ep = Ec + En

The maximum value of the total potential is Epmax = 318 keV.

Epmax is called the Coulomb barrier height, and this Coulomb barrier is located at L= 7.5fm and has an area of 0.44b (0.44E-28m^2). The fusion cross section is only a fraction of this area, as it includes the elastic scattering cross section. Although the Coulomb barrier height is lowered by free electrons and the area is increased, it seems that the nuclear fusion cross section is still insufficient to initiate a chain reaction.
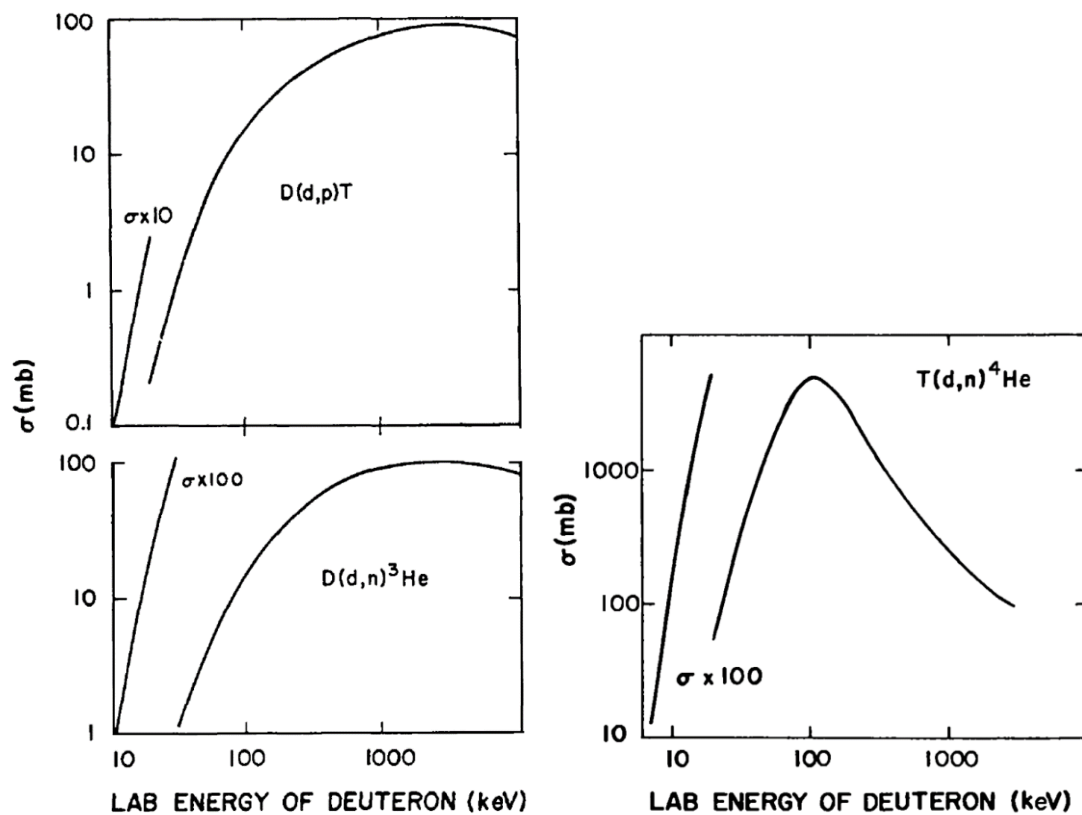
Fig. 6 DD and DT fusion cross sections [11]

Figure 6 shows the DD and DT fusion cross sections. In DD fusion, the upper left D(d,p)T reaction and the lower left D(d,n)^{3}He reaction occur almost equally. Although the coulomb forces of fusion cross section T nucleus and D nucleus are the same, the T(d,n)^{4}He reaction on the right has a huge 6b cross section for d ions with an energy of 100 keV. The exemplified formula of the Yukawa meson theory clearly shows that the reaction cross section is small, and it is necessary to modify the nuclear force potential.

Humankind knowledge of the origin of nuclear force has progressed from meson

theory to quark exchange theory, and QCD analysis of nuclear force potential is also being attempted. Figure 7 shows the nuclear force potential by QCD analysis. The Coulomb core radius of protons is calculated to be 0.84fm, while it is 0.5fm including neutrons. The nuclear force potential cannot be explained by experimental data on the DT fusion cross section or the core radius, and it is merely the one that matches the exemplified formula of the Yukawa meson theory.
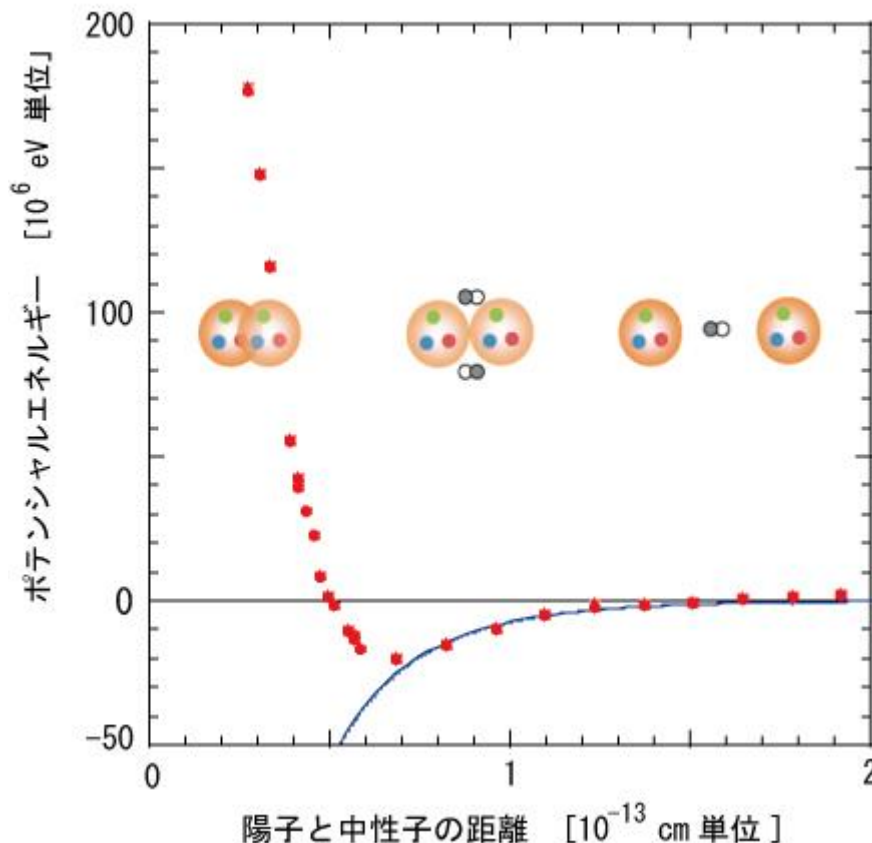
Fig. 7 Nuclear force obtained for the first time in the world using a supercomputer (red circle). The horizontal axis is the distance between protons and neutrons, and the vertical axis is potential energy. The blue solid line is the exemplified formula of the Yukawa meson theory. The schematic diagram in the figure shows that protons and neutrons, which consist of three quarks, exchange pi mesons at long distances, and directly exert forces at close distances [12].

Therefore, we decided to estimate the nuclear force potential between low-mass nuclei by referring to the reaction cross section of low-mass nuclei and neutrons where the Coulomb force does not work. These also cannot be explained by the exemplified formula of the Yukawa meson theory.

Figure 8 shows the neutron cross section for ^1H [13]. The dashed-dotted line below is

the capture, which is the reaction cross section for deuterium nuclei. The dotted elastic scattering cross section is hidden under the solid line total.
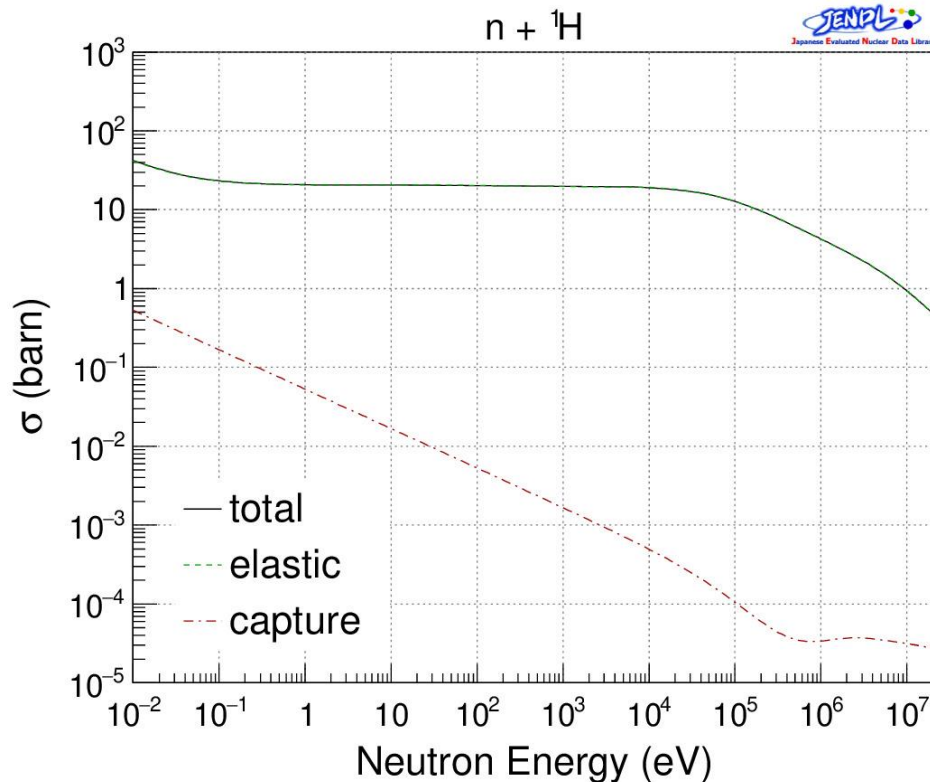
Fig. 8 Neutron reaction cross section for [1]H [13]

Elastic scattering of neutrons is said to be due to collisions with the core of the nucleus in massive nuclei. However, the charge radius of the proton (p), which is the nucleus of H, is calculated to be 0.84 fm, and if the size of the neutron (n) is also approximately the same, the elastic scattering cross section of n with respect to p should be 0.15b, but it is actually 20b. There is something like a wall with a diameter of 50 fm. This wall is called the nuclear force barrier. As the neutron energy increases, the elastic scattering cross section decreases. This indicates that the nuclear force barrier is a wall that changes with neutron energy.

Figure 9 shows the neutron cross section for [3]He [13]. Since it has an elastic scattering cross section of about 3b, the diameter of the nuclear force barrier becomes 19.6 fm. For neutrons with energies below 200 keV, it has a wide [3]He(n, p)T cross section that is inversely proportional to the square root of the energy. This indicates that the nuclear force spreads outward from the nuclear force barrier, and that the nuclear force is inversely proportional to the fifth power of the distance. It shows that the

nuclear force potential, which is the integral value of the nuclear force, decreases in inverse proportion to the fourth power of the distance as it approaches the center when infinity is assumed to be 0. The fact that the nuclear force barrier reflects neutrons means that the nuclear force potential suddenly changes to 0 or more inside the nuclear force barrier.
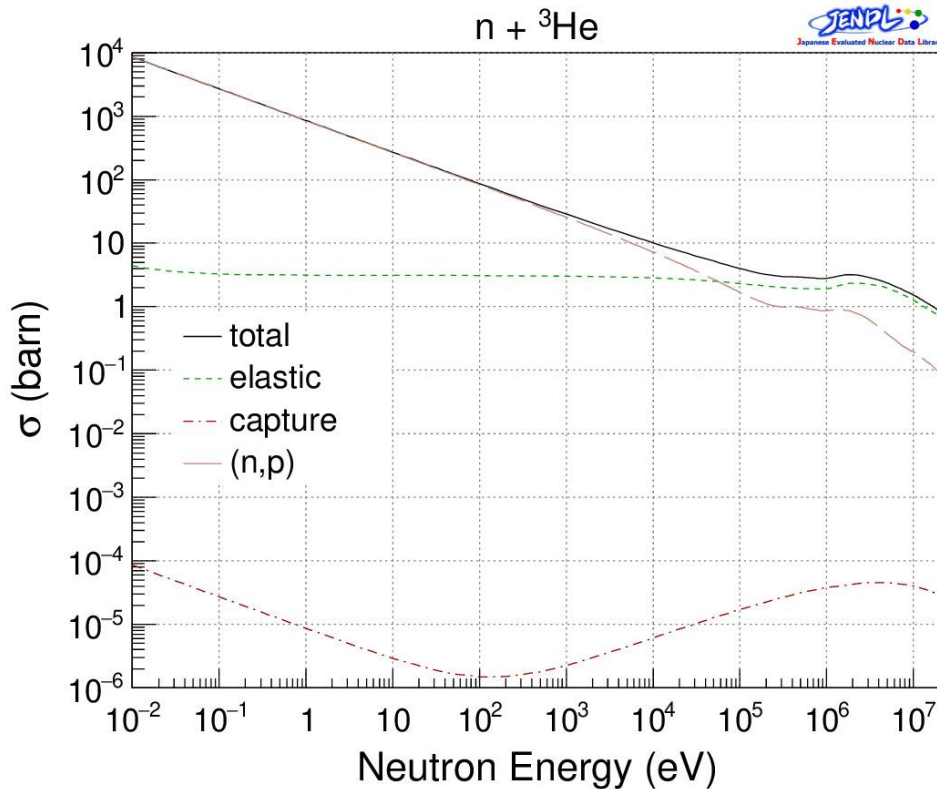
Fig. 9 Neutron reaction cross section for ^{3}He [13]

The nuclear reaction cross section of high-energy neutrons is continuous and remains almost unchanged between 200 keV and 2 MeV, which is below the elastic scattering cross section. Until now, the Charge core was used as the size of the atomic nucleus, and it was thought that the nuclear force was also generated from this core part. However, the nuclear force is generated from the surface of the nuclear force barrier, and near the surface of the nuclear force barrier, a stronger nuclear force acts on approaching neutrons, and a pocket is formed that binds the neutrons.

Neutrons that enter from outside the elastic scattering cross section and are captured by the nuclear force, which is inversely proportional to the fifth power of the distance, will always fall into the pocket without balancing the inertial force even if they are accelerated by the nuclear force and increase in speed. Such neutrons have angular

momentum with respect to the ^{3}He nucleus because they are coming in toward a position away from the ^{3}He nucleus center. The neutrons that enter the pocket undergo nuclear fusion in a short period of time by the tunnel effect, causing a ^{3}He(n, p)T reaction that emits p-particles to release the angular momentum.

The capture cross-section is 8 orders of magnitude narrower than the ^{3}He(n, p) T cross-section, and the neutrons are entering the center of the ^{3}He nucleus almost exactly. This is because only γ rays are emitted in the ^{3}He (n, γ) ^{4}He reaction of capture, so the reaction cannot occur unless the angular momentum is almost zero.
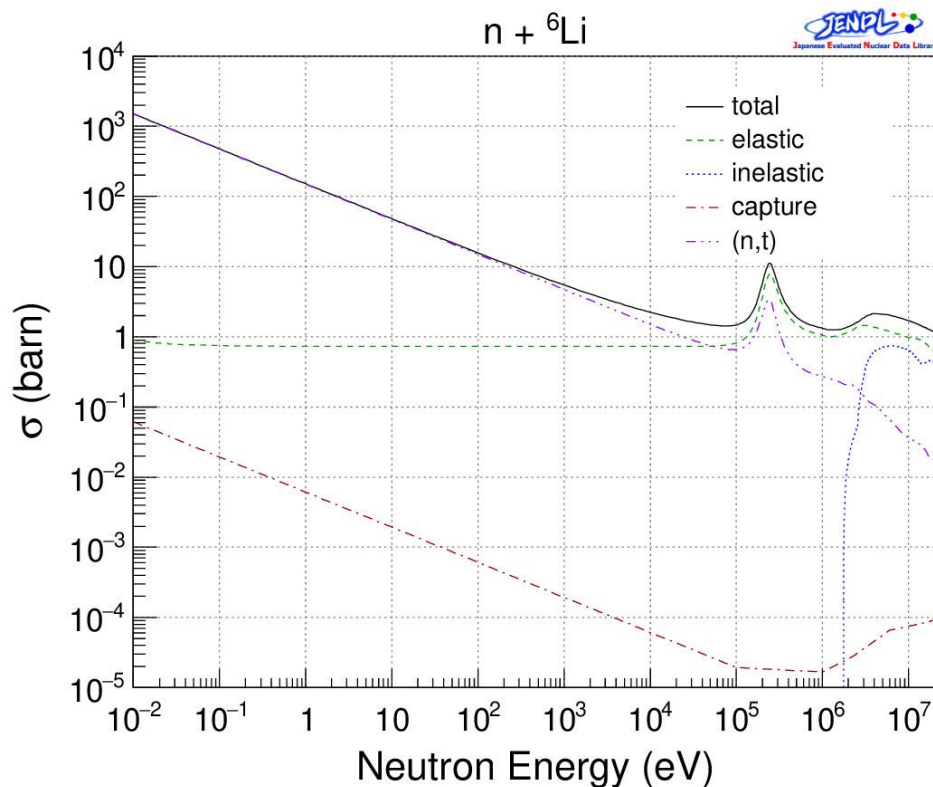
Fig. 10 Neutron cross section for ^{6}Li [13]

Figure 10 shows the neutron cross section for ^{6}Li [13]. The spread of the nuclear force tends to be smaller as the fusion energy is lower. While the ^{6}Li (n, t)^{4}He reaction emitting T particles has a large cross section, the capture ^{6}Li (n, γ)^{7}Li reaction cross section is 4.5 orders of magnitude narrower here as well.

Figure 11 shows the neutron cross section for ^{2}H [13]. The nuclear force barrier is less than ^{1}H and about 3.5b greater than T. It is not the case that the larger the mass number, the smaller the size of the nuclear force barrier. If the fusion energy is positive (when the mass decreases), the capture ^{2}H(n, γ)T reaction that produces T, an unstable

nucleus, also occurs.
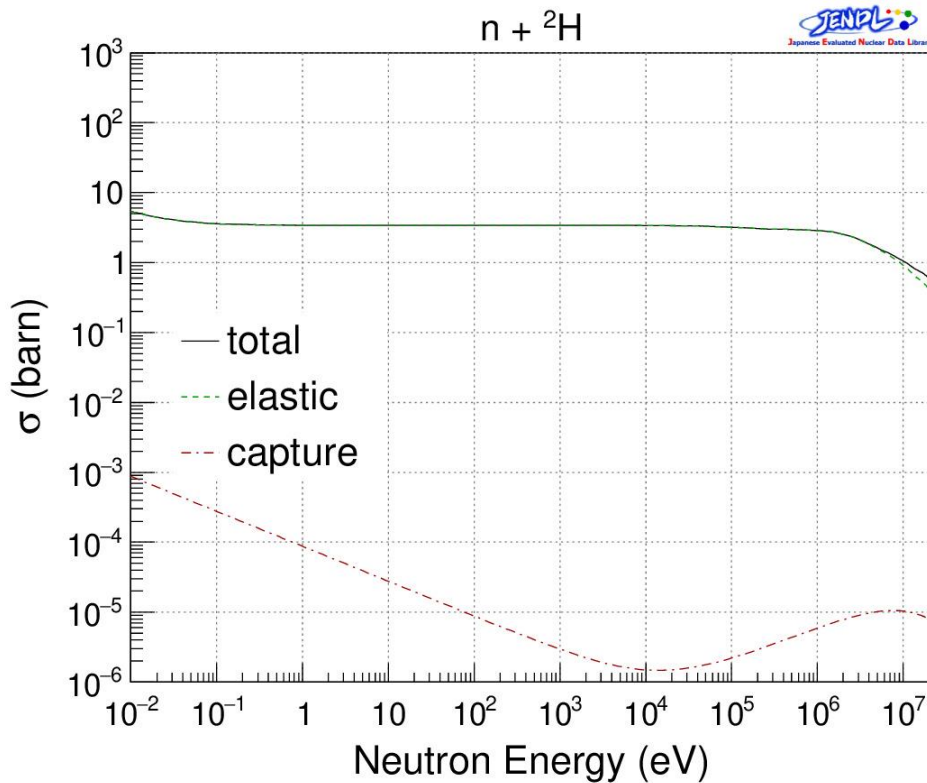
Fig. 11 Neutron cross section for ^{2}H [13]

The reason why there is a peak in the reaction cross section in Figure 6 is that the Coulomb barrier prevents the passage of low-energy particles, while the high-energy particles decrease in inverse proportion to the square root of the energy, like neutrons. Since the nuclear force is generated from the nuclear force barrier wider than the charge core, the Coulomb barrier becomes lower and wider than the exemplified formula of the Yukawa meson theory. We think that this nuclear force barrier diameter varies depending on the combination of nucleons. If we consider that the nuclear force barrier against d ions exists in a place where the T nucleus is farther from the center and has a smaller Coulomb force than the D nucleus, the reason why the T nucleus has a larger reaction cross section than the D can be explained. As shown in Figure 6, the presence of free electrons in a metal lowers the Coulomb barrier, so the reaction cross section on the low-energy side increases dramatically.

We think that 1st reason has been overturned above.

7. Evidence that the 2nd and 3rd reasons collapse

7-1. 3-body fusion particle

Table 1 Normal DD fusion primary and secondary reaction product particles

Primary reaction $d + {}^2H \rightarrow {}^3H$ (1.0MeV) + p (3.0MeV) $\rightarrow 3He$ (0.8MeV) + n (2.5MeV) Secondary reaction ${}^3H + {}^2H \rightarrow \alpha$ (3.5MeV) + n (14.1MeV) ${}^3He + {}^2H \rightarrow \alpha$ (3.7MeV) + p (14.7MeV)

Table 1 summarizes the energies of primary and secondary reaction product particles in normal DD fusion. The highest energy particle in the primary reaction is the 3.0 MeV proton. When ${}^3H$ and ${}^3He$ produced in the primary reaction react with ${}^2H$, the secondary reaction particles are up to 14.7 MeV protons and 3.7 MeV alpha particles.
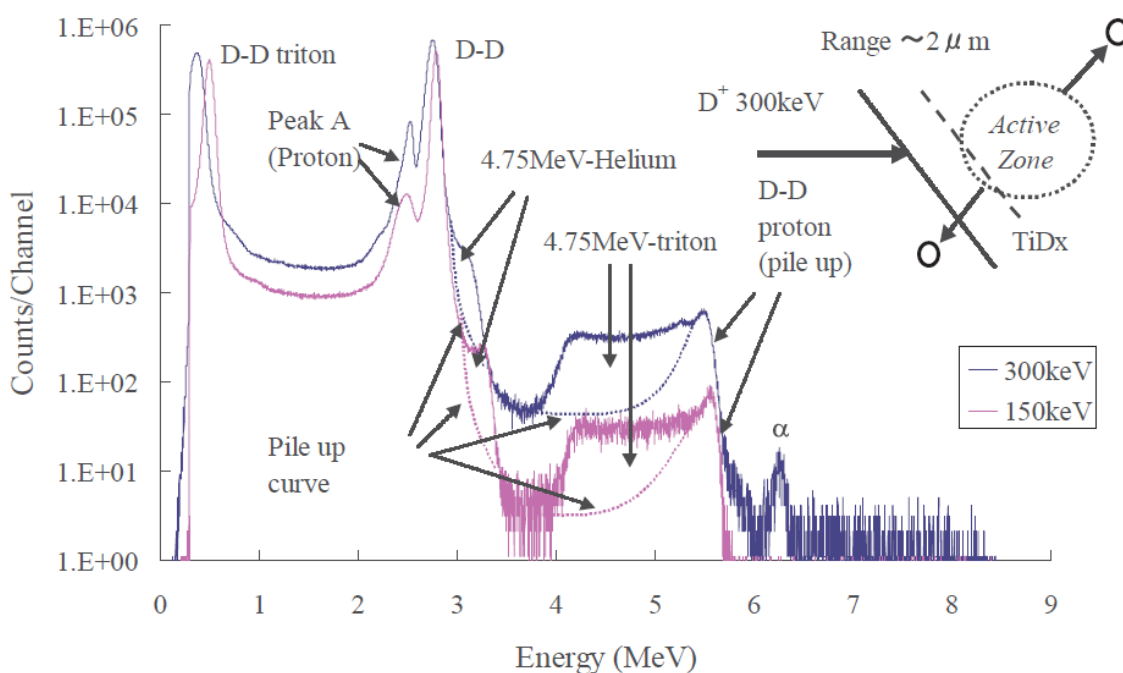
Fig.12 Charged-particles spectra emitted from TiDx sample implanted with 300keV-deuteron beam [14].

However, in experiments [14] [15] in which Ti metals are irradiated with d ion beam of 150 KeV or 300 keV, particles exceeding the above energy have been confirmed. Figure 12 shows the measured particles during low-energy deuteron irradiation for TiDx by Uneme et al [14]. Particles not generated by DD fusion such as 4.75MeV-Helium

and 4.75MeV triton have been confirmed. Figure 13 shows the charged-particles spectra by Kasagi et al. [15]. Proton particles of 17.2 MeV or less have been confirmed for [A], and alpha particles of 6.7 MeV or less have been confirmed for [B].
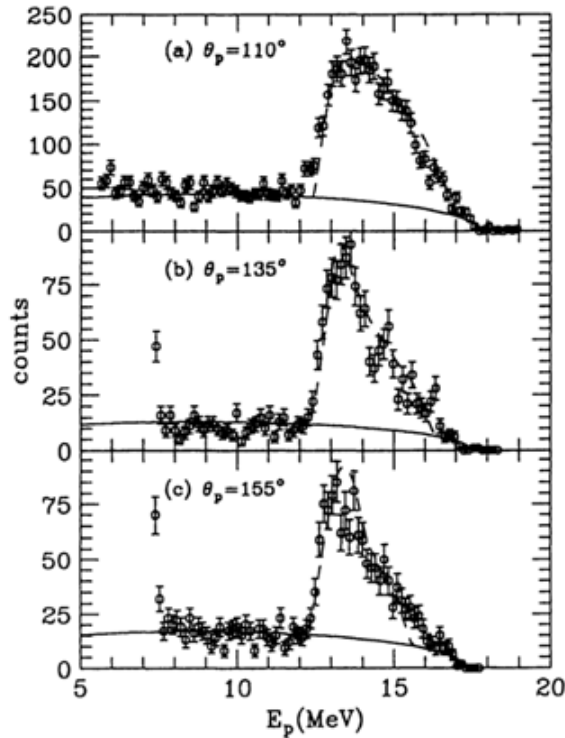
Fig. 13[A] High energy proton spectra measured at (a) 110°, (b) 135° and (c) 155°. Solid lines represent available phase spaces of protons emitted in the three-body reaction. Dashed lines are the calculated spectral shapes of protons emitted in the sequential reaction and are superimposed on the solid lines. The spectrum shown in (a) was measured with a 200-μm thick Al absorber, whereas the spectra in (b) and (c) were measured with a 15-μm one. [15]
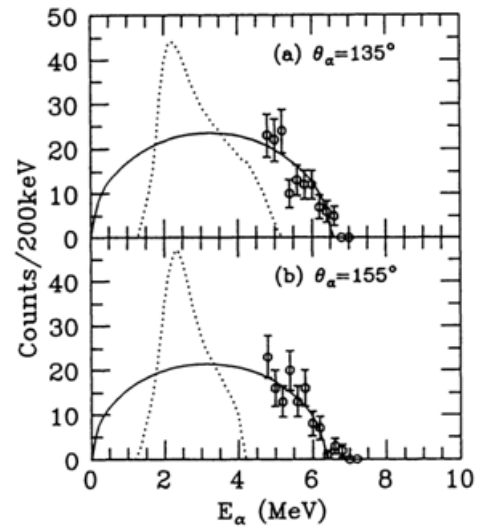
Fig. 13[B] Alpha-particle spectra measured at (a) 135° and (b) 155°. Solid lines represent available phase spaces of α particles emitted in the three-body reaction. Dotted lines are the calculated spectral shapes of α particles emitted in the sequential reaction [15].

Table 2 Particles produced when DDD 3-body fusion reaction occurs

DDD 3-body fusion
$$\underline{d + {}^2H} + {}^2H \rightarrow {}^5He \ (3.45\text{MeV}) + p \ (17.2\text{MeV})$$
$$\rightarrow {}^3H \ (4.75\text{MeV}) + {}^3He \ (4.75\text{MeV})$$
$$\rightarrow \alpha \ (7.9\text{MeV}) + d \ (15.8\text{MeV})$$

These particles are high-energy charged particles that cannot exist unless the DDD 3-body fusion shown in Table 2 occurs. However, it is not possible to have two D nuclei in one interstitial site. Because fusion is instantaneous, there is no significant probability that another nucleus will enter the nuclear reaction, nor will it reach the adjacent Pd crystal lattices during fusion. Humankind has not been able to figure out the reason for the generation of such particles.

The fact that such 3-body fusion occurs means that a large amount of ^{4}He in the excited state is generated by DD fusion in the metal, and the excited state is maintained until it reacts with the third D nucleus. These particles are evidence that the probability of ^{4}He generation in metal crystals increases dramatically and that the generated excited ^{4}He nuclei have a long lifetime. This evidence undermines the 2nd and 3rd reasons. There are slow nuclear reactions in the metal, and the nuclear fusion chain reaction in the metal crystal is not explosive because of these slow nuclear reactions.

7-2. Long-lived excited ^{4}He nuclei in metals

Why, then, does the probability of ^{4}He generation in metal crystals increase dramatically, and why is it possible for the generated excited ^{4}He nuclei to survive for a long time? In order to discuss this, it is necessary to estimate the mechanism from the shape of the nuclear force potential constructed in Session 6.
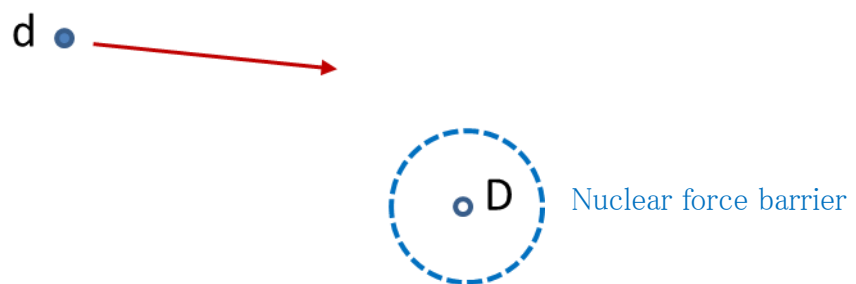
Fig. 14 Imaginary view of d ion entering the D nuclei.

Figure 14 is an imaginary view of d ion entering the D nuclei. Low-energy d ion enter from outside the nuclear force barrier, is captured by the nuclear force and fall into the pocket. At this time, the D nuclei also acquires kinetic energy and becomes d ion. By the time the d ions fall into each other's pockets, the magnetic flux generated by the gyration is absorbed by the metal, reducing both velocity and angular momentum. When two d ions enter each other's pockets, they do not have the necessary angular momentum, so the nuclear reaction that ejects particles does not occur, without being

able to scatter back to infinity. And they become a state where they bounce off the opponent's barrier and turn each other. We named this state a binary nucleus. Figure 15 is imaginary view of DD binary nucleus.
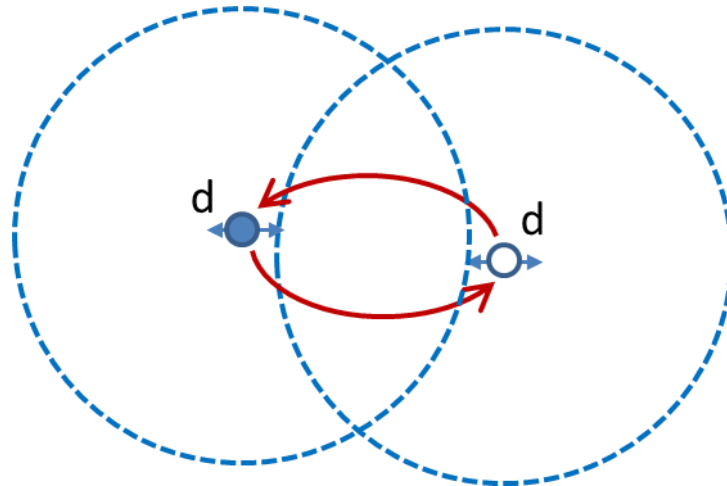
Fig. 15 Imaginary view of DD binary nucleus.

The binary nucleus immediately stops and settles into the lattice as a quasi-^{4}He atom clad in electrons. Every time the d-nucleus, which is a charged particle, bounces off the nuclear force barrier, it is accelerated, emits electromagnetic waves according to the Larmor formula, and loses energy over a long period of time. This binary nucleus state corresponds to ^{4}He excited nuclei that exist only in metals. Capture ^{2}H(d,γ)^{4}He reaction occurs when the angular momentum becomes almost zero. At this time, the γ- rays are so small that they cannot be detected from the outside.

The 3-body fusion product proves the existence of this intermetallic DD binary nucleus. Because the nuclear reaction time is short, there is no significant probability of 3-body fusion in which another nucleus enters the nuclear reaction. If the deuterium density is high, additional interstitial D nuclei can be incorporated into the nuclear force barrier of the d nuclei that make up the nascent binary nucleus. In this case, since sufficient nuclear energy and angular momentum still remain, 3-body fusion occurs.

7-3. Other reactions that make up the chain reaction

When the d ion undergoes a nuclear reaction with ^{4}He, ^{6}Li is produced in the capture reaction, but no reaction releasing p or n occurs. As a result, the elastic scattering cross section is widened as well as Figure 8. The ^{4}He nucleus cannot capture d ions by nuclear force and form a binary nucleus, and ^{6}Li is generated by the capture reaction only with d ions that have entered the center exactly. Therefore, the production of ^{6}Li on

this route is small, and another route is required. It is possible to generate ^{6}Li by nuclear fusion, in which d ion enter the DD binary nucleus that has advanced energy release. Figure 16 is an imaginary view of ^{6}Li formation.
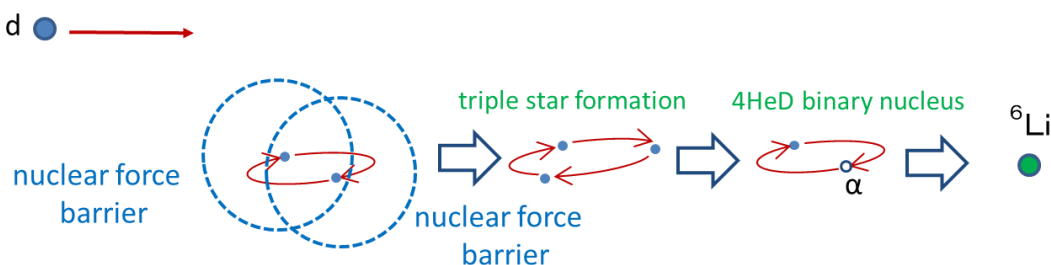
Fig. 16 Imaginary view of ^{6}Li formation.

When a d ion undergoes a nuclear reaction with 6Li nuclei, there are five reactions that release particles. The nuclear force of ^{6}Li spreads widely outside the nuclear force barrier, and it is a type that takes in low-energy d ions as shown in the reaction cross section in Figure 9. In the metal, both the velocity and the angular momentum of the d ion are absorbed and slowed down by the time the d ion falls into the nuclear force barrier of ^{6}Li. After this, if you proceed to the capture reaction, ^{8}Be will be generated. However, since ^{8}Be is an unstable nucleus, even if ^{8}Be is produced, it will quickly split into two α nuclei.
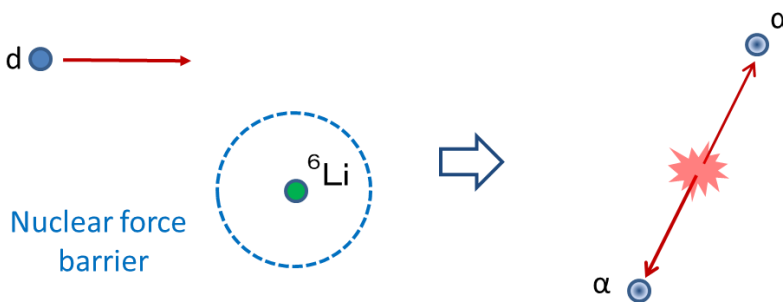
Fig. 17 Imaginary view of α ions generation

If the d-ion causes nuclear fusion with ^{6}Li nucleus and ^{8}Be is produced, it emits an energy of 22.3 MeV. If split into two alpha nuclei, two 11.2 MeV alpha ions are produced to release 22.4 MeV energy. If the d ions lose more than 5.1 MeV of fusion energy by the time they fall into the nuclear force barrier of 6Li, of the above five reactions, ^{6}Li(d,p t)^{4}He, ^{6}Li(d,n ^{3}He)^{4}He, ^{6}Li(d,p)^{7}Li, ^{6}Li(d,n)^{7}Be cannot occur, but ^{6}Li(d,α)^{4}He reaction can occur, producing two α ions with equal remaining energies. Figure 17 shows an imaginary picture of a d ion entering a ^{6}Li nucleus and two α ions

being generated in a metal.

Fig. 18 Imaginary view of d ion generation

Figure 18 is an imaginary view of d ion generation. As for the α ions cross section for the D nuclei, the elastic scattering cross section is broadened as in Figure 8. In particular, when the energy of α ions is as high as 1 MeV, the elastic scattering cross section is much larger, and D nuclei almost certainly receive kinetic energy and become d ions. In this way, many d ions are generated.

From the above, the reasons 1 to 3 are overturned, and the nuclear fusion chain reaction shown in Table 3 is established.

Table 3 Nuclear fusion chain reaction ($^4\underline{He}$ represents the DD binary nucleus.)

A) α + ^{2}H→ α + d
B) d + ^{2}H → $^4\underline{He}$
C) d + $^4\underline{He}$ → ^{6}Li
D) d + ^{6}Li → 2α (22.4MeV)

8. Experimental reactor
8-1. Experimental reactor and Pd sample

As already published, we built an experimental reactor with the structure shown in Figure 19 [4]. The Pd sample used was 99.95% φ76×1t, weight: 53.70g vacuum annealed at 1400°C for 1h. Figure 19 shows the texture of the Pd sample. The grain size is about 0.5 mm. We selected the method of doping with ^{6}Li ions as a method of forming a solid solution with a small amount of ^{6}Li. As an alternative to high-energy radiation from the natural world, an 8000 Bq 241 Am α-ray source that emits 8000 α-rays per second was placed above the Pd sample, and deuterium gas was introduced inside.
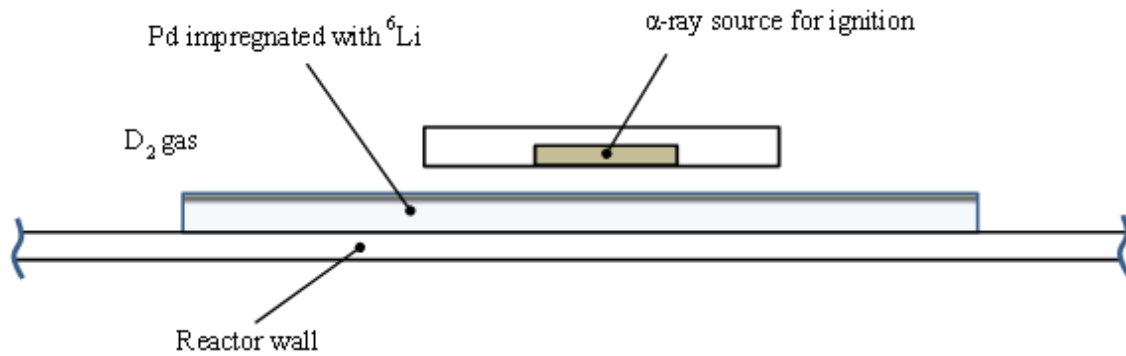
Fig. 19 Experimental Fusion Reactor [4].
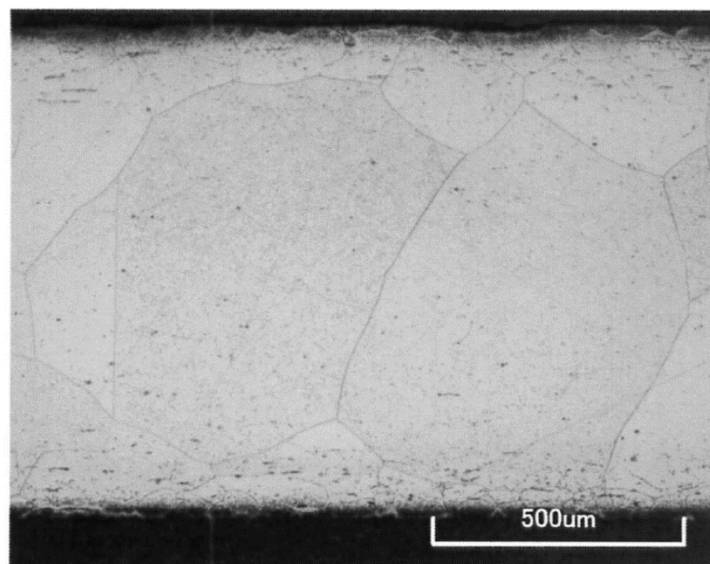
Fig. 20 Crystal grains of sample Pd

We initially estimated the ^{6}Li concentration at 5μm depth in Figure 2 to be 0.0045 mol%, so we doped the Pd sample with 9.81×10^{13} ions/cm^2 of 180 keV ^{6}Li ions. However, the estimated value changed to 0.059 mol% as a result of matching with the SIMS measurement conditions that Prof. Odawara told us later. After additional annealing at 1000°C for 1 hour, we additionally doped ^{6}Li ions at 5.0×10^{15}/cm^2 so that the peak concentration was 0.177 mol%, which is three times as high as 0.059 mol%. Figure 21 is a calculation diagram of the ^{6}Li distribution of the Pd test piece when 5.1×10^{15} ions/cm^2 of ^{6}Li ions of 180 keV including the first time are toasted.
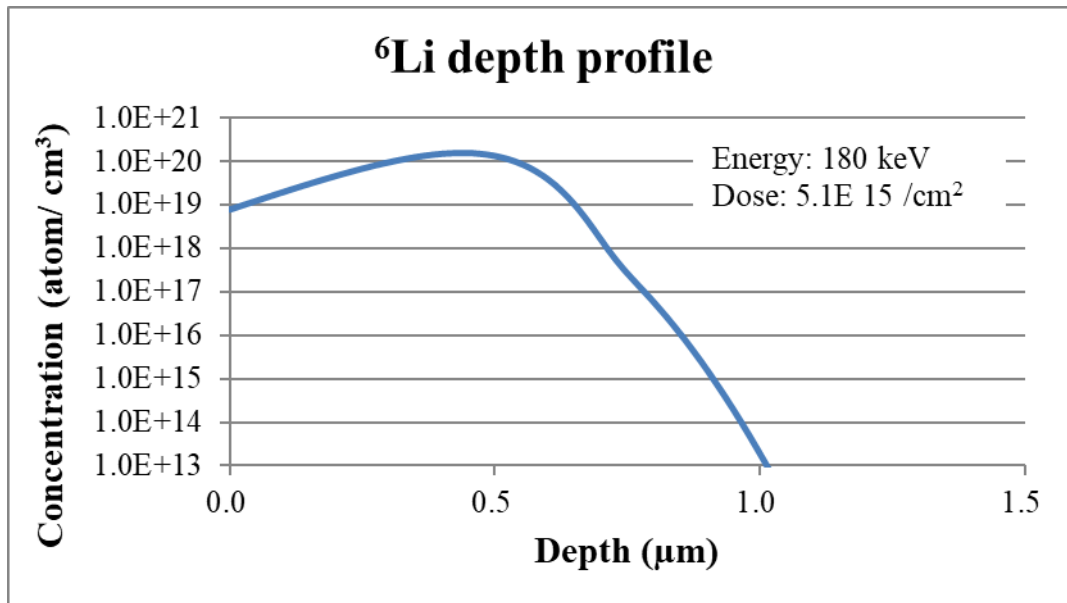
Fig. 21 ^{6}Li depth profile doped with Pd at 180 keV

However, as we learned later, the additional annealing at 1000°C was performed in a nitrogen (N_2) gas atmosphere containing 2% hydrogen (H_2) gas. After that, the inside of the furnace is cooled, the atmosphere gas is changed to Ar at 600°C, and it is taken out into the atmosphere containing 0.00005 mol% of H_2 gas at 100°C. Figure 21 shows the phase diagram of Pd-H at a hydrogen pressure of 0.02 bar calculated by CaTCalc [16]. The solid solution amount of hydrogen in Pd at 600°C and 0.02 bar is 0.127 mol%. From this point, the hydrogen partial pressure was almost 0 and the temperature was lowered, so the solid solution amount of hydrogen decreased. It is believed that the hydrogen was involved in the reaction during baking after the start of the experiment.

The region along the y-axis on the left side of Figure 22 is the α-phase of Pd, and the region surrounded by two circular arcs and the x-axis at around 0.375 in mol fraction H is the α'-phase. Above 39.98°C at 0.02 bar there is no α' phase. At 1 bar, the upper end of the α' phase in the phase diagram comes to 144°C with a mol fraction H of 0.34. However, no matter how much the pressure is increased, it is impossible for the mol fraction H to reach 0.5, that is, Pd:H = 1:1 due to the characteristics of metallic Pd. Transformation from the α phase to the α' phase should be avoided because the expansion causes strain inside the sample and causes the crystals to become finer.

Pd-xH P=0.02bar
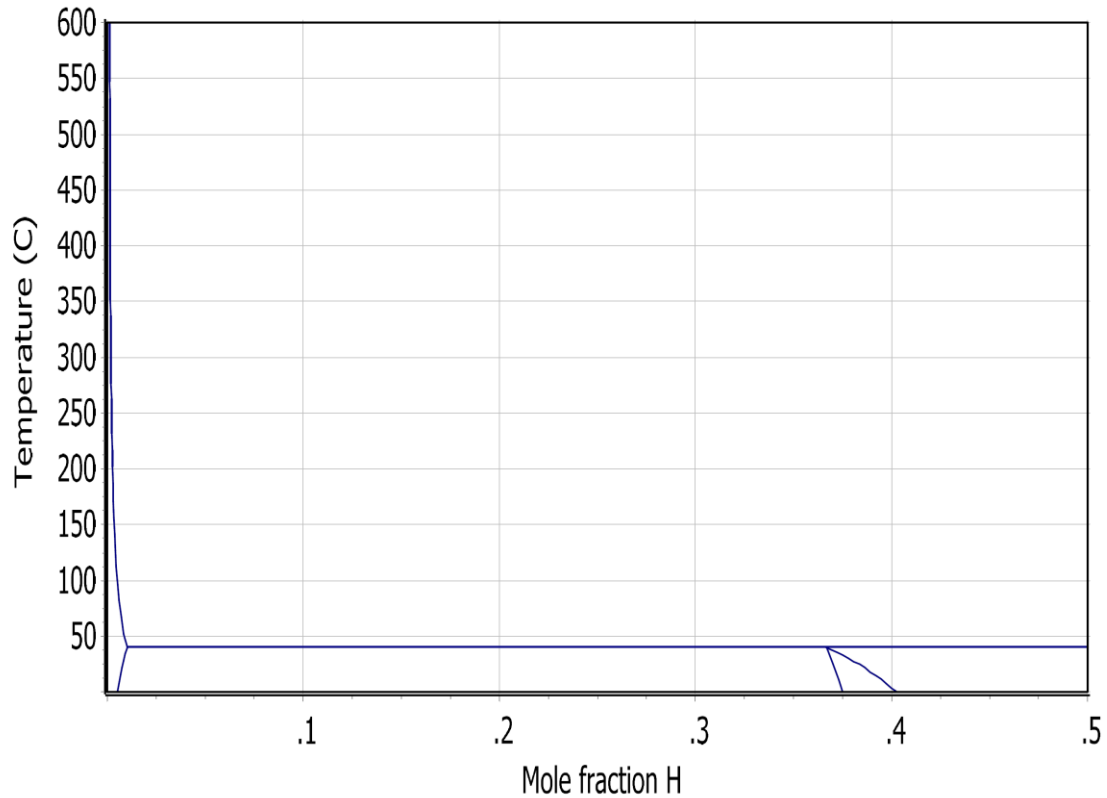
Fig. 22 Pd-H estimation state diagram [16]

18-2. Phenomenon that occurred in an experimental nuclear reactor

The phenomena that occurred in the start-up experiment of the reactor are listed below together with their considerations. In addition, since the display was about half when the γ-ray survey meter was calibrated later, it was found that the actual γ-ray exposure dose was about twice the value below.

A) During baking prior to startup of the experimental reactor, 25 hours after heating to 75°C, the γ- ray survey meter at a distance of 40 cm from the reactor center exceeded 0.4 μSv/h at 0.3 Pa, γ-ray emission of 0.100 μSv/h or more, which is three times normal, continued for 1.5 hours.

Considering that 1 g of hydrogen gas contains 6.02×10^{23} hydrogen atoms, the radiation dose of 8000 Bq from the α-ray source is extremely small. The energy of α-rays of 241Am is 5.4 MeV, and there is no known nuclear reaction in which α-rays with this level of energy react with H or ^{6}Li to produce γ-rays. The mechanism by which the γ- rays from the reactor were emitted is presumed as

follows.

It is highly probable that α-particles collide with interstitial H nuclei in the channeling paths of Pd metal, producing many low-energy p-ions. It has been confirmed that p-ions cause elastic scattering to ^{6}Li nuclei, but no nuclear reactions have been confirmed to my knowledge. However, it corresponds to the case where p enters instead of n in Figure 10, and it is considered that ^{6}Li(p,^{3}He)^{4}He reaction occurs. In the Pd crystal lattice, the p-ions form a binary nucleus with the ^{6}Li nucleus by the same nuclear force as the (n,t) reaction in Figure 10, and proceed to the capture reaction. However, since the ^{7}Be nucleus is an unstable nucleus, a ^{6}Li(p,e+)^{7}Li reaction occurs on the way and emits a positron. We think that the positron annihilation γ- rays were observed.

Assuming that the thickness of the furnace wall made of SUS316 is 1 cm, the positron pair annihilation γ-ray is 0.511 MeV, the mass absorption coefficient of γ-ray for iron is 0.718, and the number of γ-rays is calculated. It is calculated to be 6.05×107/h, which is 2.1 times the number of α-rays from the α-ray source (8000/sec). The distribution of ^{6}Li in this sample is a very small band area of less than 1 μm near the surface, and the reaction area is even narrower because the concentration is non-uniform. Considering that only a small portion of the α-rays contributed to the reaction, the probability of the reaction was extremely high given the number of γ-rays concerned, and it is thought that the activation conditions for the nuclear fusion chain reaction were satisfied.

B) After that, when 0.258cc of deuterium gas corresponding to 0.00446 mol% of Pd sample of 53.7g was supplied, there was γ- ray emission followed by neutron explosion for about 1 second. The pressure at this time was 20 Pa. The total exposure dose during the 5 minutes of the explosion was 4.37 μSv, which was 2000 times the background dose. After that, there was a mistake of excessive deuterium supply, and a small neutron burst instantaneously reaching 16 μSv/h occurred 2 to 3 minutes after the start of baking to reset the experiment.

The neutron explosion that follows the γ- ray emission after introducing deuterium gas is considered as follows, the generated ^{7}Li collides with the d ions generated by the nuclear fusion chain reaction, and some of them cause ^{7}Li(d,n)^{4}He^{4}He reactions. In other words, the neutron explosion is evidence that the d ions of the nuclear fusion chain reaction were generated, and proves the establishment of the nuclear fusion chain reaction.

However, it was not possible to confirm heat generation in the reactor. The reason why no exotherm was observed was that the reaction was slight. An

appropriate amount of D enters the area where the amount of ^{6}Li at a certain depth from the surface is appropriate, and a chain reaction occurs only temporarily in the area where α rays reach, and the reaction area did not spread large enough to confirm heat generation. Although it was an unintentional mixture of H, if there was no mixture of H, the start-up of the reactor could not have been confirmed. In addition, it was confirmed that γ-rays and neutrons are generated when H and ^{7}Li are mixed in the reactor.

C)   Furthermore, after supplying 3.415 cc of deuterium corresponding to 0.059 mol% to the Pd sample planned in the initial experiment, when baking was performed again, at 0.503 Pa, the γ-ray emission exceeded 0.600 μSv/h temporarily and the γ-ray survey meter alarm sounded. This was followed by a γ-ray emission lasting over 30 minutes, during which a small neutron explosion occurred. After that, several smaller neutron explosions were confirmed during baking.

4. Summary of conclusions

1) "Heat after Death" is an important phenomenon.

Heat generation after completion of electrolysis generated in heavy water electrolysis experiment, the so-called "Heat after Death" is precisely the nuclear fusion chain reaction that human beings are aiming for as a future energy source.

2) The exemplified formula of the nuclear force potential in the Yukawa meson theory needs to be revised for the following reasons. The nuclear force is generated not from the Coulomb core, but from the nuclear force barrier outside it.

・The exemplified formula cannot explain the high shielding effect in metal.

・The exemplified formula cannot explain DDD-3 body fusion particles.

・The exemplified formula cannot explain the reaction cross section of DD fusion and DT fusion cannot be explained.

・The exemplified formula cannot explain the reaction cross section of low-mass nucleons and neutrons.

・The exemplified formula cannot explain the generation of ^{6}Li in the electrode.

3) In metals, non-radiative and non-explosive nuclear fusion chain reactions are established by nuclear fusion via binary nuclei.

4) Further ingenuity is required to generate heat in the experimental nuclear reactor. It is important to expand the region of the optimum ^{6}Li concentration of the sample, continue the reaction, and expand the reaction region.

References

[1] Kazuo Ooyama "Nuclear Fusion Mechanism in Metal Crystals", Proceedings JCF18, p55-92(2017)

[2] S. Pons, M. Fleischmann "Heat After Death", Proceedings ICCF4, 8-1

[3] M. Okamoto, O. Odawara et al "A Role of Lithium for the Neutron Emission in Heavy Water Electrolysis", Ikegami, H., ed. Third International Conference on Cold Fusion (1992), Frontiers of Cold Fusion. 1993, Universal Academy Press, Inc., Tokyo, Fig.1 bottom

[4] Kazuo Ooyama "Start-up of Metal Crystal confinement Fusion Reactor", Proceedings JCF20, p28-46(2019)

[5] S. Pons, M. Fleischmann "Electrochemically induced nuclear fusion of deuterium", J. Electroanal Chem., 1989. 261: p. 301 and errata in Vol. 263.

[6] H. Yukawa "On the Interaction of Elementary Particles", Proc. Math. Phys. Soc. Japan, 17, 48 (1935)

[7] Tadahiko Mizuno "常温核融合　研究者たちの苦悩と成果 (Cold Fusion Researchers' Anguish and Achievements)", Kogakusha, P49

[8] Jirota Kasagi, Hideyuki Yuki at al "Strongly Enhanced DD Fusion Reaction in Metals Observed for keV D+ Bombardment", Journal of the Physical Society of Japan, 71, p2881 (2002)

[9] F. Raiola et al "Enhanced electron screening in d(d,p)t for deuterated metals", Eur. Phys. J. A 19, 283(2004)

[10] H. Yukawa, "On the Interaction of Elementary Particles", Proc. Math. Phys. Soc. Japan, 17, 48 (1935)

[11] N. Jarmie "Low-Energy Nuclear Fusion Data and Their Relation to Magnetic and Laser Fusion", LA-8087 UC-34c Issued: April 1980.

[12] N. Ishii, S. Aoki and T. Hatsuda "Nuclear Force from Lattice QCD", Physical Review Letters vol. 99, 022001(2007)

Fig.6: https://www.s.u-tokyo.ac.jp/ja/press/2007/images/10/01-b.jpg

[13] Shibata, K. et al. Japanese Evaluated Nuclear Data Library Version3 Revision-3: JENDL-3.3. J. Nucl. Sci. Technol. 39, 1125 (2002). Japan Atomic Energy Agency HP

[1]H: https://wwwndc.jaea.go.jp/jendl/j5/fig1/n_001-H-001_f1.jpg

[2]H: https://wwwndc.jaea.go.jp/jendl/j5/fig1/n_001-H-002_f1.jpg

[3]H: https://wwwndc.jaea.go.jp/jendl/j5/fig1/n_001-H-003_f1.jpg

[3]He: https://wwwndc.jaea.go.jp/jendl/j5/fig1/n_002-He-003_f1.jpg

[6]Li: https://wwwndc.jaea.go.jp/jendl/j5/fig1/n_003-Li-006_f1.jpg

[14] Y. Isobe, S. Uneme et al. "Search for Multibody Nuclear Reactions in Metal Deuteride Induced with Ion Beam and Electrolysis Methods", JJAP 41 (2002) 1546-1556, Part. 1, No. 3A March 2002

[15] Jirota Kasagi et al. "Energetic protons and α particles emitted in150- keV deuteron bombardment on deuterated Ti", J. Phys. Soc. Japan, 1995. 64(3): p. 777-783.

[16] K. Shobu "New thermodynamic equilibrium calculation software", CALPHAD, 33 (2009), pp 279-287.

Experiments without nuclear reactions

Kazuo Ooyama

Ooyama Power Inc.

k1@ ooyama-power.com

Abstract   In 1994, Sergio Focardi reported experimental results showing heat generation in the Ni-H system [1]. Years later, Focardi accepted Andrea Rossi's offer to collaborate. Rossi created a Ni-H reactor, called it E-cat, made Giuseppe Levi et al write a paper and published as internet [2]. At the same time, Rossi filed patent applications for chemical reactors in various countries and obtained patents [3][4], then pitched the patent to investors around the world as the Cold Fusion patent. In order to determine the authenticity of E-cat, we filed an invalidation trial against the Japanese patent [5]. In the process of the offense and defense, we got Rossi's assurance that "the LENR (Cold Fusion) is unfeasible"[6].

On May 22, 2008, Arata et al. gave a lecture on the generation of excess heat and ^{4}He from ZrO_2Pd nano powder and conducted a public experiment. At this time, the 2008 paper was distributed as a document [7]. The following year, he published experimental results of ZrO_2Pd35 and $ZrO_2Ni30Pd5$ nanopowder in a 2009 paper [8]. The calorific value of ZrO_2Pd35 is greatly reduced from the 2008 paper and is within the range of sintering and crystallization energies [8]. It is written that the calorific value of ZrO2Ni30Pd5 is higher [8], but since the powder was not exposed to deuterium gas before the experiment, it seems that the oxidation heat of deuterium is the main factor. The figure presented as evidence for ^{4}He production in the 2009 paper is evidence that ^{4}He is not produced [8].

Keyword: Cold Fusion, Sergio Focardi, Ni-H, Andrea Rossi., ECAT, Yoshiaki Arata, Nanopowder, Zr-Pd, Zr-Ni-Pd, Deuterium

1. Introduction

CF (Cold Fusion) research began in 1989, when Ponds et al. reported abnormal heat generation in the electrolysis of heavy water [9]. However, because the theory was not settled, researchers tend to think that the temperature rise that they do not understand is CF. Furthermore, as experimental reports of errors and fabrications are mixed in, CF research has lost its direction and is stuck in a stalemate. This paper aims to avoid misleading future researchers by presenting past experiments and information that we believe do not have nuclear reactions.

2. Ni-H system
2-1. Ni-H system by Sergio Focardi et al.
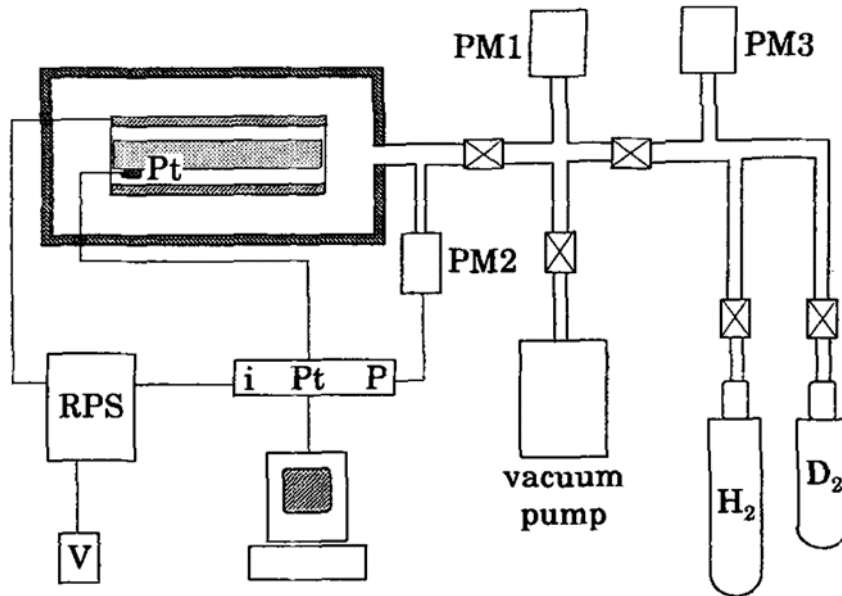
Fig.1 Schematic layout of the experiment by S. Focardi et al [1]

a)

1)	cell vessel
2)	external SS tube
3)	CF35 flanges
4)	heater
5)	ceramic cylinder
6)	sample holder
Th_{Pt}	Pt100 temperature sensor
Tc_e	type K thermocouple
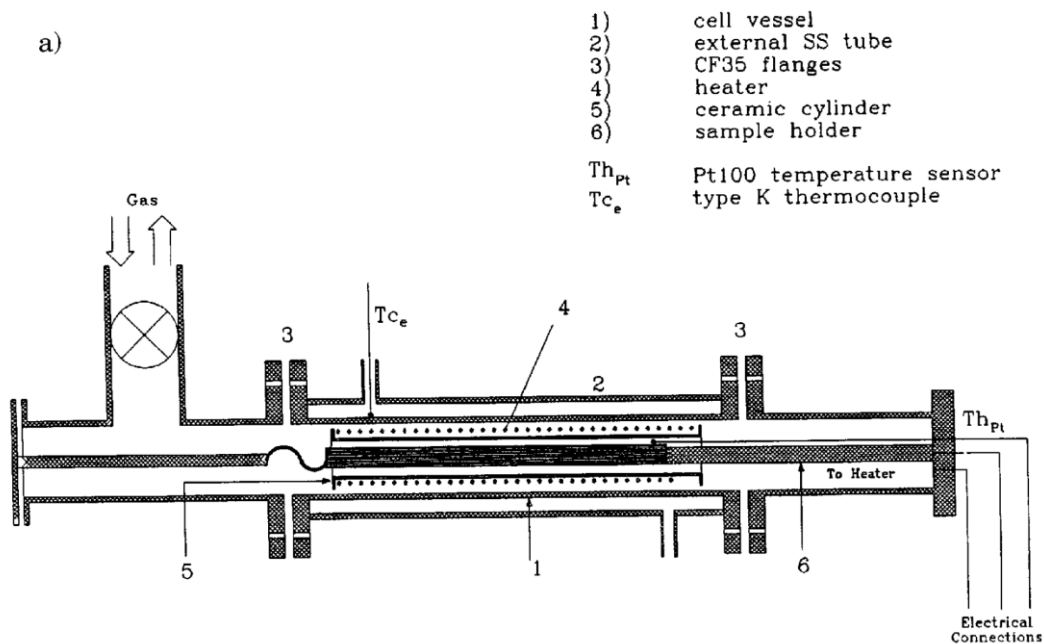
Fig. 2 Schematic diagram of the reaction vessel (Cell) [9]

We understand that the 1994 paper by Sergio Focardi et al. was the first to announce that nuclear fusion also occurs in the Ni-H system. Figure 1 is a schematic layout of the experiment by Focardi et al. Since the layout around the sample in this figure is unclear, a schematic diagram of the reaction vessel (Cell) quoted from the 1998 paper is shown in Figure 2. The sample in the center is the Ni sample, which seems to follow the temperature of the heater because it is wrapped in a ceramic cylinder wrapped with a

heater wire. However, the emissivity of stainless steel is as follows, with the blackbody as 1

Metallic luster 0.07

Rolled stainless steel 0.45

When the inner surface of the cell, which is reduced by hydrogen, becomes metallic luster, the emissivity drops to a maximum of 1/6.5, and the surface of the heater wire is also reduced and the emissivity is lowered. Heat conduction deteriorates, and the heater temperature rises relative to power consumption. Since the Ni sample is surrounded by the heater, even if the surface of the Ni sample is reduced, the emissivity is lowered, and the heat conduction is deteriorated, the temperature of the Ni sample follows the temperature of the heater.

In addition, the heat conduction of the gas between the heater and the vessel also has a large effect. The thermal conductivity of gases at 100°C is as follows [12]. The unit is W/m·K.

Hydrogen 0.2118

Water vapor 0.0235

Air 0.0317

The difference in thermal conductivity between hydrogen and water vapor is nearly 10 times, and that of air is nearly 15 times. By moisture-absorbed ceramic emits water vapor, and oxides on the metal surface are reduced by hydrogen, when water vapor mixes with hydrogen gas, the thermal conductivity changes. In addition, there is a large change in air leaking into the hydrogen gas, which has a pressure lower than the atmospheric pressure.
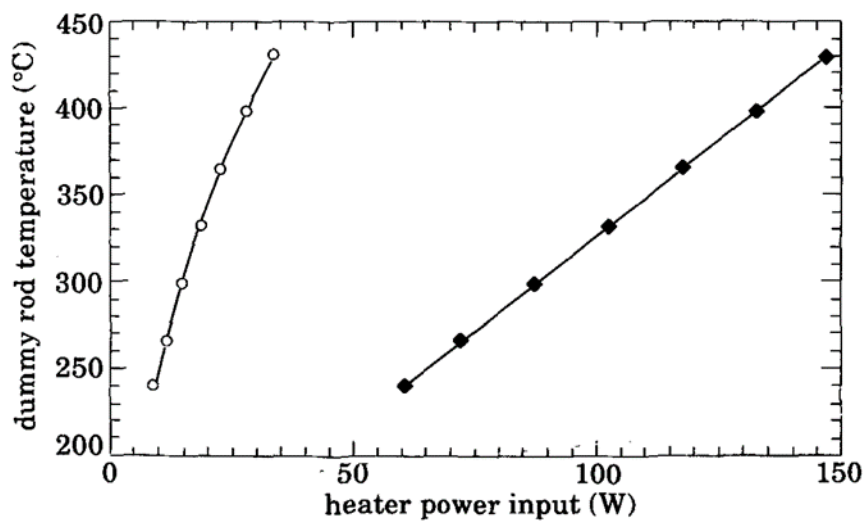
Fig.3 Power-temperature relations for the dummy rod at different values of the pressure inside the chamber.

◆ Hydrogen (p = 570 mbar), ○ Vacuum. [1]

Fig. 3 shows the relationship between the power and temperature of the dummy rod in the chamber [1]. The electric power required for the dummy rod to reach 240°C is 60W in hydrogen gas, but only 10W in vacuum. This indicates that Focardi's experimental system seems to generate heat when the heat conduction between the Ni sample and the vessel deteriorates due to the inclusion of impurity gases. The same is true when the heater wire and the inner surface of the vessel are reduced with hydrogen and mirror-finished.

Figure 4 is temperature vs. heater-power curves family for a loaded nickel sample at different values of power [1]. Unloaded Ni rod seem to mean the curve for the sample on the first cycle of thermal cycling in hydrogen. It seems to indicate that the heat conduction between the sample and the vessel gradually deteriorates with repeated thermal cycles. The 20W line is probably the temperature drop in the first cycle, and the 50W line is the temperature drop when the heat conduction between the sample and the vessel deteriorates after repeating the thermal cycle many times.
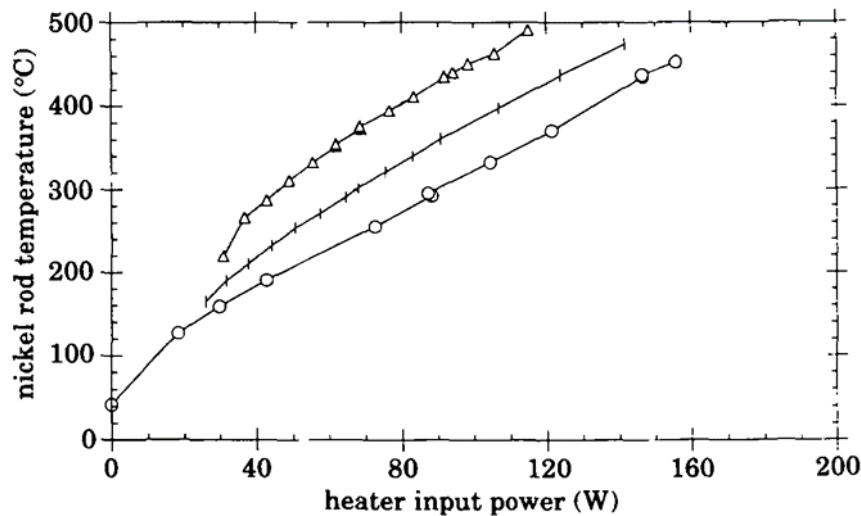
Fig. 4 Temperature vs. heater-power curves family for a loaded nickel sample at different values of power «imbalance». ○ 0 W, + 20 W, △ 50 W. The dummy rod and the unloaded Ni rod are represented by the 0 W lower «imbalance» curve [1].

Figure 5 shows the heat generation of nickel when a counterclockwise heat cycle is applied, and the difference in the temperature of the Ni rod with respect to the heater coil temperature during the temperature drop is written as evidence of heat generation [1]. It is not explained that the Ni rod temperature is lower than the heater coil

temperature when the temperature rises. The change in Ni rod temperature simply shows a delay with respect to the heater coil temperature during the thermal cycle, and it seems that the Ni rod surface is reduced at high temperatures, the emissivity decreases, and the delay in temperature change increases.
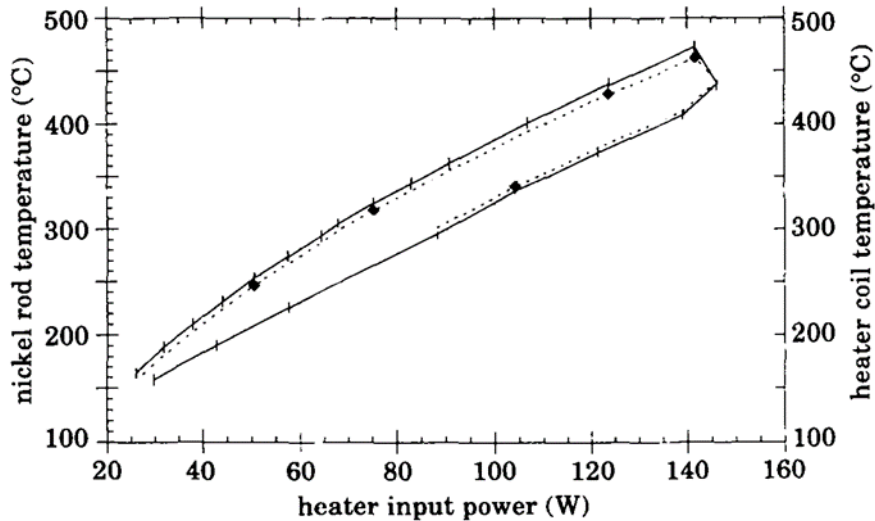
Fig. 5 Heater coil and nickel rod cycles in the (W, T) diagram, at 20 W power ≪imbalance≫. ✛ rod temperature, ◆ coil temperature[1].

Although it is such a paper, since Focardi was a famous physicist in Italy, it seems that it passed the peer review.

2-2. ECAT

Focardi's Ni-H system was noticed by businessman A. Rossi, and he offered Focardi a joint research project. Focardi helped develop Rossi's Energy Catalyzer (E-Cat) from 2007 until his death in 2013[13].

E-Cat was not reported to the general public in Japan, but Dr. Eiichi Tanaka, an adviser to Hamamatsu Photonics, introduced it in a booklet published by the Japan Radioisotope Association [14]. This introductory article covers the following topics: Rossi developed a Ni-H reactor of about 10kw under the name of Energy Catalyzer (E-Cat). Since January 2011, he has invited a limited number of people to conduct experimental demonstrations. (On the other hand, the number of visitors to the experimental demonstration was limited, the details of the reactor of the device were not disclosed, and there were many technically unclear points in the measurement of the calorific value, and many people questioned the results.) On October 28, 2011, 107 E-Cat units were connected to build a device with a nominal output of 1 MW, and a

limited number of people, including anonymous customers, were invited to conduct an experimental demonstration. It was reportedly sold to an unnamed customer (U.S. Navy?) for US$2 million. And, according to Rossi, "Heat is generated when nickel nuclei and hydrogen nuclei react to form copper. The bulk of the reaction is 62Ni and 64Ni, which react with the protons of the hydrogen nuclei and are converted to 63Cu and 65Cu, respectively." [14]

On October 6, 2014, a non-peer-reviewed reproduction experiment report written by six Bologna University scientists, including Giuseppe Levy, will be published [2]. Conducted at an independent laboratory in Lugano, Switzerland, this non-peer-reviewed paper is known abroad as the Lugano Report. The Lugano Report is a 53-page report, and the contents of this paper are introduced below. However, the paper states that "Rossi operated the E-Cat to insert fuel, start the reactor, shut down the reactor, and extract powder. " [2].

Fig. 6 E-cat during startup [2]

Figure 6 shows E-cat in action. E-cat is designed to be heated by coil heaters from the surroundings, and heat generation is estimated from the surface temperature.

Table 1 is a record of the 32-day experiment. The temperature was maintained at around 1,250°C for the first 10 days and around 1,400°C for the remaining 22 days, and the COP (Coefficient of Performance) was always maintained at 3 or higher. We doubt that raising the temperature will increase the COP. E-Cat constitutes an unstable system

if the reaction becomes active and the COP increases by increasing the temperature. At the hotter sites, the reaction will be more active, and the temperature should rise until something breaks. It would be strange if the temperature distribution were not uneven, but it is not so uneven. If this is not the case, there is a high possibility that it is simply being heated by an electric heater and is not self-heating.

Looking at Figure 6 from this point of view, one heater wire is sufficient for heating with less than 1 kW of power, but a three-phase wire is used, which complicates the device. The fact that the COP is about 3 raises the suspicion that the power consumption of only one of the 3-phase wires is being measured while heating with the 3-phase wires.

Table 1 For each of the 16 thermography files recorded (One file corresponds to two days of data logged.) we have, subsequently: average power consumption of the E-Cat, power emitted by the E-Cat by radiation, power emitted by convection, sum total of the last two values, sum total of watts emitted by both sets of rods by radiation and convection, power dissipated by Joule heating, COP (Coefficient of Performances), and net production.

File No.	E-Cat body average T (°C)	File No.	Consumption (W)	Radiation (W)	Convection (W)	TOT. (W)	Rods (W)	Joule heating (W)	COP	Net Production (W)
1	1260.00	1	815.86	1740.98	387.34	2128.32	307.98	37.77	3.13	1658.21
2	1257.77	2	799.84	1733.30	386.46	2119.76	307.98	36.98	3.18	1664.88
3	1256.09	3	791.48	1724.95	385.23	2110.18	307.98	36.49	3.20	1663.17
4	1257.21	4	790.69	1729.30	385.49	2114.79	307.98	36.41	3.21	1668.49
5	1243.40	5	785.79	1676.89	381.43	2058.32	307.98	36.13	3.16	1616.64
6	1398.99	6	923.71	2381.64	427.64	2809.28	352.82	42.43	3.59	2280.82
7	1405.58	7	921.91	2416.68	429.64	2846.32	352.82	42.18	3.64	2319.41
8	1404.04	8	918.24	2407.26	429.16	2836.42	352.82	41.89	3.64	2312.89
9	1401.46	9	917.90	2392.29	427.82	2820.11	352.82	41.75	3.62	2296.78
10	1392.26	10	913.40	2348.43	425.64	2774.07	352.82	41.93	3.59	2255.42
11	1396.49	11	904.77	2373.08	427.23	2800.31	352.82	41.52	3.65	2289.88
12	1400.86	12	906.98	2397.95	428.56	2826.51	352.82	41.60	3.67	2313.95
13	1401.59	13	910.47	2401.80	429.87	2831.67	352.82	41.62	3.67	2315.64
14	1400.56	14	908.13	2394.93	428.70	2823.63	352.82	41.55	3.67	2309.87
15	1410.27	15	905.01	2451.10	432.02	2883.12	352.82	41.46	3.75	2372.39
16	1412.31	16	906.31	2454.71	431.47	2886.18	352.82	41.25	3.74	2373.94

Table 2 shows the measured values of Li and Ni ions in fuel and ash by ToF-SIMS and their abundance in nature. Looking at the analysis results of the fuel before the start of the experiment and the ash after the experiment, the isotope ratio of ^{7}Li and ^{6}Li is

reversed, and almost all Ni isotopes transmuted into ^{62}Ni. Also, the EDS (Energy Dispersive X-ray Spectroscopy) spectrum of the fuel contained iron powder, but the ash contained no Fe.

Table 2 ToF-SIMS measurement of Li and Ni ions in fuel and ash and natural abundance [2]

Ion	Fuel		Ash		Natural abundance [%]
	Counts in peak	Measured abundance [%]	Counts in peak	Measured abundance [%]	
^{6}Li$^+$	15804	8.6	569302	92.1	7.5
^{7}Li$^+$	168919	91.4	48687	7.9	92.5
^{58}Ni$^+$	93392	67	1128	0.8	68.1
^{60}Ni$^+$	36690	26.3	635	0.5	26.2
^{61}Ni$^+$	2606	1.9	~0	0	1.8
^{62}Ni$^+$	5379	3.9	133272	98.7	3.6
^{64}Ni$^+$	1331	1	~0	0	0.9

Even if it is conceivable that ^{7}Li reacts with ^{1}H and is consumed, it is unlikely that ^{6}Li will increase. On the 32nd day, the fever did not disappear, but Rossi turned off the power to the heater, which ended the fever experiment. It seems impossible in an unstable system to target and stop the moment when Ni isotopes other than ^{62}Ni burn up, even if he had done preliminary tests. Previously, he claimed to transmute to Cu, but this time they have no data on Cu isotopes. Rossi probably wanted to make people think that all the Fe was also transmuted into ^{62}Ni, but there are too many types of nuclide transmutation, and conversely it becomes unreliable.

A number of follow-up peer-reviewed reports exist for this non-peer-reviewed Lugano Report. Many of the reports of fever have come from A.G. Parkhomov et al of Russia. A well-known paper by Parkhomov et al., in 2009, reported fever for seven consecutive months [15]. An unusual example is a report by the China Institute of Atomic Energy [16]. However, nuclide transmutations are not reproduced. There are also negative papers, and a similar reproducible experiment was conducted, and the negative result was reported in "Investigations of the Lugano HotCat Reactor"[17]. At the JCF, there was a lecture on nuclear transmutation in the Lugano Report [18] and a lecture on the follow-up study by Parkhomov in 2005 [19].

Rossi filed a patent application related to the E-Cat, patented them in 46 countries [3] [4] and sold them as cold fusion patents. Japanese Patent No. 6145808 has been filed as a chemical reactor that is 1/00 of F24J in the International Patent Classification, but the scope of claim includes LENR and Li exists in the matter specifying the invention [4].

Therefore, we, who believe that cold fusion is related to Li, cannot deny the possibility of cold fusion 100%, and in order to obtain information through direct

offense and defense, we filed a patent invalidation trial [5]. On January 19, 2022, in the case of a chemical reactor, the invalidation decision was finalized on the grounds of violation of industrial applicability because the chemical reactions used were all endothermic reactions, and in the case of LENR, the invalidation decision was finalized on the grounds of violation of the enablement requirement, violation of the support requirement, and violation of the clarity requirement [6]. At the defense, Rossi argued that the invention was a chemical reactor, and argued that "the LENR was unfeasible"[6].

3. Nanopowder-based experiments

3-1.   Energy contained in nanopowder

Since metal powder has surface energy, sintering reduces the surface area and generates heat. Below are the surface energies of various metals [20].

Cu 1670 erg/cm^2

Ag 1140 erg/cm^2

Au 1400 erg/cm^2

Assuming that the surface energy of Pd is 1140 erg/cm^2, which is the same as that of Ag, and the nanopowder is a sphere of 5 nm, the sintering energy is 114 J/g. If it is not a true sphere and has four times the surface area, it may generate heat of about 456 J/g. ZrO_2 as the base material should also be amorphous, so if the heat generation is about 400 to 500 J/g per sample weight including the base material (not per Pd or hydrogen weight), there is a possibility that the heat generation due to sintering or crystallization energy.

Incidentally, Japanese regular gasoline has a calorific value of 33.31 MJ/ℓ and a specific gravity of 0.737, so it has a calorific value of 45.2kJ/g. This level of heat generation is desirable in order to assert the possibility of a nuclear reaction rather than a chemical reaction based only on the amount of heat generated.

3.2 Generated energy from nanopowder experiments by Arata et al.

In 1999, Arata et al. announced that they confirmed the generation of excess heat and He from Pd nanopowder [21], and conducted a public experiment on May 22, 2008. Figure 7 is a diagram of the experimental setup that was published in the paper distributed as materials for the public experiment [7].
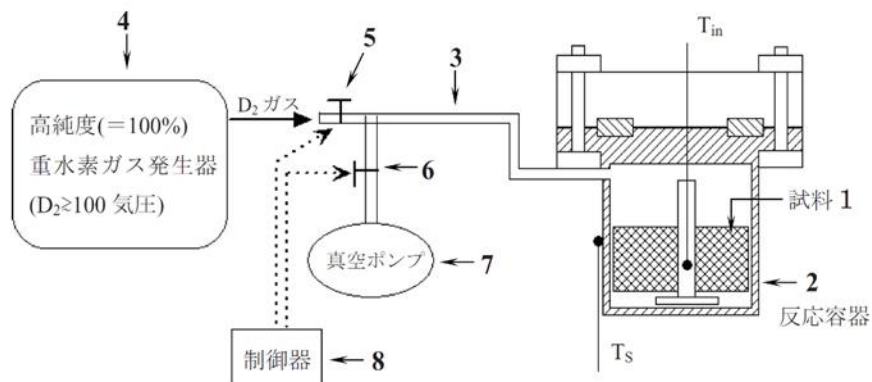
Fig. 7 Arata et al.'s experimental device [7]

1: Sample, 2: Reaction vessel, 3: Stainless steel pipe, 4: High purity (=100%) deuterium gas generator (D2≥100 atm), 5, 6: Valve, 7: Vacuum pump, 8: Controller
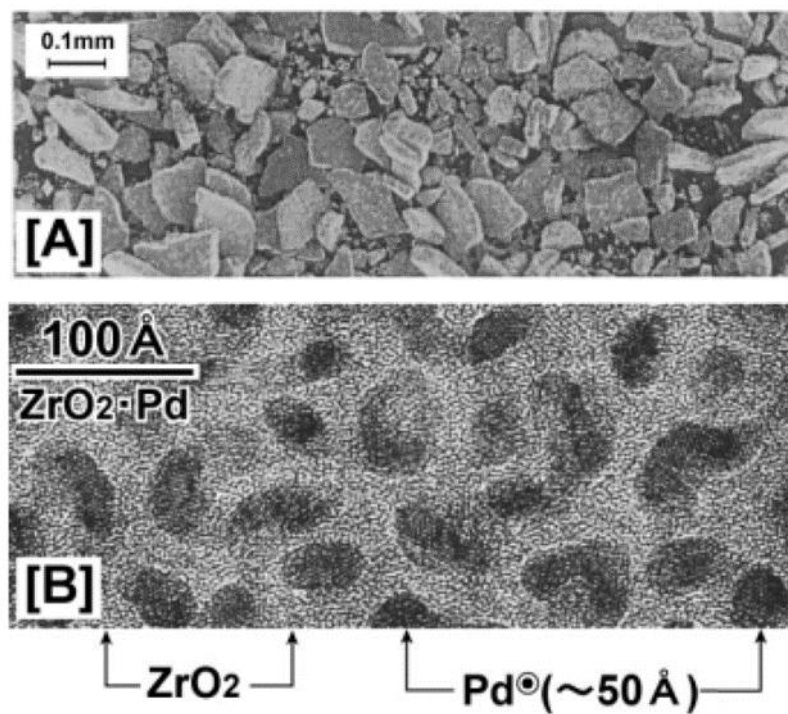
Fig. 8 Sample form [22]

The paper contains many descriptions whose details are mysterious. The paper will be referred to as the 2008 paper below. The sample is only described as ZrO_2-Pd alloy (6.5g) [7]. By checking the references, we found a 2003 paper with an electron micrograph of the sample in Figure 8 [22]. From the paper, it was found that the sample was created by Shinichi Yamaura et al. First, an amorphous alloy of Zr65Pd35 (Zr65%

Pr35%）was prepared and then heated in air at 553°K for 24 hours to make a nanostructured composite material of ZrO_2 (zirconia) and Pd. [23].

Looking at Figure 8 [A], the sample is a powder of various sizes that looks like finely ground thin flakes. Looking at the enlarged view of Figure 8 [B], it constitutes a form in which Pd nanopowder of about 50 Å = 5 nm is dispersed in zirconia ZrO_2.

Figure 9 shows the heat generation situation in the 2008 paper [7]. In the text, it is described that a 6.5 g sample generated about 4.4 kJ in the first "Jet-Fusion" zone and about 250 kJ in the subsequent "Skirt-Fusion" [7]. This means that 39.1 kJ was generated per 1 g of sample. At the 2008 paper, the calorific value approaching that of gasoline was presented.
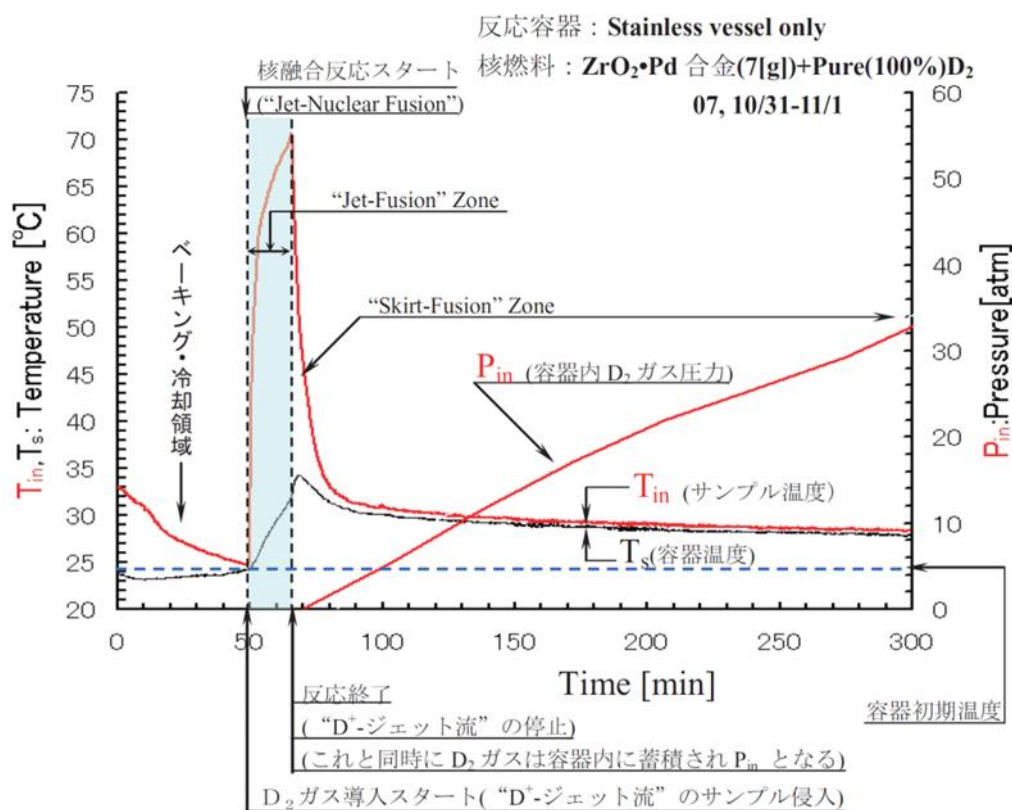
Fig. 9 Heat generation of ZrO_2Pd35 nanopowder in 2008 paper [7]

However, in a 2009 paper [8], $ZrO_2Ni30Pd5$ nanopowder is superior, and various coming outs of ZrO_2Pd35 nanopowder are written. Figure 10 shows the heat generation situation in the 2009 paper [8]. It says, "For the case of ZrPd powder, the generated power is only 1 [watt] lasting only 10 minutes, and the total lasting time is about 32 minutes [8]." Assuming that the calorific value decreases steadily over time for 22 minutes after cutting 1W, the total calorific value is about 1.26kJ/Pd1g. Converting to 1

g of the sample, it was about 399 J/g, which was drastically reduced to a level that could be explained by heat generation due to sintering and crystallization energy.
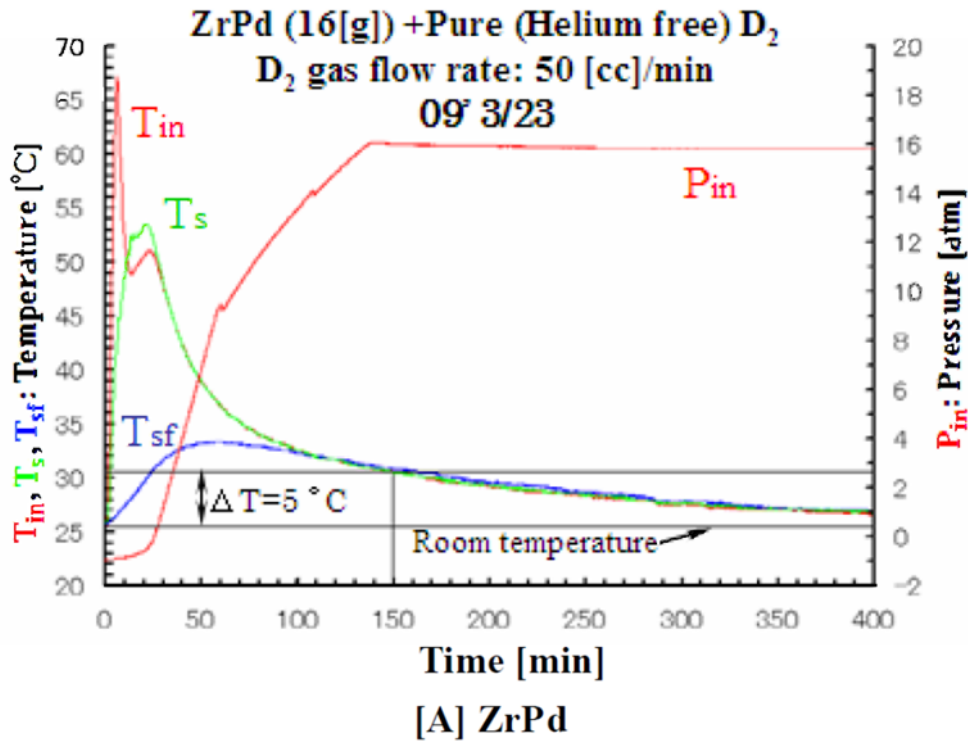
Fig. 10 Heat generation of ZrO_2Pd35 nanopowder in the 2009 paper [8]

Figure 11 is a diagram of ZrO_2Pd35 nanopowder X-ray diffraction intensity published in the 2009 paper. [A] is the original ZrO_2Pd35 nanopowder after heat treatment, with most of the palladium element present as palladium oxide (PdO). [B] is the powder after deoxidization treatment, and the strength of PdO is greatly reduced. [C] is the powder after the experiment (after D_2 gas loading), and it is written that "The intensity of PdO is almost the same as [B]." However, the 1-2% change cannot be read from this figure, and it is possible that the material will oxidize when it is taken out into the atmosphere. At least, it can be said that the 2008 paper included the heat of formation of D_2O due to the reduction of PdO.
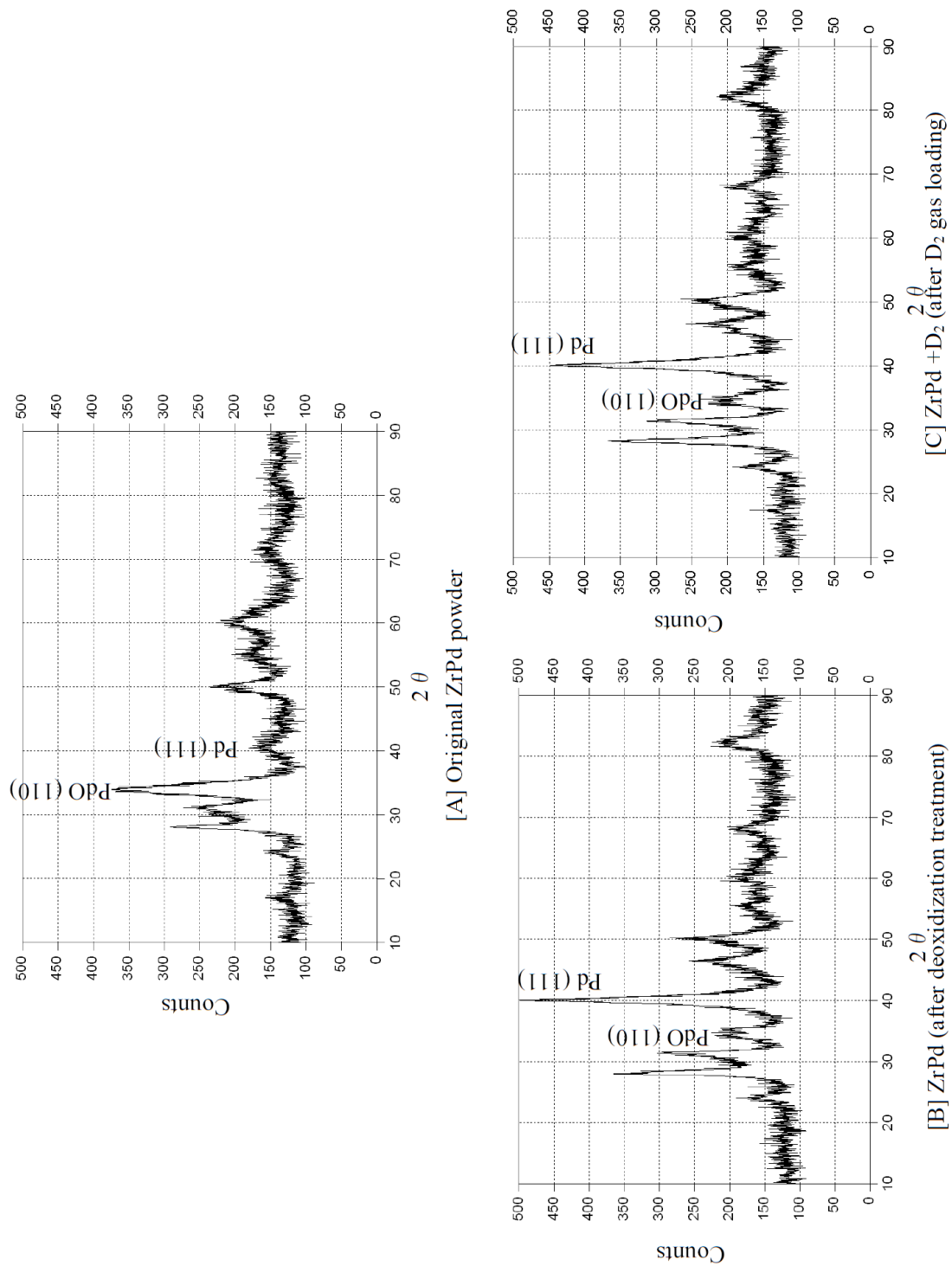
Fig.11 X-ray diffraction analysis of ZrO_2Pd35 nanopowder [8]

Note: Based on the X-ray analysis results, the process of "deoxidization treat" is unnecessary for ZrNiPd powder. [8]

The 2009 paper describes the $ZrO_2Ni30Pd5$ nanopowder as "In the case of ZrNiPd powder, the generated power is 4 [watt] lasting 60 minutes" per gram of Pd [8]. The total calorific value is about 14.4kJ/g of Pd, which is about 652J /g of sample. When creating $ZrO_2Ni30Pd5$ nanopowder, since it is a nanopowder, it should be heat-treated in the air after creating an amorphous alloy. However, the note in Figure 11 states that "the process of deoxidization treat is unnecessary for ZrNiPd powder". X-ray diffraction intensity data is not presented, and the reduction treatment of the ZrNiPd powder through deuterium gas is omitted.

If the reduction treatment is omitted, the X-ray diffraction intensity of the ZrNiPd powder should be presented to explain why it is unnecessary. Since the reduction treatment was omitted, the ZrNiPd powder naturally contains a large amount of PdO and NiO, and it can only be assumed that the generated heat contains more heat of D_2O formation. Since the combustion heat of H_2 is 285 kJ/mol, 31.8 kJ of H_2O heat of formation is produced when NiO and PdO are reduced to produce 1 g of Pd. The total calorific value of ZrNiPd powder is about 14.4kJ/Pd1g, which is not enough for this heat of D_2O formation. It is said that ZrNiPd powder generates more heat per gram of Pd than ZrPd powder, but this is natural because Pd is less and D_2O generation heat is greater.

3.3 Helium generation by Arata et al.'s nanopowder experiments

Figure 12 is a diagram presented in the 2008 paper as "mass spectrometric results of fuel (D_2) and reactive products (^{4}He)" [7]. However, this diagram does not show the process of nuclear transmutation of all of the D_2 gas into ^{4}He, but simply shows the process of concentrating the ^{4}He contained in the used gas with a concentrator.

The 2009 paper presents Figure 13, in which the lower left shows a device for concentrating helium by permeating deuterium through a Pd cylinder [8].
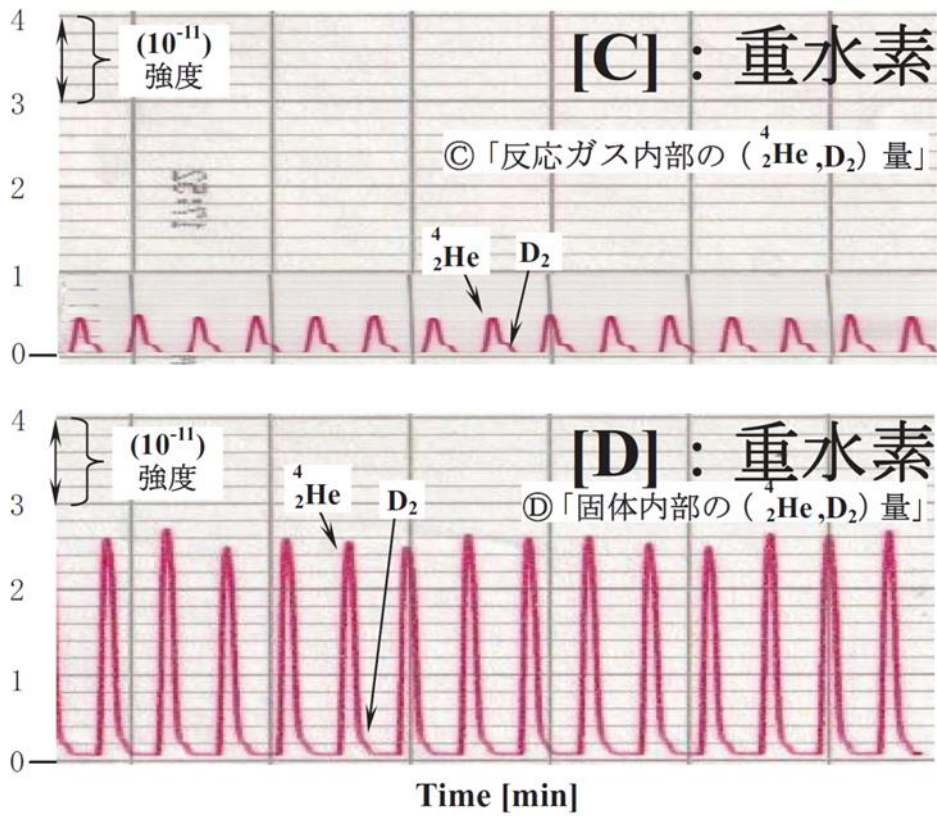
Fig. 12 Mass spectrometry result [7]
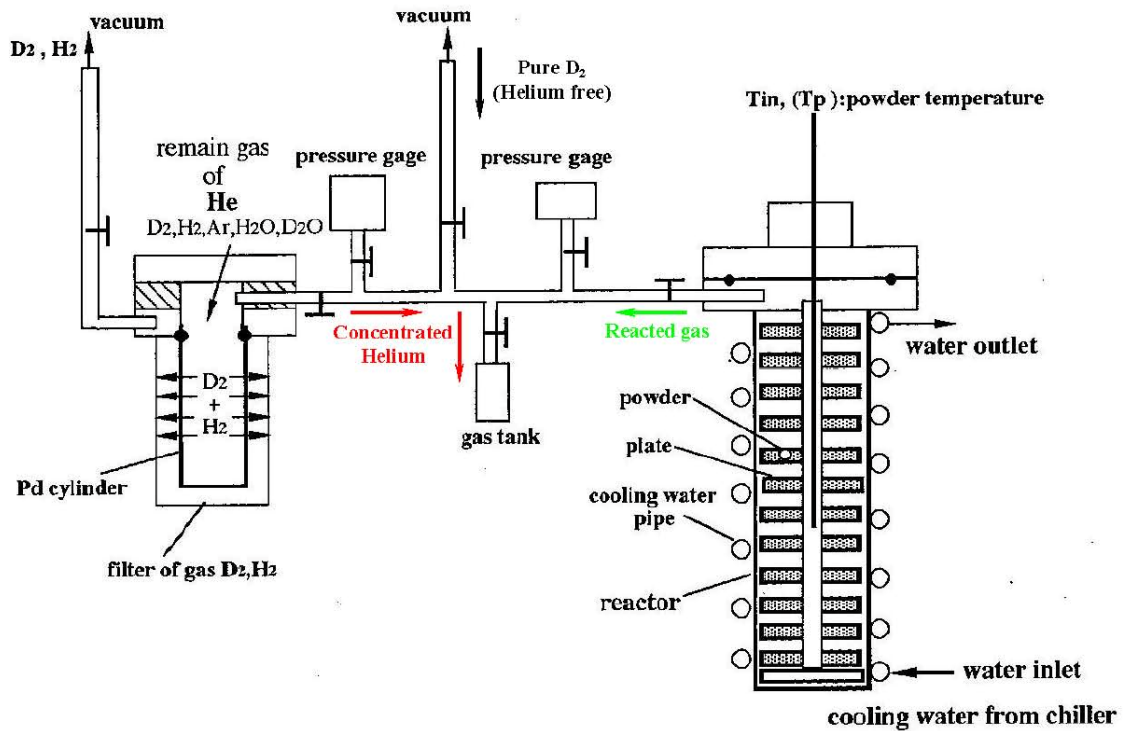
Fig. 13 Helium concentrator installed in the experimental device (lower left) [8]
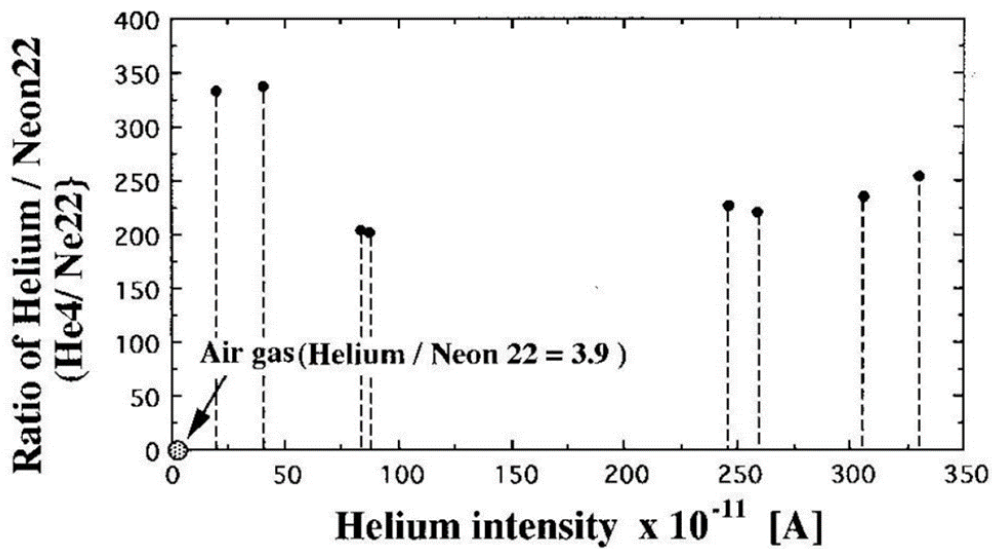
Fig.14 Helium intensity and the intensity ratio of Helium per Neon22
detected from reacted gas of ZrNiPd powder using "QMS" [8]

The 2009 paper states that "'^{4}He was produced using ZrNiPd nanopowder," and presents Figure 14 as evidence [8]. It is not written why Figure 14 is evidence. They probably thought that the ^{4}He/^{22}Ne value was larger than the lower left ^{4}He/^{22}Ne = 3.9 air, indicating ^{4}He production. However, since the horizontal axis is the Helium intensity proportional to the amount of ^{4}He, if ^{4}He is produced without ^{22}Ne, ^{4}He/^{22}Ne must be rising. The fact that ^{4}He/^{22}Ne is almost constant regardless of Helium intensity is evidence that **^{4}He is not produced.** This diagram simply shows that the deuterium gas used in the experiment contained ^{4}He at a constant ratio to ^{22}Ne.

4. Summary of conclusions

1) In a device that heats the sample with a heater, if it is claimed that the sample heats up because the sample temperature rises, it is necessary to pay attention to changes in thermal conductivity due to changes in emissivity and gas.

2) E-cat is not LENR, as A. Rossi himself testified that LENR is not feasible.

3) In nanopowder-based experiments, attention should be paid to nanopowder growth, zirconia crystallization, changes in oxygen content, and excess heat should be displayed relative to the amount of sample.

4) Transmutation products have not yet been confirmed in nanopowder-based experiments.

References

[1] S. Focardi, R. Habel and F. Piantelli, "Anomalous Heat Production in Ni-H Systems." IL Nuovo Cimento Note Brevi, Vol. 107 A, N. 1 Gennaio 1994

[2] Giuseppe Levi, Evelyn Foschi, Bo Höistad, Roland Pettersson and Lars Tegné, "Observation of abundant heat production from a reactor device and of isotopic changes in the fuel.", Bologna University, October 6, 2014 https://amsacta.unibo.it/4084/1/LuganoReportSubmit.pdf

[3] Europe Patent no. 3049733, Canada Patent no. 2920500, Mexico Patent no. Mx/A/2016/002006, Australia Patent no. 61/999582, Russia Patent no. 2016129722, China Patent no. 3049733, Souse Africa Patent no. 2016/04152, US Patent no. 9115913 B1

[4] JP6145808

[5] Invalid 2020-800094

[6] Invalidation of Trial Decision 2020-800094, Petition, as of June 11, 2021, page 5, line 33 to page 6, line 7

[7] Yoshiaki Arata, and Yue Chang Zhang, The Establishment of Solid Nuclear Fusion Reactor. J. High Temp. Soc., 2008. 34(2): p. 85.

[8] Yoshiaki Arata, Yue Chang Zhang, X.F. Wang, "Production of Helium and Energy in the Solid Fusion", ICCF15, (2009/10)

[9] Fleischmann, M., Pons, S. Electrochemically induced nuclear fusion of deuterium. J. Electroanal. Chem., 1989. 261: p. 301 and errata in Vol. 263.

[10] S. Focardi et al., "Large excess heat production in Ni-H systems", Nuovo Cimento A 111, p1233 (1998).

[11] "Emissivity of stainless steel", https://ureruzo.com/ondo_ritu.htm

[12] "Thermal conductivity of gas at 100℃", https://www.netugakugijutu.com/tech/tc_gas/

[13] "Sergio Focardi", https://en.wikipedia.org/wiki/Sergio_Focardi

[14] Eiichi Tanaka, Perspective "Expectations for New Nuclear Energy by Low-Energy Nuclear Reactions", Isotope News January 2013 No.705

[15] A.G. Parkhomov et al., "Nickel-hydrogen heat generator, continuously working for 7 months" Journal of Emerging Areas of Science, Volume 7, No. 23-24, 2019, https://nlslash.nl/parkhomov2e2s.pdf

[16] Bu-Jia Qi et al., "Anomalous heat production in hydrogen-loaded metals: Possible nuclear reactions occurring at normal temperature" China Institute of Atomic Energy, PO 275 (49), Beijing 102413, https://brillouinenergy.com/newwebsite/wp-content/uploads/2018/11/AnomalousHeat_Jiang_2015_English.pdf

[17] Mathieu Valat, Alan Goldwater, Robert Greenyer, Robert Higgins and Ryan Hunt,

"Investigations of the Lugano HotCat Reactor", J. Condensed Matter Nucl. Sci. 21 (2016) 81–96

[18] Norman D. Cook, "A Hypothesis Concerning the Connection Between the "Mössbauer Effect" and the "Rossi Effect", JCF16-7 abstract (Dec/2015)

[19] M. Nakamura et al., "Expectations on the new heat-generation-reaction between metal and hydrogen", JCF17-10 abstract (Mar/2017)

[20] Hisashi Suzuki, Review "Sintering of Powder", Powder and Powder Metallurgy, Vol.13, No.5, October 1966

[21] Yoshiaki Arata, M.J.A. Yue Chang Zhang, "Anomalous production of gaseous 4He at the inside of "DScathode" during D2O-electrolysis", Proc. Jpn. Acad., Ser. B, 1999. 75: p. 281.

[22] Yoshiaki Arata and Yue Chang Zhang, "Development of Compact Nuclear Fusion Reactor Using Solid Pycnodeuterium as Nuclear Fuel", ICCF10

[23] Shin-ichi Yamaura, Ken-ichiro Sasamori, Hisamichi Kimura, and Akihisa Inoue, "Hydrogen absorption of nanoscale Pd particles embedded in ZrO2 matrix prepared from Zr–Pd amorphous alloys." J. Mater. Res., 2002. 17(6): p.1329.

Gas analysis by a quadrupole mass spectrometer during anomalous heat generation observed in the interaction of Ni-based nano-multilayer metal composite and hydrogen gas.

Tomonori Takahashi[1], Takehiko Itoh[1,2], Yasuhiro Iwamura[2], Shinobu Yamauchi[1] and Jirohta Kasagi[2]

[1]CLEAN PLANET Inc., Tokyo, 105-0022 Japan

[2]Research Center for Electron Photon Science, Tohoku University, Sendai, 982-0826 Japan

E-mail : tomonori.takahashi@cleanplanet.co.jp

Abstract

Our team at Tohoku University have been conducted fundamental research to develop a new energy source using anomalous heat generated by Condensed Matter Nuclear Reactions.

As for anomalous heat, it was reported that heat generations beyond 100eV/H or D were observed during NEDO project [1]. The anomalous heat was obtained by heating nano-sized particles, such as $CuNiZr-O_X$ or $PdNiZrO-O_X$, up to 200~300°C with D_2 or H_2 gas. On the other hand, transmutation reaction of Cs into Pr induced by D_2 gas permeation through nano-sized Pd and CaO multilayer composite was reported [2].

Based on these papers, a new type of excess heat experiment was developed using nano-sized metal multilayer composites and hydrogen gas, resulting in the observation of excess heat [3]. In this experiment, gas analysis using a Quadrupole mass spectrometer (Q-mass) was performed on the gas released when the sample was heated to find out if there is a correlation with heat generation. Q-mass was installed near the Turbo Molecular Pump (TMP) of the exhaust pipe and installed in a position where the generated gas could be detected without interfering with the chamber during the heat generation experiment.

As an evaluation method for gas analysis, the peak intensity of Ar was used as a standard. Attention was paid here to the magnitude of the difference between the peak intensities for the Ar peaks of the major atmospheric components and those during heat generation experiments the thermal evaluation experiment.

As a result, the O_2 peak intensity showed a fairly specific intensity ratio to the standard Ar peak ratio. This is an anomalously strong peak that cannot be explained simply by air leak or contamination adhesion. It may suggest the possibility that O_2 gas was generated from the sample for unknown, not specified reason.

In the future, we plan to evaluate the relationship between the heat generation mechanism and gas generation by proceeding with gas analysis of samples that generate a larger amount of excess heat.

Key Words: Excess heat, Anomalous heat, Hydrogen gas, Nano-sized metal, multilayer composite, Heat burst

1. Introduction

It has been reported that anomalous excess heat was observed using metal composites that absorbed H2 gas [1, 3]. Nano-sized metal multilayer composites on Ni substrates and H_2 gas. However, the reaction mechanism and conditions under which these phenomena occur have not been elucidated. In this experiment, gas analysis using a Quadrupole mass spectrometer (Q-mass) was performed on the gas released when the sample was heated to find out if there is a correlation with heat generation. We are now investigating the reaction mechanisms and conditions under which anomalous excess heat is generated. Our goal is to gain key factors for understanding what is happening in nanosized metal multilayer composites.

2. Experimental

A schematic of the experimental setup is shown in Fig 1(a). Two nano-sized metal multilayer composites were placed in the center of the chamber. The stainless-steel chamber (type 304) had two ports for gas introduction and exhaust. H2 gas and its pressure were monitored with a Pirani gauge. The chamber can be evacuated with a turbomolecular pump. Multilayer samples could be heated by a ceramic heater (MS-1000R, Sakaguchi EHC Voc Co., Ltd.) with an embedded thermocouple. The heater temperature was measured with a thermocouple. The surface temperature of the sample was evaluated with an infrared radiation thermometer (IR-CAQ3CS; Chino Co., Ltd.). Input power for the heater came from his DC power supply in constant voltage

mode. The input voltage and current were measured by both voltage and current monitors provided by power supply-independent voltmeters and ammeters, respectively. A detailed view of the Ni-based nano-sized metal multilayer composite is shown in Fig. 1(b). It consists of a Ni plate (25mm square, 0.1mm thick) and a Cu-Ni multilayer thin film (25mm diameter circle, 10nm thick). Two nano-sized metal multilayer composite samples were heated via a SiO2 plate with a ceramic heater (25 mm square, 2.2 mm thick). Any energy-producing reaction on the sample surface causes the temperature of the embedded thermocouple (heater temperature) to rise. Figure 3 shows a photograph of the experimental setup and a STEM image of the Cu-Ni multilayer thin film.
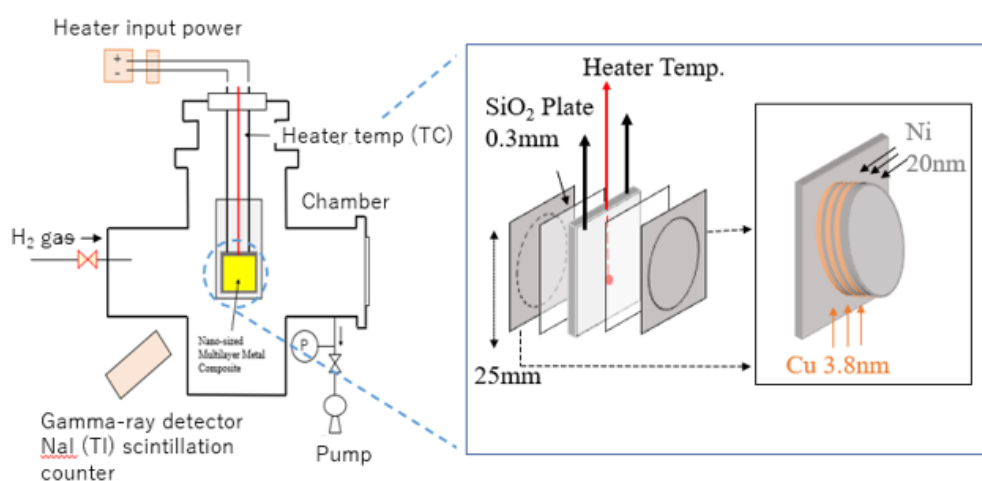
Figure 1. Experimental Set-up; (a) Schematic of Experimental Apparatus, (b) Detail Drawing around Nano-sized Multilayer Metal Composite.

A schematic of the experimental setup is shown in Fig. 2(a). The Q-mass was installed near the Turbo Molecular Pump (TMP) of the exhaust pipe and installed in a position where the generated gas could be detected without interfering with the chamber under thermal evaluation. A schematic of the experimental setup is shown in Fig. 2(b).
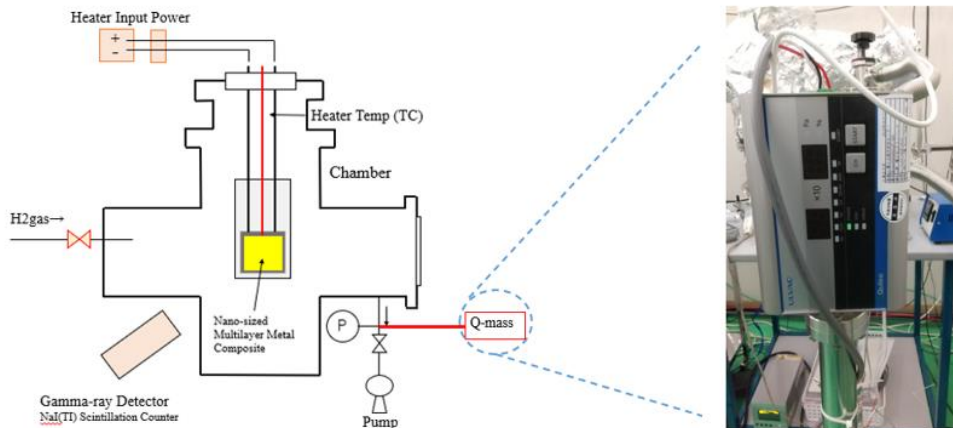
Figure 2. Experimental Set-up; (a) Schematic of Experimental Apparatus, (b) Appearance of current Q-mass
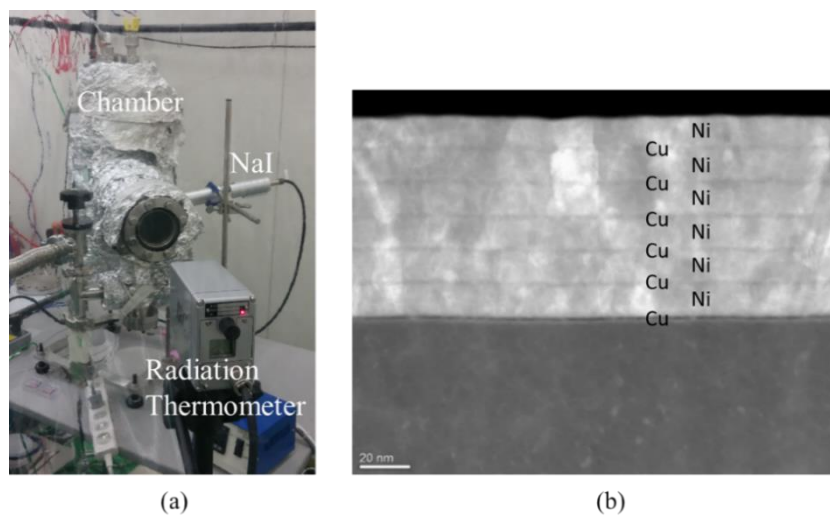
Figure 3. Photos of Experimental Apparatus and Cross-sectional View of Nano-sized Metal Multilayer Composites; (a) Outer View of the Present Experimental Set-ups, (b) STEM (Scanning transmission electron microscope) Image of Cu-Ni Multilayer Thin Film.

A Ni plate (25 mm square, 0.1 mm thick, 99.9% purity) was cleaned with acetone and annealed at 900°C for 72 h in vacuum (<10-5 Pa). After that, it was cooled down to room temperature in a furnace and washed with HNO/H2O to remove impurities on the surface of the Ni plate. The surface of the plate was covered with

layers of Cu (3.8 nm) and Ni (20 nm) obtained by alternately sputtering 3.8 nm thick Cu layers and 20 nm thick Ni layers. The manufacturing process is performed by magnetron sputtering.

Two nano-sized metal multilayer composites were placed in a chamber and baked at a temperature above 900°C for 1-2 days to remove HO on the surface. After baking, H2 gas was introduced into the chamber to about 250 Pa at 300°C. H2 gas was typically loaded for about 15–17 hours. Then with a turbomolecular pump he evacuated the H2 gas while at the same time he heated the sample to 500-900°C. Immediately after, Q-mass was observed, and the gas components during the exothermic reaction were observed. Q-mass observations were made immediately after the sample was heated to 500-900°C and at thermal equilibrium.

These processes give rise to exothermic reactions and excess heat is observed. After 6~8 hours, the heater input was typically reduced, and the sample cooled to near 100°C. These processes (H2 loading, sample heating and cooling) were repeated several times with different heating temperatures.

3. Results and Discussion

3.1. Contaminant classification method for Q-mass measurement evaluation

The important thing about generated gas analysis evaluation is It is important to distinguish whether the detected gas peak is from products or just contamination. However, this is the trickiest part. Therefore, as a precondition for distinguishing between products and contamination, the gas peak ratios of nitrogen, oxygen, and argon, which have a large atmospheric component abundance ratio, already exist, so the subsequent gas analysis evaluation was based on this. Specifically, the peak intensity of argon, which changes relatively little, was used as a reference, and the argon peak intensity ratio of nitrogen, oxygen, and other major gases was evaluated. (Fig. 4)

65 四重極質量分析計のパターン係数

注釈　質量スペクトルの見方
パターン係数は最大のピーク強度を100とした
時の各ピークの相対強度を示したものである。
例　CH_4
$^{12}CH_4{}^+ : 100, CH_3{}^+ : 85.6, CH_2{}^+ : 17.1,$
$CH^+ : 8.6, C^+ : 2.6, ^{13}CH_4{}^+ : 1.1$
参考文献　E・Stenhagan.et al : Atlas of Mass Spectral Data.(John Wiley & Sons, 1969)

E. Stenhagan.et al : Atlas of Mass Spectral Data. (John Wiley & Sons. 1969)

Figure 4**. Intensity ratio reference value of major peaks due to atmospheric components in gas analysis**

3.2. Q-mass background measurement

Figure.5(a) shows the measurement results of gas analysis as the atmospheric background. The gas peak ratio of nitrogen and carbon monoxide in No. 28 and the gas peak intensity of oxygen in No. 32 based on the peak intensity of argon were the same as the literature values, although there was some deviation. Fig. 5(b) shows the measurement results of background gas analysis when the temperature of the ceramic heater in the chamber is increased to around 900°C. Compared to the results under the background condition at room temperature, the gas peak ratio of nitrogen and carbon monoxide in No. 28 based on the peak intensity of argon does not change, but the gas peak intensity of oxygen in No. 32 is slightly higher. Although there is a slight increase in the O2 peak ratio, it is not a sudden change, so this is also used as a reference data.

Q-mass Peak intensity ratio (air)
No.28: $2.26×10^{-10}$ (A)
No.32: $3.49×10^{-11}$ (A)
No.40: $3.15×10^{-12}$ (A)

If Ar is standard 1, then
N_2(+CO): O_2 : Ar = 71.7 :11.1 : 1

(a)

Q-mass Peak intensity ratio (air)
No.28: $1.51×10^{-11}$ (A)
No.32: $3.39×10^{-12}$ (A)
No.40: $2.11×10^{-13}$ (A)

If Ar is standard 1, then
N_2(+CO): O_2 : Ar = 71.6 :16.1 : 1

(b)
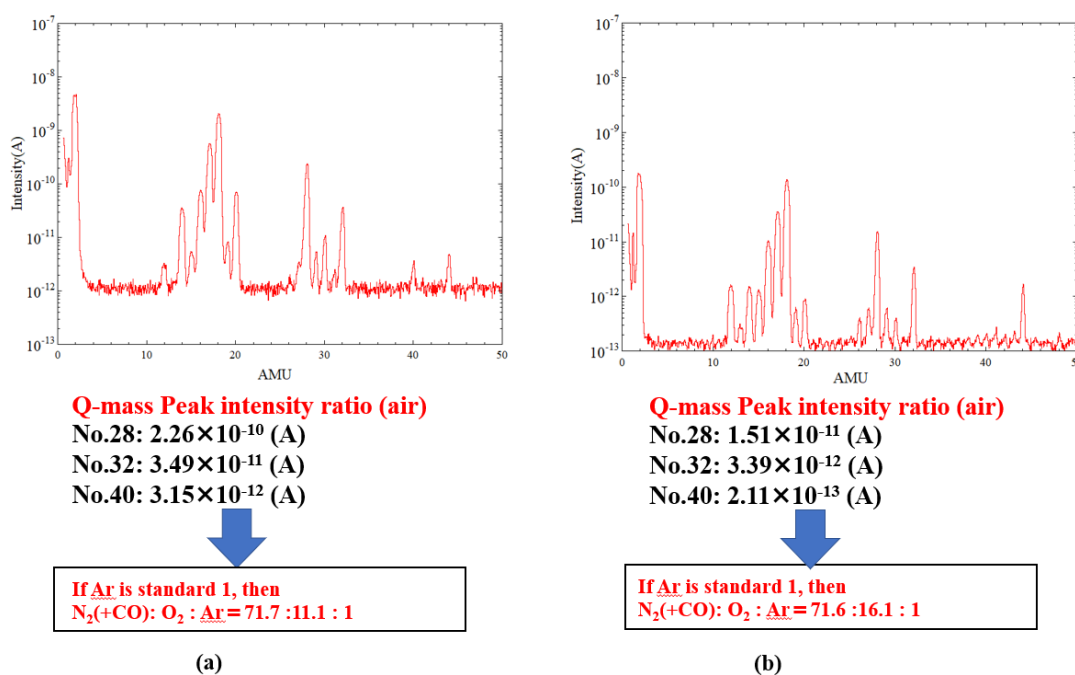
Figure 5. Measurement results and raw spectra for gas analysis as atmospheric background; (a) Q-mass measurement result as room temperature background, (b) Q-mass measurement result as background at 900°C chamber temperature

Figure. 6 is a comparison table of gas analysis literature values and actually measured background data. As mentioned earlier, the background measurement results at room temperature were generally equivalent to the reference values, but in the chamber baking measurements with the heater temperature raised to 900°C, the oxygen peak ratio increased slightly. was However, since it did not change dramatically, this was also used as a reference value in the thermal evaluation experiment.

	BG Air	BG Chamber baking	standard value
測定真空度(Pa)	$1\sim3×10^{-5}$	$3\sim6×10^{-5}$	
Ar peak (A)	$3.15×10^{-12}$ (A)	$2.11×10^{-13}$	
O_2 Peak (A)	$3.49×10^{-11}$ (A)	$3.39×10^{-12}$	
N_2 Peak (A)	$2.26×10^{-10}$	$1.51×10^{-11}$	
O_2 /Ar peak ratio	11.1	16.1	11.5
N_2 /Ar peak ratio	71.7	71.6	50

Figure 6. Q-mass background measurement numerical data comparison table

3.3. Q-mass CuNi multilayer measurement

We will look at the gas analysis during thermal evaluation using a standard sample Ni bulk CuNi multilayer film in thermal evaluation. Even with similar standard sample CuNi multilayer films, there is a large difference in the amount of excess heat due to slight differences in conditions. We are looking at differences in Q-mass analysis results for CuNi multilayer films with different amounts of excess heat. Figure.7 shows the timing of Q-mass measurement and the measured values of heater temperature and input power supply at that time. The red graph shows the heater temperature (°C), and the blue graph shows the input power (W). Comparing the graphs of samples (a) and (b) shows almost no difference in heater temperature, but when comparing the input power (W), sample (a) requires less. It can be said that the (a) sample generates more excess heat.

The timing of Q-mass measurement was evaluated at two points: the timing immediately after the heater temperature began to rise and reached the maximum temperature, and the timing at thermal equilibrium when the heater temperature stabilized.
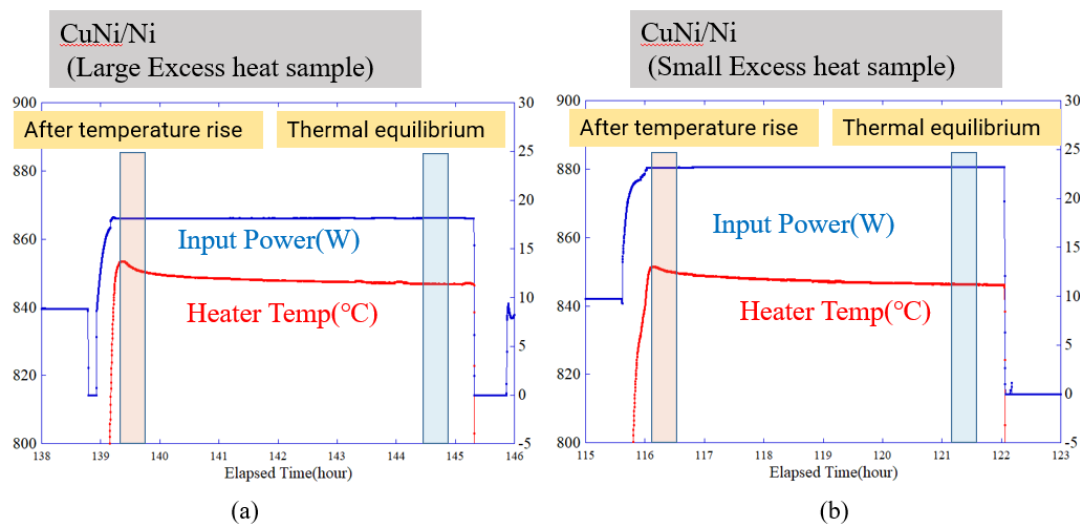
Figure 7. Timing of Q-mass measurement during thermal evaluation using standard sample Ni bulk CuNi multilayer film, measured values of heater temperature and input power supply at that time; (a) When using Large Excess heat sample, (b) When using Small Excess heat sample

Figure. 8 shows only the gas analysis immediately after heating. The horizontal axis of the graph is the actual chamber heater temperature, and the vertical axis is the ratio of the oxygen gas peak intensity to the argon peak intensity. The red dotted line and the blue dotted line in the graph show the background measurement, and the intensity ratio of the O_2 peak was compared with the magnitude relationship of the excess heat and the hydrogen absorption condition. The amount of O_2 gas generated during thermal evaluation on the standard sample is higher than that of the background measurement. In addition, when comparing samples large excess heat sample and small excess heat sample, it was found that the large excess heat sample generated more oxygen gas than the small excess heat samples. In addition, even if the difference in pressure conditions during hydrogen absorption is compared, the intensity of the O_2 peak is clearly greater in the measurement results when hydrogen is absorbed under high pressure conditions than under low pressure conditions.

From the Q-mass measurement results in Fig. 8, we can see the following.

(1) The amount of O_2 gas generated during the thermal evaluation with the standard sample was larger than that of the background measurement.
(2) Even when comparing gas analyzes of samples with a large amount of excess heat and samples with a small amount of excess heat, the amount of O_2 gas generated is greater in the measurement of the sample with a larger amount of excess heat.
(3) Even if we compare the difference in pressure conditions for hydrogen absorption, the measurement results when hydrogen is absorbed under high pressure conditions are clearly more pronounced than those under low pressure conditions.
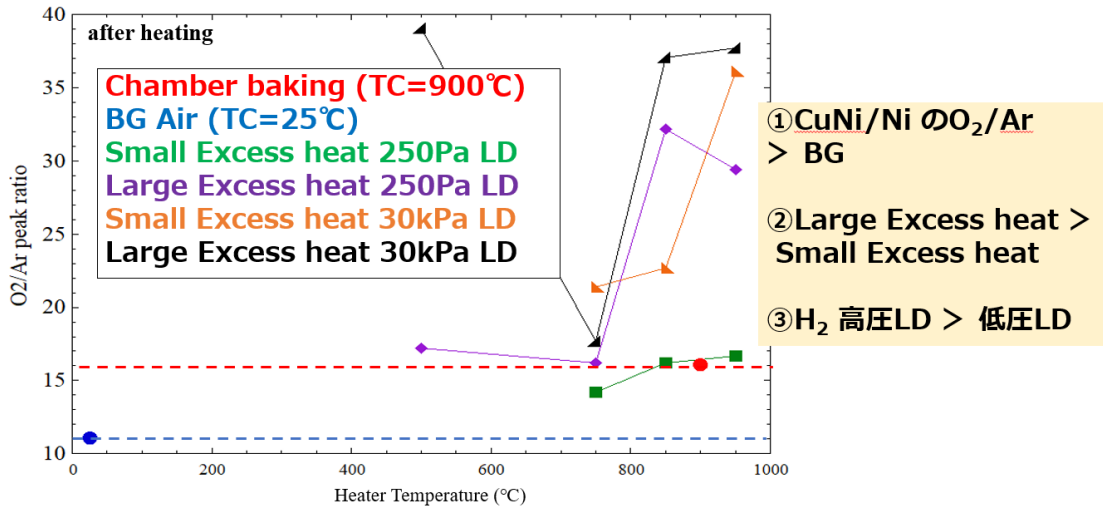
Figure 8. Q-mass measurement data showing the ratio of O₂ peak intensity to Ar peak intensity immediately after heating.

Figure. 9 shows a comparison between immediately after heating up the heater and at thermal equilibrium under the hydrogen absorption condition of high pressure 30kPaLD. The horizontal axis of the graph is the actual heater temperature, and the vertical axis is the ratio of the O_2 gas peak intensity to the argon peak intensity. The red dotted line and the blue dotted line in the graph indicate the background measurement, and the intensity ratio of the O_2 peak was compared between the measurement timing immediately after heating and the measurement timing during thermal equilibrium. This trend shows that the amount of O_2 gas generation rate for Ar is clearly higher when measured immediately after temperature rise than when measured during thermal equilibrium.

From the Q-mass measurement results in Fig. 9, followings can be considered.

(1) The amount of O_2 gas generated immediately after temperature rise is clearly larger than the amount of gas generated during thermal equilibrium. This is the tendency regardless of the amount of excess heat.

(2) The rate of O_2 gas generation against Ar gas immediately after temperature rise is clearly higher than the reference value for background measurement. On the other hand, the O_2 evolution rate at thermal equilibrium was not significantly different from the background.
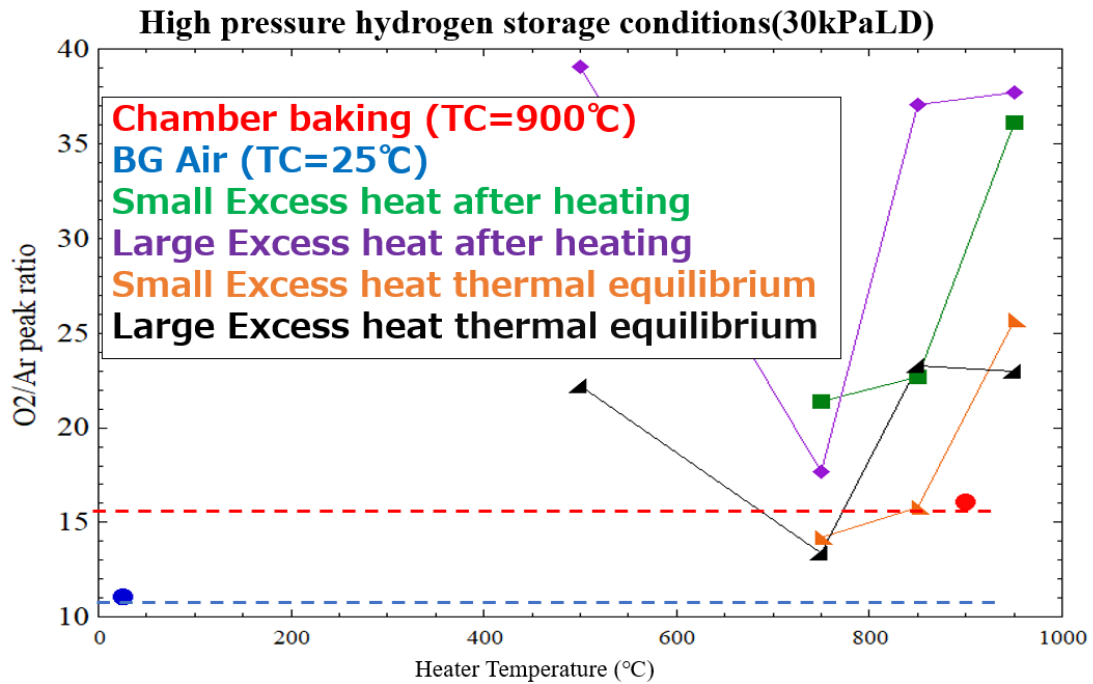
Figure 9. Q-mass measurement data showing the ratio of O_2 peak intensity to Ar peak intensity under high pressure hydrogen absorption conditions.

Figure. 10 shows the ratio of O_2 peak intensity to Ar under each measurement condition based on the Q-mass measurement data immediately after heating, where the gas generation rate was higher, based on the room temperature background measurement data. It can be seen that O_2 gas is clearly generated more than the background, regardless of the magnitude of excess heat, the difference in hydrogen absorption pressure, immediately after temperature rise, or at thermal equilibrium. In terms of the numerical values, basically, the higher the excess heat quantity and the higher the pressure of hydrogen storage, the higher the O_2 generation ratio tends to be. From this, it can be considered that there is some kind of correlation between this numerical value and excess heat.

Under any measurement conditions, the O_2 generation rate with respect to Ar is greater than 1 on the vertical axis of the graph, indicating that more O_2 is generated than the background. A comparison of a sample with a large excess heat sample and a small excess heat sample shows a clear difference if the other conditions are the same.
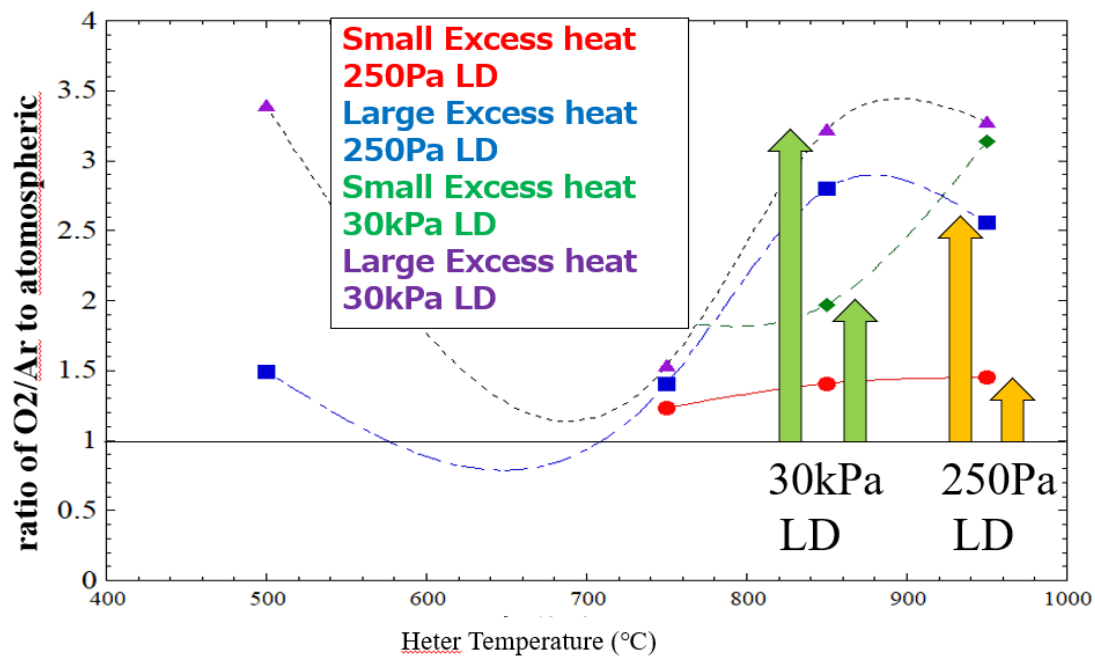
Figure 10. Q-mass measured ratio of O_2 peak intensity to Ar peak intensity compared to background measurements. Measurement timing is only immediately after temperature rise.

4. Concluding Remarks

We modified the conventional experimental procedure and piping structure for thermal evaluation to a piping structure that enables gas analysis, and constructed an experimental procedure and analysis method that actually includes gas analysis.

In addition, when analyzing the gas analysis data, the amount of oxygen gas generated was clearly larger than the background of the Ni-based metal sample, and the chamber was baked, and the heater temperature was raised to nearly 900°C. However, the amount of oxygen gas generated did not change dramatically.

However, during the thermal evaluation of the CuNi multilayer film, although there was a difference in the intensity ratio of the oxygen peak to the argon peak for each condition, it showed an abnormally strong peak that could not be explained by atmospheric leaks or simple contamination.

From the contents including gas analysis this time, in the sample under excessive heat evaluation, we obtained results indicating the possibility of a correlation between the magnitude of O2 gas generation and excess heat.

Acknowledgements

References

[1] A. Kitamura et.al, "Excess heat evolution from nanocomposite samples under exposure to hydrogen isotope gases", International Journal of Hydrogen Energy 43, p.16187-16200, 2018.

[2] Y. Iwamura et.al, "Elemental Analysis of Pd Complexes: Effects of D2 Gas Permeation", JJAP, 41, p.4642-4650, 2002.

[3] Y. Iwamura et al., "Progress in Energy Generation Research using Nano-Metal with Hydrogen/Deuterium Gas", J. Condensed Matter Nucl. Sci. 35, 285–301 (2022).

Elemental analysis towards the clarification of anomalous heat generation phenomena observed in the interaction of Ni-based nano-multilayer metal composite and hydrogen gas

S Yamauchi[1], Takehiko Itoh[1,2], Yasuhiro Iwamura[2], Tomonori Takahashi[1] and Jirohta Kasagi[2]

[1]CLEAN PLANET Inc., Tokyo, 105-0022, Japan

[2]Research Center for Electron Photon Science, Tohoku University, Sendai, 982-0826, Japan

E-mail: shinobu.yamauchi@cleanplanet.co.jp

Abstract

Previous results by our group demonstrated nano-sized metal multilayer composites on Ni substrate and hydrogen gas induced heat bursts and excess energy generation. To understand the mechanism of this anomalous heat generation, it is essential to investigate the samples which produced excess energy in our experiments. Thus, we performed analysis of the samples after having performed the experiment, using Scanning Electron Microscopy (SEM)/ Energy Dispersive X-ray spectroscopy (EDX) and Time-of-Flight Secondary Ion Mass Spectrometry (TOF-SIMS) to evaluate the morphology and chemical composition on the sample surface where such heat bursts may have occurred.

First, the specimens were observed under SEM/EDX (JSM-6500F, JEOL), then specific regions with common characteristics were identified in the samples that produced excess heat energy in the experiment. These areas were selected as measuring points for performing TOF-SIMS (TOF.SIMS 5, ION-TOF GmbH) analysis.

The morphological observations using SEM showed the presence of some particles in the middle of crystal gains in a Ni substance. EDX data indicated that Ni was the major element in the surface components, whereas the particles contained higher O ratios (at% >20) than the matrices (at% <1). Furthermore, the presence of O was confirmed by ion maps from TOF-SIMS as a high-intensity region of O at the measurement points where the particles were observed densely. This area rich in O can be attributed to the existence of many particles. Meanwhile, O was not found at the points of the less particles in the same heat-producing specimen. Regarding a quantitative evaluation of O element, the depth profile obtained from TOF-SIMS revealed that the intensity of O is also higher in the region of numerous particles compared to the area of less particles. As regards the amount of excess energy of each sample, the value gained from specimen containing numerous particles was higher than the value gained from the sample which had less particles.

These findings might imply that the existence and distribution of regions with high concentration of O indicates some phenomenon which is related to the production of anomalous heat energy. As for the process of forming the clumps rich in O element, the mechanism remains to be clarified. Nevertheless, it might be an important factor in understanding this phenomenon of energy generation.

Keywords: Excess heat, H_2 gas, Nano-sized metal multilayer composite, SEM-EDX, TOF-SIMS

1. Introduction

Two electrochemists, Fleischmann and Pons, announced their electrolysis experiment with palladium and deuterium generating nuclear energy in the form of heat in 1989 [1]. This phenomenon was considered to be the possible occurrence of D-D reaction in the Pd electrode, then it was presumed to be the discovery as "Cold fusion". Following their work, many studies have been conducted worldwide on low-energy nuclear reactions in metals that Pd and D_2 gas produce anomalous heat energy. Nuclear transmutation phenomena associated with D_2 gas permeation through Pd thin films was reported as well [2-4]. Meanwhile, some experiments have been demonstrating the producing excess heat power using metals and hydrogen gas instead of D_2 gas.

Our group has carried out heat generation experiments using nano-sized metal multilayer composites on Ni substrate and H_2 gas [5-8]. Excess heat generation, which was not possible to be explained by normal chemical reactions, has been observed in our experiments. However, little is known about this novel mechanism. Previously, we have shown some reports on the samples after the experiment [9]. This paper explores new results of the analyses about this phenomenon that may provide clues to the elucidation of the mechanism of excess heat generation.

2. Materials and Methods

Ni plates (25 mm square and 0.1 mm thickness, purity up to 99.9%, Furuuchi Chemical Co.) were utilized as a substrate of experimental sample. To prepare the specimens, they were annealed in vacuum (<10−4Pa) at 900°C for 72 h after having been washed with acetone. Then chemical etching was performed with HNO_3/H_2O to remove impurities on the surface. The acid-etched surface was coated with layers of Cu (3.8 nm) and Ni (20 nm) using Argon ion beam sputtering method as shown in Fig. 1.

Sample; nano-sized metal multilayer composite

Cu-Ni multilayer film
Thickness: Cu 3.8nm, Ni 20nm x 6 layers
Total: 143 nm

Ni
Cu
Ni
Cu
Ni
Cu
Ni
Cu
Ni
Cu
Ni
Cu

Ni substance 0.1 mm
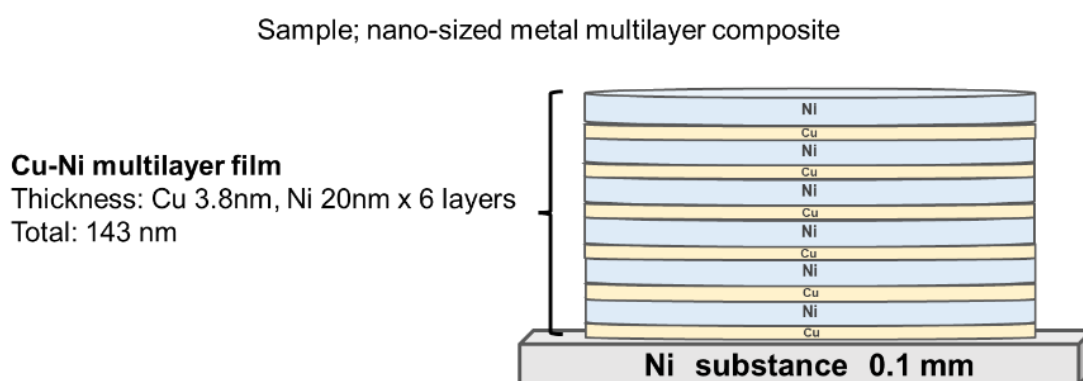
Figure 1. Nano-sized metal multilayer composite sample; 6 layers of Cu 3.8 nm and Ni 20 nm.

The specimens, nano-sized metal multilayer composites samples, were positioned in the center of the chamber, which was made of stainless steel, then heated

up by a ceramic heater (MS-1000R; Sakaguchi E. H Voc Corp.) in which a thermocouple (PtPtRh13%) was embedded. The temperature was measured by the thermocouple. Heater input power was provided by a DC power source with constant voltage mode. The input voltage and current were evaluated by voltage and current monitors offered by the power supply and independent voltmeter and amperemeter, respectively. H_2 gas was injected into the chamber until around 230 Pa at 250℃. After absorption of H_2 gas, specimens were heated up to 500 - 900℃ during the experiment.

After the experiment was performed, the specimens were examined using Scanning Electron Microscopy (SEM)/ Energy Dispersive X-ray spectroscopy (EDX) and Time-of-Flight Secondary Ion Mass Spectrometry (TOF-SIMS). The morphology and chemical composition on the sample surface where such heat bursts may have occurred were evaluated. The analysis procedures are as follows. Firstly, the specimens were observed under SEM/EDX (JSM-6500F, JEOL). SEM observations were carried out at an accelerating voltage of 5 kV or 15 kV. Additionally, EDX analysis was conducted with an acceleration voltage of 15 kV. Then, specific regions with common characteristics were identified in the samples that produced excess heat energy in the experiment. These areas were selected as measure points for performing TOF-SIMS analysis to obtain the two-dimensional elemental distributions and depth profiles. TOF-SIMS measurements were conducted with a TOF-SIMS 5 (ION-TOF, GmbH) equipped with 25 keV Bi^1+ primary ion gun, ion current was 0.8 pA, and the field of view was 100×100 μm^2. The bunching mode was employed to obtain results with higher mass resolution.

3. Results and discussion
3.1 Morphological and chemical characterization by SEM/EDX

Fig. 2 shows SEM images of a specimen on which no experiment was performed, as a control. No contaminants or irregularities were observed on the sample surface. The EDX spectrum of point 1, where the sample surface without experiment indicates that it is essentially composed of Ni and Cu, which are composition of the sample substrate and metal multi-layers film, with low contents of C, O and Al.
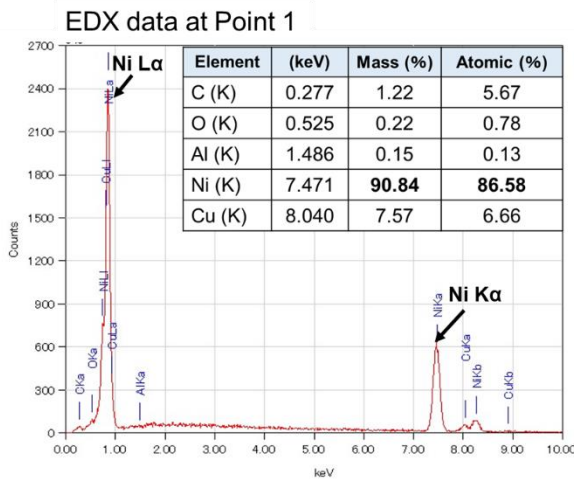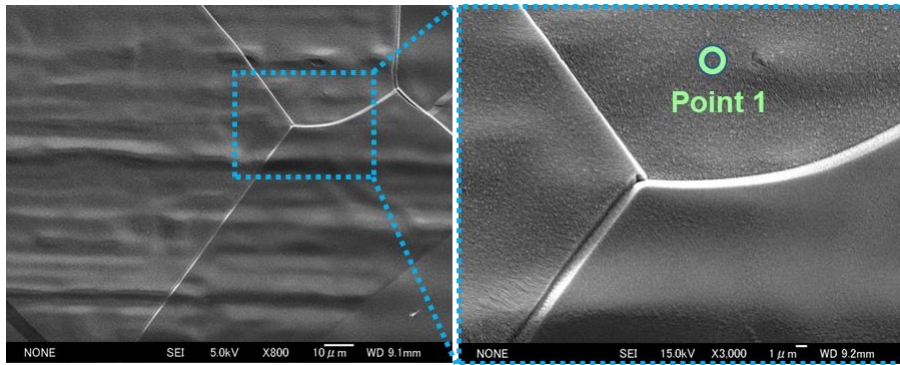
Figure 2. Morphologic observation of the sample surface without experiment as a control and EDX spectrum by SEM/EDX.

The surface of a sample on which the experiment has been performed is demonstrated in Fig. 3. Some elongated particles could be observed within the grain boundaries of Ni substance (Fig.3A). A subsequent study was carried out by using SEM in backscattered mode (COMPO), which allowed us to study the heterogeneity in chemical composition. Fig. 3C is the COMPO image of the same area of Fig. 3B. Light elements like C, O appear darker in the COMPO image compared to heavier elements, such as Ni or Cu. There can be seen particles (darker) in the matrix of Ni grain boundaries (brighter) in the image. This means that the particles consist of elements lighter than Ni. Fig. 3D, 3E are magnified images of Fig. 3B. and Fig. 3C, respectively, in secondary electron mode (SE, for 3B and 3D) and Backscattered mode (COMPO, for 3C and 3E). The particles are approximately 5µm in size. Point 2 on Fig 3D was chosen in the matrix area in Ni grain boundaries. The EDX spectra obtained from point 2 showed that it essentially contains Ni with low contents of C, O, Si, and Cu. Point 3 on Fig. 3D was chosen in the darker region (particle) in the COMPO image. The EDX spectra obtained from point 3 showed that this region is composed of O (at 33.74%) and Ni (at 60.99%), with low C, Si and Mn content.
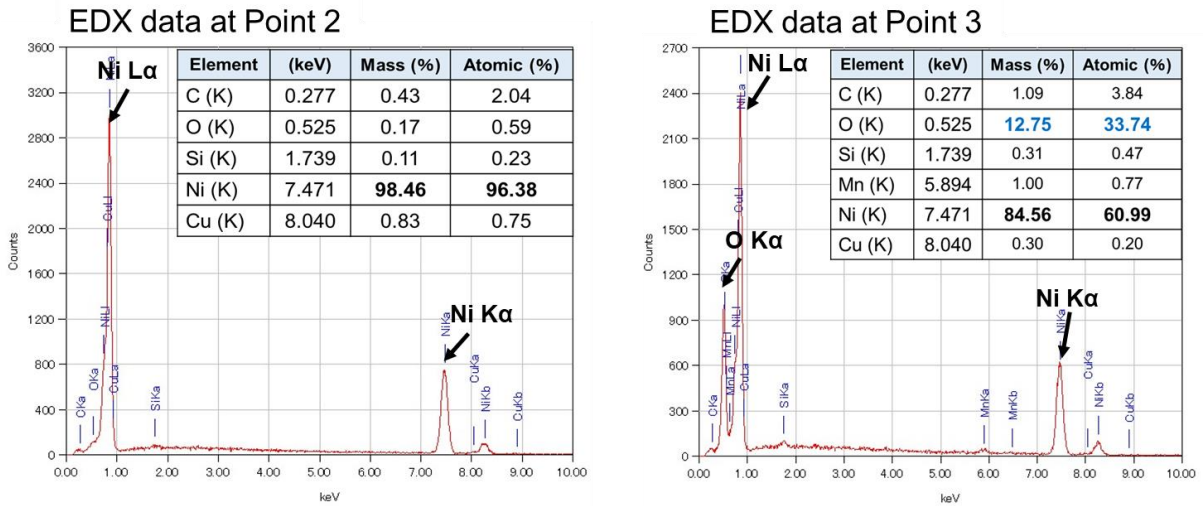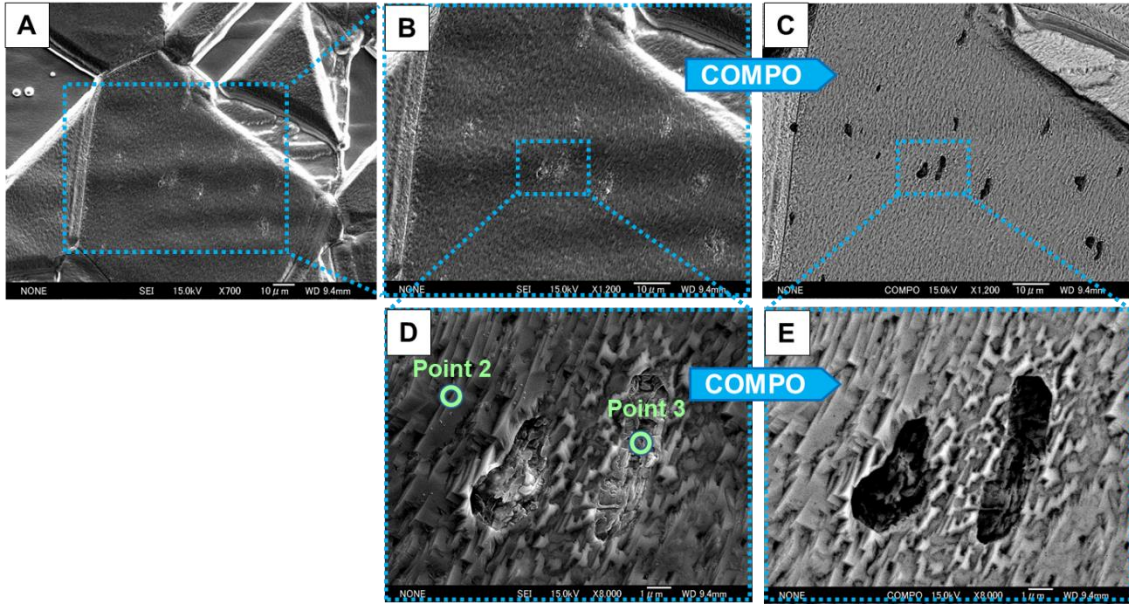
Figure 3. Morphologic observations of a sample surface after performing the experiment and EDX spectrum by SEM/EDX.

Fig.4. shows the SEM images and EDX results of a specimen which was prepared under slightly modified conditions. The excess heat power obtained from this sample was higher than that previous one though the same experiment was performed on both. Numerous particles are observed indicating the presence of lighter elements in COMPO image (Fig. 4C). Fig. 4D and 4E are magnified images of Fig. 4B. Elongated particles are identified like on the previous sample (Fig. 4E), and some clumps are seen (Fig. 4D). The elemental composition at the point 4 on Fig. 4E (the particle) from EDX result, is O (at 21.84%), Ni (at 74.82%), with trace amounts of C, Al, Si, Mn, and Cu. Point 5 on Fig. 4D is inside the clump, and it consists of O (at 38.10%), Ni (at 60.44%) with low contents of C, Al, Si, and Mn. In contrast, at point 6 on Fig. 4B, chosen in the matrix in Ni grain boundaries, we have found that Ni was the major element with a small amount of C, O, Al, Si, Mn, and Cu. The elements C, O, Al, Si, Mn were presumed to originate from the Ni substance as impurities. However, the O

ratios at the points of particles and clump seem to be quite higher than what could result from impurities from Ni bulk or air. This phenomenon, i.e., the presence of particles which, due to the above observations, we call "region of high oxygen concentration" (RHOC), is characteristic to the specimens that produced higher excess heat.

3.2 TOF-SIMS analysis at the point of region of high oxygen concentration (RHOC) by SEM/EDX

Fig. 5A shows the SEM image of the specimen producing higher excess heat, and it reveals that this specimen also had numerous particles and clumps. The square area where many particles were found was selected as a measure point (Point 1) for performing TOF-SIMS. In addition, a region where less particles were observed (Point 2) was examined as well to compare the chemical components in the same specimen (Fig 5B). The ion maps of H^-, C^-, O^-, Ni^-, and Cu^- show the TOF-SIMS results in each of these points. The color scale means a major or minor concentration (higher towards light and lower towards dark) of the given element. The signals of these ions could originate from sample components or surface contaminations. The distribution of secondary ion counts of Ni^- and Cu^- is almost uniform and consistent with the sample composition. The presence of C^- and O^- may be due to surface contamination or air, while that of H^- due to H_2 gas during the experiment. Comparing the results from each point, significant differences can be identified in the distribution of O^-. The signal intensity of O^- exhibits higher values in the area where the particles were observed densely than in the region where less particles existed. The depth profiles from each of these locations are shown below the images. On these one can observe that the signal intensities gradually decreased by the distance from the surfaces. All values were nearly the same except O^- in those points. The intensity of O^- demonstrates higher value in the point 1, where numerous particles were observed, than in the area where less particles were present (point 2). There was a slight increase in intensity of O^- between 600 - 800 data points indicating the interface of Ni substance and Cu-Ni multilayer film. Thus, the ion maps and depth profiles from TOF-SIMS analysis confirmed the results of SEM/EDX showing the presence of the region of high oxygen concentration (RHOC) in the sample surface.

EDX data at Point 4

Element	(keV)	Mass (%)	Atomic (%)
C (K)	0.277	0.57	2.30
O (K)	0.525	7.24	21.82
Al (K)	1.486	0.05	0.09
Si (K)	1.739	0.20	0.34
Mn (K)	5.894	0.38	0.33
Ni (K)	7.471	91.17	74.82
Cu (K)	8.040	0.38	0.29

EDX data at Point 5

Element	(keV)	Mass (%)	Atomic (%)
C (K)	0.277	0.20	0.68
O (K)	0.525	14.53	38.10
Al (K)	1.486	0.15	0.23
Si (K)	1.739	0.18	0.28
Mn (K)	5.894	0.34	0.26
Ni (K)	7.471	84.60	60.44

EDX data at Point 6

Element	(keV)	Mass (%)	Atomic (%)
C (K)	0.277	1.01	4.69
O (K)	0.525	0.22	0.77
Al (K)	1.486	0.18	0.36
Si (K)	1.739	0.29	0.58
Mn (K)	5.894	0.23	0.24
Ni (K)	7.471	97.68	93.01
Cu (K)	8.040	0.40	0.35
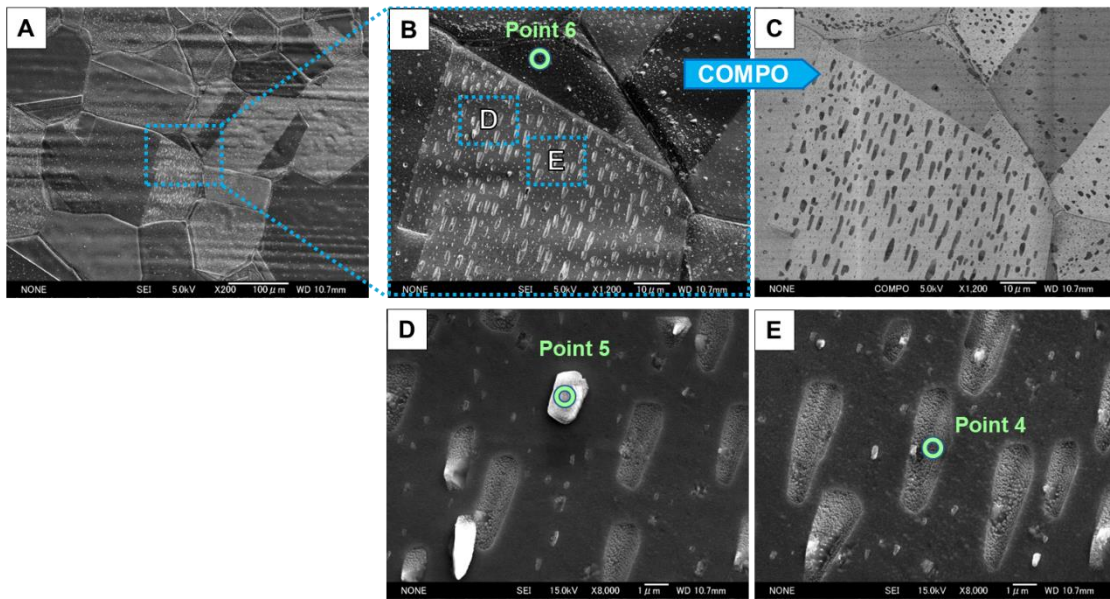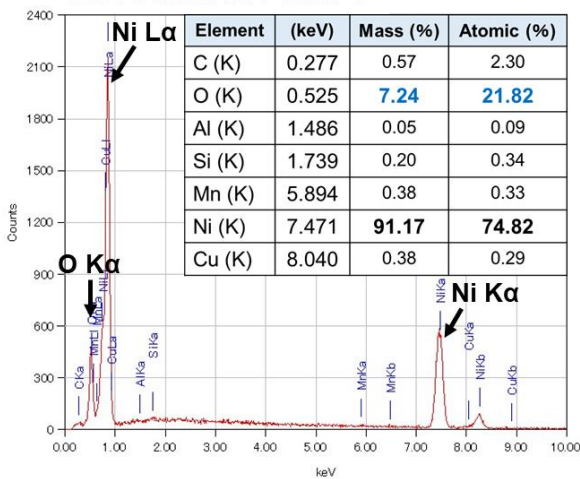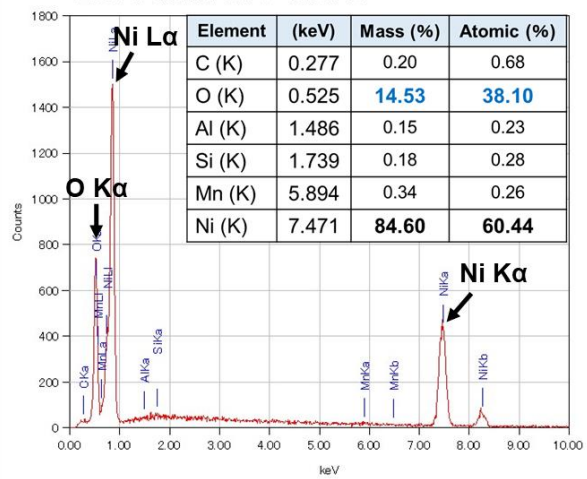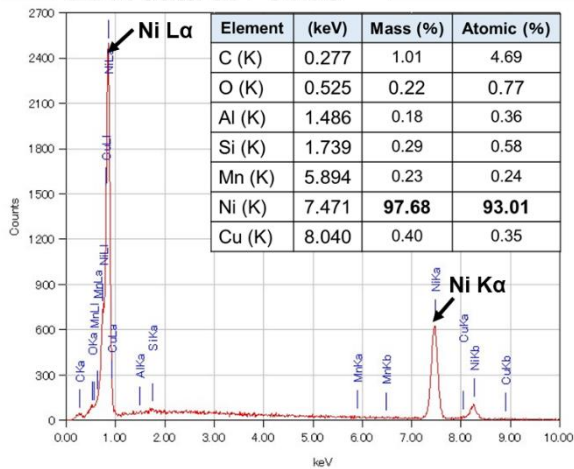
Figure 4. Morphologic observation of a sample surface after performing the experiment and EDX spectrum by SEM/EDX.
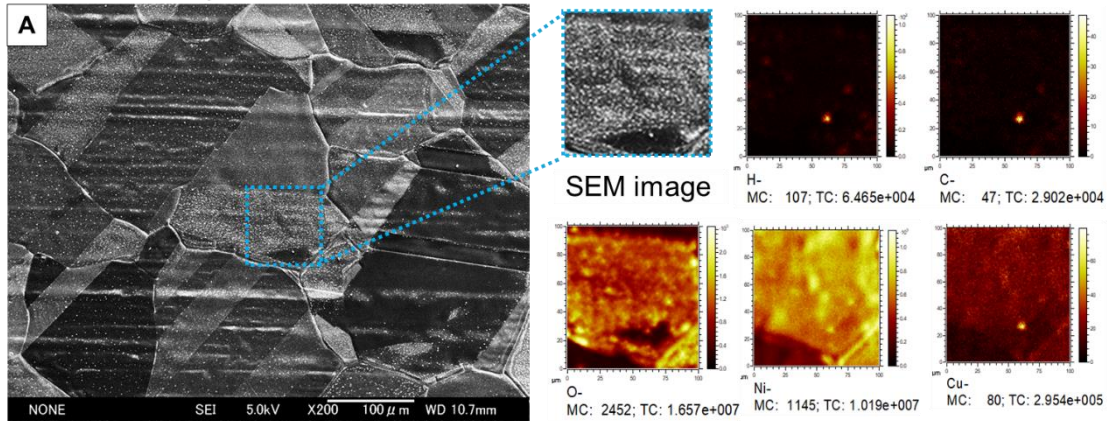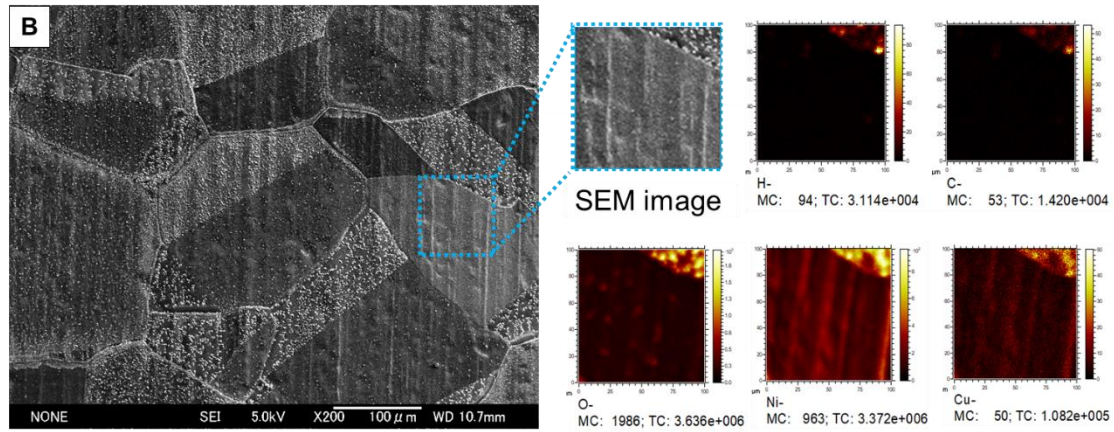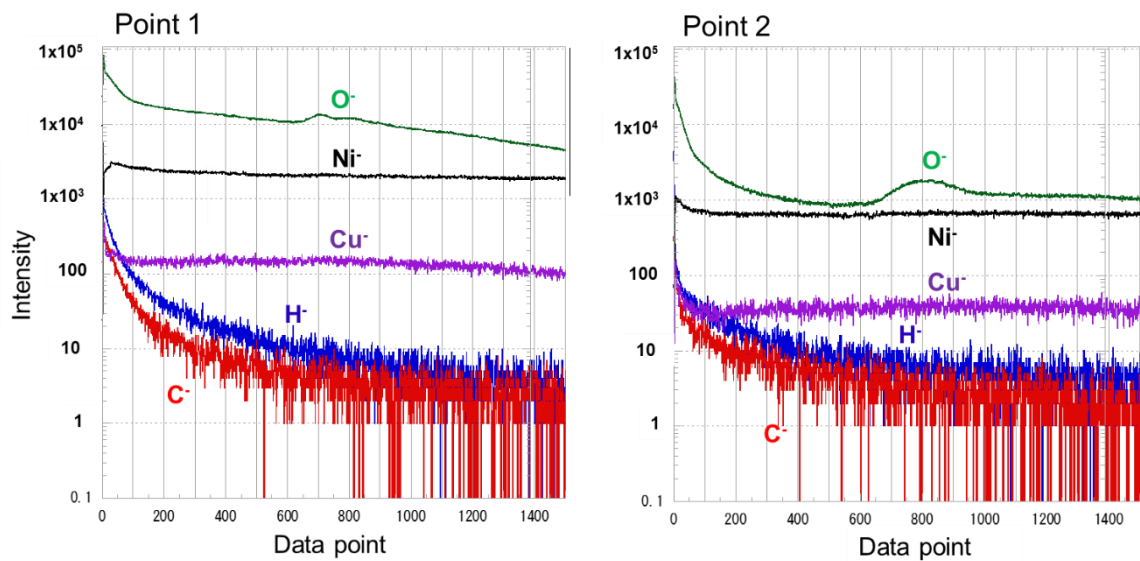
Figure 5. TOF-SIMS maps of H⁻, C⁻, O⁻, Ni⁻, and Cu⁻ and depth profiles from each area, the numerous RHOC were presented (point 1) or less RHOC were observed (point 2). The ion map images were obtained from a deep region of depth profiles.

3.3. The effect of the region of high oxygen concentration (ROHOC) in the sample and the excess heat evaluation.

Fig. 6 shows the excess heat power obtained from the specimens in which no RHOC was detected (Sample Cu-Ni), some RHOC were observed (Sample 1), and numerous RHOC were presented (Sample 2). Comparing these results, Sample 2 demonstrated the highest excess power in these specimens. Although the specimen in which no RHOC was present also produced some excess heat, the value was lower than in Sample 1. This result might suggest that the presence of RHOC is related to excess heat generation.
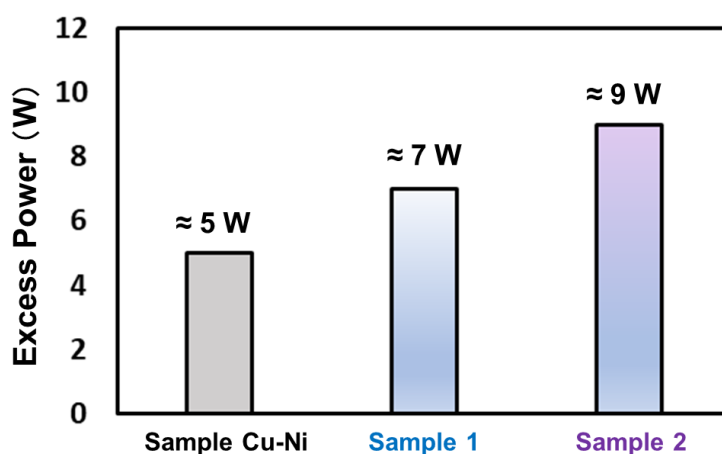
Figure 6. Excess power from the samples with no RHOC (Sample Cu-Ni), some RHOC (Sample 1), and numerous RHOC (Sample 2).

4. Conclusion

The morphological observations using SEM showed the presence of numerous particles on the surface of the sample that produced high excess energy. EDX results indicated that Ni was the major element in the surface components, whereas the particles contained higher O ratios (at% >20) than the matrices (at% <1). The presence of O was confirmed by TOF-SIMS, which showed that the measurement points where particles appeared densely were high-intensity regions of O.

The particles, the region of high oxygen concentration (RHOC) could be a feature of the samples which produce high excess power. As regards the amount of excess energy of each sample, the value gained from specimen where numerous RHOC was observed was higher than the value gained from the sample which had less RHOC. These findings might imply that the existence and distribution of RHOC indicate some phenomenon which is related to the production of anomalous heat energy. As for the process of forming the particles rich in O element (RHOC), the mechanism remains to be clarified. Nevertheless, it might be an important factor in understanding this phenomenon of energy generation. Further investigation will be necessary to arrive at a definitive conclusion of this study.

Acknowledgement

References

[1] M. Fleishmann and S. Pons, "Electrochemically Induced Nuclear Fusion of Deuterium", *J. Electroanol. Chem.*, **261** (1989)301-308

[2] Y. Iwamura, T. Itoh, N. Gotoh, I. Toyoda, "Detection of anomalous elements, X-ray and excess heat in a D_2-Pd system and its interpretation by the electron-induced nuclear reaction model", *Fusion Technology.*, **33**, 476-492 (1998).

[3] Y. Iwamura, T. Itoh, M. Sakano, N. Yamazaki, S. Kuribayashi, Y. Terada, T. Ishikawa, D. Sekiba, H. Yonemura, K. Fukutani, "Observation of low energy nuclear transmutation reactions induced by deuterium permeation through multilayer Pd and CaO thin film," *J. Condensed Matter Nucl. Sci.*, **4**, 132-144 (2011).

[4] Y. Iwamura, T. Itoh, S. Tsuruga, "Transmutation reactions induced by deuterium permeation through nano-structured Pd multilayer thin film", *Current Science.*, **108** (4), 628-632 (2015).

[5] Y. Iwamura, T. Itoh, J. Kasagi, A. Kitamura, A. Takahashi, K. Takahashi, R. Seto, T. Hatano, T. Hioki, T. Motohiro, M. Nakamura, M. Uchimura, H. Takahashi, S. Sumitomo, Y. Furuyama, M. Kishida, H. Matsune, "Anomalous Heat Effects Induced by Metal Nanocomposites and Hydrogen Gas", *J. Condensed Matter Nucl. Sci.*, **29**, 119-128 (2019).

[6] Y. Iwamura, "Heat generation experiments using nano-sized metal composite and hydrogen gas", *Cold Fusion: Advances in Condensed Matter Nuclear Science*, Ed. Jean-Paul Biberian, Elsevier, Amsterdam, 157-165 (2020).

[7] Y. Iwamura, T. Itoh, S. Murakami, M. Saito, J. Kasagi, "Excess energy generation using a nano-sized multilayer metal composite and hydrogen gas", *J. Condensed Matter Nucl. Sci.*, **33**, 1-13(2022).

[8] Y. Iwamura, J. Kasagi, T. Itoh, T. Takahashi, M. Saito, Y. Shibasaki, S. Murakami, "Progress in Energy Generation Research using Nano-Metal with Hydrogen/Deuterium Gas", *J. Condensed Matter Nucl. Sci*., **35**, 285–301 (2022).

[9] M. Saito, T. Itoh, Y. Iwamura, S. Murakami, J. Kasagi, "Elemental Analysis for Elucidation of the Anomalous Heat Generation Phenomena", Proceedings of the 20st Meeting of Japan CF Research Society, JCF20, December 13-14, 2019, Fukuoka, p.80-91.

Photon Radiation Analysis for Heat Burst Phenomena during Hydrogen Desorption from Nano-sized Metal composite

Takehiko Itoh[1,2], Yoshinobu Shibasaki[2], Jirohta Kasagi[1],
Tomonori Takahashi[2], Shinobu Yamauchi[2] and Yasuhiro Iwamura[1]

1 Research Center for Electron Photon Science, Tohoku University, 982-0826 Japan
2 CLEAN PLANET Inc., 105-0022 Japan

We have constructed an optical system to measure photon radiation for a wide energy region, in order to study the anomalous heat generation in nano-sized metal composite with hydrogen gas. In the present work, heat burst phenomena frequently occurring during heat generation were studied in detail by using an improved measurement system. It is found that the photon emission increases over all energy regions in synchronization with a sudden rise of the heater temperature. This suggests that the sample has a sudden energy generation, which increases radiation power as well as the surface temperature, resulting in a rise of the heater temperature. We found that there is a correlation between the visible and infrared intensities, but the correlation function is different for each burst. In comparison with the radiation from the sample before hydrogen introduction, the radiation intensity in the high-energy part is increased during the burst.

1. Introduction

In recent years, in a system consisting of nanostructured metals (Ni, Cu, etc.) and hydrogen (deuterium or light hydrogen), anomalous heat generation that generates an order of magnitude greater thermal energy than normal chemical reactions without emitting CO_2 reactions have been reported. If power generation technology using this phenomenon is put into practical use, we will be able to obtain clean, powerful and inexpensive energy, and the social and economic impact will be immeasurable.

We have been conducting research on anomalous heat generation using nanostructured metal materials and have so far confirmed abnormal heat generation phenomena that cannot be explained by chemical reactions [1-3]. However, basic and systematic data are lacking, and the reaction mechanism is unknown. We are working on the elucidation of the mechanism as well as the use of exothermic phenomena.

The outline of the experimental method is as follows.
(1) A nano-multilayer reaction film is placed on both sides of a heater with a built-in thermocouple. (Fig.1).
(2) Place this in a vacuum vessel and evacuate.
(3) After hydrogen is absorbed, the nano-multilayer film is rapidly heated at the same time as the vacuum is exhausted to release hydrogen, thereby inducing a reaction.

We have evaluated anomalous excess heat with a thermocouple built into the heater. Recently, experiments have been conducted by adding light radiation sensor for temperature measurement. We measured the heater temperature continuously together with the light radiation emitted from the surface of the sample. In these experiments, we often observed heat burst phenomena, in which the temperature of the heater suddenly rises [4,5].

Our experimental method is characterized by the fact that it is performed under vacuum conditions and that it uses a thin film, which allows us to directly observe the radiation emitted from the surface when an anomalous heating phenomenon occurs. We presume that radiation from this surface is accompanied by information related to anomalous exothermic reactions. For example, Kasagi point Analysis of the radiation intensity spectra in a wide energy region is decisive in the consideration of the size of the reaction region (hotspot formation) [6]. Therefore, observing these heats burst phenomena in detail is one of the ways to understand the mechanism of the AEH (Anomalous Excess Heat) production, such as elementary reactions, the size of the reaction region, and the location of the reaction.
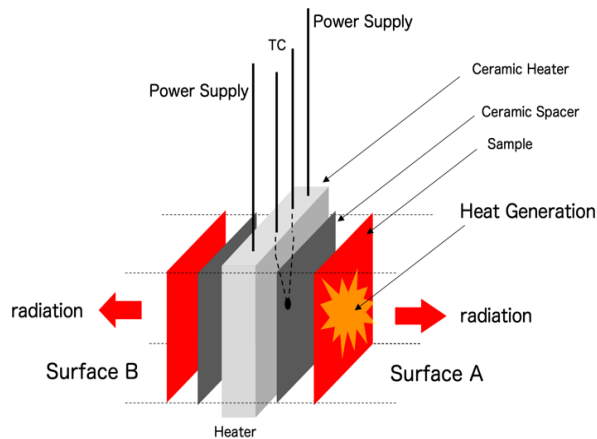
Fig. 1   Schematic diagram of the experiment

2. Experimental Apparatus & Procedure

Experimental Apparatus

   A photograph of the equipment is shown in Fig. 2(a). A heater is placed in the center of the vacuum chamber, and samples are placed on both sides. The sample is made by alternately depositing 3.8 nm Cu, 10 nm Ni, 3.8 nm CaO, and 10 nm Ni on a Ni substrate using magnetron sputtering (Fig.2(b)). On one side of the sample, four types of measuring instruments are installed to observe the photon radiation emitted from the surface (Fig.2(b)). The near-infrared and visible light passes through a focus lens and is guided by an optical fiber, which is then branched to perform spectral measurement with a FTIR (Fourier Transform Infrared Spectrometer) Hamamatsu C15511 (wavelength 1.5-2.5 μm) for near-IR, and a spectroscope Hamamatsu C10027 (wavelength 0.3-0.9 μm) for visible light, respectively. Mid-infrared light is measured by a mid-infrared detector (TMHK-CLE1350; wavelength 3-5.5 μm) through a BaF window. Another mid-infrared detector is installed to observe the back side. We are also observing X-rays (5keV-150keV) by SDD through the Be window.

   Mid-infrared measurement is performed every second. Near-infrared and visible light spectra are measured for 1 minute at a time interval of 5 minutes.
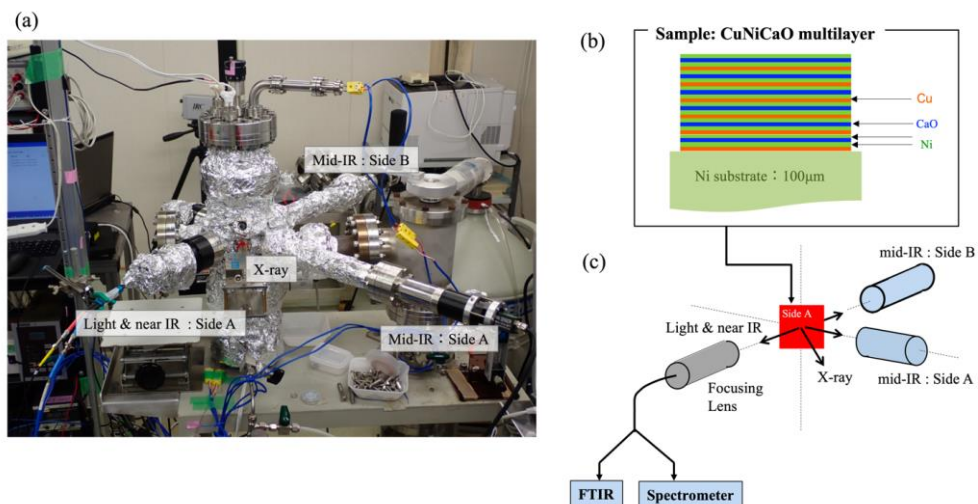
Fig.2 Experimental equipment (a) Photograph of equipment
(b) Cross-sectional view of nanostructure (c) Optical measurement system

Photon radiation measurement

Prior to the measurements of the samples, photon emissions from carbon nanotube (CNT) films were measured by the optical system mentioned above, in order to correct the detection efficiency for each detector: The radiation from the CNT can be regarded as the blackbody radiation because of its emissivity of 0.98 ~ 0.99. The surface temperature of the CNT is the output reading of Mid-IR with setting emissivity 1.0 and is controlled by the input heater power. Efficiency correction factors were obtained by dividing the calculated blackbody spectrum by the measured raw spectrum. The measurement was performed for several temperatures and the correction factors determined finally were those averaged ones. Fig. 3 shows the efficiency corrected spectra with various colored dots. The lines are the calculations that reproduce the corrected spectra by using the blackbody approximation with temperature as a parameter; they correspond to 690K, 715K, 763K and 800K, respectively for blue, green, orange, and red line. These redetermined temperatures are well reproduced with those of the output of Mid-IR within +/- 2 K. The green area in the figure is the observation area of the mid-infrared detector. Also, the red region indicates the near-infrared region, and the blue region indicates the visible light region.
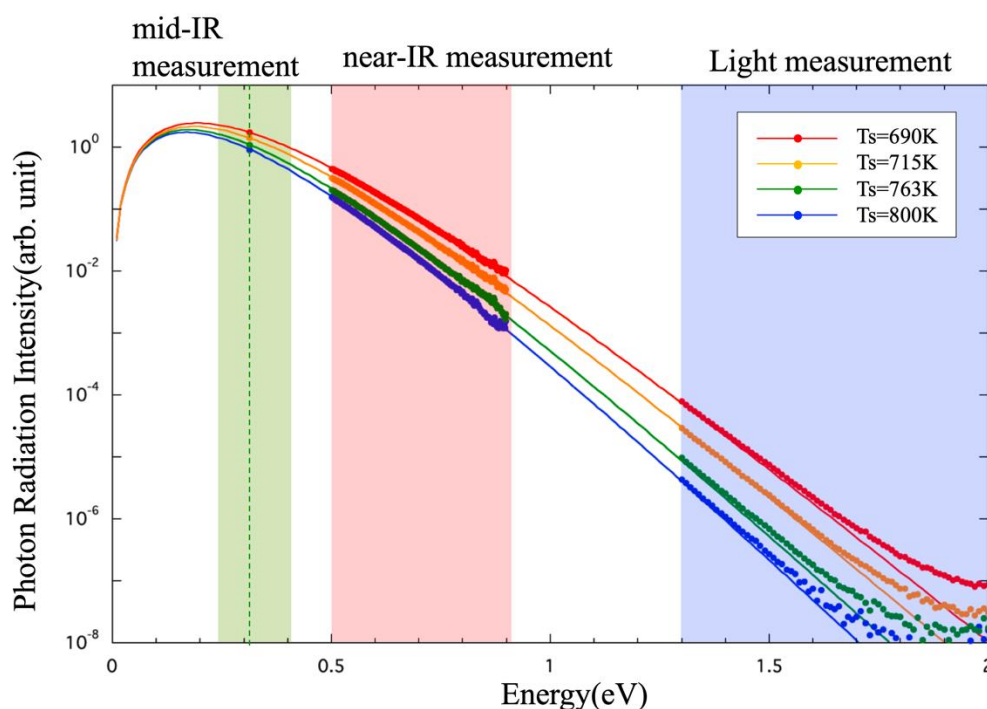
Fig.3 photon radiation spectrum using CNT standard sample.

Experimental Procedure

The experimental method is as follows.

(1) Sample preparation: The sample is made by alternately depositing 3.8 nm Cu, 10 nm Ni, 3.8 nm CaO, and 10 nm Ni on a Ni substrate using magnetron sputtering (Fig. 2b).

(2) Sample setting: We set the sample on both sides of the heater and evacuate the vacuum chamber. Then we heat them for about 3 days at a temperature about 900 C, for a vacuum bake-out.

(3) Measurement before introduction of H_2 gas: Keeping the chamber in vacuum, we start the measurement of radiation together with the recording of the data logger including the heater temperature and output of Mid-IR. By changing the heater input power, measured are the reference data corresponding to no excess heat for the condition without H_2 gas. Excess heat can be evaluated using these reference data.

(4) Hydrogen absorption of sample: For the sample to absorb H2 gas, we fill the chamber with H2 gas up to a pressure of 250 Pa and keep the heater temperature at 300°C for about 12 hours.

(5) Measurement during desorption of H2: After H2 absorbed, we rapidly heat up the heater by increasing the heater input voltage at the same time as evacuating to release hydrogen: This may induce an anomalous heat generation phenomenon. As in (3), the measurement is started under the condition that the heater input voltage is constant. Data acquisition with this input voltage (or input power) is typically performed for 6 to 8 hours.

(6) In order to obtain another data for different input voltage, we repeat from (4) and perform (5) by changing the heater input voltage.

3. Results & Discussion

Fig. 4 is an example of the experimental results in which heat burst occurred (experiment 1). The horizontal axis indicates time, and time 0 is the start time of introducing hydrogen (process (4) mentioned above). In this case, the heater input power was 31 W after the thermal equilibrium in the process (5). The red line is the heater temperature, the black line is the heater input power, and the green line is the radiation intensity of the mid-infrared light. As shown in this graph, although the heater input was maintained at 31W, a phenomenon of a sudden and spontaneous rise in the heater temperature--heat burst--was observed six times. As seen, the intensity of the mid-infrared light increases in synchronism with the burst.

When the heat burst occurred, visible light and near-infrared light also increased synchronously with the heat burst. In Fig. 5, observed radiation intensities of the near-infrared and visible light are shown: The spectrum measurements started at 12.5h, each measurement was performed for 1 minute and repeated at intervals of 5 minutes. In the figure, the blue squares are the visible light radiation integrated between 1.6-1.8 eV, and the red circle indicates the intensity of near-infrared integrated from 0.55 to 0.75 eV. The heat temperature and the radiation intensity of mid-infrared light are also plotted with thin lines and squares, respectively. One can clearly see that the visible light, near-infrared, and mid-infrared radiation increase synchronously with the sudden rise of the heater temperature.
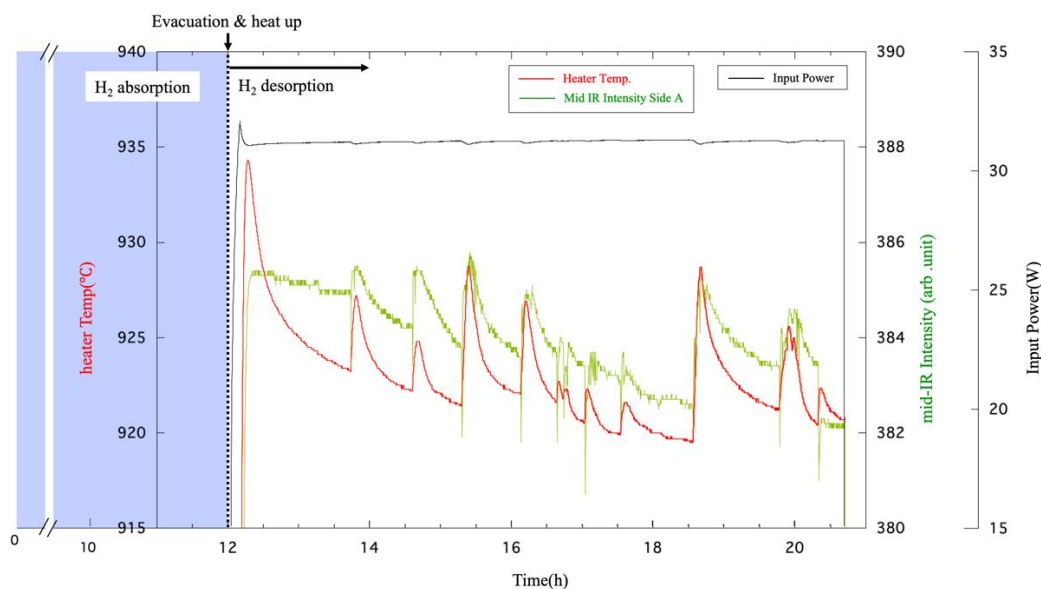
Fig.4 Time evolution of Heater temperature, mid-infrared intensity, heater input power in Experiment1
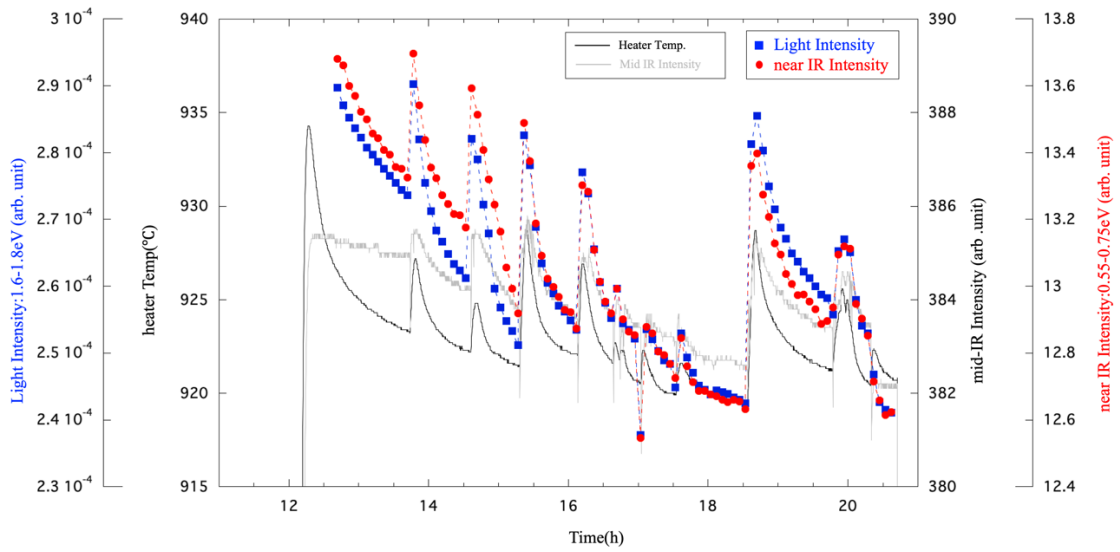
Fig.5 Time evolution of visible light intensity and near-infrared light intensity in Experiment1

We compare the light spectrum before and after the heat burst. Fig. 6(a) is an enlarged plot from 18 to 20 hours in Fig. 5. A heat burst occurred immediately after 18.536 h, and the light intensity increased rapidly at 18.619 h. The spectra measured at 18.536 h just before the heat burst and at 18.619 h just after the heat burst are compared in Figs 6(b), 6(c) and 6(d): Fig. 6(b) shows whole spectrum for energy from 0.5 to 1.8 eV, while Fig. 6(c) and 6(d) show enlarged near-infrared regions of 0.55-0.75 eV and visible light regions of 1.6-1.8 eV, respectively. It shows that the intensity of the photon radiation increases over the observed area when the heat burst occurs.

(a)
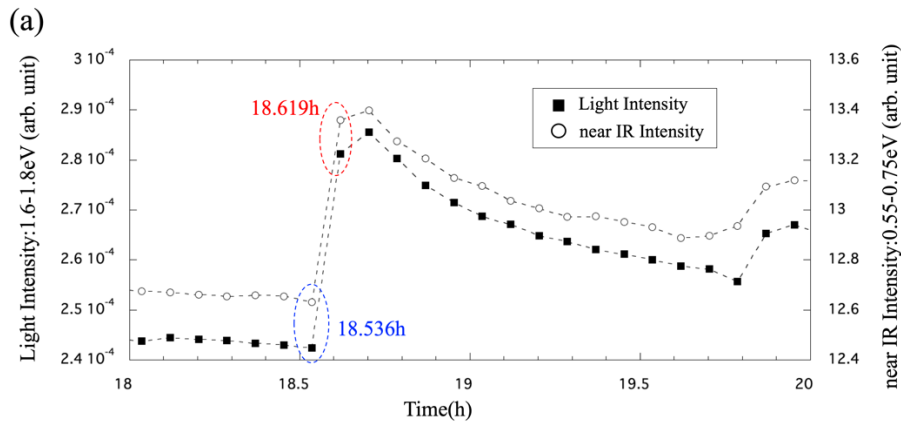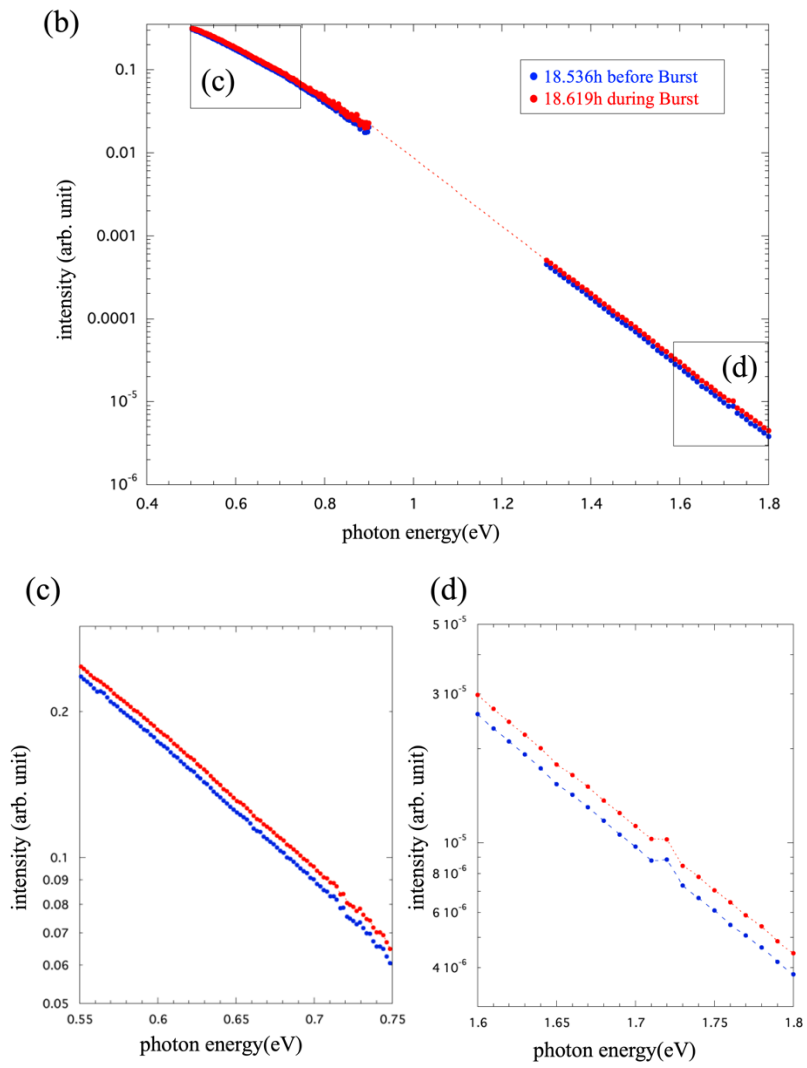
Fig.6 Comparison of optical spectrum before and during heat burst in Experiment 1
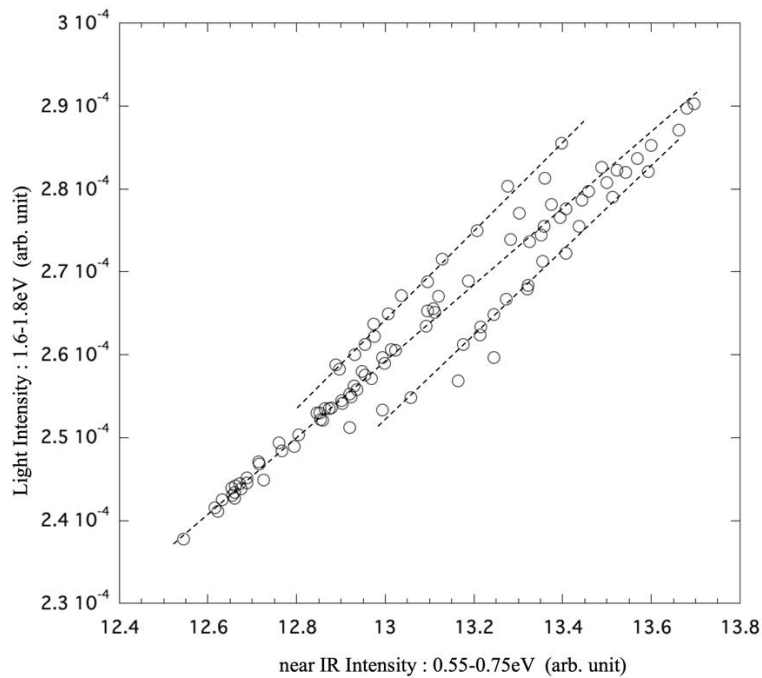
Fig.7 Correlation between near-infrared light intensity and visible light intensity

Fig. 7 shows the correlation between near-infrared intensity and visible light intensity. The horizontal axis indicates the intensity of near-infrared, and the vertical axis indicates the intensity of visible light. From this figure, a positive correlation can be seen in the correlation between visible light and near-infrared. It seems, also, there are three lines (linear correlation functions) rather than one. Thus, it is indicated that the distribution of visible light and near-infrared are in three different states.

A closer analysis of the data revealed that each burst could be classified as belonging to a different correlation line. This is illustrated in Fig. 8(a) and 8(b), where three correlation lines and bursts are grouped into three colors. As seen, the red line corresponds to the 5th burst, the blue line corresponds to the 1st and 2nd bursts, and the green line corresponds to the remaining bursts. This means that each burst emits photons with a different intensity distribution in the infrared - visible light region and implies that it is not a simple photon emission from a homogenized thermal equilibrium state.
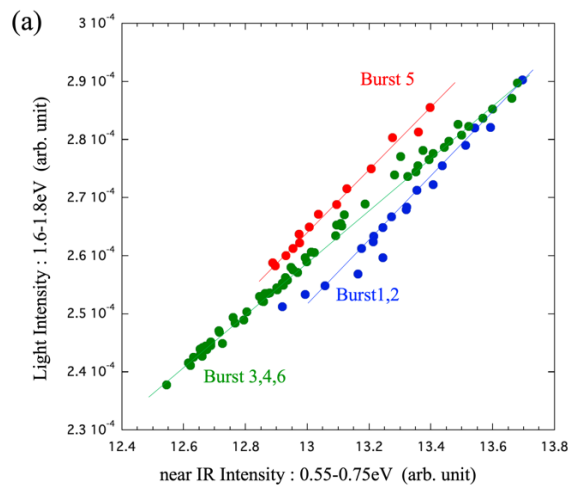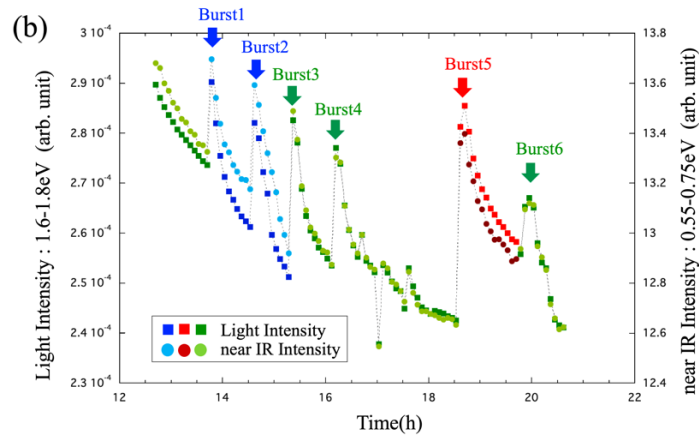
Fig.8 (a) Correlation between near-infrared light intensity and visible light intensity, (b) Time evolution Light & near IR Intensity time evolution of Experiment 1

When another measurement was performed with the same sample as Experiment 2, similar results as in Experiment 1 were obtained as shown in Fig. 9. The orange line is the heater temperature, the green line is the mid-infrared light intensity, the blue square is the visible light intensity integrated from 1.6 eV to 1.8 eV, and the red circle is the near-red from 0.55 eV to 0.75 eV. In Experiment 2, eight heat bursts occurred, and the intensity of mid-infrared, near-infrared, and visible light increased synchronously with the heat bursts. The correlation between the near-infrared light intensity and the visible light intensity shows, again, three lines, i.e., linear correlations as shown in Fig.10(a). Also, in Fig. 10(b), the bursts are grouped into three correlations colored by red, green, and blue, as seen in Fig. 8 for Experiment 1. One can say that the red line corresponds to 7th burst, the green group to the 6th burst and the blue line to the rest.
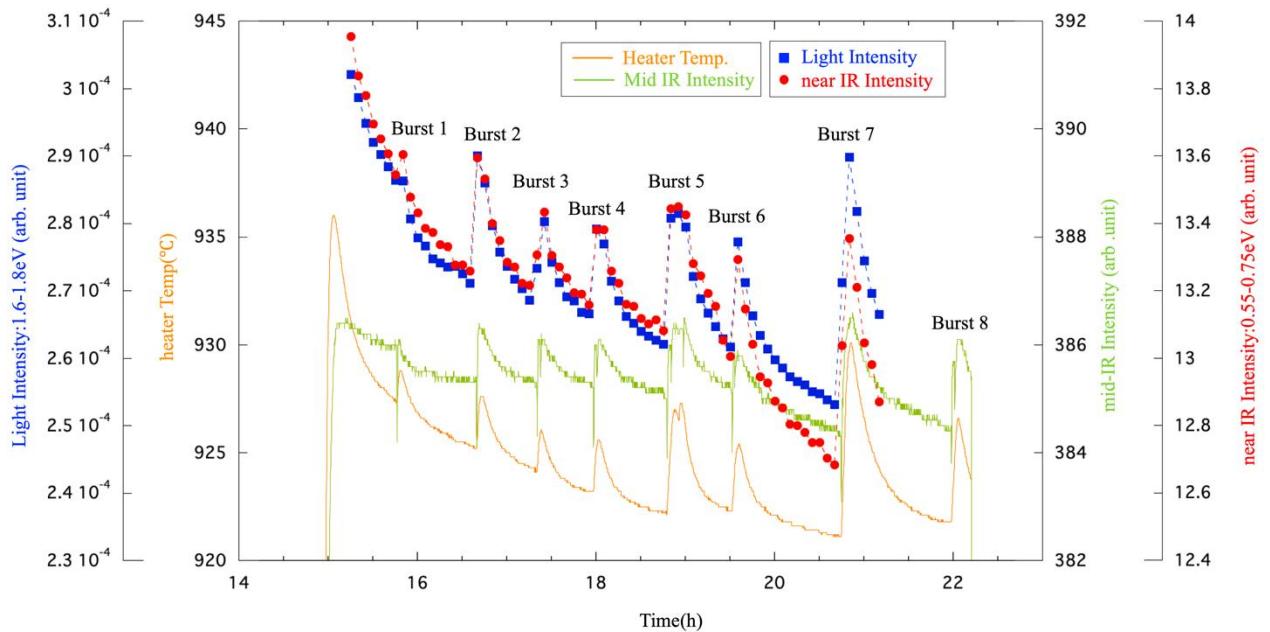
Fig.9 Time evolution of Heater temperature, mid-infrared intensity, heater input power, Light Intensity and near-IR intensity in Experiment2
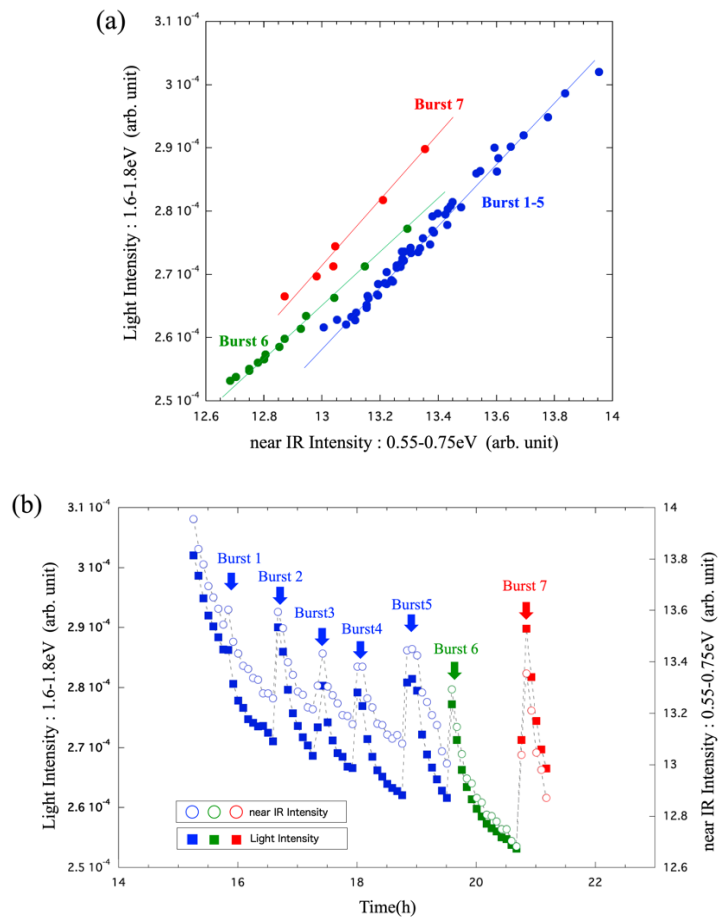
Fig.10 (a) Correlation between near-infrared light intensity and visible light intensity, (b) time evolution of Light Intensity and near-IR intensity in Experiment 2
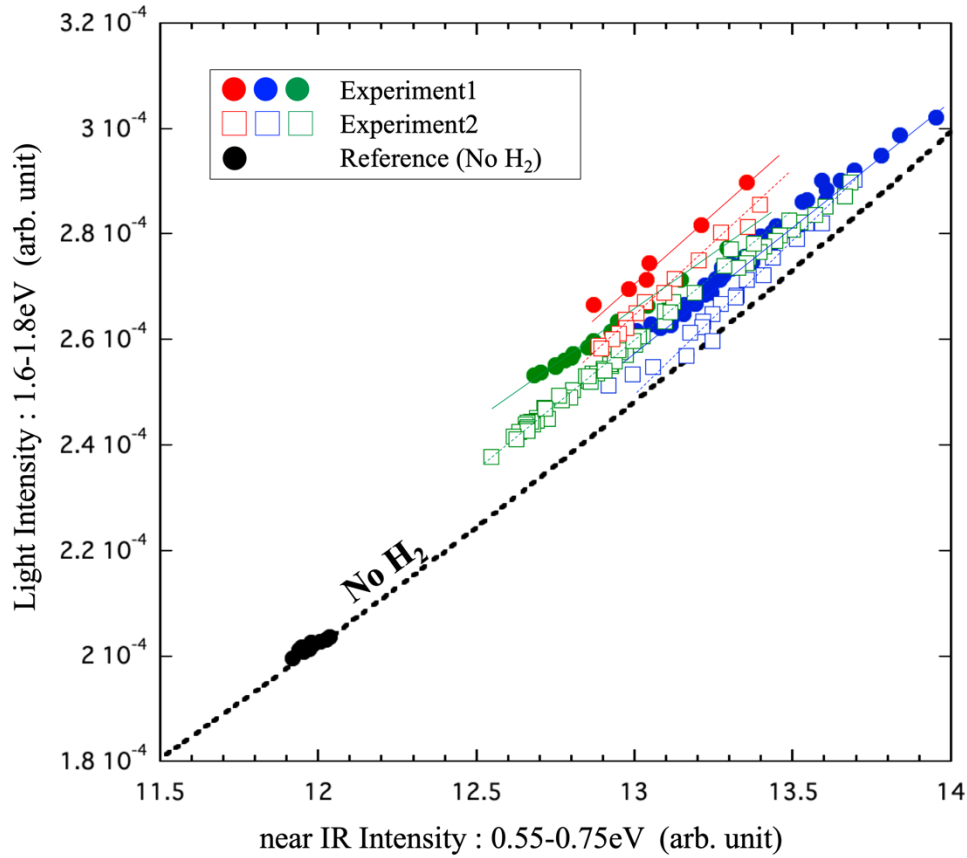
Fig.11 Correlation between near-infrared light intensity and visible light intensity
in Experiment1,2 and Reference Experiment

In Fig. 11, plotted are the correlation between the near-infrared and visible light intensities on the same graph. The circles and squares are the data of Experiments 1 and 2, respectively. As discussed above, they were grouped by the bursts classified with red, blue, and green colors. Fig.11 shows that the intensities of visible and infrared light are distributed in the same region in Experiments 1 and 2, although there are different dependencies for each burst.

In addition, also on the graph, data from the reference experiment without hydrogen absorption are plotted with the black circles. They were measured when the same heater input was applied as in Experiments 1 and 2. The black dashed line is a correlation line determined so as to reproduce the black data and extrapolated to larger region. Extrapolation to such larger values is a little risky. However, since the two minimum points in Experiment 2 are on the line, we infer that the correlation data should be distributed on the black line unless hydrogen absorption.

The following two points can be pointed out.

(1) Compared to the condition without hydrogen (heater Input is the same), both visible and near-infrared radiation intensities in Experiments 1 and 2 are increased. This is due to the fact that excess heat generation induces temperature rise of the sample surface.

(2) Compared to the correlation curve of the reference experiment (black dashed line), the correlation data of Experiments 1 and 2 are not on the curve but always larger for the visible light intensity. This indicates that the distribution of thermal radiation in the bursts is increased in the higher energy region than in the reference experiment.

In Fig. 12, the radiation spectrum measured during the heat burst was compared with the one regarded as the reference. For a spectrum during the heat burst, the one measurement at 20.93 h in Experiment 1 was chosen (we call Measurement 1) and, for a reference spectrum, the other at 14.95

h in Experiment 2 was chosen (we call Measurement 2). The reason for selecting the two measurements is the following. As shown in Fig. 12(a), the two measurements give almost equal radiant intensity in the near IR region, but the Light radiant intensity is deferent: one on the reference curve while the other maximum.

Fig.12(b) shows the thermal emission spectra of Measurement 1 and Measurement 2. Fig. 12(c) shows an expanded spectrum in the near-infrared region (0.5-0.8 eV), and Fig.12(d) shows an expanded spectrum in the visible region (1.6-2 eV). As can be seen in the figure, the two spectra are almost identical in the near-infrared region. On the other hand, in the visible light region, the spectrum of Measurement 1 is stronger than that of Measurement 2 over the entire measurement region. In other words, it can be inferred that in the burst, the radiation intensity on the high energy side is more enhanced in the thermal radiation distribution.
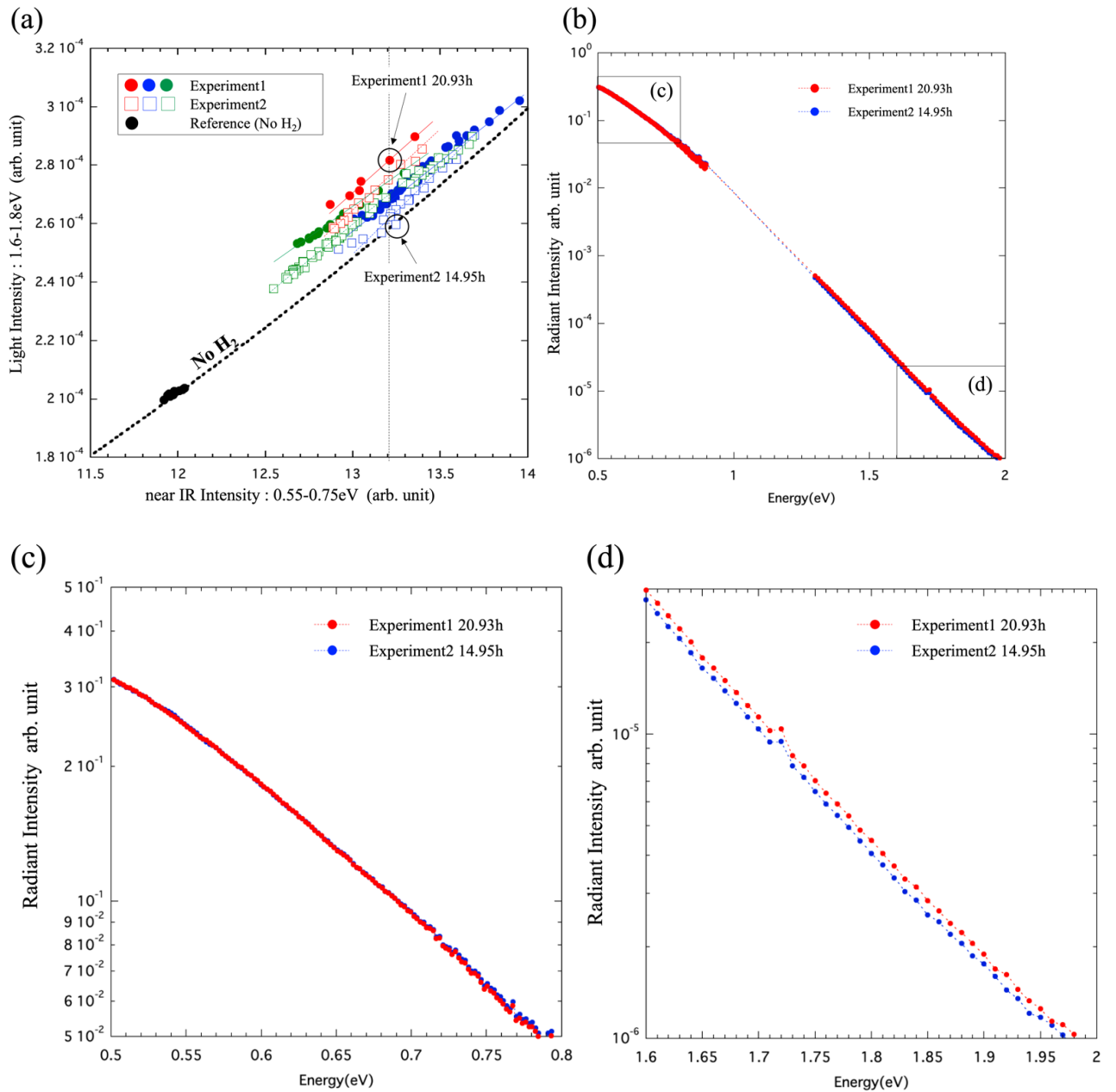
Fig.12 Comparison of optical spectrum Heat Burst (Measurement 1; time 20.93h in Experiment 1) and Normal heating (Measurement 2; time 14.95h in Experiment 2)

The above observations of thermal radiation during the burst revealed the following.
(1) During the burst, the overall intensity of radiation increases over the mid-infrared to near-infrared and visible light regions.
(2) The correlation between the intensity of visible and near-infrared light, which is related to the distribution of thermal radiation, is different for each burst.
(3) During the burst, the high-energy part of the radiation is enhanced over the reference.

This distribution of optical radiation is considered to be related to the reaction mechanism (hot spot, etc.) and will be analyzed in detail in the future. Further, we are planning to expand the measurement energy range and observe the radiation distribution over a wide range.

4. Conclusion

We have been studying the phenomenon of anomalous heat generation using hydrogen and nano-sized metal multilayer films. In addition to the heater temperature, we measure the amount of heat emitted from the surface of the sample. We have assembled an optical system to measure photon radiation for a wide energy region. Using this measurement system, simultaneous detection of light radiation was performed when heat bursts occurred.

When heat bursts occur, the emission of these lights increases in synchronization with the heater temperature and increases in the entire region from mid-infrared to visible light. This suggests that the sample has a sudden energy generation, which increases radiation power as well as the surface temperature, resulting in a rise of the heater temperature.

The correlation between visible light intensity and near-infrared light intensity during heat bursts revealed different dependencies for each burst. This suggests that the reaction state (elementary reaction, reaction area, hotspot size etc.) may be different for each burst. The distribution of thermal radiation in a burst has a distribution that increases in the high-energy side compared to the reference distribution. In the future, we will expand the measurement range of emitted light and perform more detailed analysis.

References

[1] T. Itoh, et.al., J. Condensed Matter Nucl. Sci. 24 (2017) 179–190.
[2] Y. Iwamura, et.al., J. Condensed Matter Nucl. Sci. 33 (2020) 1–13.
[3] Y. Iwamura, et.al, J. Condensed Matter Nucl. Sci. 36 (2022) 285–301
[4] T. Itoh et al., Proceedings of the 21st Japan CF Research Society, JCF21, p.15-25.
[5] T. Itoh et.al, J. Condensed Matter Nucl. Sci. 36 (2022) 274–284
[6] J. Kasagi, Abstract of ICCF22 8-13 Sep,2019 Assisi Italy p.10

Replication experiments on nuclear transmutation induced by deuterium permeation through Pd/CaO multilayer film

Shunji Tsuji-Iio

Tokyo Institute of Technology

e-mail: shnjiio@gmail.com

Abstract The nuclear transmutation by deuterium permeation through a Pd/CaO multilayer film was tested by elemental analysis employing TOF-SIMS and EDX. The transmutation from ^{133}Cs to ^{141}Pr was observed even when deposited Cs and Pd/CaO multilayers were placed at the pumping side. We newly found two other transmutations, ^{136}Ba to ^{140}Ce and ^{104}P to ^{112}Sn. These products through nuclear transmutations have magic numbers of nucleon of 82 or 50.

Key word: nuclear transmutation, D_2 gas permeation, CaO/Pd multilayer film, magic number of nucleon, elemental analysis, TOF-SIMS, EDX, praseodymium, cerium, tin

1. Introduction

The nuclear transmutation from Cs to Pr induced by deuterium permeation through a Pd/CaO multilayer film has been reported [1]. The transmutation has been confirmed by other groups and the amount of Pr estimated from ICP-MS was found to be roughly proportional to permeated D_2 gas volume [2]. We conducted its replication experiments employing RF sputtering to form Pd/CaO multilayer films and Cs was deposited on the surface by an electro-chemical method. We tested the other transmutations such as Ba to Sm claimed by the Iwamura group. During this process we found other nuclear transmutations by deuterium permeation through Pd/CaO multilayer films.

2. Experimental arrangement

Substrates of Pd (purity: 99.99%) with a thickness of 0.1 mm and area of 25 x 25 mm^2 were obtained from Tanaka Kikinzoku Kogyo. No pretreatments such as annealing at high temperature nor washing with aqua regia to remove impurities on the surface t as employed by the Iwamura group were applied since we had no chemical equipment for them. The surface was just wiped with ethanol and then alternating CaO and Pd layers were deposited on a Pd film by RF sputtering with Ar gas. The thicknesses of CaO and Pd were controlled by sputtering durations to be around 2 nm and 18 nm, respectively, except the final Pd layer with about 40 nm to duplicate the Iwamura experiments. Cs or

other atoms were deposited on the surface by an electro-chemical method. D_2 gas bellow 130 kPa down to around 80 kPa was permeated for several days keeping the film temperature around 100°C to 140°C. Figure 1 shows the time variations of the D_2 gas pressure of a gas vessel and a gas reservoir with volumes of 20 L each in the upper stream side of a Pd/CaO multilayer film. The permeated amount of D_2 gas is evaluated by the change in the pressure times the total volume of 40 L. The real time flow rate was monitored with a flow meter in between the gas vessel and the gas reservoir. An example photo of the multilayer film after D_2 gas permeation is shown in Fig. 2. Seven circular dips were made on the film surface since seven holes behind them were used to pump D_2 gas with a scroll pump. The temperature of a multilayer film was measured with a thermocouple screwed to a S.S. fitting to fix the multilayer film on a flange for pumping with a Viton O-ring.

Elemental analysis was made utilizing TOF-SIMS (Time of Flight Secondary Ion Mass Spectroscopy) with a mass resolution of 11,000@29u (FWHM) and EDX (Energy Dispersive X-ray Spectroscopy) with an energy resolution of about 10 eV by utilizing a semi-conductor detector cooled with liquid nitrogen.
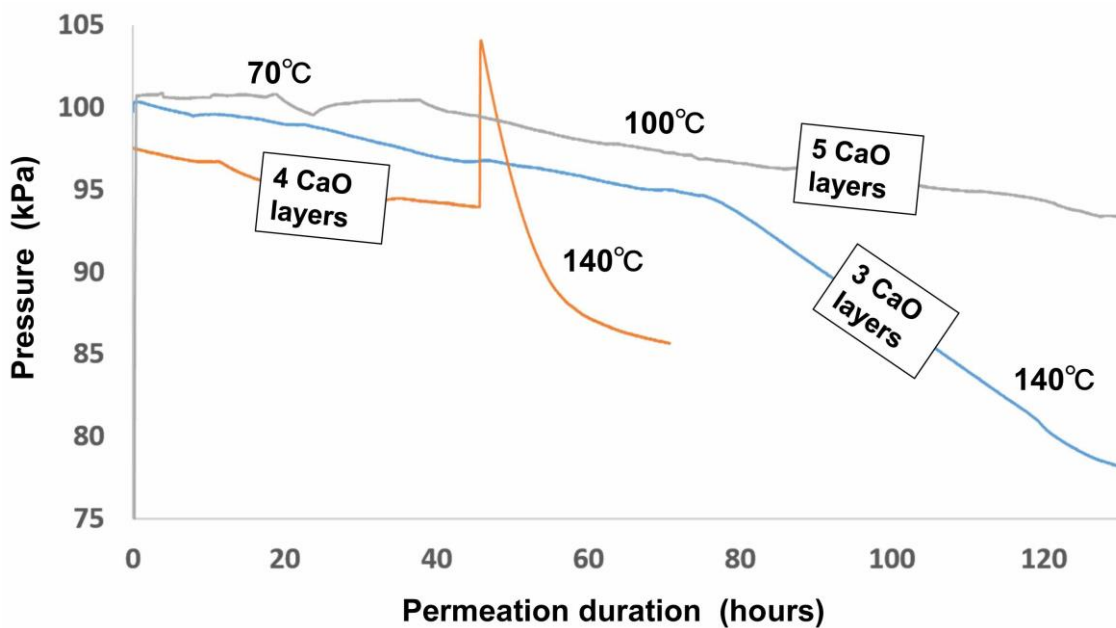
Fig. 1. The time evolutions of the D_2 gas pressure during permeations through three different numbers of CaO layers. By raising the temperature of Pd/CaO multilayer films, the pressure dropped faster which means the permeation rate
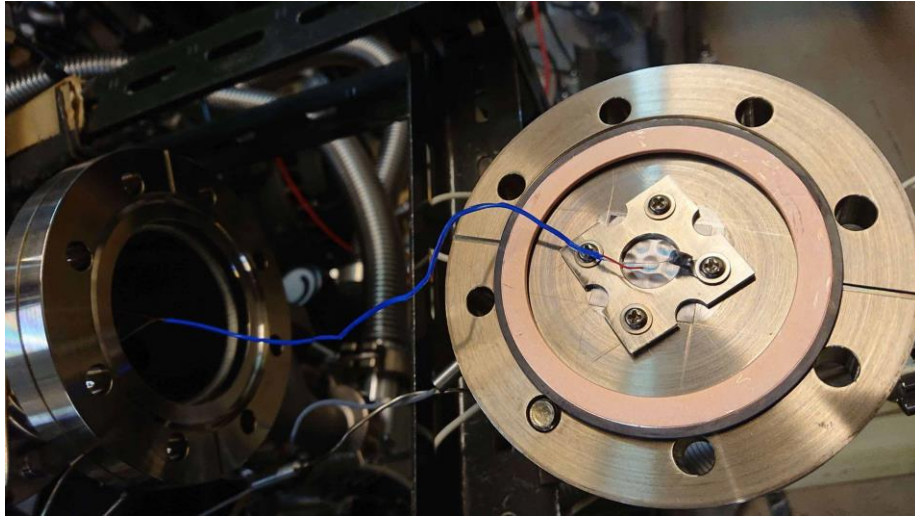
Fig. 2.   A photo of a Pd/CaO multilayer film fixed on the inner surface of a pumping flange taken after D_2 gas permeation. A blue electrical wire is used to monitor the film temperature with a thermocouple.

3. Results

We found the following points,

a) The number of CaO layers or its width are not important parameters, so that the presence of a CaO layer near the surface is a key to induce nuclear transmutation.

b) The nuclear transmutation from ^{133}Cs to ^{141}Pr was observed even when deposited Cs and Pd/CaO multilayers were placed at the down-stream, i.e., pumping side. The depth profiles of elements by TOF-SIMS are plotted in Fig. 3 in cases of two CaO layers. T Pr atoms were found to be distributed not only near the surface but also in CaO layers. It is interesting to note that points of statistically significant counts above one start to appear at the right hand-side, i.e., the upper stream side in the case that the Cs and CaO layers were in the down-stream side.

c) Although we could not confirm the existence of ^{149}Sm nor ^{150}Sm above background levels of counts by TOF-SIMS after D_2 permeation through electro-chemically deposited Ba on Pd/CaO multilayer films, we found ^{140}Ce presumably through nuclear reaction of ^{132}Ba + 4D with TOF-SIMS counts with about one order of magnitude higher compared with those of ^{141}Pr as shown in Fig. 4. Figure 5 is an X-ray spectrum obtained by EDX which includes clear characteristic X-ray peaks of Ce lines. A TOF-SIMS spectrum has a clear peak of ^{112}Sn beside a ^{40}Ca$_2$^{16}O$_2$ peak (Fig. 6).

d)
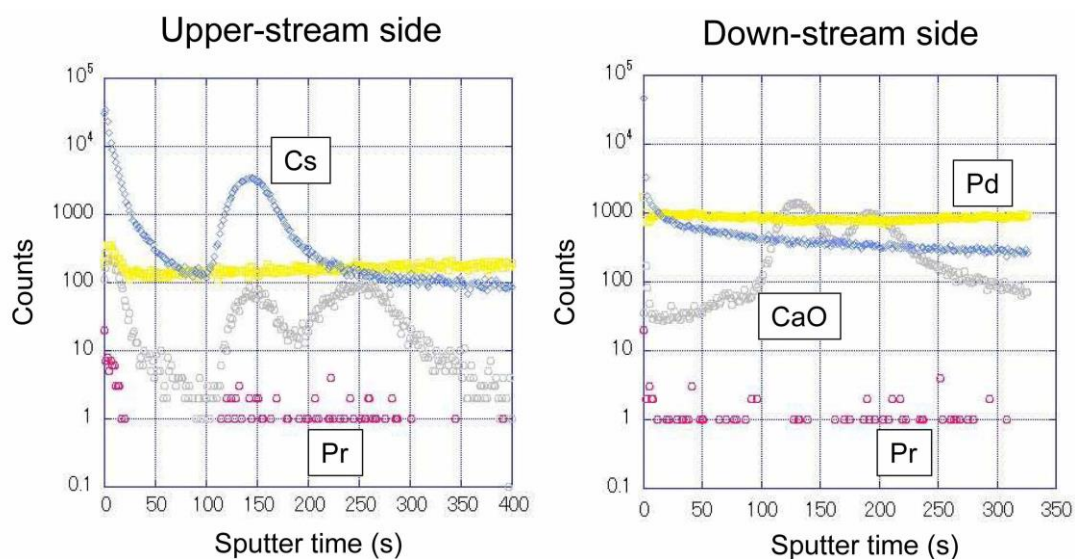
Fig. 3.　Depth profiles of elements and CaO molecules obtained by TOF-SIMS in two cases of films with two CaO layers and deposited Cs placed at the upper or down stream side. The Cs profile in the left-hand side shows that Cs atoms had accumulated in the first CaO layer.
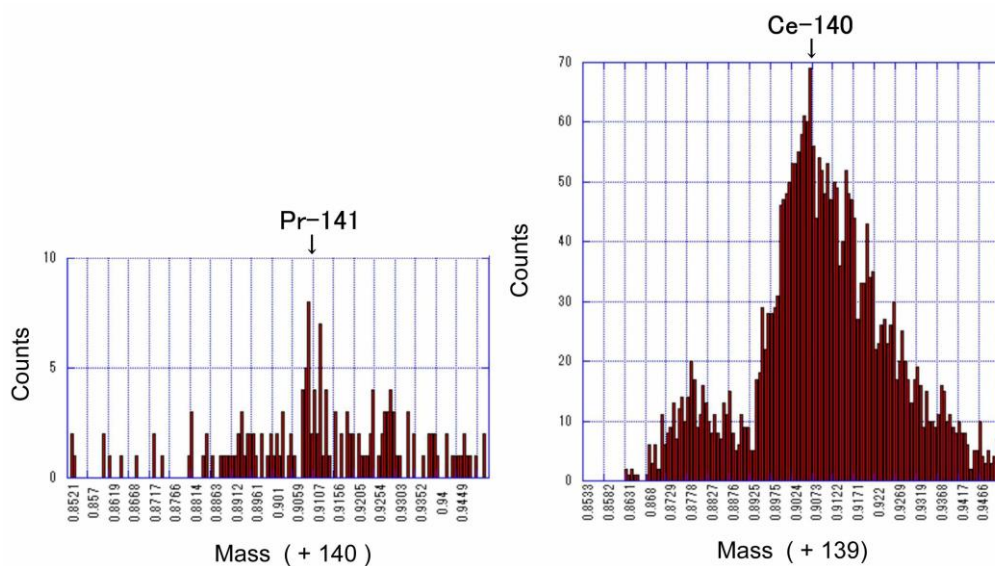
Fig. 4.　Typical mass spectrum of ^{141}Pr and ^{140}Ce obtained by TOF-SIMS.

e)　Pr and sometimes Sn characteristic X-ray lines were detected just above background

levels as in Fig. 7 after D_2 permeation through a Cs deposited Pd/CaO multilayer film.

f) Although γ rays were always monitored with a spatial radiation dose meter placed near to the pumping flange with a Pd/CaO multilayer film in an integration mode during D_2 permeation, γ rays above background levels were never detected.

g) In addition to the misidentification of $^{40}Ca_2O$ as ^{96}Mo made by Iwamura *et al*., which has been revealed by detailed TOF-SIMS analysis [3], we could not confirm ^{137}Ba to ^{149}Sm nor ^{138}Ba to ^{150}Sm, ^{137}Ba had not been enriched beforehand in contrast to the reported case [4] though. D_2 gas permeation through a Pd/CaO multilayer film with W deposited by RF sputtering did not produce elements with masses just below 190 such as ^{190}Pt or ^{190}Os claimed by Iwamura *et al*. [5], neither.

X-ray energy (keV)
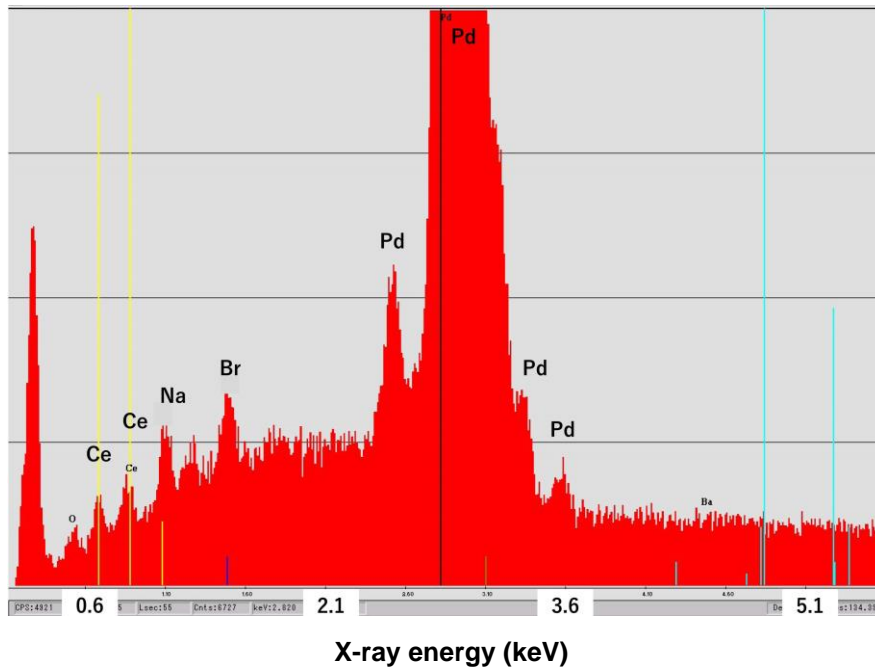
Fig. 5. X-ray spectrum obtained by EDX which has clear Ce peaks.
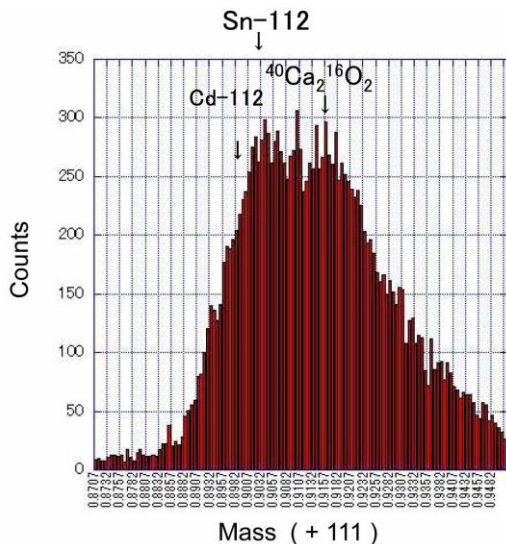
Fig. 6. Mass spectrum just below 112 which shows ^{112}Sn and $^{40}Ca_2^{16}O_2$ peaks.
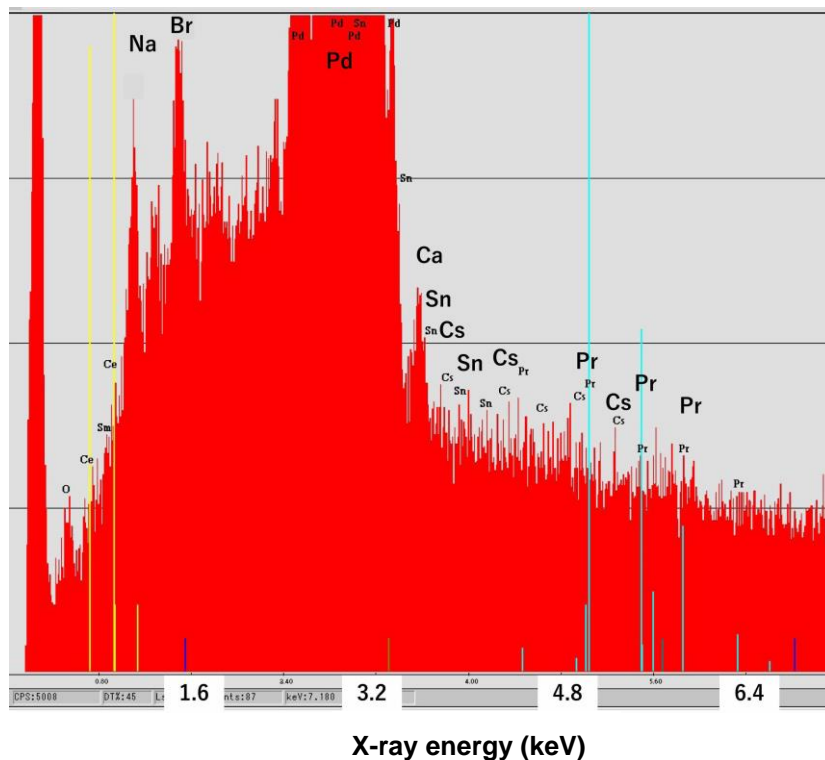
Fig. 7.   X-ray spectrum obtained by EDX which includes subtle Cs and Pr peaks. Blue vertical lines indicate the location of characteristic X ray's lines of Pr.

h) Although ^{44}Ca atoms were always present in a multilayer film, the count of ^{48}Ti of TOF-SIMS had never been above ground levels. A peak of ^{32}S^{16}O might be misidentified as ^{48}Ti peak.

4.   Discussion

Nuclear transmutations to ^{141}Pr or ^{140}Ce can be interpreted to be possible since the numbers of neutrons in the nuclei are both 82, which is one of the magic numbers of neutrons. The number of protons in Sn is also another magic number of 50. ^{112}Sn is presumably generated as a product of ^{104}Pd and four deutrons. Although ^{104}Pd atoms are always present with a natural abundance of 11.1% among Pd isotopes in multilayer films, ^{112}Sn was not always detected with significant counts by TOF-SIMS. From these observations, the nuclear transmutations appear to occur easily by D$_2$ permeation

through a Pd/CaO multilayer film in the order of ^{136}Ba + 2D → ^{140}Ce, ^{133}Cs + 4D → ^{141}Pr and ^{104}Pd + 4D → ^{112}Sn.

The presence of Pr even when Cs and Pd/CaO multilayers were placed in the pumping side, we can exclude a speculation that the density of deuterium atoms enhanced in the upper side of a CaO layer might be a key to the nuclear transmutation.

Based on the hypothesis that nuclei which have a magic number of neutrons can be products of nuclear transmutation by D_2 permeation, we tested the following reactions; ^{86}Sr + 2D → ^{90}Zr, ^{87}Sr + D → ^{89}Y, ^{84}Sr + 4D → ^{92}Mo and ^{86}Sr + 2D → ^{90}Zr. As a result, none of them were experimentally confirmed by TOF-SIMS, each reaction was tested once by D_2 permeation for several days though.

None of another set of nuclear transmutations which produce nuclei with magic numbers of protons such as ^{46}Ti + 6D → ^{58}Ni, ^{48}Ti + 6D → ^{60}Ni, ^{49}Ti + 6D → ^{61}Ni, ^{50}Ti + 6D → ^{62}Ni, ^{57}Fe + 2D → ^{61}Ni, ^{56}Fe + 2H → ^{58}Ni, ^{59}Co + D → ^{61}Ni, ^{59}Co + H → ^{60}Ni and ^{109}Fe + 3D → ^{115}Sn was experimentally confirmed neither.

The presence of ^{40}Ca^{44}CaF$_3$ at 140.9133 m/e may interfere the quantification of the amount of Pr at 140.9077 when mass analysis with low resolution such as a quadrupole mass spectrometer employed by Hioki *et al*. [2] since commercially available quadrupole mass spectrometers have mass resolutions of about 0.5.

5. Conclusions

Two nuclear transmutations of ^{136}Ba to ^{140}Ce and ^{104}Pd to ^{112}Sn by D_2 permeation through a Pd/CaO multilayer film at temperatures below about 140°C were newly found by TOF-SIMS and EDX analysis. Including the nuclear transmutation of ^{133}Cs to ^{141}Pr, ganma rays above background levels were never detected during D_2 permeation. The number of CaO layers and its width were demonstrated to be not important parameters for the nuclear transmutations. The magic numbers of nucleon were found to be related to the products of nuclear transmutation by D_2 permeation.

References
1) Y. Iwamura, M. Sakano and T. Itoh, Jpn. J. Appl. Phys. 41 (2002) 4642-4650.

2) T. Hioki, N. Takahashi, S. Kosaka *et al*., Jpn. J. Appl. Phys. 52 (2013) 107301.

3) A. Murase, N. Takahashi, S. Hibi *et al*., J. Condensed Nucl. Sci., 6 (2012) 34-43.

4) Y. Iwamura, T. Itoh, M. Sakano *et al*., Proc. ICCF11 (2004).

5) Y. Iwamura, T. Itoh and S. Tsuruga, Current. Sci., 108 (2015) 628-632.

Rising Characteristics of MHE Power with CNZ Material

Akito Takahashi[1], Masahiko Hasegawa[1], Yutaka Mori[1], Yuichi Furuyama[2], Tomoya Yamauchi[2] , Masato Kanasaki2

[1] Technova Inc., 100-0011 Japan,
[2] Graduate School of Maritime Sciences, Kobe University, 658-0022 Japan

E-mail: hagegawa@technova.co.jp

Our R&D aim is to increase and continue longer the excess thermal power (Wex) by the anomalous heat effect (AHE) aka cold fusion, through clarifying the mechanism of MHE (nano-metal hydrogen energy) reaction1-4).

In the previous reports2, 4), we reported that the close correlation between AHE power level and the loading ratio of hydrogen (H/Ni) in the reaction material is the key condition. After exceeding the turning point of H/Ni=1.0 (nominal value), Wex was started to increase steeply, and a few days later it started to decrease at the near full H/Ni loading ratio (H/Ni>>1.0) which was dependent on condition of the MHE sample-material under elevated temperature. The characteristics of H/Ni evolution shows that the absorption of hydrogen on the T-sites from the O-sites in the FCC lattice of Ni nano-islands in the MHE sample-material under elevated temperature over 300 degree C is important factor for the AHE excess thermal power generation in enhanced level as 200W/kg-sample.

Existence of two types of MHE reaction sites in the MHE sample-material was of conclusion. The first one is the coupling quantum mechanical motion of 4 protons plus 4 electrons from 4 O-sites to a central T-site3). These sites are the hydrogen absorption sites in the FCC lattice of nano scale island of Ni. The second one is on the SNHs2,3,4) on the surface of Cu-Ni nano-islands. The AHE power of high level (25-35W) is mainly dependent on the dynamic evolution of H/Ni ratio over 1.0 in MHE sample-material (in our previous case CNZ9s-r and CNZ9s-rr; Cu1Ni7/zirconia, 140-150g by repeated calcination). The conceived mechanism of MHE reaction is the dynamic condensation/collapse motion of 4H/TSC formed at around T-sites, by phonon excitation movement of 4 protons + 4 electrons of surrounding O-sites2,3). The largest Wex phase of MHE reactions (model is the 4H/TSC WS fusion3,4)) are taking place at around T-sites.

The whole MHE reactions are rather complex phenomena in the reactor. Hydrogen (H2) gas, which is existing in/around the sample material as fuel substance for the MHE reaction, is changing from gas molecule to hydrogen atom at the SNHs and absorbed in O-sites and finally absorbed in T-sites in the Ni lattice. These processes exceed with several endothermic and exothermic reactions through the absorption of hydrogen and desorption in their chemical processes. Heat power by these chemical reactions are small enough to neglect, compared to our observed much higher Wex power level.

Several factors and methods are under investigation in our R&D to increase and prolonger Wex. This time, the beginning rise-up phase data after start of heating with latest CNZ9ss-rr and CNZ8ss-rr samples (see Appendix) are analysed about hydrogen absorption dynamics and starting dynamics of MHE reaction along with temperature rise-up, in order to investigate better condition of the MHE reaction enhancement. Relation of initial heat burst and following Wex plateau period is of interest.

Main conclusion is as follows. Optical phonon (harmonic oscillators of O-site protons) excitation for full occupation of protons at O-sites (H/Ni=1.0) enhances 4H/TSC formation QM probability at around T-sites. By controlling H/Ni = 1.0 + alpha (here alpha less than 2.0), we can control MHE thermal power level (hence 4H/TSC WS fusion rate).

References:

1) Yutaka Mori, Akito Takahashi, Masahiko Hasegawa, Joji Hachisuka, Yuichi Furuyama; New MHE Experiments by D-System, Proc. JCF-22 Meeting, 2022

2) Masahiko Hasegawa, Akito Takahashi, Yutaka Mori, et.al, Characteristics of Excess Thermal Power Generation in MHE Experiments by D System, Proc. JCF-22 Meeting, 2022

3) Akito Takahashi, Physics of Cold Fusion by TSC Theory, J. Condensed Matt. Nucl. Sci., 12, 191-198, 2013

4) Akito Takahashi, Masahiko Hasegawa, Yutaka Mori, Understanding of MHE Power Generation Patterns by TSC Theory, preprint to ICCF24 paper, submitted to JCMNS, 2022

(PDF) Understanding of MHE Power Generation Patterns by TSC Theory (researchgate.net)

Appendix: Some experimental raw data and TSC theory prediction
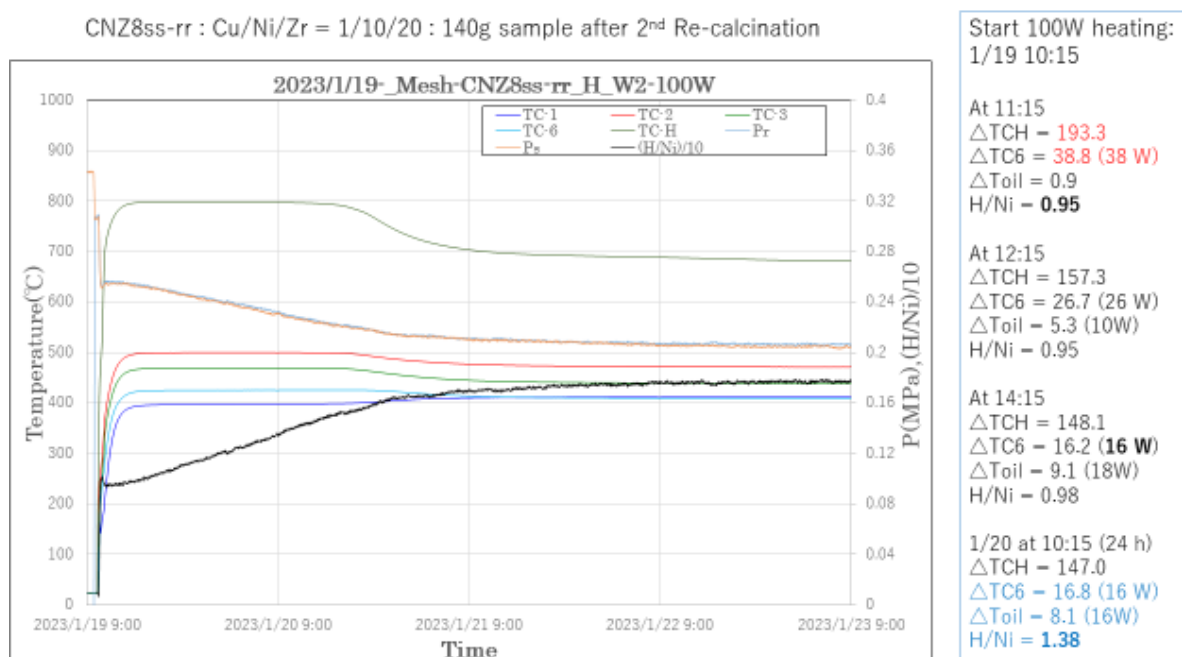

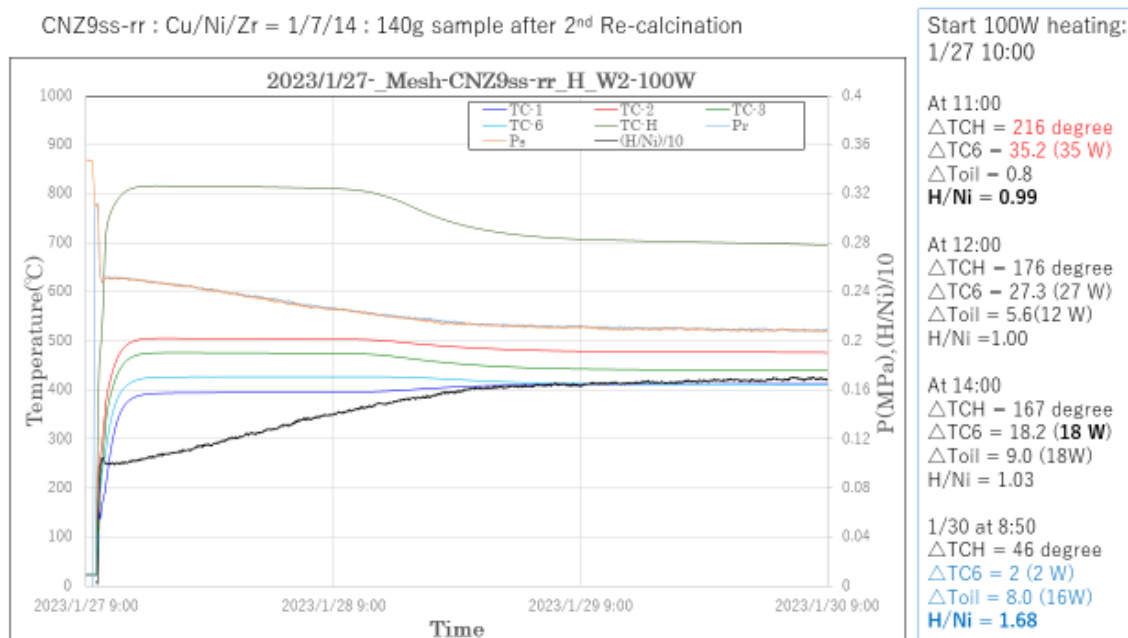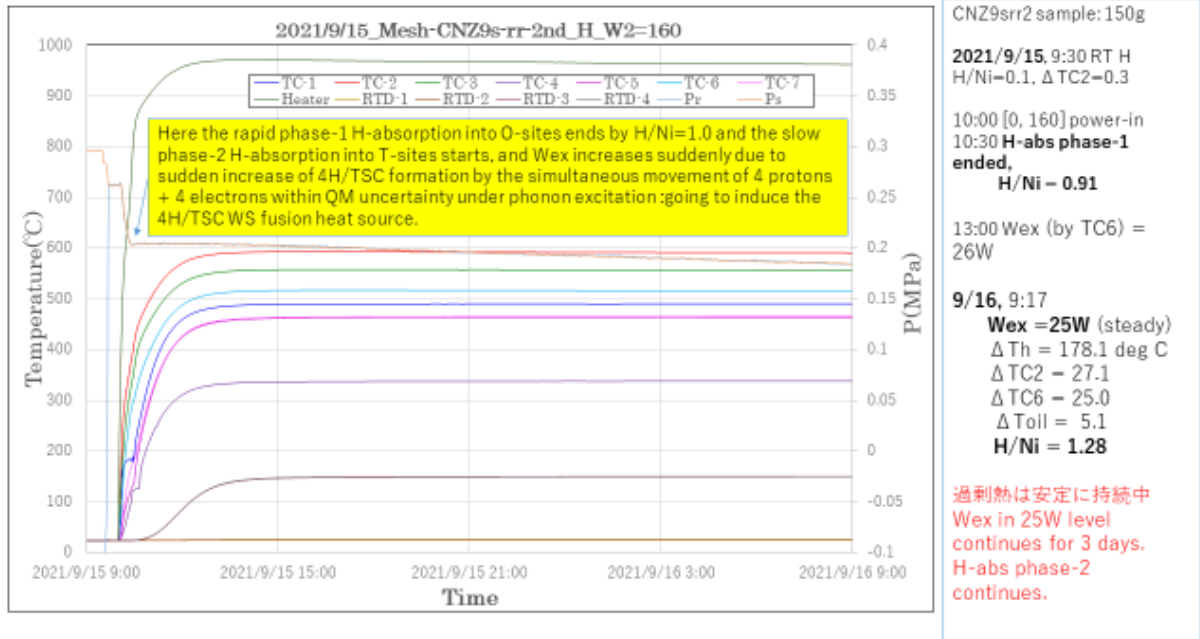Fig.1 Raw MHE data for CNZ8ss-rr 140g sample with mesh holder of D-system

Fig.2 Raw MHE data for CNZ9ss-rr 140g sample with mesh holder of D-system

△T values in the following are increased degree C from calibration blank run data.

△TCH or △Th: Temperature Increment at RC center

△TC6: Temperature Increment of H2 gas in RC, to be used for Wex estimation

△Toil: Temperature Increment at cooling oil outlet point, as heat collection (very long time constant due to large heat capacity of oil coolant system by radiation transfer)

H/Ni : Hydrogen loading ratio (0.4 *mol* Ni for two sample CNZ materials, respectively)

Calibration blank run was made using zirconia beads as dummy sample.

Fig.3 Raw MHE data for CNZ9s-rr 150g sample with mesh holder of D-system
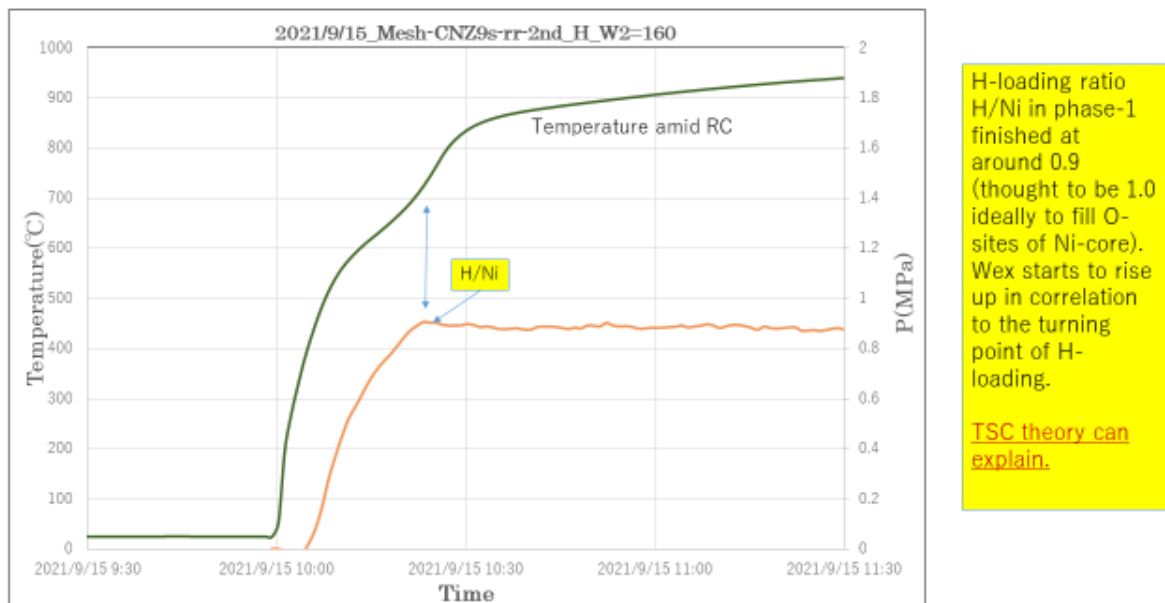
Fig.4 Typical rise-up correlation between excess power generation and H/Ni ratio
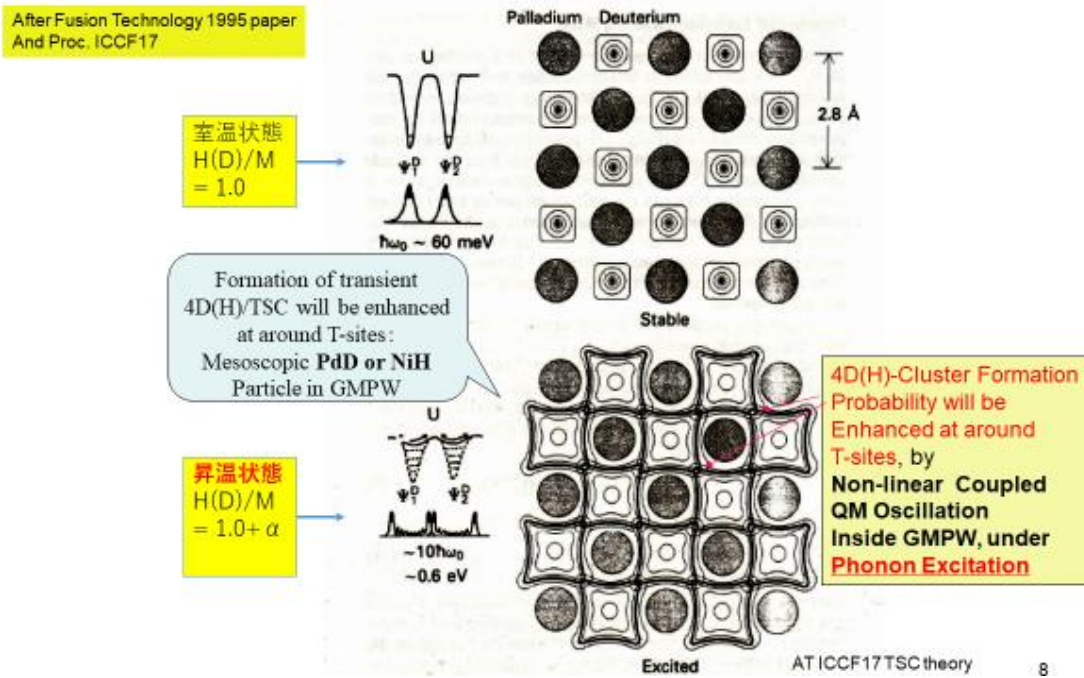
Slide-1: H/Ni loading ratio and 4H/TSC formation condition in Ni(or Pd)-core lattice
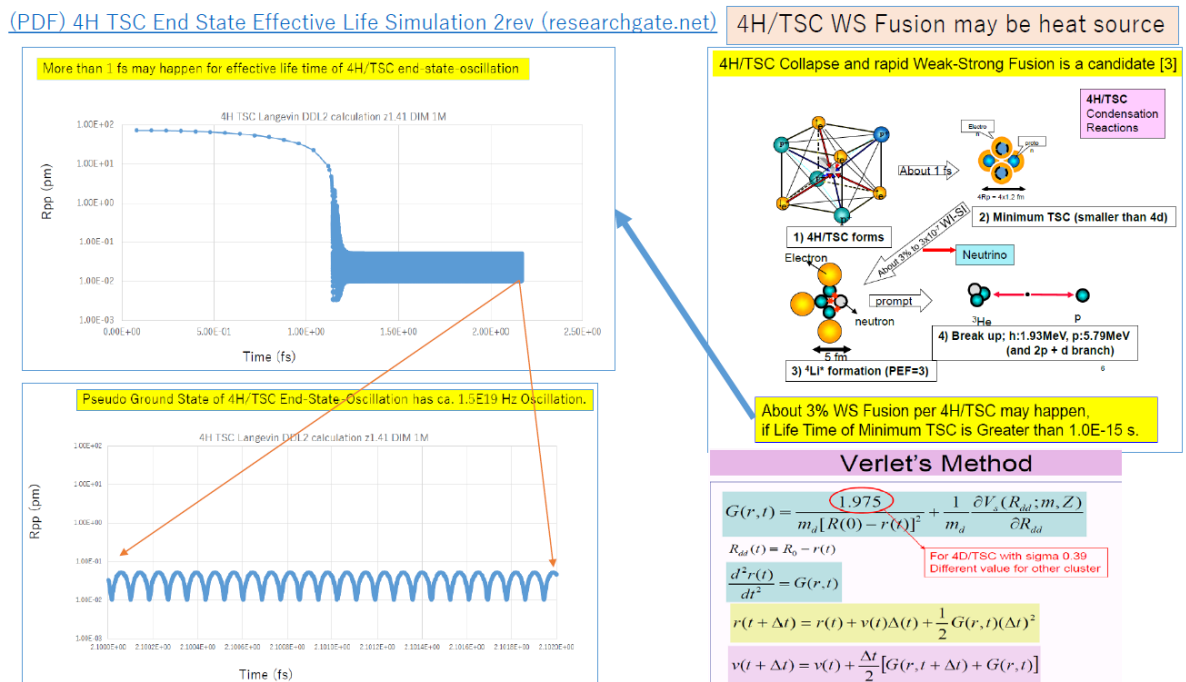
Slide-2: Model and simulation of 4H/TSC WS fusion
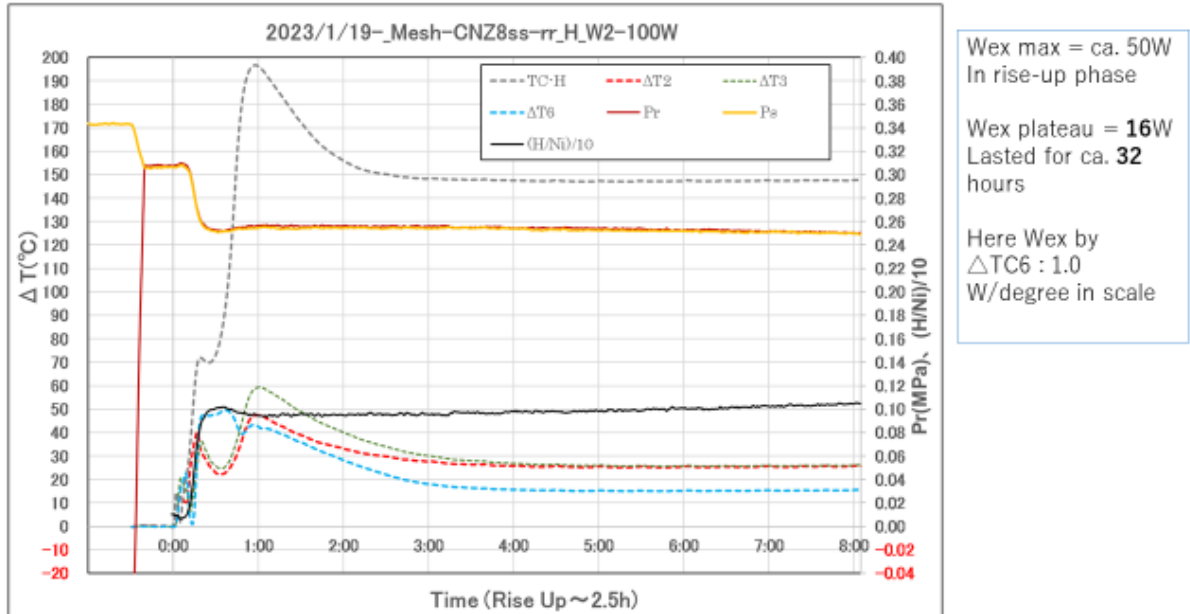
Fig.5: Evolution of AHE power (sky blue dot) in correlation with H/Ni ratio for CNZ8ss-rr
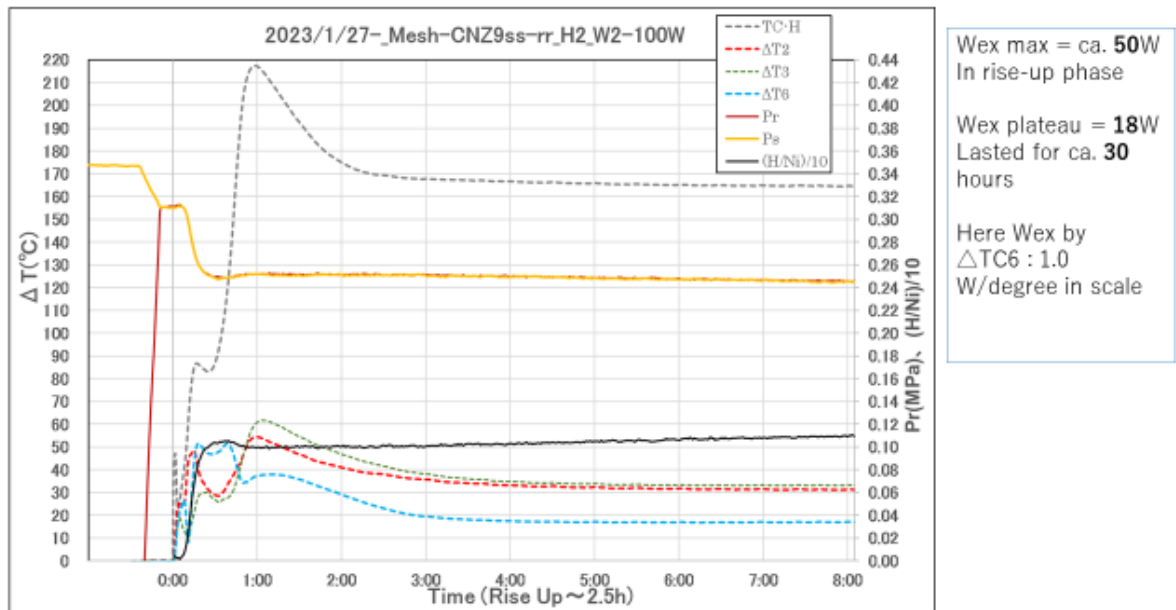
Fig.6: Evolution of AHE power (sky blue dot) in correlation with H/Ni ratio for CNZ9ss-rr
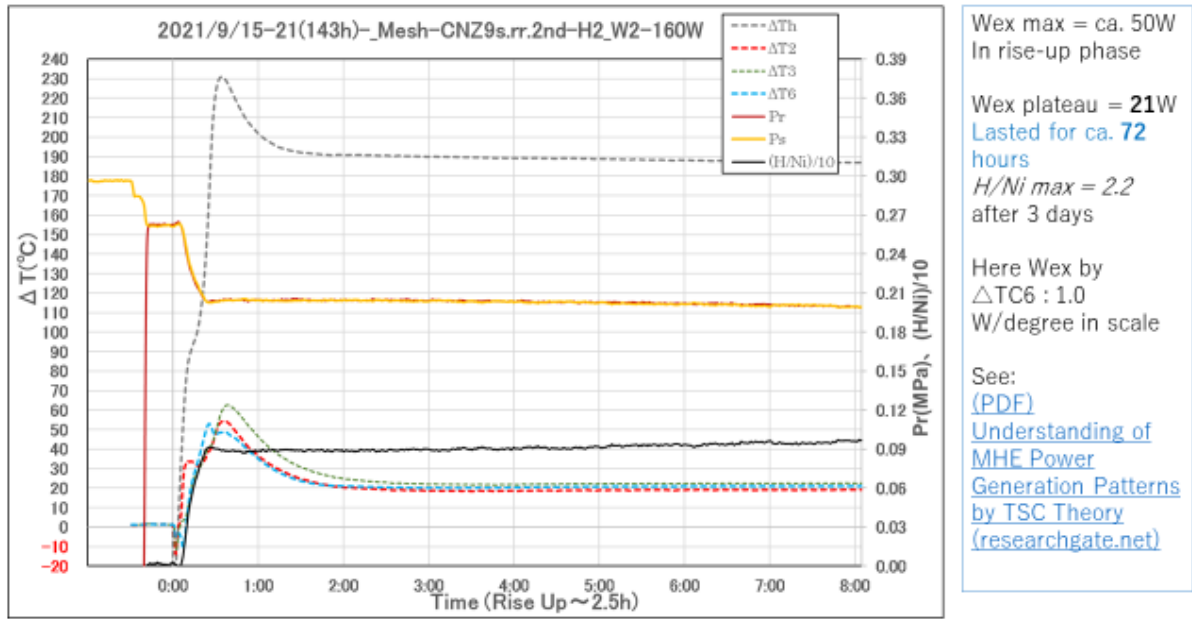
Fig.7: Evolution of AHE power (sky blue dot) in correlation with H/Ni ratio for CNZ9s-rr,
By increased W2 heating (160 W)

Heat generation of metal composite powder caused by the various pulse flow of hydrogen gas: Optimization of gas-jet nozzle length

Yuta Toba[1], Ken Naitoh[1], Tomotaka Kobayashi[1], Daiki Okada[1], Ryuki Nakagawa[1]
[1]Waseda University, Tokyo, Japan
E-mail: k-naito@waseda.jp

Abstract Anomalous heat generation in exposure of metal powder (Ni or Pd) to hydrogen (or deuterium) gas was observed in previous research. Anomalous effect in hydrogen (or deuterium) gas absorption by mixed oxides of Pd and Zr is also reported. In our previous report, we conducted experiments of anomalous heat generation (absorption of hydrogen gas by Pd-Ni-Zr composite powder) with the pulse flow of hydrogen gas generated by a solenoid valve using a small reaction chamber, while having gas-jet nozzle length from the solenoid valve to the small reaction chamber of 325 mm. In this report, we conducted experiments by extending gas-jet nozzle length, due to 2.5 times longer gas-jet nozzle length optimized (825 mm). Hydrogen gas is absorbed in about 530 K and 0.5 MPa by Pd-Ni-Zr composite powder with pulse flow. Then, about 60 K of temperature rise was observed for the longer gas-jet nozzle length, whereas being temperature rise of about 50 K without extending gas-jet nozzle length. The temperature rise increased by 16 % due to the 2.53 times longer gas-jet nozzle length.

1. Introduction

Anomalous heat generation in exposure of nickel or palladium powder to hydrogen or deuterium gas was observed in previous research [1,2]. Anomalous effect in hydrogen (or deuterium) gas absorption by mixed oxides of Pd and Zr is also reported [3, 10].

Our purpose is to develop a new energy generator using anomalous heat, which is accelerated by very high compression obtained by a collision of the high-speed multi-jets repeatedly [4-7]. Therefore, we focused on the heat generation during hydrogen gas absorption by metal composite powder at higher pressure conditions.

We have developed a reaction system with a small chamber and have conducted some fundamental experiments to evaluate the anomalous heat in the hydrogen gas absorption of metal powder. We have added two new important factors for increasing anomalous

heat, which are (1) supply speed of gas injected and (2) increase of upstream tank pressure of hydrogen gas injected.

(1) In our previous report, two valve opening speeds for hydrogen gas jets induced into the chamber were first tested, which were a very slow opening speed of about 180 seconds in case of the needle valve for considering safety and a fast opening of 20 microseconds in case of the solenoid valve. For the solenoid valve at about 0.8 MPa, we confirmed more temperature rise over 10 K [8]

(2) Next, as results at high gas tank pressure over 5 MPa with fast opening of the solenoid valve, hydrogen gas injection to Pd-Ni-Zr composite powder resulted in a temperature rise of over 100 K [9].

However, the period of 20 microseconds is not satisfactory, because we want to open the valve during less than 0.01 microseconds, which will bring a shocking impact of hydrogen gas to metal powder. As there are still no valves inducing shocking impact, we here use a principle of compressible supersonic fluid-dynamics, i.e., increase of gas-jet nozzle (pipe) length from the solenoid valve to the small reaction chamber.

It is well known that the special pressure gradient at the front of the hydrogen gas pulse flow by conventional solenoid valve is dull in comparison with shock wave as a discontinuous jump of physical quantities (Figure 1: right figure). After the dull pressure gradient runs to donwstream, shock wave can be obtained, if extending gas-jet nozzle length. The change of pressure gradient can be explained by considering wave travelling speed related to sound speed. Hydrogen gas upstream (left side) with relatively higher temperatures and pressures has a faster wave traveling speed related to sound speed. Thus, high temperature and pressure domain can catch up with hydrogen gas downstream (right side) with relatively lower temperatures and pressures (Figure 1: left figure). This fluid dynamics mechanism brings shock wave, i.e., a discontinuous jump of pressure and temperature within the mean free path level. [12].

This leads to more increase in anomalous heat generation (absorption of pulsed hydrogen gas by Pd-Ni-Zr composite powder [10]).
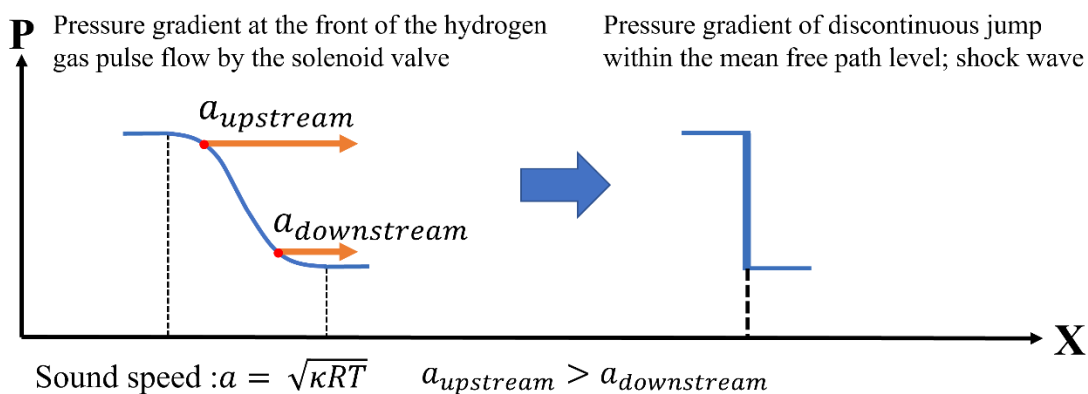
Figure 1. Image of the pressure gradient at the front of the pulse flow of hydrogen gas

2. Experimental devise

Figure 2-a shows the schematic of the reaction system, which is constructed of the reaction chamber, heater, K-type thermocouple, gas supply device, two pressure gauges, safety valve, solenoid valve, needle valve, three-way valve, and vacuum pump.

The reaction chamber having about 2 mL of volume, was made of stainless steel (SUS316L). The heater (GBSD-300, AS ONE CORPORATION) for preheating the reaction chamber can be heated in the range of 100 - 300 °C. The space between the heater and the reaction chamber was filled with glass beads. The K-type thermocouple (HTK0227, Hakko electric co., ltd.), whose tip was embedded in the sample, was used to measure the sample temperature. The gas supply device provided hydrogen gas (1.0 MPa maximum) while performing experiments. Two pressure gauges measured pressure of gas in the reaction chamber and pressure of provided gas. The safety valve (RAT2V-1000, IBS Inc.) was installed not to break down the reaction system, and the valve opens when the pressure in the reaction chamber exceeded 1.0 MPaG. In the experiments, the solenoid valve (valve opening speed: 20 microseconds) (Figure 2-b) made a pulse flow of hydrogen gas, and the needle valve (Figure 2-c) regulated its flow rate. The three-way valve was used for switching gas loading and evacuation. The scroll pump (ISP-250C, ANEST IWATA Corporation) was used for evacuation. The ultimate pressure (the lowest pressure that can be reached within a realistic evacuation time) of the vacuum pump was 1.6 Pa. Gas-jet nozzle length is that from the solenoid valve to the reaction chamber. In each experiment, the gas-jet nozzle length can be varied by changing the pipe length in the length change part (Green color in Fig. 2a).

Specifications of the reaction system are shown in Table 1.
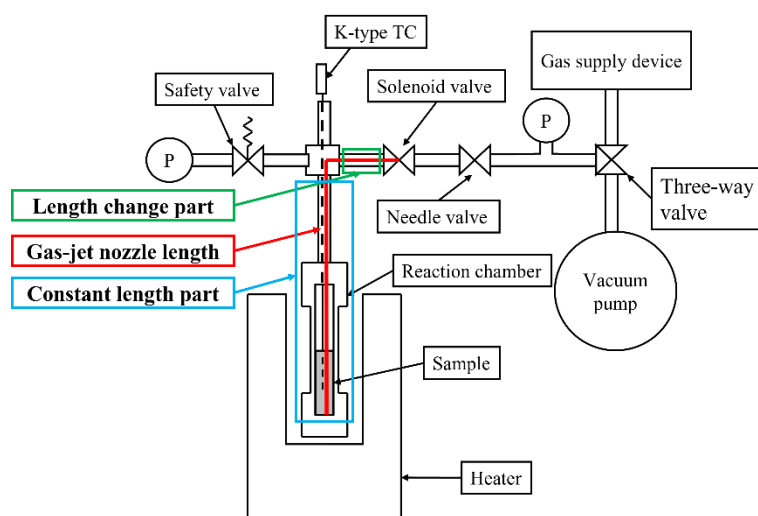
a) Schematic of the reaction system

b) Needle valve

c) Solenoid valve

Figure 2. The reaction system

Table 1. Specifications of the reaction system

|	
Material of reaction chamber	SUS316L
Volume of reaction chamber	2 mL
Maximum temperature of heater	300 °C
Maximum pressure of loading gas	1.0 MPa (5 MPa at experiment No. 5)
Cracking pressure of relief valve	1.0 MPaG
Ultimate pressure of vacuum pump	1.6 Pa
Gas-jet nozzle	ϕ 4.35

3. Metal powder sample employed and procedure of experiment

The experimental procedure is shown in Figure 3. First, the sample (Pd-Ni-Zr composite powder, designated PNZ10r [10]) was set in the reaction chamber. Then, the

reaction chamber was preheated with the heater. After that, the reaction chamber was evacuated with the vacuum pump. After the evacuation, hydrogen gas was loaded to the upstream side of the solenoid valve. After that, the solenoid valve opened, and the pulse flow of hydrogen gas was injected into the reaction chamber (Figure 4). The temperature rise of the sample was measured by the K-type thermocouple. At the end of the experiment, the reaction chamber was evacuated again not to leave the injected gas in the reaction chamber.
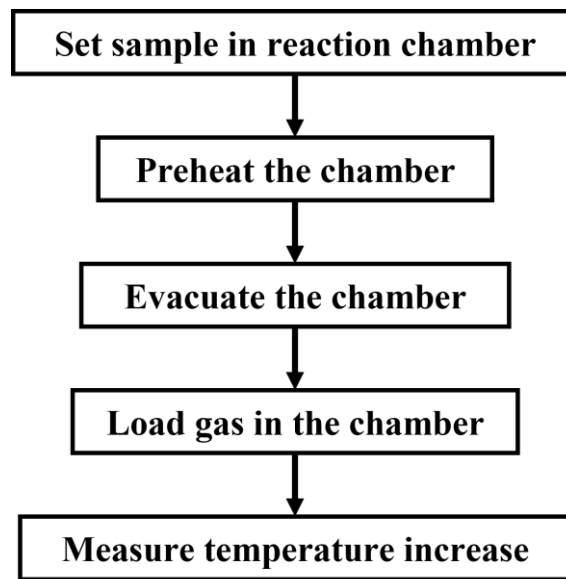
Figure 3. Experimental procedure
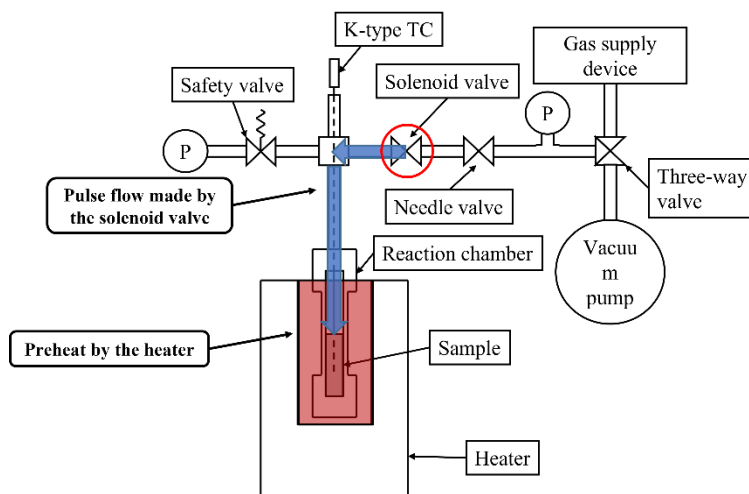
Figure 4. Image of an experimental procedure

4. Results and Discussion

Experimental conditions

Experimental conditions are shown in Table 2. In the experiments, Pd-Ni-Zr composite powder (PNZ10r, provided by Technova Inc. [10]) was used as a sample, and the average initial temperature was controlled at 260 °C. In each experiment, new samples were used. The experiments were conducted using hydrogen gas and the pressure of the loaded gas was 0.5 MPa. The experiments were conducted by varying the gas-jet nozzle length from 325 mm to 1325 mm (Figure 5).

Table 2. Experimental conditions

Sample	Pd-Ni-Zr composite powder [10]
Sample mass	3.0 g
Kind of gas	Hydrogen
Gas pressure	0.5 MPa
Initial temperature	260 °C
Gas-jet nozzle length	325 mm – 1325 mm
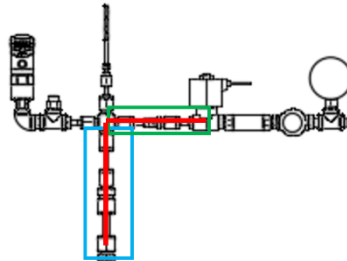
a) Gas-jet nozzle length: 325 mm
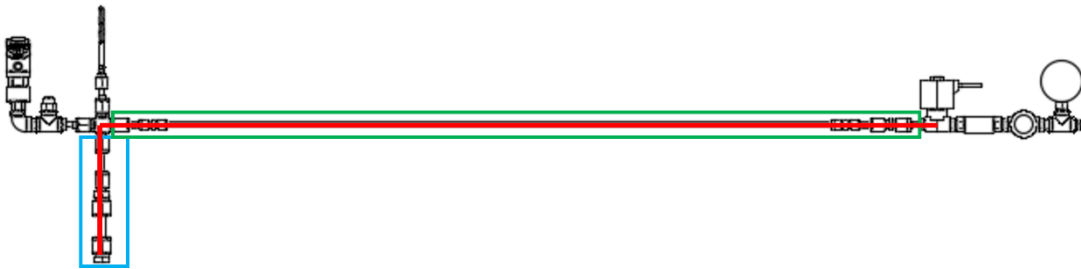
b) Gas-jet nozzle length: 1325 mm

Figure 5. Overview of the reaction system

Experimental results

Table 3 summarizes experimental conditions and results, while Figs. 6 to 10 show temperatures plotted against time for various gas-jet nozzle lengths. In each experiment,

the sample temperature rise begins just after the pulse flow of hydrogen gas is injected into the reaction chamber.

It is stressed that extension of gas-jet nozzle length from 325 mm to 825 mm brings increasing temperature rise, whereas more extension from 825 mm to 1325 mm results in depression of temperature rise.

Figure 8 shows the experimental result for gas-jet nozzle length of 825 mm, which indicates a temperature rise of 62.9 K, the highest temperature rise in this report, at 10 seconds after the beginning of the temperature rise. The estimated calorific value of heat generation are 87.0 J and 8.70 W. In estimation of calorific value, these three assumptions are considered.

1. The sample temperature was uniform during the experiment.
2. The sample absorbs all the generated heat.
3. Heat exchange with the outside during the experiment is not considered.

The calorific value is estimated by using Eqs. 1 and 2 derived from the above assumptions.

$$Q[J] = \Delta T_{max}[K] \times C_{sample}[J/K] \tag{1}$$
$$P[W] = Q[J]/t[s] \tag{2}$$

In Eqs. 1 and 2, Q and P denote generated heat and power respectively. ΔT_{max} denotes the amount of sample temperature increase in the experiment, C_{sample} $(= 1.38\,[J/K])$ denotes the heat capacity of the sample, and t denotes the time from the start of the experiments to the sample temperature becoming maximum.

Table 3. Experimental results

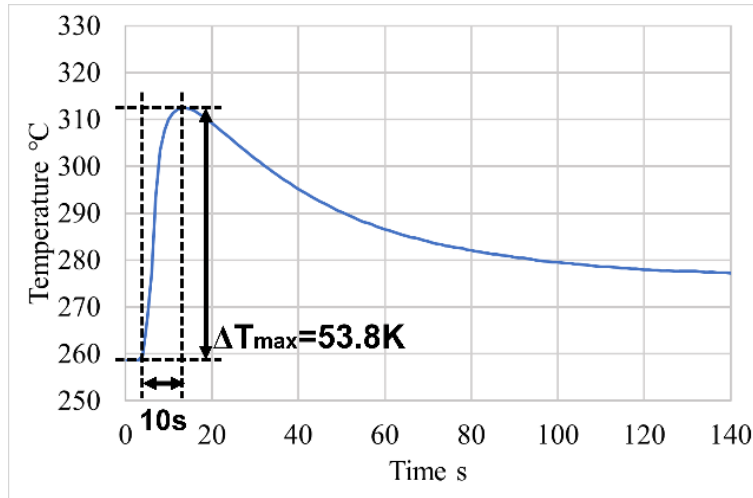| Gas-jet nozzle length	Sample	Gas pressure	Initial temp.	Temp rise
325 mm	Pd-Ni-Zr 3.0 g	0.5 MPa	258.7 °C	53.8 K
625 mm	Pd-Ni-Zr 3.0 g	0.5 MPa	256.1 °C	58.6 K
825 mm	Pd-Ni-Zr 3.0 g	0.5 MPa	257.1 °C	62.9 K
1025 mm	Pd-Ni-Zr 3.0 g	0.5 MPa	261.2 °C	49.8 K
1325 mm	Pd-Ni-Zr 3.0 g	0.5 MPa	257.7 °C	44.2 K

Figure 6. Results of the experiment (Gas-jet nozzle length: 325 mm)
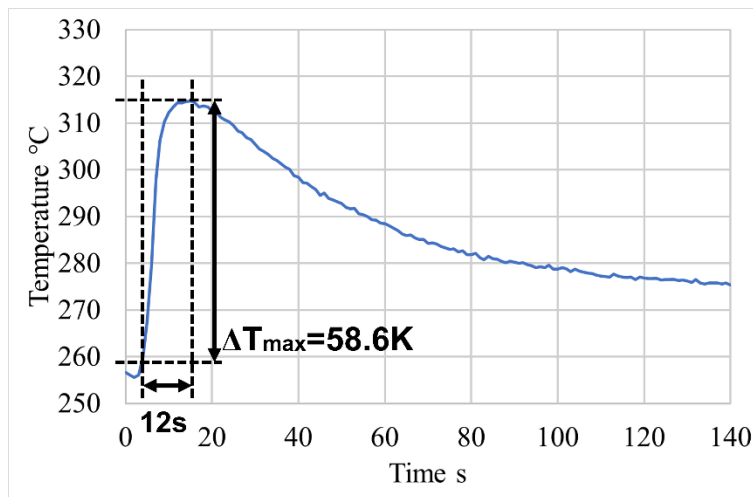

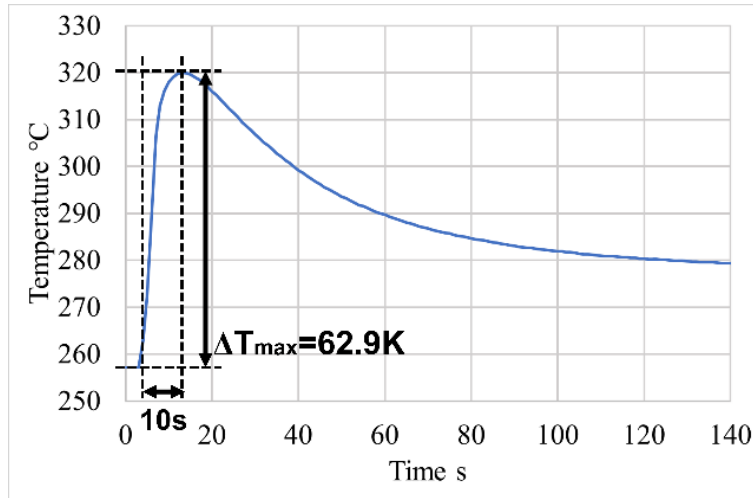Figure 7. Result of the experiment (Gas-jet nozzle length: 625 mm)

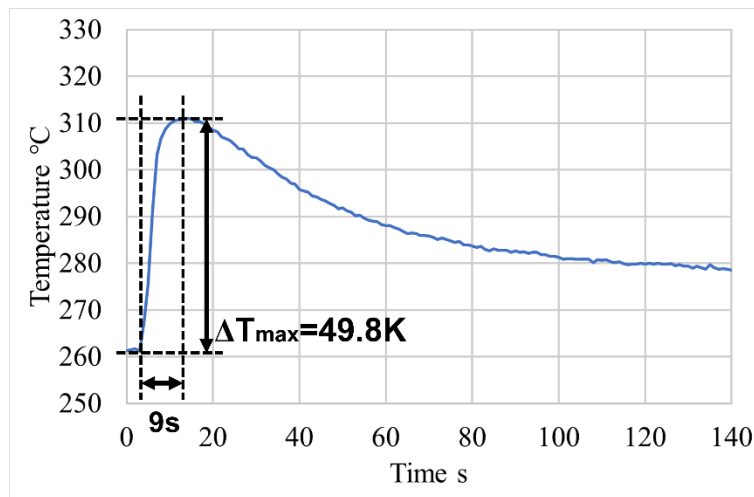Figure 8. Results of the experiment (Gas-jet nozzle length: 825 mm)

Figure 9. Result of the experiment (Gas-jet nozzle length: 1025 mm)
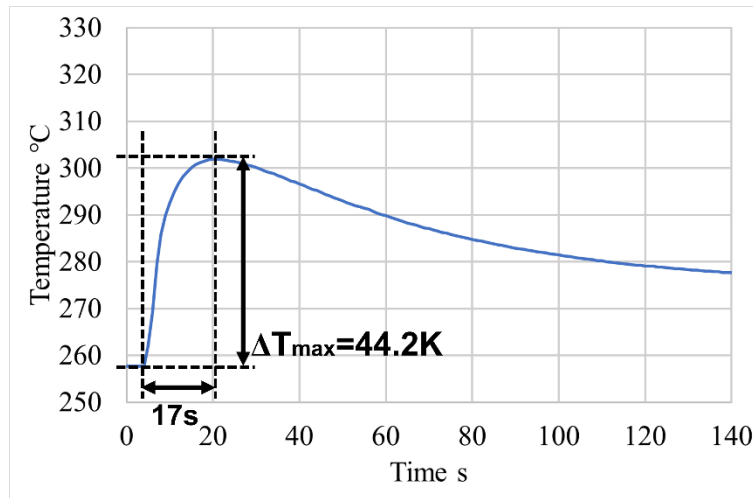
Figure 10. Result of the experiment (Gas-jet nozzle length: 1325 mm)

Effect of gas-jet nozzle lengths on the temperature rise

Figure 11 shows temperature rise of sample plotted against gas-jet nozzle length.

For gas-jet nozzle length extended from 325 mm to 825 mm, temperature rise increases according to longer gas-jet nozzle length. This increase of temperature rise can be explained by the fluid-dynamical mechanism that dull pressure gradient at the front of hydrogen gas jet pulse becomes that of shock wave, as we write in the section of introduction with Fig. 1.

Next, for gas-jet nozzle lengths extended from 825 mm to 1325 mm, temperature rise decreases. This decrease in temperature rise will occur because of dissipation due to viscosity of gas, i.e., attenuation of pressure gradient by overextending gas-jet nozzle length.
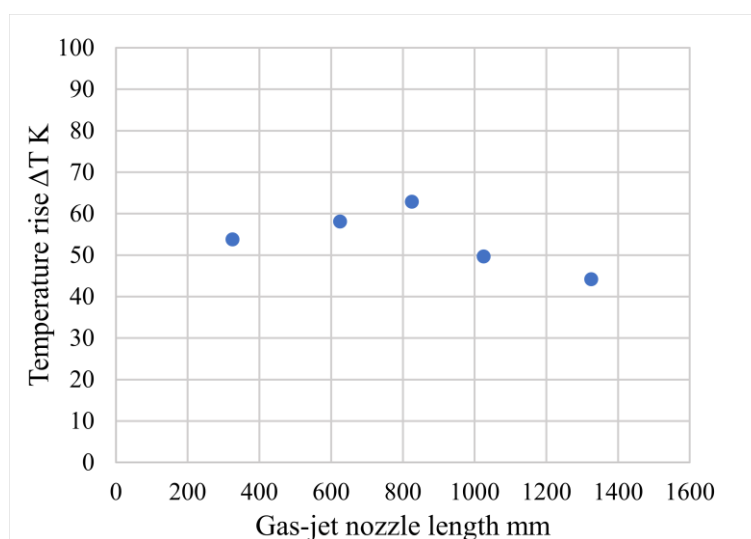

Figure 11. Temperature rise plotted against gas-jet nozzle length

Conclusion

Experiments of anomalous heat generation due to absorption of pulsed hydrogen gas to Pd-Ni-Zr composite powder were conducted while varying gas-jet nozzle length from solenoid valve to small reaction chamber.

For gas-jet nozzle length of 825 mm, 62.9 K of temperature rise was observed as maximum, with calorific values of 87.0 J and 8.70 W, whereas about 50 K of temperature rise for gas-jet nozzle length of 325 mm and also 44.2 K of temperature rise for more extending gas-jet nozzle length of 1325 mm. These results suggested that anomalous heat generation (due to absorption of hydrogen gas by Pd-Ni-Zr composite powder) can be accelerated by optimizing gas-jet nozzle length.

Acknowledgment

References

[1] Y. Iwamura et al., "Anomalous Heat Effects Induced by Metal Nano-composites and Hydrogen Gas", *J. Condensed Matter Nucl. Sci.* 29, 119-128, 2019.

[2] Y. Arata and Y. Zhang, "The Establishment of Solid Nuclear Fusion Reactor", *J. High Temp. Soc.* 34, 85-93, 2008.

[3] A. Kitamura et al., "Anomalous effects in charging of Pd powders with high density hydrogen isotopes", *Physics Letters A*, 373(35), 3109–3112, 2009. doi: 10.1016/j.physleta.2009.06.061

[4] T. Kobayashi and K. Naitoh, "Quasi-stability theory with multi-dimensional Taylor expansion: revealing transmutation of atoms in cold fusion", *22nd International Conference on Condensed Matter Nuclear Science (ICCF22) Book of Abstracts*, 18-19, 2019.

[5] R. Konagaya et al., "Development of weak cold-fusion engine (Fusine) assisted by molecular chemical reaction: based on double focusing-compression over 1,000 bar and 7,000 K due to pulsed supermulti-jets colliding", *22nd International Conference on Condensed Matter Nuclear Science (ICCF22) Book of Abstracts*, p.15, 2019.

[6] K. Naitoh et al., "Fundamental Experimental Tests toward Future Cold Fusion Engine Based on Point-compression due to Supermulti-jets Colliding with Pulse (Fusine)", *J. Condensed Matter Nucl. Sci.* 24, 236-243, 2017.

[7] T. Kobayashi, K. Naitoh, Y. Wake, Y. Naridomi, A. Takahashi, R. Seto, H. Ido, J. Hachisuka, "Development of reaction system with small chamber for fundamental experiments measuring anomalous heat effect", *Proc. of JCF20*, 1-8, 2020.

[8] T. Kobayashi, K. Naitoh, J. Shigemura, D. Okada, Y. Nomura, "Heat generation of metal composite powder caused by the pulse flow of hydrogen gas", *Proceedings of the 22nd*

Meeting of Japan CF Research Society JCF 22, pp. 40-49, 2022.

[9] T. Kobayashi, K. Naitoh, D. Okada, R. Nakagawa, Y. Toba, "Fundamental experiments of anomalous heat effect in metal composite powder exposed to pulsed high-pressure hydrogen gas", *Abstracts of the 23rd Meeting of Japan CF Research Society JCF 23*, 10, 2023

[10] A. Takahashi et al., "Latest Progress in Research on AHE and Circumstantial Nuclear Evidence by Interaction of Nano-Metal and H(D)-Gas", *J. Condensed Matter Nucl. Sci.*, 33, 14-32, 2020.

[11] R. Konagaya, K. Naitoh, T. Kobayashi, Y. Isshiki, et al., "Two Prototype Engines with Colliding and Compression of Pulsed Supermulti-Jets through a Focusing Process, Leading to Nearly Complete Air Insulation and Relatively Silent High Compression for Automobiles, Motorcycles, Aircrafts, and Rockets", *SAE Technical Paper*, 2020-01-0837, 2020. doi:10.4271/2020-01-0837

[12] A. Sasoh. (2020). Compressible Fluid Dynamics and Shock Waves: First Edition. Springer.

Fundamental experiments of anomalous heat effect in metal composite powder exposed to pulsed high-pressure hydrogen gas

Tomotaka Kobayashi[1], Ken Naitoh[1], Daiki Okada[1], Ryuki Nakagawa[1], Yuta Toba[1],

Masaharu Uchiumi[2], Daisuke Nakata[2]

[1]Waseda University, Tokyo, Japan
[2]Muroran Institute of Technology, Hokkaido, Japan

E-mail: winningshot1996@asagi.waseda.jp

Abstract Anomalous heat generations in hydrogen or deuterium gas absorption by nickel or palladium powder were reported. We have developed a reaction system with a small chamber and have conducted fundamental experiments on hydrogen gas absorption by metal powder. In our previous reports, positive correlations between the temperature rise and both initial temperature and hydrogen gas pressure were observed. A larger temperature rise in the experiments with the pulse flow was also observed in the previous experiments. In this report, we improved a reaction system for experiments with high-pressure hydrogen gas and conducted a fundamental experiment of hydrogen gas absorption with Pd-Ni-Zr composite powder to obtain a larger temperature rise. As a result, over 150 K of temperature rise is observed in the experiment conducted under the condition of 300 °C of initial temperature and 8 MPaG of the hydrogen gas. In addition, the influence of a small amount of oxygen gas included in the reaction chamber initially on temperature raise is also tested. The observed temperature rise in the experiment with residual air is larger than that of the experiment without residual air.

Keywords: Anomalous heat, Metal composite powder, Hydrogen gas, Pulse flow, High pressure

1. Introduction

It is known that anomalous heat is generated when hydrogen or deuterium is absorbed by nickel or palladium [1-4]. In previous research, anomalous heat generation is observed in several patterns. For example, Miley reported anomalous heat in the electrolysis using nickel film [2], Arata reported anomalous heat generation in the long-term exposure of metal powder (nickel or palladium) to hydrogen (or deuterium) gas [3], and Kitamura reported anomalous effects in hydrogen (or deuterium) gas absorption by mixed oxides of palladium and zirconium [4].

Our purpose is to develop a new energy generator using anomalous heat, which is

143

accelerated by very high compression obtained by the collision of the high-speed multi-jets repeatedly [5-9]. Therefore, we focused on heat generation during hydrogen gas absorption by metal composite powder. We have developed a reaction system with a small chamber (Fig. 1) and have conducted some fundamental experiments to evaluate the anomalous heat in the hydrogen gas absorption of metal powder (especially under the rapid pressure increase).

In our previous report, we conducted experiments on low-pressure (< 1 MPaG) hydrogen gas absorption by Pd-Ni-Zr composite powder (PNZ10r, provided by Technova Inc.) [10] with pulsed flow generated by the solenoid valve. In the experiment under the condition of 240 °C of initial temperature and 0.8 MPaG of the hydrogen gas pressure, 35 K of temperature rise was observed (Fig. 2) [11]. In addition, the positive correlations between the temperature rise and both initial temperature and hydrogen gas pressure were observed in past experiments [12].

In this report, we develop a reaction system for experiments with high-pressure hydrogen gas (Fig. 2) and conduct a fundamental experiment of hydrogen gas absorption with Pd-Ni-Zr composite powder (PNZ10r) to obtain a larger temperature rise. In addition, we also experiment with a small amount of air left in the reaction chamber to measure the effect of oxygen on heat generation.
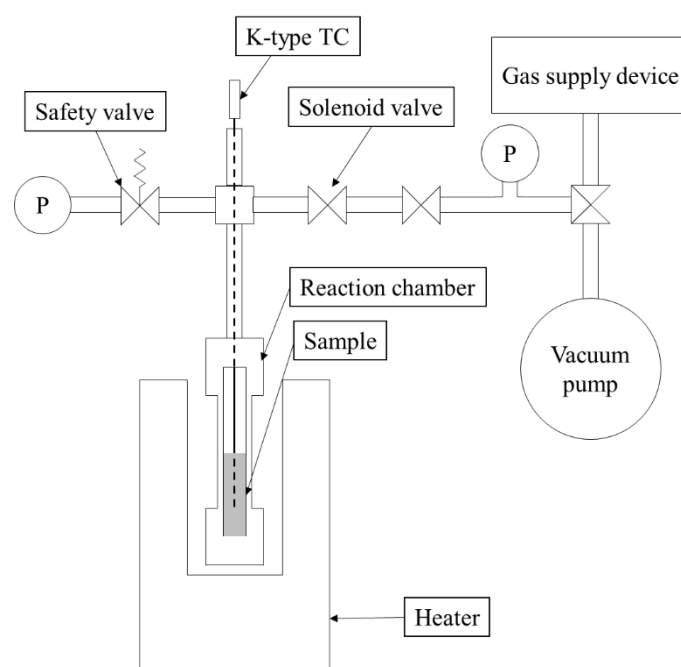
Fig. 1. Reaction system in our previous report [11]
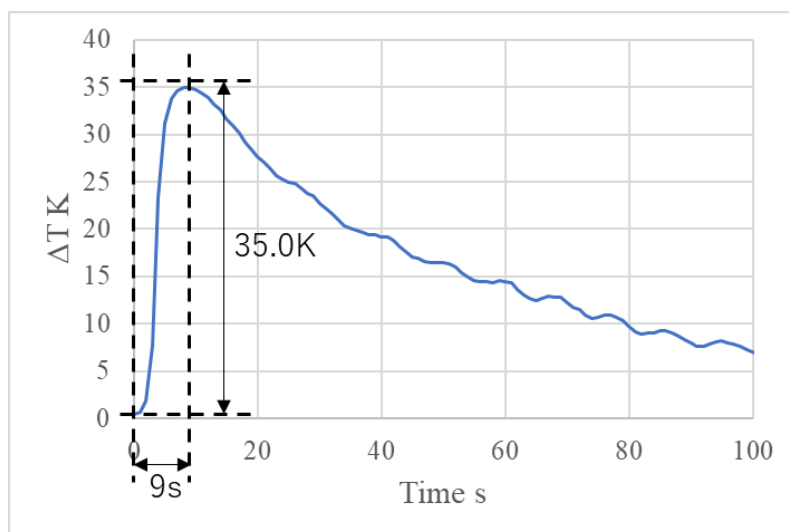
**Fig. 2.** Experimental result in our previous report [11]

2. Experimental device

In this report, we improve a reaction system for experiments with high-pressure hydrogen gas (Fig. 3) and conduct a fundamental experiment of hydrogen gas absorption with Pd-Ni-Zr composite powder (PNZ10r) to obtain a larger temperature rise. The reaction system for experiments with high-pressure hydrogen gas pulse is designed to operate at 10 MPaG and cleared the airtightness test at 9.5 MPaG. In this report, air-operated valves that can operate under high pressure (over 1 MPaG) are installed in the reaction system. The air-operated valves can be operated remotely.

The outline of the reaction system is shown in Fig. 3. The system is constructed of a heater, reaction chamber, K-type thermocouple, safety valve, pressure sensor, three air-operated valves, hand valves, high-pressure gas tank, and vacuum pump.

The reaction chamber having about 2 mL volume is made of stainless steel (SUS316L). The heater is used for preheating the reaction chamber. It can be heated in the range of 100 - 300 °C. The K-type thermocouple, whose tip is embedded in the sample, is used for measuring the sample temperature. The high-pressure gas tanks (nitrogen or hydrogen gas) are used to supply gas during the experiments. The hydrogen gas is provided as pulse flow by the air-operated valve. The maximum pressure in the experiment is 8 MPaG. The pressure of the gas provided in the reaction chamber is measured by the pressure sensor. The safety valve opens when the pressure in the chamber exceeds 10 MPaG to prevent the breaking down of the system. The vacuum pump is used for evacuation. The ultimate pressure of the vacuum pump is 1.6 Pa.

Specification of the reaction system is shown in Table 1.
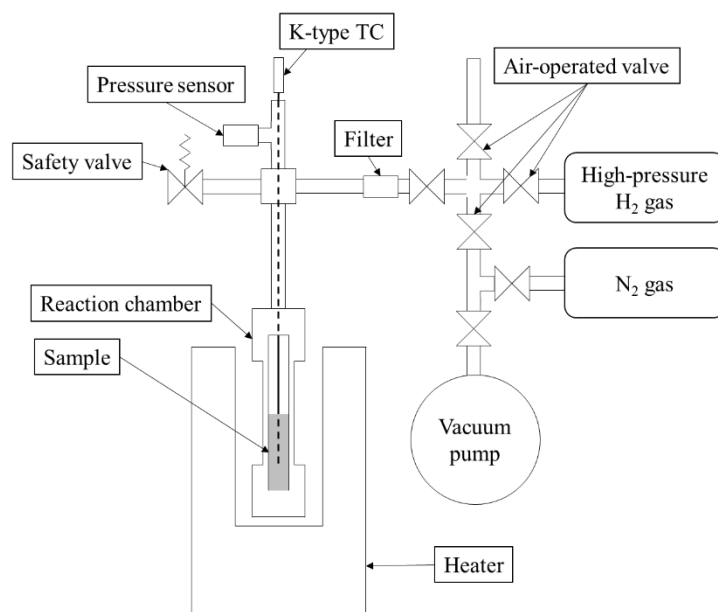
Fig. 3. Outline of the reaction system

Table 1. Specification of the reaction system

Material of reaction chamber	SUS316L
Volume of reaction chamber	2 mL
Ultimate pressure of vacuum pump	1.6 Pa
Maximum pressure of loading gas	8 MPaG
Maximum temperature of heater	300 °C

3. Procedure of the experiment

The procedure of the experiment is shown in Fig. 4. First, the sample (Pd-Ni-Zr composite powder [11]) is set in the reaction chamber (no sample is set in the control experiment). Then, the chamber is preheated by the heater. After that, the chamber is evacuated by the vacuum pump. In the experiment with a small amount of air, evacuation is stopped at 0.09 MPaG (0.1 atm of air left). After the evacuation, hydrogen gas is loaded to the upstream side of the air-operated valve. After that, the air-operated valve is opened, and the pulse flow of the hydrogen gas enters the chamber. The temperature increase of the sample is measured by the K-type thermocouple. At the end of the experiment, loaded hydrogen gas was replaced with nitrogen gas.
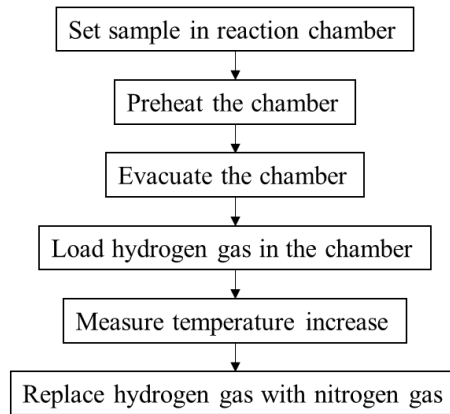
Fig. 4. Procedure of the experiment

4. Experimental result

Experimental conditions are shown in Table 2. In the experiments, 3.0 g of Pd-Ni-Zr composite powder (PNZ10r, provided by Technova Inc.) [10] is used as a sample.

The experiments are conducted using hydrogen gas. The experiments are conducted in the range of loaded gas pressure 1 - 8 MPaG and initial temperature of sample 300 °C.

Table 2. Experimental conditions

Sample	Pd-Ni-Zr composite powder (PNZ10r) [10]
Sample mass	3.0 g
Kind of gas	Hydrogen
Gas pressure	1.0 – 8.0 MPaG
Initial temperature	300 °C

4.1 Result of the control experiment (without the sample)

In this report, the control experiment is conducted separately. In the control experiment, PNZ10r is not used (the control experiment is conducted with no sample powder).
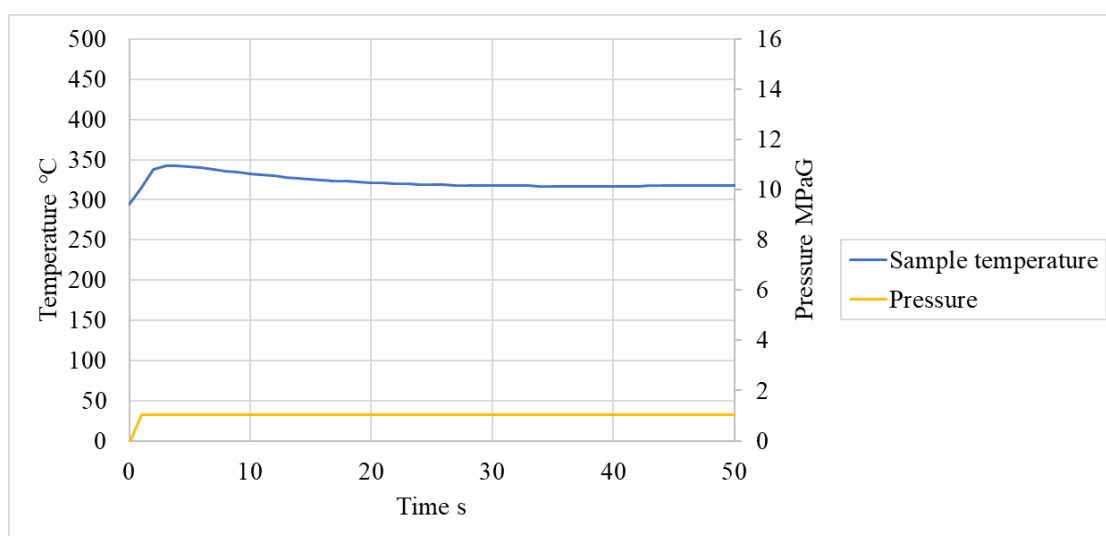
Figure 5 shows the result of the control experiment (using no PNZ10r, 8.0 MPaG of gas pressure, and 300 °C of initial temperature). A blue line shows the time histories of measured temperature (of gas in the reaction chamber), while a yellow line shows the time histories of pressure in the reaction chamber. In the experiment, 18.5 K of temperature rise was observed simultaneously with the hydrogen gas loading. It is considered that this temperature rise is due to adiabatic compression. From this result, it is considered that the temperature rise due to the heat generation can be obtained by subtracting that in the control experiment from that in the experiment with a sample.

147
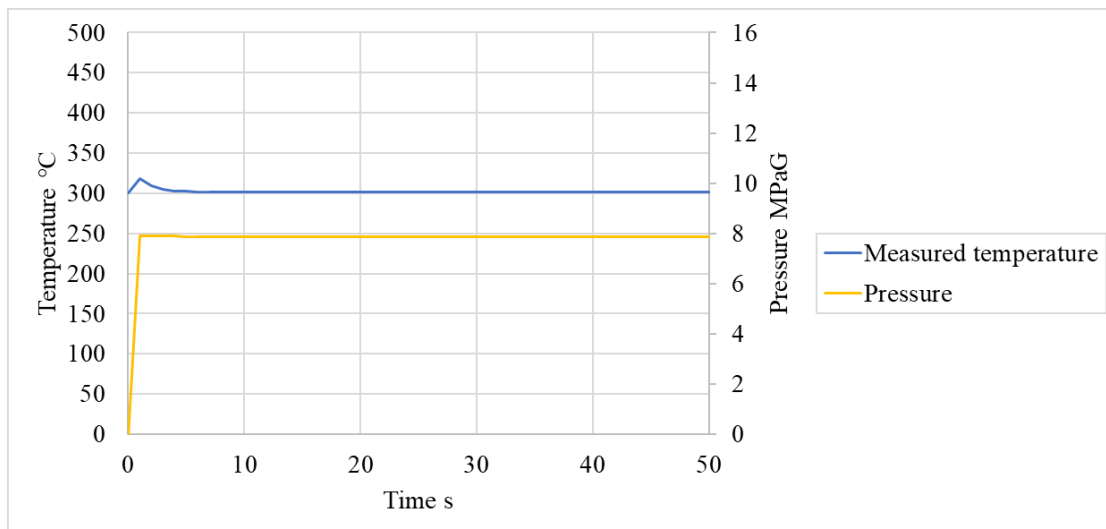
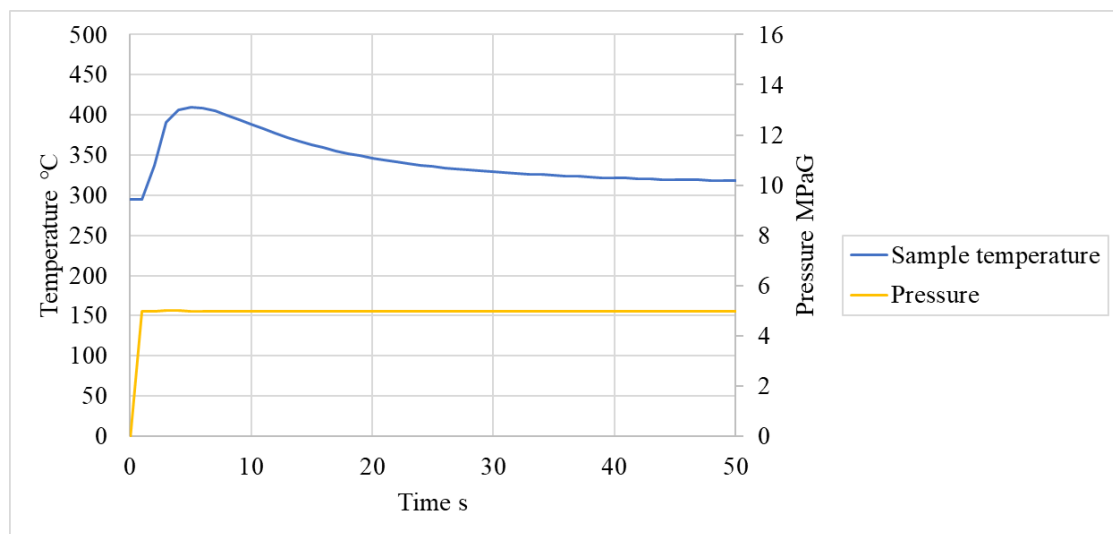**Fig. 5.** Result of the control experiment (without PNZ10r, 300°C, 8.0 MPaG)

4.2 Result of the experiments with the sample

Figure 6 shows the result of the experiment (using 3.0 g of PNZ10r, 1.0 MPaG of gas pressure, and 300 °C of initial temperature). A blue line shows the time histories of temperature for the PNZ10r sample, while a yellow line shows the time histories of pressure in the reaction chamber. In the experiment, temperature rise begins just after hydrogen gas loading. 47.7 K of temperature rise was observed about 5 seconds after the beginning of the temperature rise. Considering the control experiment, the temperature rise due to the heat generation in this experiment is 29.2 K.
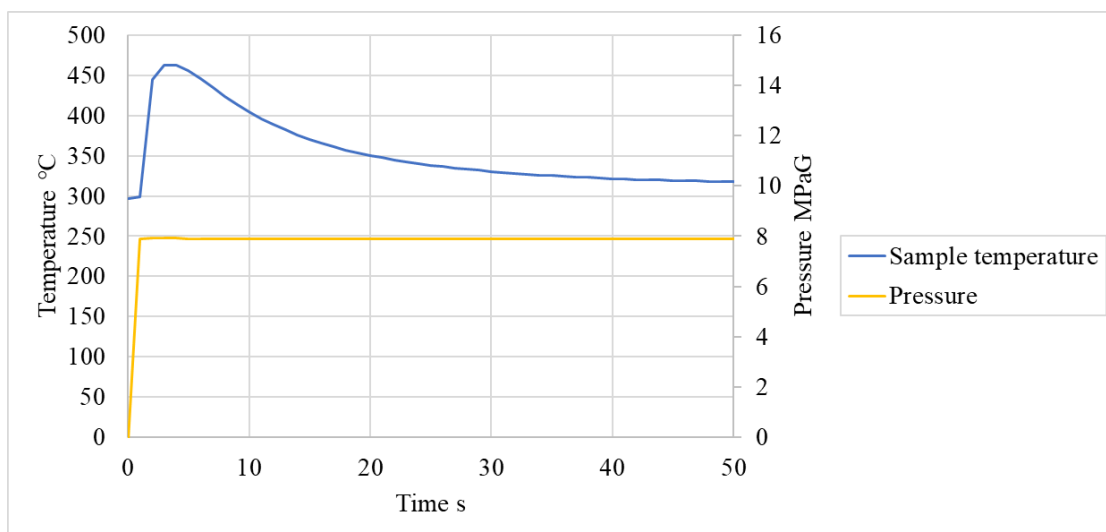

Fig. 6. Result of the experiment (PNZ10r 3.0 g, 300°C, 1.0 MPaG)

148

Figure 7 shows the result of the experiment (using 3.0 g of PNZ10r, 5.0 MPaG of gas pressure, and 300 °C of initial temperature). In the experiment, temperature rise begins just after hydrogen gas loading. 115.0 K of temperature rise was observed about 5 seconds after the beginning of the temperature rise. Considering the control experiment, the temperature rise due to the heat generation in this experiment is 96.5 K.
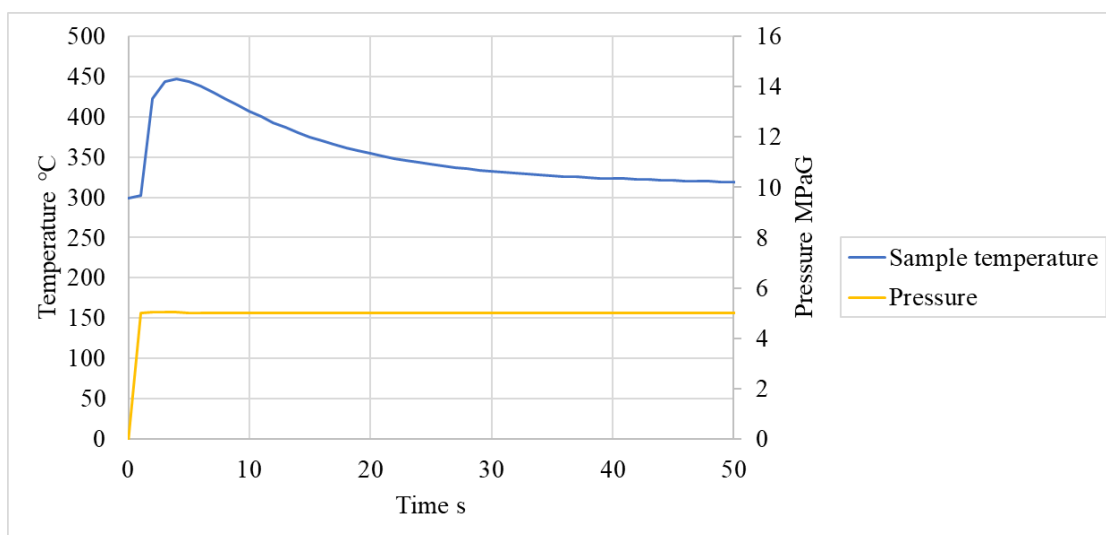

Fig. 7. Result of the experiment (PNZ10r 3.0 g, 300°C, 5.0 MPaG) [13]

Figure 8 shows the result of the experiment (using 3.0 g of PNZ10r, 8.0 MPaG of gas pressure, and 300 °C of initial temperature). In the experiment, temperature rise begins just after hydrogen gas loading. 166.9 K of temperature rise was observed about 4 seconds after the beginning of the temperature rise. Considering the control experiment, the temperature rise due to the heat generation in this experiment is 148.4 K.

Fig. 8. Result of the experiment (PNZ10r 3.0 g, 300°C, 8.0 MPaG)

The experiment with a small amount of air left in the reaction chamber is also conducted. Figure 9 shows the result of the experiment (using 3.0 g of PNZ10r, 5.0 MPaG of gas pressure, and 300 °C of initial temperature). In the experiment, temperature rise begins just after hydrogen gas loading. 148.2 K of temperature rise was observed about 4 seconds after the beginning of the temperature rise. Considering the control experiment, the temperature rise due to the heat generation in this experiment is 129.7 K.

Fig. 9. Result of the experiment
(PNZ10r 3.0 g, 300°C, 5.0 MPaG, with a small amount of air)

5. Comparison of the experimental results with and without residual air

According to Figs. 7 and 9, temperature rise due to the heat generation in the experiments (using 3.0 g of PNZ10r, 5.0 MPaG of gas pressure, and 300 °C of initial temperature) were 96.5 K (without residual air) and 129.7 K (with residual air). The temperature rise in the experiment with residual air is about 30 % larger than that of the experiment without residual air.

6. Conclusion

In this report, we improve the reaction system for the experiments with high-pressure hydrogen gas and conduct fundamental experiments of hydrogen gas absorption with PNZ10r. In the experiment conducted under the condition of 300 °C of initial temperature and 8 MPaG of the hydrogen gas, about 150 K of temperature rise due to the heat generation is observed.

Moreover, the influence of a small amount of air included in the reaction chamber initially on temperature rise is also tested. The observed temperature rise in the experiment with residual air is larger than that of the experiment without residual air.

Aiming at a larger temperature rise, we will conduct further experiments with the focusing compression due to supermulti-jets colliding. We will also consider the detail of the heat generation and model it to estimate the calorific value of anomalous heat.

References

[1] Y. Iwamura et al., "Anomalous Heat Effects Induced by Metal Nano-composites and Hydrogen Gas", *J. Condensed Matter Nucl. Sci.* 29, 119-128, 2019.

[2] G. H. Miley and J. A. Patterson, "Nuclear transmutations in thin-film nickel coatings undergoing electrolysis", *J. New Energy* 1, p.5, 1996.

[3] Y. Arata and Y. Zhang, "The Establishment of Solid Nuclear Fusion Reactor", *J. High Temp. Soc.* 34, 85-93, 2008.

[4] A. Kitamura et al., "Anomalous effects in charging of Pd powders with high density hydrogen isotopes", *Physics Letters A*, 373(35), 3109–3112, 2009. doi:10.1016/j.physleta.2009.06.061

[5] T. Kobayashi and K. Naitoh, "Quasi-stability theory with multi-dimensional Taylor

expansion: revealing transmutation of atoms in cold fusion", *22nd International Conference on Condensed Matter Nuclear Science (ICCF22) Book of Abstracts*, 18-19, 2019.

[6] A. Takahashi et al., "Latest Progress in Research on AHE and Circumstantial Nuclear Evidence by Interaction of Nano-Metal and H(D)-Gas", *J. Condensed Matter Nucl. Sci.* 33, 14-32, 2020.

[7] R. Konagaya et al., "Development of weak cold-fusion engine (Fusine) assisted by molecular chemical reaction: based on double focusing-compression over 1,000 bar and 7,000 K due to pulsed supermulti-jets colliding", *22nd International Conference on Condensed Matter Nuclear Science (ICCF22) Book of Abstracts*, p.15, 2019.

[8] K. Naitoh et al., "Fundamental Experimental Tests toward Future Cold Fusion Engine Based on Point-compression due to Supermulti-jets Colliding with Pulse (Fusine)", *J. Condensed Matter Nucl. Sci.* 24, 236-243, 2017.

[9] T. Kobayashi, K. Naitoh, Y. Wake, Y. Naridomi, A. Takahashi, R. Seto, H. Ido, J. Hachisuka, "Development of reaction system with small chamber for fundamental experiments measuring anomalous heat effect", *Proc. of JCF20*, 1-8, 2020.

[10] A. Takahashi et al., "Latest Progress in Research on AHE and Circumstantial Nuclear Evidence by Interaction of Nano-Metal and H(D)-Gas", J. Condensed Matter Nucl. Sci., 33, 14-32, 2020.

[11] T. Kobayashi et al., "Heat generation of metal composite powder caused by the pulse flow of hydrogen gas," *Proceedings of the 22nd Meeting of Japan CF Research Society*, 40-49, 2022.

[12] T. Kobayashi, J. Shigemura, K. Naitoh, Y. Mori, R. Seto, J. Hachisuka, "Temperature and pressure dependence of anomalous heat generation occurring in hydrogen gas absorption by metal powder", *J. Condensed Matter Nucl. Sci.* 36 (2022) 318–326.

[13] T. Kobayashi, K. Naitoh, D. Okada, R. Nakagawa, Y. Toba, M. Uchiumi, D. Nakata, "Estimation of the heat generation of the metal composite powder absorbing the pulsed flow of hydrogen gas", *J. Condensed Matter Nucl. Sci.*, 2023 submitted.

Heat Measurement in Hydrogen Desorption Experiment using a Pd-Ni Sample

Nagayuki Yanagidate[*], Tomo Nemoto, Sora Komukai,
Aiko Shoji, Shinya Narita

Iwate University
Morioka, Iwate, 020-8551, Japan
[*]g0322185@iwate-u.ac.jp

Abstract

In this study, hydrogen absorption and desorption experiments were performed using samples of Ni membranes that were deposited on a Pd foil. Consequently, an increase in the sample temperature was observed with gas release from the sample. In previous experiments, a constant current was applied to the sample to control hydrogen desorption by heating the sample with Joule heat; however, this method resulted in unstable sample temperature measurements owing to changes in the power supply caused by changes in the sample resistance. Therefore, the experimental system was modified to supply constant power. In the experiment employing a modified system, an exothermic phenomenon similar to that in previous experiments was observed. The maximum excess heat estimated from heat generation is approximately 0.3 W.

1. Introduction

Some groups have reported that excess heat is observed in hydrogen absorption and desorption processes involving metal composite samples such as Cu-Ni [1,2]. The phenomenon observed in these experiments may have originated from a low-energy nuclear reaction in condensed matter. The following sample conditions may be related to their occurrence:

- The specific properties of the metal composite samples
- The fineness of the structure, such as the presence of fine particles and a thin membrane

Considering these conditions, H and D absorption and desorption experiments were conducted using a Pd foil sample coated with a fine-structured Ni membrane at the interface. Subsequently, unusual thermal behaviors were observed, such as short-period fluctuations in the temperature or bust-like heat generation in the H/D desorption process [3,4]. These anomalous events may also be related to the nuclear effects. However, in previous desorption experiments, a constant current was applied to stimulate H/D diffusion; thus, it is possible that the Joule heating due to the power fluctuations in the sample affected the temperature variation. Subsequently, a new constant power supply system was developed and used to

conduct desorption experiments.

In this study, hydrogen absorption and desorption experiments were performed using a Pd-Ni sample with a modified experimental system that is expected to make heat measurement more precise.
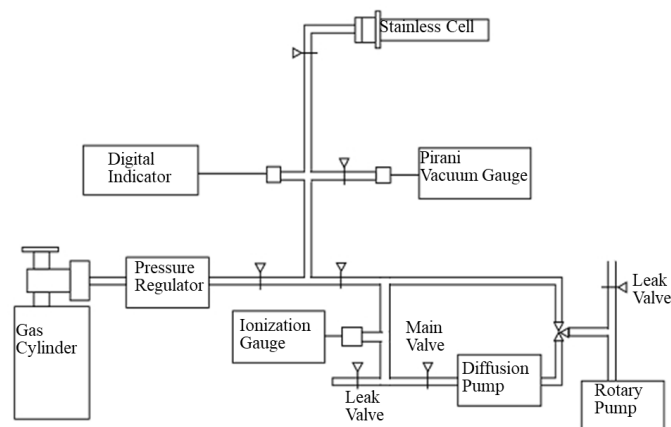
2. Experiment

2.1 Sample preparation

Pd-Ni samples comprising a Ni membrane coated on the surface of a Pd foil were prepared using the following procedure: a fine structure was formed on the surface of the Pd foil (10 mm $\times$ 10 mm $\times$ 0.1 mm) via etching using an Ar^+ ion beam. The surface morphology was examined using atomic force microscope (AFM), which revealed several projections with a height of approximately 200 nm and a width of approximately 2 μm [3]. Subsequently, a Ni membrane with a thickness of approximately 100 nm was coated on the surface of the Pd foil using Ar^+ ion sputtering.

2.2 Absorption experiment

The fabricated Pd-Ni complex sample was placed in the stainless cell of the absorption experimental setup, exposed to H_2 gas (purity:99.99999% or higher) at 5 atm, and pressurized for approximately 24 h. The weight of the samples was measured before and after loading, and the loading ratio (H/Pd) was calculated based on the difference in the weights. The H/Pd is typically 0.7–0.8. A schematic of the experimental setup is shown in Fig. 1.


Fig. 1. Schematic of the absorption apparatus.

2.3 Desorption experiment

In the desorption experiment, the Pd-Ni sample was placed in a chamber that was evacuated to 10^{-4} Pa using a rotary pump and a turbo-molecular pump (TMP). A DC power supply (TEXIO: PPX20-5) was then used to provide constant power (0.6 W) to stimulate hydrogen

diffusion from the sample via Joule heating. Subsequently, desorption experiments were conducted for approximately 24 h, and the sample temperature and pressure in the chamber, voltage applied to the sample, and current, were monitored every 0.1 s. Two types of thermometers were used to measure the sample temperatures: a thermocouple (K-type) and an IR thermometer (Chino: IR-CAEJCS).

In addition, a camera was used to observe sample deformation during the desorption experiments. Yamaguchi et al. observed that heat generation correlated with sample deformation in their experiments, wherein Pd multilayer samples were employed. Deformation is caused by internal stresses arising from hydrogen diffusion in the sample and the embrittlement of the sample metal [5]. A schematic of the setup used for the desorption experiments is shown in Fig. 2.
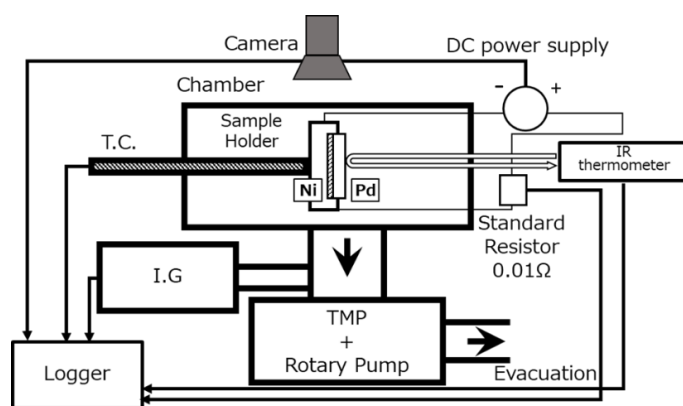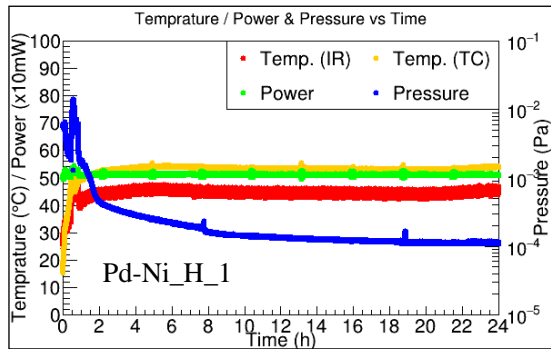

Fig. 2. Setup for the desorption experiment.

3. Results and Discussion

Figure 3(a) shows the time dependences of the sample temperature, power consumption, and pressure in the chamber for one of the desorption experiments (Pd-Ni_H_1). An intermittent temperature increase that occurred concurrently with the pressure behavior was observed approximately 0.5 h after applying the electric power; thereafter, the temperature did not change significantly. The power of the samples remained almost constant during the experiments. It is noteworthy that the periodic fluctuations in the power are owing to the noise of the data logging system. Figure 3 (b) shows an enlarged plot of the first 4 h of the experiment, where a clear correlation between the temperature and pressure changes can be observed. This occurred 0.5 h after the experiment and continued for approximately 0.4 h. The increase in the sample temperature at this time is approximately 4°C for the thermocouple and 14°C for the IR thermometer. It was assumed that the main reason for the difference in the indicated values between the two thermometers is that the IR was not properly calibrated. The results of the 4 runs ("Pd-Ni_H_1," "Pd-Ni_H_2," "Pd-Ni_H_3," "Pd-Ni_H_4") that had

been conducted so far are shown in Fig. 4. A similar behavior is observed in every run.

For reference, an experiment was performed using a Pd-Ni sample without H loading (hereafter referred to as the blank experiment), and the results are shown in Fig. 5. No significant changes in the sample temperature or pressure in the chamber were observed, similar to the desorption experiments. Therefore, a reaction originating from heat evolution is considered to occur during the hydrogen diffusion process.
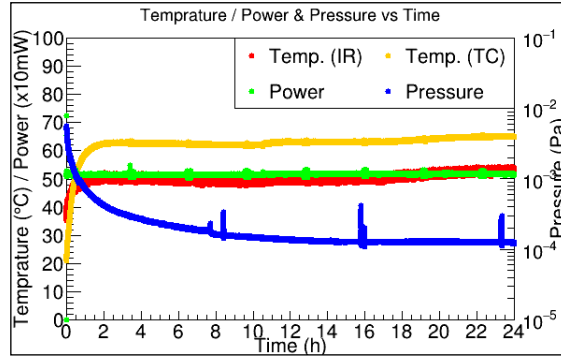

Fig. 3(a). Time dependence of the temperature, power, and pressure in the desorption experiment.
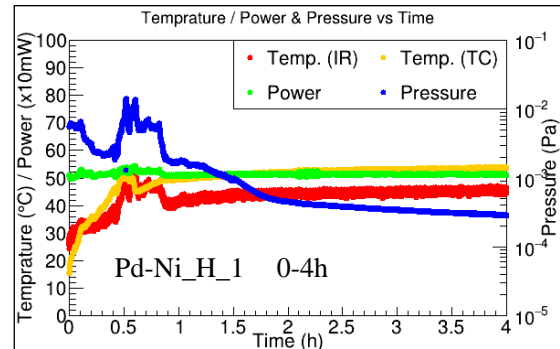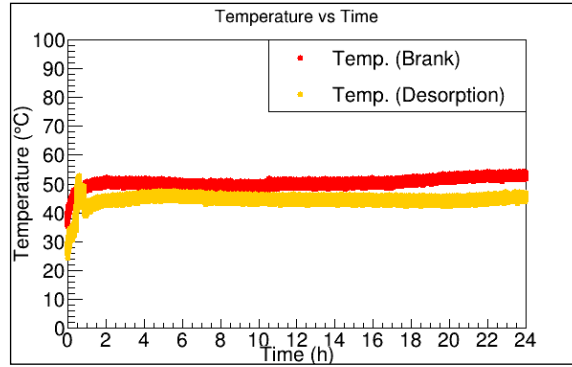

Fig. 3(b). Time dependence of the temperature, power, and pressure in the desorption experiment at the start of the experiment.
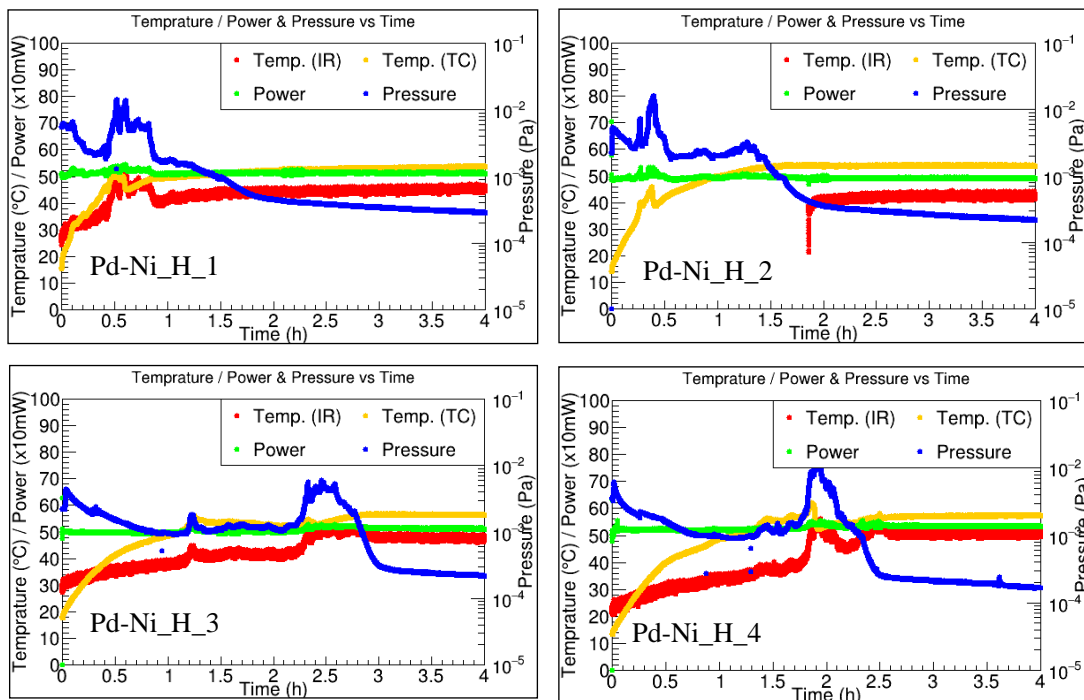
Fig. 4. Time dependence of the temperature, power, and pressure in the four desorption experiments.

156

Fig. 5. Time dependence of the temperature, power, and pressure in the blank experiment.

Fig. 6. Time dependence of the temperature in the blank (red) and desorption experiments (orange).

The excess heat was estimated from the difference between the temperature observed in the blank experiment, $T_b(t)$, and that observed in the desorption experiment, $T_f(t)$. During this process, the following should be noted: the condition under which the sample was placed in the holder was not exactly the same for each experiment, and the temperature reached by the sample may have differed even when the same electric power was supplied in the blank experiment. Subsequently, the difference between the temperature at the end of the desorption experiment, $T_f(t_{end})$, (it was assumed that no H remains in the sample at that time) and that at the end of the blank experiment, $T_b(t'_{end})$, was considered (see Fig.6); and the actual temperature difference ΔT was obtained as follows.

$$\Delta T = [T_f(t) + \{T_b(t'_{end}) - T_f(t_{end})\}] - T_b(t)$$

The excess heat was then calculated using the ΔT and the results of a reference experiment conducted beforehand to investigate the correlation between the power supplied to the sample and the temperature increase.
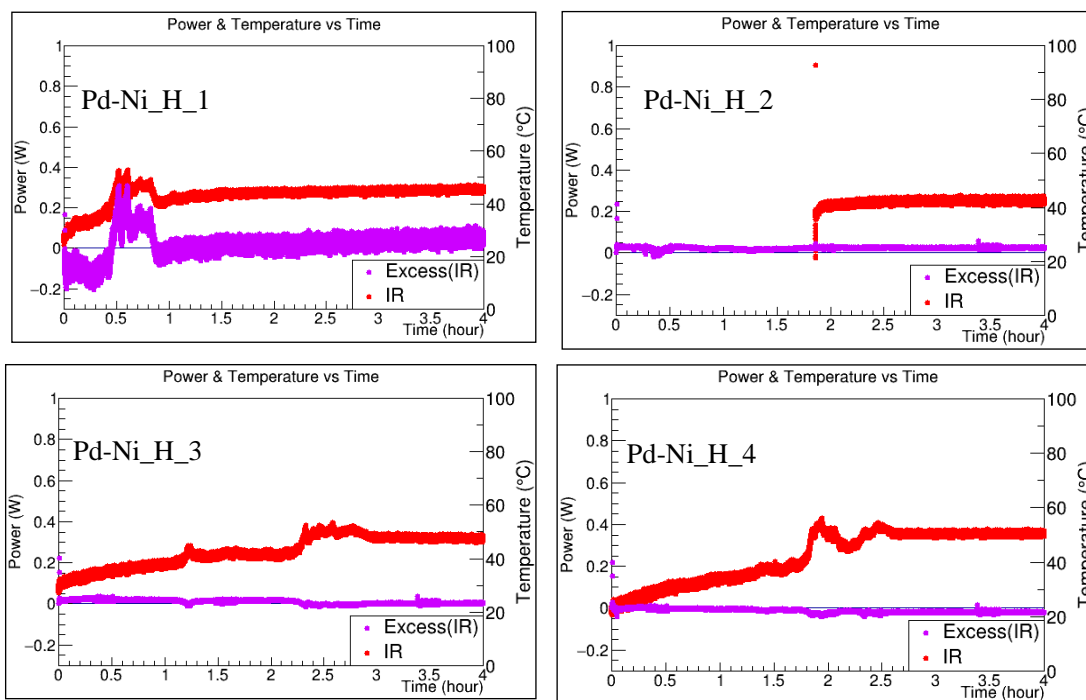
157

Fig. 7(a). Excess heat obtained in the temperature measurements using an IR thermometer.
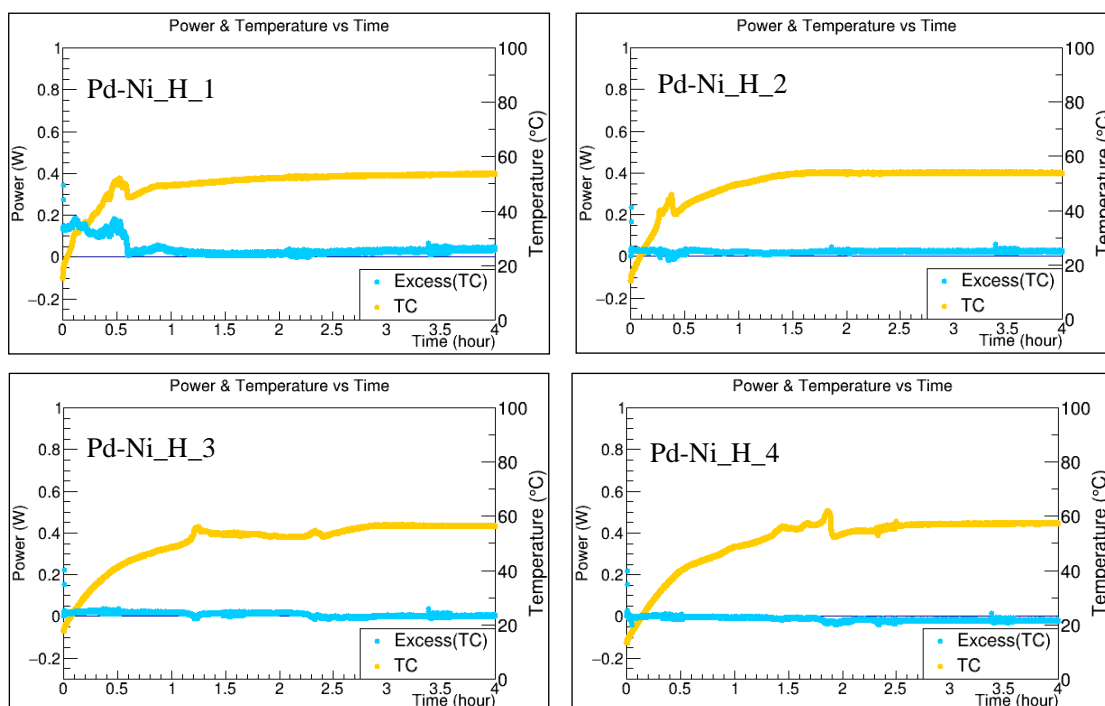

Fig. 7(b). Excess heat obtained in the temperature measurements using a thermocouple.

The excess heat obtained from the temperature measurements using the IR and thermocouples is shown in Fig. 7(a) and 7(b), respectively. For "Pd-Ni_H_1," an maximum excess heat of approximately 0.3 W was observed 0.5 h after the start of the experiment for about 1 h. However, from the thermocouple measurements, a maximum excess heat of approximately 0.2 W was observed immediately after the start of the experiment for approximately 0.5 h. The difference in the behavior between these results suggests that there are improvements that should be considered in the excess heat calculation, including the accuracy of temperature measurement. No significant excess heat was observed in the other runs, "Pd-Ni_H_2," "Pd-Ni_H_3," and "Pd-Ni_H_4." Additionally, there are still many uncertainties in the temperature measurements, which should be resolved in further studies.

A camera was used to observe the temperature increase and sample deformation of the Pd-Ni sample in "Pd-Ni_H_1." Fig. 8(a) and Fig. 8(b) show the samples immediately after and 1 h after the start of the desorption experiment, respectively. The area surrounded by the dotted red lines represents the Pd-Ni sample. The Ni side exhibited convex deformation before and after the generation of the indicated excess heat. Deformation was observed in the sample subjected to excess heat, and this may be associated with the model proposed by Yamaguchi et al [5]. It is necessary to examine in more detail the correlation between the magnitude of the excess heat generated and degree of deformation, and the correlation between the timing of deformation and heat evolution.
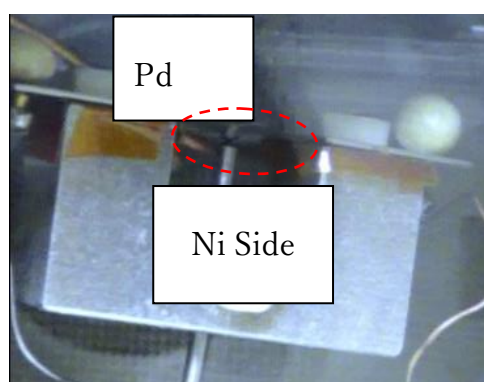
Fig. 8(a). Image of the Pd-Ni sample immediately after the start of the desorption experiment.
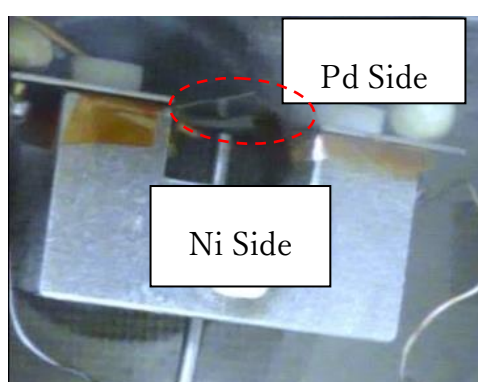
Fig. 8(b). Image of the Pd-Ni sample 1h after the start of the desorption experiment.

4. Summary

Hydrogen absorption and desorption experiments were performed in this study using samples of Ni membranes deposited on a Pd foil using a modified experimental system that applied constant power to the sample to enable the precise measurement of the heat generated. Moreover, the excess heat was evaluated based on the obtained temperature changes. Consequently, intermittent temperature increases with high reproducibility were observed. In one of the four runs, a significantly high qunatity of excess heat was observed in the early stages of the desorption experiment. Based on the evaluations, the maximum excess heat is approximately 0.3 W. However, further investigation is still required because of the systematic uncertainties in the temperature measurement and increase in the calibration data with the input power and temperature. Moreover, the sample was deformed, which might be correlated with the generation of excess heat. This phenomenon may be the key to determining an induced mechanism for the reaction that results in heat generation.

References

[1] Takahashi et al., J. Condensed Matter Nucl, Sci. 33 (2020) 14.

[2] Y. Iwamura et al., Proc. of JCF21, (2020) 1.

[3] M. Endo et al., Proc. of JCF20, (2019) 61.

[4] S. Narita et al., Proc. of JCF22, (2022) 50.

[5] E. Yamaguchi et al., Jpn. J. Appl. Phys., 29 (1990) L666.